

NORTHWESTERN UNIVERSITY

Building the Nanoplasmonics Toolbox Through Shape Modeling and Single Particle Optical  
Studies

A DISSERTATION

SUBMITTED TO THE GRADUATE SCHOOL IN PARTIAL FULFILLMENT OF THE  
REQUIREMENTS

for the degree

DOCTOR OF PHILOSOPHY

Field of Chemistry

By

Emilie Ringe

EVANSTON, ILLINOIS

August 2012

© Copyright by Emilie Ringe 2012  
All Rights Reserved

## ABSTRACT

### Building the Nanoplasmonics Toolbox Through Shape Modeling and Single Particle Optical Studies

Emilie Ringe

Interest in nanotechnology is driven by unprecedented properties tailorability, achievable by controlling particle structure and composition. Unlike bulk components, minute changes in size and shape affect the optical and electronic properties of nanoparticles. Characterization of such structure-function relationships and better understanding of structure control mechanisms is crucial to the development of applications such as plasmonic sensors and devices. The objective of the current research is thus twofold: to theoretically predict and understand how shape is controlled by synthesis conditions, and to experimentally unravel, through single particle studies, how shape, composition, size, and surrounding environment affect plasmonic properties in noble metal particles. Quantitative, predictive rules and fundamental knowledge obtained from this research contributes to the “nanoplasmonics toolbox”, a library designed to provide scientists and engineers the tools to create and optimize novel nanotechnology applications.

In this dissertation, single particle approaches are developed and used to unravel the effects of size, shape, substrate, aggregation state and surrounding environment on the optical response of metallic nanoparticles. Ag and Au nanocubes on different substrates are first presented, followed by the discussion of the concept of plasmon length, a universal parameter to describe plasmon energy for a variety of particle shapes and plasmon modes. Plasmonic sensing (both refractive

index sensing and surface-enhanced Raman spectroscopy) and polarization effects are then studied at the single particle level.

In the last two Chapters, analytical shape models based on the Wulff construction provide unique modeling tools for alloy and kinetically grown nanoparticles. The former reveals a size-dependence of the shape of small alloy particles (such as those used in catalysis) because of surface segregation, while the latter uniquely models the shape of many particles commonly studied for plasmonic applications.

The new models and descriptive parameters developed in this work help predict and understand shape and size effects in metal nanoparticles relevant for interdisciplinary applications of plasmonics, and help guide both non-specialists and nanotechnology researchers.

## ACKNOWLEDGMENTS

I would like to first acknowledge my advisors, Richard Van Duyne and Laurence Marks.

By being such a successful, approachable and friendly scholar, Rick has been a phenomenal role model. His enthusiasm and unmatched support, coupled with his tremendous care to ensure my career and personal life were going as I wished, made him a great advisor and also a great friend.

Rick, thank you.

By being such a curious, rigorous, and involved scholar, Laurie taught me more than the tremendous amount of knowledge he consciously shared with me. I thank him for pushing me and asking me the right questions, letting me grow and flourish in the intellectually challenging environment he created for me. Laurie, thank you.

I would also like to specially thank my committee, Profs. Seideman, Weiss, Geiger, and Schatz. Prof. Seideman, as my qualifiers committee chair, has been genuinely curious and interested, I am thankful for the opportunity to interact with her. Profs. Weiss and Geiger deserve more than is typically reserved for committee members, as they have helped me in other aspects, in particular my career path. Prof. Weiss has been of great help through my faculty applications as well as my exams. Prof. Geiger has been a tremendous mentor and teacher; for the six years I interacted with him, he has inspired me to be inquisitive and persuasive, which helped me and will help me through my career. Prof. Schatz deserve a special thank for his willingness to participate in my Ph.D. defense, in addition to the many fruitful interactions we have had over the years.

A number of other professors at Northwestern deserve thanks. My master advisor, Prof. Jim Ibers, has provided me with much support as well as his characteristic humorous comments. Profs. Kenneth Popplemeir and Peter Stair have provided me with useful input on my research ideas. A number of other professors also should be recognized for their participation in my life at Northwestern, in particular Profs. Monica Olvera de la Cruz, Eric Weitz, Mark Ratner, and Mercuri Kanatzidis.

Of course, over four years many people have been involved in my scientific and personal life; they all deserve acknowledgements, may it be for synthesizing particles, having afternoon coffee, celebrating my achievements, or being at the other end of the telephone when things are not so joyful. So many people, that I am afraid I will forget some. First and foremost, both of my groups deserve many, many thanks for their support and discussion, in the lab, the office, or in front of a drink at group events.

The highly collaborative work I have carried out by being part of the Materials Research Science and Engineering Center (MRSEC, made possible by Monica Olvera de la Cruz and her helpers, Martha Tanner, William Kung, and Ashley Walter) provided me tremendous opportunities for scientific interactions. The entire MRSEC plasmonics subgroup (IRG-3) deserves special thanks, in particular those with whom I have directly interacted: Kwonam Sohn, Jiaying Huang, Mark Langille, Jian Zhang, Michelle Personick, Chad Mirkin, Jeff McMahon, and George Schatz. Other collaborations have taught me new techniques and phenomena, and for that I would like to thank Natalie Ray, Sam Kleinman, Daniel Wells, George Oh, Luke Koscielski, Adel Mesbah, Andrew Senesi, Phoebe Li, Teri Odom, Andrej Grubisic, David Nesbitt, Marty Blaber, Jon

Dieringer, Claire Cobby, Leslie Au, and Younan Xia. It has been a pleasure and an honor to develop such great scientific relationships.

Thanks also to Paul Mulvaney, who hosted me in his group for 3 months. This was a fantastic experience which taught me in both the science and cultural realm. Prof. Mulvaney has a tremendous group and he deserves it, thanks to all of them as well.

Many thanks to all who have contributed to my social life, in and out of the office, on campus or elsewhere. This is a very long list, but you know who you are. Special thanks to Bhavya Sharma, Ashish Basuray, Sam Kleinman, Deniz Alpay, Fernanda Cardinal, Julia Baldauf, the staff at Artica, and Doug Abram.

Thanks also to everyone in the chemistry department and the TGS support staff, especially Beth Ludwig who was always there to help out. I have shared many great moments with the presidential fellows and have built lasting friendships; they and TGS deserve warm thanks.

And, last but not least, my family, both immediate and extended, past and present, has played a key role in this achievement. In particular, Aimé-Jean became a very close friend through the years; without him I would not be the same. Nicole has always been there, anytime, and I am tremendously grateful for her help and support. René has always encouraged me and it is a pleasure to make him proud. Dominic has helped me think about what I want from life, and has helped me take it a little lighter.

Thanks to all of the above and all those I forgot. My time at Northwestern has been phenomenal, beyond all my expectations, and I will always remember and cherish it.

## LIST OF ABBREVIATIONS

ALD	atomic layer deposition
BSPP	bis(p-sulfonatophenyl) phenylphosphine dihydrate dipotassium salt
CTAB	cetyltrimethylammonium bromide
DFM	dark field microscopy
EELS	electron energy loss spectroscopy
FCC	Face-centered cubic
ITO	indium tin oxide
LSPR	localized surface plasmon resonance
mPEG-SH	methoxy-poly(ethylene glycol)-thiol
MPPE	multiphoton photoelectron emission
PVP	polyvinylpyrrolidone
RI	refractive index
RIE	reactive ion etching
RIS	refractive index sensitivity
SEM	scanning electron microscope/microscopy
SERS	surface-enhanced Raman spectroscopy
TEM	transmission electron microscope/microscopy

DEDICATION

## TABLE OF CONTENTS

Section	Page #
ABSTRACT	
ACKNOWLEDGEMENTS	
LIST OF ABBREVIATIONS	
DEDICATION	
CHAPTER 1 Introduction to Nanoparticle Shape and Optical Properties	
1.1 Plasmons in Small Metal Nanoparticles	
1.2 Nanoparticle Shape Modeling	
CHAPTER 2 Materials and Methods	
2.1 Synthesis	
2.1.1 Au Cubes	
2.1.2 Au Decahedra, Au Truncated Bitetrahedra, Au Icosahedra	
2.1.3 Au Octahedra	
2.1.4 Ag Cubes	
2.1.5 Ag Bipyramids	
2.1.6 Ag-Coated Au Nanorods	
2.1.7 Ag Colloids for SMSERS	
2.2 Instrumental Methods: Single Particle Structure-Function Measurements	
2.2.1 Correlated LSPR/TEM	

2.2.2 Polarization Experiments	
2.2.3 Correlated SEM/LSPR and SEM/LSPR/TEM	
2.2.4 Correlated LSPR/SERS/TEM	
2.2.5 Correlated ALD/LSPR/TEM	
2.2.6 Correlated LSPR/SPIM/TEM	
2.2.7 Refractive Index Sensitivity Measurements	
2.2.7.1 Non-Correlated RIS Measurements	
2.2.7.2 Correlated RIS/TEM	
2.2.8. Other Experimental Observations and Notes	
2.2.8.1 Reactive Ion Etching	
2.2.8.2 Size and Corner Rounding Measurements from TEM Images	
2.3 Computational Methods	
2.2.1 Alloy Wulff Construction Code Overview	
2.2.2 Kinetic Twinned Wulff Construction Code Overview	
<b>CHAPTER 3</b> Unraveling the Effects of Size, Composition, and Substrate on the LSPR Properties of Au and Ag Nanocubes: A Systematic Single Particle Approach	
3.1 Introduction to Size, Composition, and Substrate Effects	
3.2 Previous Studies on Au Nanocubes	
3.3 Experimental Results and Discussion	
3.3.1 Effect of Size	
3.3.2 Effect of Composition	

3.3.3 Effect of Substrate	
3.3.4 Quadrupole and Dipole Modes in Ag Nanocubes	
3.3.5 Effect of Corner Rounding	
3.4 Computational Results and Discussion	
3.4.1 Effect of Substrate Composition and Layering Morphology	
3.4.2 Effect of Particle-Substrate Distance	
3.5 Conclusions	
CHAPTER 4 Plasmon Length: a Universal Parameter for the Size Dependence of Plasmonic Phenomena	
4.1 Correlated LSPR/TEM of Sharp Au Nanostructures	
4.1.1 Side Length as a Size Parameter: Shape-Dependent Descriptor, Shape Dependent Retardation Effects	
4.1.2 Plasmon Length: a Universal Parameter to Describe Size Effects	
4.1.3 Substrate Effects on Au Nanostructures	
4.1.4 Important Findings, Advantages and Limitations of the Plasmon Length Parameter	
4.2 Effective Plasmon Length: Going Beyond a Single-Parameter Model to Describe Corner Rounding and Size Effects	
4.2.1 Correlated LSPR/TEM on Ag Bipyramids	
4.2.1.1 Single Particle Comparisons	
4.2.1.2 Single Parameter Fits	
4.2.1.3 Multiple Parameter Fits	
4.2.1.3.1 Grouped Fit	

4.2.1.3.2 Plane Fit	
4.2.1.3.3 Effective Plasmon Length Fit	
4.2.1.4 Bipyramids Fits Discussion	
4.2.2 Correlated LSPR/TEM on Nanocubes	
4.2.2.1 Au Nanocubes	
4.2.2.2 Ag Nanocubes	
4.2.2.2.1 Single Parameter Fits on the Energy and FWHM of the Dipolar and Quadrupolar Resonances	
4.2.2.2.2 Multiparameter Fits: Planar and Effective Plasmon Length Approach	
4.2.2.2.2.1 LSPR Energy	
4.2.2.2.2.2 Plasmon Linewidth	
4.2.2.3 Multiparameter Modeling in Nanocubes: Effect of Composition and Discussion	
4.2.3 Origin of Simultaneous Rounding and Size Effects and Shape Comparisons	
4.3 Plasmon Length Applications to High Order Modes in Ag and Au Nanoparticles	
4.3.1 High Order Modes in Ag Nanocubes	
4.3.2 High Order Modes in Au Decahedra	
4.3.3 Higher Order Modes and Sensing Applications	
4.4 Conclusions	
CHAPTER 5 Sensing Using Plasmon Resonances and Plasmon-Enabled Spectroscopy	
5.1 Au and Ag Nanostructures for Localized Surface Plasmon Resonance Sensors	

5.1.1 Single Particle Refractive Index Sensitivity	
5.1.1.1 Correlated Single Particle Refractive Index Sensitivity Measurements of Au Decahedra, Au Truncated Bitetrahedra, and Ag Colloids	
5.1.1.2 Uncorrelated Single Particle Refractive Index Sensitivity Measurements of Au Decahedra	
5.1.1.3 Guidelines for Sensor Applications Based on Single Particle Studies	
5.1.2 Alumina Coating on Single Nanoparticles	
5.1.2.1.1 Au Decahedra	
5.1.2.1.2 Ag Nanocubes	
5.1.2.2 Effect of Alumina Coating on Refractive Index Sensitivity	
5.2 Plasmon-Enabled Sensing: Single Molecule, Single Particle Surface-Enhanced Raman Spectroscopy of Crystal Violet	
CHAPTER 6 Single Particle Studies of Polarization Effects in Plasmon Resonances	
6.1 Polarization Phenomena in Localized Surface Plasmon Resonances	
6.2 Plasmon Polarization in Isolated Au Nanostructures	
6.2.1 Au Decahedra	
6.1.2 Au Truncated Bitetrahedra	
6.2 Plasmon Polarization in Single Bimetallic Nanostructures: Hiding Anisotropy	
6.2.1 Correlated pol-LSPR/TEM of Au rods @ Ag shells	
6.2.2 Single Particle pol-LSPR of Au rods @ Ag shells	
6.3 Plasmon Polarization in Chains and Aggregates of Spheroid Au Particles	

6.3.1 Plasmon Polarization in Dimers of Spheroid Au Particles	
6.4 Plasmon Polarization in Aggregates of Sharp Au Particles	
6.4.1 Plasmon Polarization in Dimers of Sharp Au Particles	
6.4.2 Plasmon Polarization in Aggregates of 3 or More Sharp Au Particles	
6.5 Plasmon Polarization in Ag and Au Nanostructures: Comparison of one-Photon and Multiphoton Techniques Reveals Photoemission Mechanism	
6.5.1 Possible Photoemission Mechanisms	
6.5.2 Experimental Approach to Determine the Photoemission Mechanism in Ag Nanocubes	
6.5.3 Results from Polarization Experiments	
6.5.4 Corner Rounding Effects on Photoemission Intensity	
6.5.5 Conclusions	
CHAPTER 7 The Wulff Construction for Alloy Nanoparticles	
7.1 Introduction to Alloy Nanoparticles	
7.2 Previous Modeling of Alloy Nanoparticle Shape	
7.3 Mathematical Derivation of the Alloy Wulff Construction	
7.3.1 Parameters Definition	
7.3.2 Bulk and Surface Energy Definition and Derivations	
7.3.3 Energy Minimization and Final Equation Derivation	
7.4 Results of Shape Modeling Using the Alloy Wulff Construction: CuAu, AuPd, AgAu, and AgPd	
7.4.1 Energy and Unit Cell Parameter Values Used	

7.4.1.1 Bulk Free Energy	
7.4.1.2 Unit Cell Parameter	
7.4.1.3 Homogeneous Surface Free Energy	
7.4.2 Equilibrium Bulk and Surface Composition	
7.4.3 Equilibrium Particle Shape	
7.4.4 Equilibrium Total Energy as a Function of Initial Composition	
7.4.5 Size-Dependence of Results	
7.5 Discussion	
7.5.1 Comparison with Previous Models	
7.5.2 Comparison with Experimental Results	
7.5.3 Model Limitation and Possible Extensions	
<b>CHAPTER 8</b> The Kinetic Wulff Construction for Twinned Nanoparticles	
8.1 Introduction: Nanoparticle Growth and Modeling	
8.2 The Modified Wulff Construction	
8.3 Mathematical Derivation of the Kinetic Wulff Construction for Twinned Nanoparticles	
8.3.1 The kinetic Wulff Construction for Single Crystal	
8.3.2 The kinetic Wulff Construction for Twinned Nanoparticles	
8.4 Examples of Shape Modeling Using the Kinetic Wulff Construction for Twinned Nanoparticles	
8.4.1 Singly Twinned Particles	
8.4.2 Decahedral (5-Fold Twin) Nanoparticles	

8.5 Graphical User Interface for Thermodynamic and Kinetic Wulff Modeling	
8.6 Discussion: Model Limitations and Possible Extensions	
REFERENCES	
APPENDIX A MATLAB Codes	
A.1. LSPR Analysis Codes	
A.1.1 bcreator	
A.1.2 averageforb	
A.1.3 spectramathb	
A.1.4 nsnsmpack	
A.2. Alloy Wulff Construction	
A.2.1. Basic Wulff Model	
A.2.2 Subfunction Wulffbasic	
A.2.3 Number of Surface Atoms in a Basic Wulff Construction Given $h_{111}$ and $h_{100}$	
A.2.4 Alloy Wulff Model with Segregation but no Starvation	
A.2.5 Subfunction model2	
A.2.6 Main Alloy Wulff Construction Function	
A.2.7 Main alloy Wulff Construction Function with Flexible Start and End Initial Concentrations	
A.2.8 Subfunction model3	
A.2.9 Minimum Surface Concentration	

A.2.10 Minimum Bulk (Internal) Concentration	
A.2.11 Minimum Total Energy for Each Starting Composition	
A.2.12 Number of Surface Atoms	
A.2.13 h111/h100	
A.3 Kinetic Wulff Construction, GUI	
A.3.1 Kinetic Wulff Model for a Monotwinned Particle	
A.3.2 Kinetic Wulff Model for a Dh Particle	
A.3.3 Kinetic Wulff GUI	
APPENDIX B OPTICAL MEAUREMENTS ON SINGLE CRYSTALS	
VITA	

- 1-Introduction (written)(double checked)
- 2-Methods (written) (double checked)
- 3-Ag Au nanocubes (written) (double checked)
- 4- Plasmon length, effective plasmon length, high order modes (written)(double checked)
- 5- sensing (written)(double checked)
- 6- polarization (written), chains (written), SPIM (written)
- 7- alloy Wulff (written) (double checked)
- 8- Kinetic Wulff (written)

## LIST OF TABLES

Table #	Figure Title	Page #
4.1	Fit parameters for the side length fit to dipolar LSPR energy and full width at half maximum (analysis of covariance)	
4.2	Fit parameters for the plasmon length fit to dipolar LSPR energy and full width at half maximum (analysis of covariance, unconstrained slopes)	
4.3	Fit parameters for the plasmon length fit to dipolar LSPR energy and full width at half maximum (analysis of covariance, slope set equal for all shapes).	
4.4	Fit parameters for the plasmon length fit to dipolar LSPR energy and full width at half maximum for Au nanostructures on Formvar (RI = 1.5) and Si <sub>3</sub> N <sub>4</sub> (RI ~ 2) (pair wise analysis of covariance, unconstrained slopes)	
4.5	Fit parameters for plasmon length fit to dipolar LSPR energy and full width at half maximum for Au nanostructures on Formvar (RI = 1.5) and Si <sub>3</sub> N <sub>4</sub> (RI ~ 2) (pair wise analysis of covariance, constrained slopes)	
4.6	Fit parameters for plasmon length fit to dipolar LSPR energy and full width at half maximum for Au nanostructures on Formvar (RI = 1.5) and Si <sub>3</sub> N <sub>4</sub> (RI ~ 2) (global analysis of covariance)	
4.7	Linear fit parameters for the effect of size and corner truncation on plasmon energy and FWHM	
4.8	Ag bipyramids fit parameters for the grouped approaches presented in Figure 4.10	
4.9	Size and shape effect on the LSPR energy of Au and Ag nanocubes	
4.10	Size and shape effect on the LSPR FWHM of Ag nanocubes	
4.11	Calculated LSPR energies for the longitudinal plasmon mode of rounded Ag and Au rods	
4.12	Fit parameters for the plasmon energy dependence on side length for the four plasmon modes of Ag nanocubes. (unconstrained slopes, analysis of covariance)	

4.13	Fit parameters for the plasmon energy dependence on plasmon length (side length/(mode number)) of Ag nanocubes (unconstrained and constrained slopes, analysis of covariance).	
4.14	Fit parameters for the plasmon energy dependence on dipolar plasmon length for the dipolar and quadrupolar resonances in Au decahedra on Formvar and Si <sub>3</sub> N <sub>4</sub> (unconstrained slopes, analysis of covariance)	
5.1	Refractive indices of glycerol-water solutions.	
5.2	Fit parameters for the plasmon energy dependence on plasmon length for various refractive index environments (unconstrained slopes, analysis of covariance)	
5.3	Fit parameters for the plasmon energy dependence on plasmon length for various refractive index environments, excluding air (unconstrained slopes, analysis of covariance)	
5.4	Fit parameters for the plasmon energy dependence on plasmon length for various refractive index environments, excluding air (unconstrained slopes, analysis of covariance)	
5.5	Effect of 10 layers Al <sub>2</sub> O <sub>3</sub> ALD (1.1 nm) on the dipolar plasmon resonance of Au decahedra deposited on c-flat grids	
7.1	Parameters used for the computation of the bulk free energy and the unit cell parameter of CuAu, AuPd, AgAu and AgPd	
7.2	Parameters used for the computation of the surface free energy of CuAu, AuPd, AgAu and AgPd	
8.1	Parameters Used for Thermodynamic Shape Modeling	
8.2	Parameters Used for Kinetic Shape Modeling	

## LIST OF FIGURES

Figure #	Figure Title	Page #
1.1	Lycurgus cup	
1.2	Dielectric function of Ag and Au	
1.3	Approximate wavelength range of localized plasmon resonances	
1.4	Localized surface plasmon resonance (LSPR) and plasmon field distribution	
1.5	Plasmon decay pathways contributing to the plasmon linewidth	
1.6	Wulff shape representation for a face centered cubic single crystal	
1.7	Representative single crystal shapes and associated surface free energies	
1.8	The effects of interface and surface free energy on the shape of nanoparticles, modeled by the Winterbottom construction	
2.1	SEM images of Au nanocubes	
2.2	TEM and SEM images of Au decahedra synthesis products	
2.3	SEM images of Au octahedra synthesis products	
2.4	TEM images of Ag nanocubes	
2.5	SEM and TEM images of Ag bipyramids	
2.6	TEM image of Au rods @ Ag shell	
2.7	Correlated dark field microscopy and transmission electron microscopy performed on standard carbon/Formvar grids	
2.8	Example of non-traditional TEM support films and their use in correlated optical/structural measurements	
2.9	Dark field microscopy setup	
2.1	Inverted optical microscope with coupling to the video camera as well as	

	the spectrograph/CCD	
2.11	Spectral processing for single particle dark field scattering experiments. Note that normalization is optional	
2.12	Representative single particle scattering spectra before and after TEM analysis	
2.13	Partial polarization scrambling due to the dark field condenser	
2.14	Correlated LSPR/SEM validation of the polarization experiments performed at the University of Melbourne	
2.15	Optical response of Au particles before and after shape identification by SEM	
2.16	Example of correlated SEM/LSPR/TEM	
2.17	Schematic of the correlated LSPR/SPIM/TEM experiment	
2.18	Scattering maps and grid sample holder for RIS measurements	
2.19	Reactive ion etching effect on single Au nanostructures	
2.20	Size and corner rounding measurement approaches	
3.1	Representative single particle LSPR spectra and TEM image of single Ag and Au nanocubes with $c \sim 78$ nm and $r \sim 12$ nm	
3.2	FDTD calculated optical response and electric field intensities for a $c = 78$ nm and $r = 12$ nm Ag nanocube on Formvar	
3.3	Effect of nanocube composition, plasmon mode, and substrate RI ( $n$ ) on the LSPR energy for Ag and Au nanocubes	
3.4	Effect of nanocube composition, plasmon mode, and substrate RI on the LSPR FWHM for Ag and Au nanocubes.	
3.5	Effect of corner rounding on the plasmonic properties of Au nanocubes	
3.6	Computational and experimental Au nanocube spectra	
3.7	Effect of substrate thickness on the optical response of a Au nanocube calculated using FDTD	

3.8	Effect of the substrate on the optical response of a Au nanocube, calculated using FDTD	
4.1	Representative TEM images and LSPR spectra for Au nanostructures on Formvar	
4.2	Representative TEM images and side length measurements for decahedron, octahedron, truncated bitetrahedron, and icosahedron	
4.3	Side length and plasmon length as descriptors of nanoparticle size	
4.4	Statistical analysis of size effects using side and plasmon length for Au cubes, decahedra, icosahedra, triangles, and octahedra	
4.5	Effect of substrate refractive index on the plasmon energy and FWHM of Au nanostructures	
4.6	Representative images and structural parameters of Ag bipyramids	
4.7	Effect of size and corner rounding on the spectra of individual Ag bipyramids	
4.8	Single parameter effects on the longitudinal dipolar resonance energy and FWHM of Ag bipyramids	
4.9	Single parameter distribution for the 123 bipyramids studied	
4.10	Grouped fits for the analysis of the simultaneous effect of size and truncation on the equatorial LSPR energy of Ag bipyramids	
4.11	Planar fit approach to describe the simultaneous LSPR energy dependence on size and corner rounding	
4.12	Effective plasmon length approach describing the simultaneous size and shape effects in Ag bipyramids	
4.13	Effect of size and corner rounding on the LSPR energy of Au nanocubes	
4.14	Correlation between size, corner rounding, dipolar energy and the dipolar and quadrupolar LSPR energy and FWHM of Ag nanocubes	
4.15	Planar fit on the simultaneous effects of size and corner rounding on the dipolar and quadrupolar plasmon energy of Ag nanocubes	

4.16	Simultaneous effects of size and corner rounding on the dipolar and quadrupolar plasmon energy of Ag nanocubes	
4.17	Effect of size and corner rounding on the longitudinal dipolar resonance of ellipsoidally capped Ag and Au nanorods	
4.18	Plasmon modes in Ag cubes	
4.19	Statistical analysis of size effects on the plasmon energy of Ag nanocubes using size and plasmon length for peak 1 (dipole), peak 2 (quadrupole), peak 3, and peak 4	
4.20	Plasmon modes in Au Decahedra	
4.21	Size-dependence of the energy and width of the equatorial dipolar and quadrupolar resonances in Au decahedra on Formvar	
5.1	Refractive index sensitivity measurements of a single Au decahedra	
5.2	Refractive index sensitivity measurements of a single Au truncated bitetrahedra	
5.3	Refractive index sensitivity values ( $m$ ) and figures of merit (FOM) for single decahedra and triangles (truncated bitetrahedra) obtained from correlated RIS/TEM	
5.4	Correlated RIS/TEM measurement of Ag nanoparticles aggregates	
5.5	Refractive index sensitivity ( $m$ -values) and sensing figures of merit (FOM) of single Au decahedra as a function of the LSPR energy in water	
5.6	Example of the plasmon redshift resulting from the deposition of 1.1 nm $\text{Al}_2\text{O}_3$ on Au decahedra (partial data)	
5.7	Representative spectra of single Ag nanocubes on c-flat grids before and after 10 layers of alumina ALD deposition	
5.8	Plasmon resonance shift caused by the deposition of 10 cycles (1.1 nm) $\text{Al}_2\text{O}_3$ on ~80 nm side length Ag nanocubes	
5.9	Representative spectrum and black and white scattering map of ALD-coated Ag nanocube after 1 month in moist air	

5.10	Refractive index sensitivity of Au decahedra with and without 1.1 nm Al <sub>2</sub> O <sub>3</sub>	
5.11	Representative data from correlated SMSERS/LSPR/TEM from aggregates of Ag colloids	
5.12	SMSERS-active Ag colloid aggregates	
6.1	Representative correlated polarization-dependent scattering spectra and TEM images of single Au decahedra	
6.2	Correlated polarization-dependent scattering spectra and TEM images of the four single Au truncated bitetrahedra observed	
6.3	Representative TEM image and solution spectrum for Au rods @ Ag shell particles	
6.4	Representative single particle correlated pol-LSPR/TEM results on Au rods @ Ag shell deposited on Formvar substrate	
6.5	Plasmon polarization of single Au rods @ Ag shell nanoparticles	
6.6	Example of correlated LSPR/TEM on Au particle dimers	
6.7	Plasmonic properties of three of the five Au T-shaped trimers studied by SEM/LSPR/TEM	
6.8	Plasmonic properties of Au linear trimers with various interparticle separation studied by SEM/LSPR/TEM	
6.9	Polarization dependence of the scattering of linear Au trimers and quadrumer	
6.10	Scattering intensity dependence on incoming light polarization for Au dimer structures	
6.11	Scattering intensity dependence on incoming light polarization for Au nanoparticle aggregates	
6.12	Scattering spectrum of an individual Ag nanocube (d ~ 160 nm) on a c-flat substrate and SPIM excitation wavelength	
6.13	Electric field intensity and expected polarization dependence of the electron emission of Ag nanocubes	

6.14	Correlated LSPR/SPIM/TEM of Ag cubes	
6.15	Polarization anisotropy of supported Ag nanocubes	
6.16	Representative polarization-dependent spectra and TEM pictures of Ag nanocubes	
6.17	Correlation between the polarization giving the highest peak intensity and the cube corner orientation	
6.18	Measured photoelectron emission rate, PE, as a function of the laser intensity using circularly polarized $\lambda = 800$ nm light	
6.19	Polarization dependence of scattering and multiphoton photoemission	
6.20	Correspondence between the direction of the cube corners and the laser polarization that results in maximum electron emission	
6.21	Experimental four-photon photoelectron emission cross-section for 8 Ag nanocubes as a function of measured cube corner rounding	
7.1	Properties of the three Wulff models discussed: the basic Wulff model, the infinite reservoir approximation, and the alloy Wulff model	
7.2	Composition-dependent bulk free energy of the studied alloys	
7.3	Composition and orientation dependence of the surface free energy of CuAu, AuPd, AgAu, and AgPd	
7.4	Composition-dependence of the surface energy ratio of the studied alloys	
7.5	Equilibrium surface composition for AgAu and CuAu modeled using the basic Wulff construction, the infinite reservoir approximation, and the alloy Wulff construction	
7.6	Effect of size and initial (homogeneous) composition on the equilibrium surface composition of alloy nanoparticles containing 1,000, 3,000, and 10,000 atoms	
7.7	Shape of {111}-dominated particle and associated $h_{111}/h_{100}$ values, from cuboctahedron to octahedron	
7.8	Effect of size and initial (homogeneous) composition on the equilibrium	

	shape of alloy nanoparticles modeled using the basic Wulff, infinite reservoir, and alloy Wulff containing 1,000 and 3,000 atoms	
7.9	Shapes and surface area ratios predicted by different models for CuAu alloy with an homogeneous Au fraction of 0.2	
7.1	Total energy calculated for a 3,000 atoms CuAu nanoparticle, with the basic Wulff, infinite reservoir approximation, and alloy Wulff	
7.11	Size-dependence of transition 1 (regime 1 to 2) and transition 2 (regime 2 to 3) for the strong alloy CuAu	
8.1	Thermodynamic Dh shape as a function of relative surface energy of {100} and {111} faces	
8.2	Schematic of step-flow growth	
8.3	Lyapunov stability	
8.4	Singly twinned particle shape as a function of relative surface energy and kinetic growth enhancement	
8.5	Effect of kinetic growth on Dh modeled with the Kinetic Modified Wulff construction	
8.6	MATLAB graphical user interface developed to compute nanoparticle shape based on modified and single crystal Wulff models	

## CHAPTER 1

### Introduction to Nanoparticle Shape and Optical Properties

The optical properties of nanoparticles have been observed for centuries, for example, as part of the 4<sup>th</sup> century AD Lycurgus cup (Figure 1.1) and medieval stained glass. Scientific interests in the color of small particles debuted later, when Faraday<sup>1</sup> synthesized the famous "Ruby Fluid" by reacting gold chloride with phosphorous in ether. Faraday recognized that the color was due to the reduction of gold to small particles, and later Mie<sup>2</sup> provided the theoretical foundations explaining the color of the particles and its dependence on metal composition as well as surrounding environment.



Figure 1.1. Lycurgus cup, a 4<sup>th</sup> century AD Roman artifact containing nanostructured metals. Left: reflected light illumination (light source positioned around the cup). Right: transmitted light illumination (light source positioned inside the cup). Images from the British Museum.

The predominantly theoretical research on the topic of (as they were called then) ultrafine particles in the early and mid-20th century focused on the shape, growth, and optical response modeling of metallic particles.<sup>2-9</sup> The development of electron microscopy in the mid-20th century provided an invaluable tool to image particles, such that experimental studies exploring morphology, stability, and catalytic activity emerged.<sup>10-25</sup> Advances in synthesis and instrumentation, coupled with the discovery of surface-enhanced spectroscopies, plasmon sensing, optical signal transduction, and single molecule detection, revived interest in the optical properties of ultrafine particles in the late 20th century, during which the term nanoparticle quickly gained momentum.<sup>26-34</sup> Recent advances in light manipulation, nanoscale computing, plasmon-enhanced catalysis and plasmonic solar cells further anchored the importance and practical applicability of plasmonic phenomena.<sup>35-49</sup>

Unlike bulk properties, which are generally fully determined by a material's composition, the optical response of nanostructures is controlled by their size and shape; e.g. small triangles do not behave like cubes or large triangles. Characterization of structure-function relationships and developing a better understanding of structure control mechanisms are thus crucial for the expansion of knowledge on this fascinating phenomenon, and harness its many sensing and information applications. Experimentally, single particle investigations provide the opportunity to study phenomena typically hidden or blurred by ensemble averaging, such as polarization, plasmon decay, and detailed shape effects. Theoretically, analytical models provide easy access to shape modeling over a large range of sizes with minimal computational burden. By employing such methods, the work in this thesis unravels new knowledge and new tools related to shape modeling and shape effects in nanoparticles. This knowledge contributes to a library of

nanotechnology resources aimed at providing tools to the scientist and engineers developing novel applications such as plasmonic sensors and devices. This library is the nanoplasmonics toolbox.

This Chapter provides introductory material on plasmonic behavior and shape modeling. Section 1.1 first describes plasmon resonances, the various factors determining their energy and decay, as well as what is expected from basic theories and what has been previously studied with single particle methods. Section 1.2 reviews previous analytical shape models, in particular those necessary to the understanding of the new models developed in Chapters 7 and 8.

### 1.1 Plasmons in Small Metal Nanoparticles

Materials with a negative real and a small positive imaginary dielectric constant in a given wavelength range, such as quasi-free electron metals, Ag, Au, etc., (Figures 1.2 and 1.3) can support surface plasmon resonances (SPRs) when submitted to electromagnetic radiation. The SPR can be of two types: propagating or localized. Propagating surface plasmons, also called surface plasmon polaritons (SPP), are oscillations of electric charges travelling at a material/dielectric interface. Specially fabricated structures can guide these oscillations for distances of tens to hundreds of  $\mu\text{m}$ ; their decay perpendicular to the interface is characterized by a  $1/e$  decay length of  $\sim 200$  nm, depending on the wavelength of illumination.<sup>39,42,43</sup>

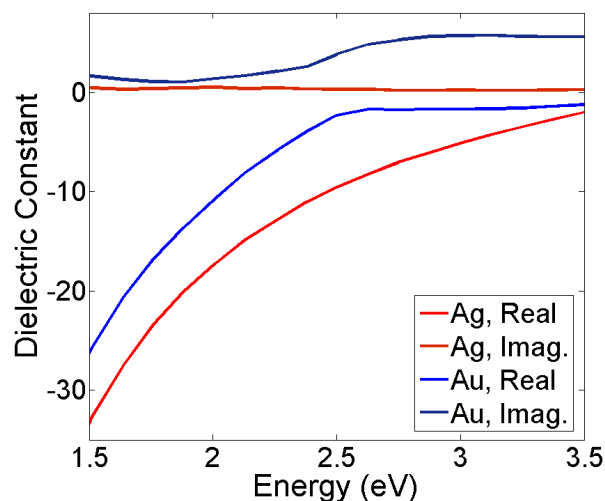


Figure 1.2. Dielectric function of Ag and Au, showing the large negative real and small positive imaginary values in the visible range. Data from ref.<sup>50</sup>

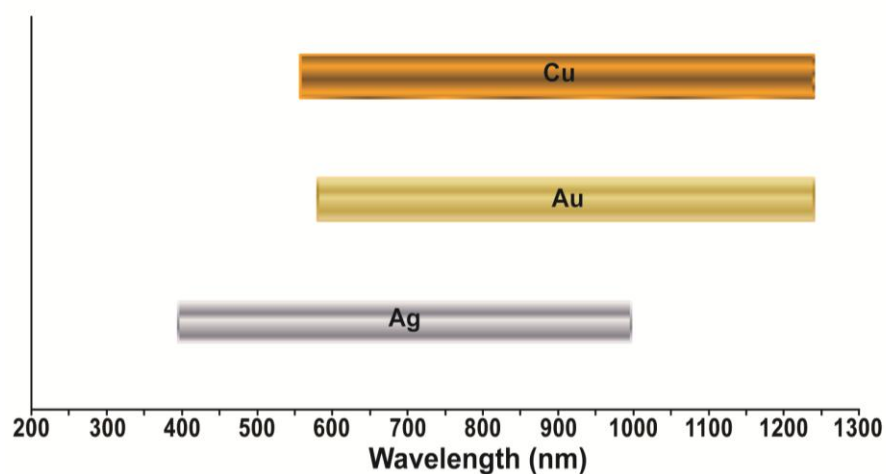


Figure 1.3. Approximate wavelength range of localized plasmon resonances, as characterized by surface-enhanced Raman activity. Reproduced from ref.<sup>51</sup>

While special phase-matching schemes are necessary to excite SPPs propagating at flat interfaces, for metallic particles smaller than the wavelength of light the photon field can couple

directly to the electron oscillation (Figure 1.4) confined to the interior volume of the structure. While oscillations occur in the entire particle, the presence of strong electric fields at the metal-dielectric interface lead to the name of this phenomenon, localized surface plasmon resonances (LSPR).

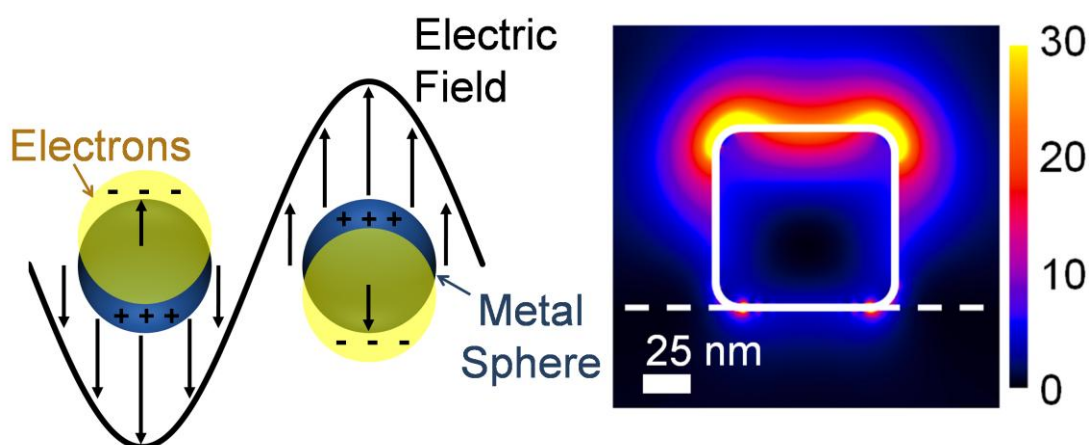


Figure 1.4. Localized surface plasmon resonance (LSPR) and plasmon field distribution. Left: LSPR schematic showing the coherent oscillation of conduction electrons excited by the electric field of light. Right: calculated field distribution of the quadrupolar plasmon mode of supported Ag cubes,<sup>52</sup> an example of short field decay length and high field concentration at the metal-dielectric interface.

The simplest model of a localized plasmon resonance can be obtained in the electrostatic limit of Mie theory<sup>2</sup>, in which the speed of light is considered infinite and thus all parts of the particles are subject to the same instantaneous field. For a particle with a dielectric constant  $\epsilon_{(\lambda)} = \epsilon_r(\lambda) + i\epsilon_i(\lambda)$  in a homogeneous medium described by  $\epsilon_m$ , the extinction efficiency  $Q_{\text{ext}(\lambda)}$  of an ellipsoid with

the electric field of the incoming radiation parallel to its main axis is obtained by the so-called Mie-Gans<sup>8</sup> theory:

$$Q_{ext}(\lambda) = \frac{2\pi V \epsilon_m^{3/2}}{GL^2 \lambda} \frac{\epsilon_i}{\left| \epsilon_r + \left( \frac{1-L}{L} \right) \epsilon_m \right|^2 + \epsilon_i^2} \quad (1.1)$$

where  $V$  is the volume of the particle,  $G$  is its projected cross-sectional area, and  $L$  is a geometric factor. The first part of the product affects the strength of the resonance, while the second part effectively determines its spectral position, as a resonance occurs when the denominator approaches zero. Mie theory predicts a strong LSPR frequency dependence on the surrounding dielectric environment, a feature commonly used in sensing applications,<sup>30,32,33,53-73</sup> where a plasmon shift can signal the presence of, e.g., a biological marker such as calcium ions, antibodies, or proteins. The metal composition, i.e. the particle dielectric function, is also expected to affect the plasmon resonance energy; this has been confirmed experimentally for a variety of single metals and alloys.<sup>52,74-79</sup> In fact, alloying was recognized early on by Faraday to alter the optical properties of very thin films, as he suggests reacting a thin gold film with potassium cyanide such that "to transmit a ray so luminous as to approach to white" as opposed to the warm green transmitted through pure gold of roughly  $1/282000^{\text{th}}$  of an inch.<sup>1</sup> A further ingredient in Mie-Gans theory to determine the position of the LSPR peak is particle shape, i.e., the  $L$  factor; analytical solutions of  $L$  are available for spheres ( $L=1/3$ ), prolate ( $L<1/3$ ), and oblate ( $L>1/3$ ) ellipsoids.<sup>80</sup> This approach describes the plasmon energy dependence on shape adequately for rods, in which a decrease of plasmon energy is observed with increasing aspect ratio.

However, the lack of analytical solutions of  $L$  for shapes other than ellipsoids severely restricts the applicability of Mie-Gans theory. Furthermore, the electrostatic limit used inhibit modeling of size effects on plasmon resonance frequency, as a constant phase around the particle is assumed. In reality, the LSPR energy of particles larger than  $\sim 20$  nm changes with particle dimension because the electron oscillation has to accommodate the difference in electromagnetic phase between one end of the particle and the other (i.e., radiative depolarization effects, also called retardation effects).<sup>81</sup> Experimental and numerical approaches are thus paramount to unraveling the relationship between size, shape, and plasmon resonance energy.<sup>31,52,62,66,68,74,79,82-</sup>

113

Yet the position of the LSPR is not its only attribute: characterization, understanding, and control of its peak width is also important. For a bulk sample of nanoparticles in solution, the peak width is a convolution of inhomogeneous and homogeneous broadening. The former is due to the shape and size inhomogeneity of the synthesis products and can be manipulated, up to a point, by controlling the reaction conditions to obtain a more or less monodisperse sample. More interesting, however, is the intrinsic linewidth of the particle, caused by homogeneous broadening. The plasmon linewidth  $\Gamma$  is related to the plasmon dephasing time  $T$  according to the equation:<sup>84</sup>

$$\Gamma = \frac{2\hbar}{T} \quad (1.2)$$

Plasmon dephasing ultimately leads to plasmon decay, which occurs via radiative and non-radiative pathways,<sup>110,111,114,115</sup> as illustrated in Figure 1.5. The relative contribution of these

pathways depends largely on the size of the particle. Nonradiative damping is dictated mainly by the metal dielectric function, which in turns is a function of the plasmon peak position. Au, for example, displays strong interband transitions at energies above 500 nm, such that plasmons are effectively impossible to observe as their lifetime is too short, i.e., their width is too large.

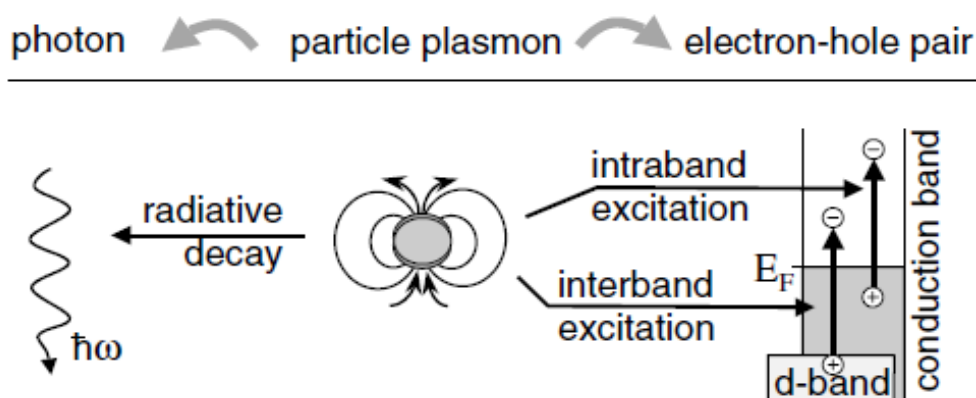


Figure 1.5. Plasmon decay pathways contributing to the plasmon linewidth. Left: radiative decay. Right: nonradiative decay. Figure from ref.<sup>110</sup>

For very small (<10 nm) particles, where the particle size is comparable to the conduction electron mean free path, electron surface scattering also becomes important. However, all particles studied in the current experimental work are between 50 and 300 nm, a size range in which radiative decay (radiative damping) dominates; this decay, in a purely dipolar regime, is believed to depend linearly on volume.<sup>84,116,117</sup>

To fully harness plasmonic phenomena and use them in sensors and devices, it is critical to quantitatively understand the factors controlling the electron oscillation; this includes the energy, linewidth, and polarization of dipolar and higher order plasmon resonances. However, even with

the recent advances in the development of shape controlled syntheses of noble metal nanostructures,<sup>62,85,94,95,102,104,105,107,118-145</sup> correlated single-particle spectroscopy and electron microscopy has shown to be an invaluable technique that can overcome the difficulties of obtaining quantitative data from the inherently inhomogeneous solution of particles generated from these syntheses. Indeed, single-particle analysis can yield unique information about line widths, polarization, and precise effects of various structural factors. Early studies on colloidal silver particles<sup>108,109,146</sup> paved the road for more recent systematic, statistics-based publications on decahedra,<sup>67,82</sup> cubes,<sup>52,147</sup> cages,<sup>117</sup> spheroids,<sup>91,148</sup> and triangular nanoprisms.<sup>84,143,149</sup> Such studies, many recently reviewed,<sup>89,116,150,151</sup> provided important new findings on the effects of size, composition, corner rounding, interparticle coupling, and surrounding environment on the plasmon energy and, less commonly, on the plasmon lifetime (i.e., peak width) and polarization. Many of the effects discussed in Section 1.1 have been experimentally verified through such analyses, albeit rarely quantified.

In this thesis, novel and improved single particle approaches are described and used to study the plasmonic properties of colloidal nanoparticles.

## 1.2 Nanoparticle Shape Modeling

Shape is a powerful tool to control the properties of nanoparticles for plasmonics, catalysis, and other applications. Therefore, much effort has been devoted to its synthetic control<sup>63,87,96,97,104,106,107,109,121-148</sup> and modeling.<sup>135,152-158</sup> However, the latter is often limited by computational power to small clusters, and while atomistic studies can provide invaluable

information, there are approximations (sometimes severe) with the potentials, structures, and/or density functionals used. Analytical techniques, on the other hand, are often more powerful than atomistic ones as they provide solutions valid for different sizes, which is often hard to extract from an atomistic calculation.

One of the classic analytical models to describe particle shape, whether small, large, free-standing or as precipitates, is the Wulff construction,<sup>9</sup> a model based upon the original experimental observations of natural crystals by Wulff, with further mathematical proofs by van Laue, Dinghas, and Herring.<sup>5-7</sup> The Wulff construction, in its basic form, relates the surface normal of a face ( $h_{(n)}$ , as depicted in Figure 1.6) to its orientation-dependent surface free energy ( $\lambda_{(n)}$ , where  $n$  is the crystallographic orientation), according to:

$$\frac{\gamma_{(n)}}{\Lambda} = h_{(n)} \quad (1.3)$$

The  $\Lambda$  term is a constant, such that the ratio of surface energy to surface normal is the same for all crystallographic orientations. Therefore, faces with lower surface energy will be more prominent. As shown for FCC lattices in Figure 1.7, if  $\{100\}$  or  $\{111\}$  faces are the most stable, cubes or octahedron are produced, while cuboctahedron are formed when the surface energy of  $\{111\}$  and  $\{100\}$  faces is comparable.

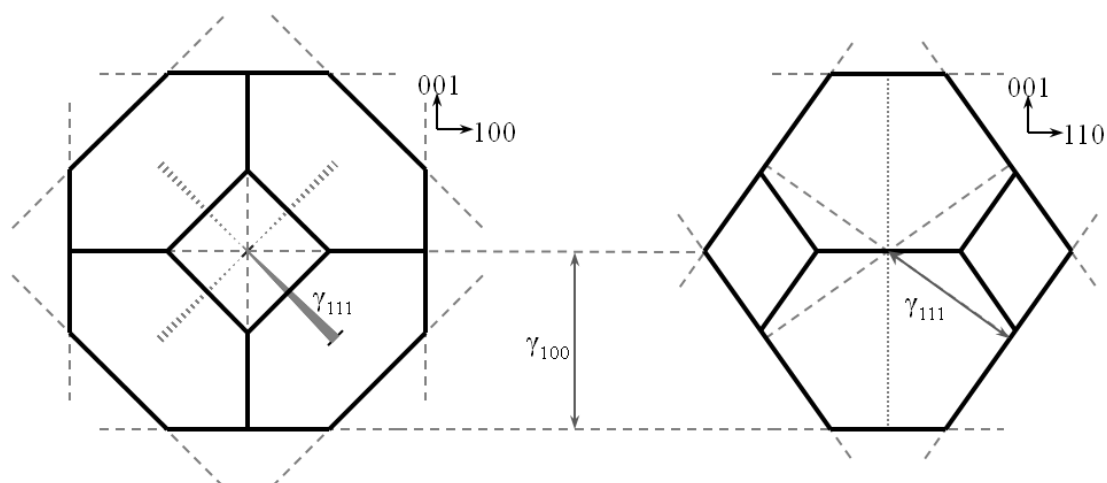


Figure 1.6. Wulff shape representation for a face centered cubic single crystal, showing the equivalency between the surface normal (drawn lines) and the surface energy ( $\gamma$  labels). Left: view along the (010) axis. Right: view along the (-110) axis. Image provided by Jim Enterkin<sup>159</sup> based on ref.<sup>9</sup>.

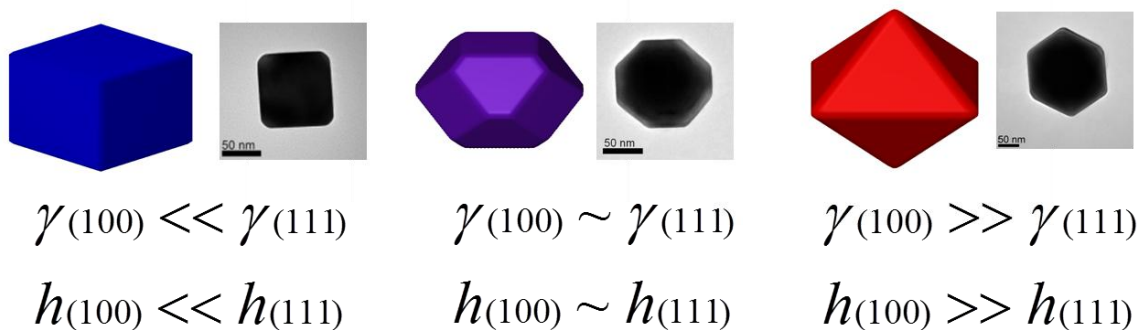


Figure 1.7. Representative single crystal shapes and associated surface free energies. Left: cube formed entirely by  $\{100\}$  facets, occurring when the  $\{100\}$  surface energy is much lower than that of the  $\{111\}$ . Middle: cuboctahedron, a mixture of  $\{100\}$  and  $\{111\}$  facets, obtained when the surface energies are of comparable magnitude. Right: octahedron formed entirely by  $\{111\}$  facets, occurring when the  $\{111\}$  surface energy is much lower than that of the  $\{100\}$ .

An extension for supported particles on a flat substrate was described by Winterbottom,<sup>3</sup> and extended to an edge by Taylor *et al.* in what they called the SummerTop construction.<sup>160</sup> These models include both an interface energy and a surface energy, such that the particle shape changes depending on its affinity for the substrate, as shown in Figure 1.8.

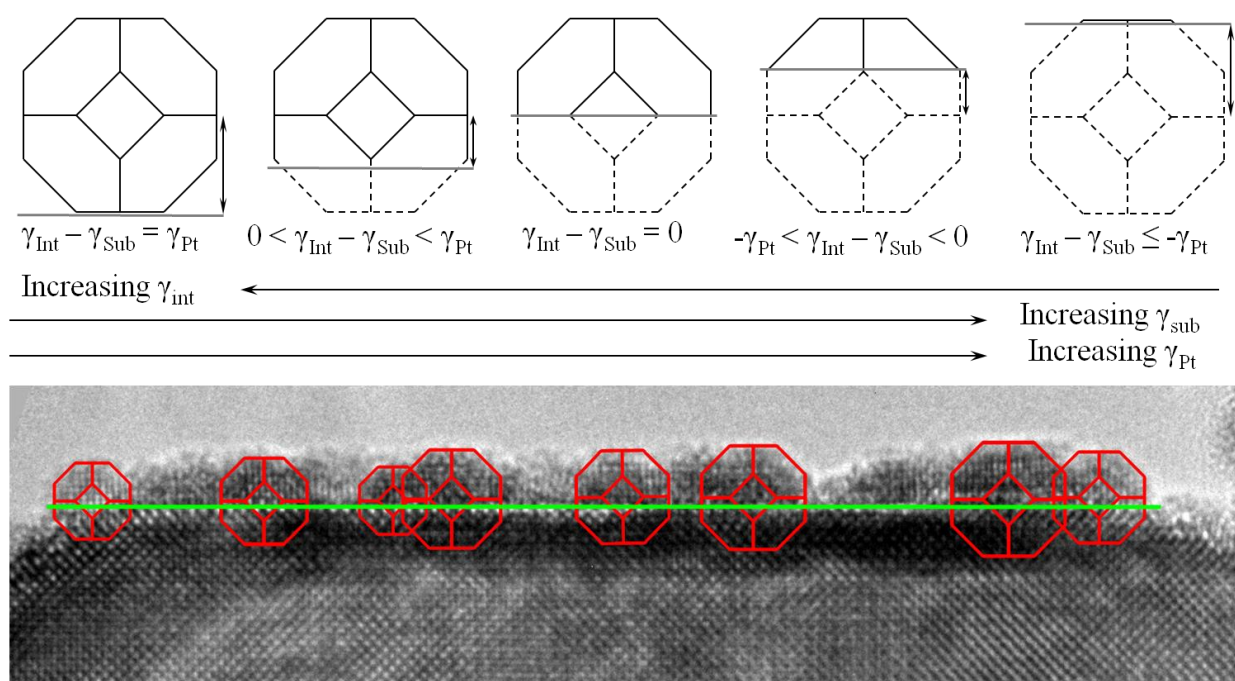


Figure 1.8. The effects of interface and surface free energy on the shape of nanoparticles, modeled by the Winterbottom construction and exemplified by Pt particles on  $\text{StTiO}_3$ .<sup>3,159</sup> The Pt particles are  $\sim 2$  nm in diameter. Top: trends relating the interface energy ( $\gamma_{\text{Int}}$ ), the substrate surface energy ( $\gamma_{\text{Sub}}$ ) and the Pt surface energy ( $\gamma_{\text{Pt}}$ ).

Not all nanoparticles are single crystals, such that further extensions of the Wulff construction were needed to model the decahedral, icosahedral, and lamellar shapes observed in electron microscopy studies.<sup>16,158,161-164</sup> The first two could be described as assemblies of tetrahedral subunits, elastically strained by ~2% and ~6% to form space-filling structures, respectively. This interpretation was confirmed using lattice<sup>15</sup> and atomic resolution imaging.<sup>24,25</sup>

The initial energetics analysis,<sup>163</sup> a homogeneous strain model coupled with a surface energy analysis of the regular structures, provided an explanation for the stability of small icosahedral particles, but did not explain that of the decahedra. A generalized the surface structure of the particles using a variant of the Wulff construction appropriate for twinned nanoparticles, called a modified Wulff construction, was later developed and provides the foundation of the kinetic model presented in Chapter 8.<sup>165,166</sup> Further development of the twinned Wulff construction have appeared, for example the coupling with a disclination strain model for the decahedral particles and a three-dimensional variant for the icosahedral particles.<sup>167,168</sup>

Given the growth of nanotechnology in the last decades, significant advances in synthesis and characterization methods have been made, for example the discovery of new shape-control strategies,<sup>63,87,96,97,104,106,107,109,121-148</sup> attempts to measure nanoparticle phase maps,<sup>21,22,134,169</sup> as well as more precise structural characterization using aberration corrected high resolution TEM.<sup>170-174</sup> Numerical modeling advances have followed experimental progress, for example better elasticity models<sup>175</sup> and atomistic methods exploiting DFT.<sup>134</sup> However, these do not always directly apply to the large particles used for plasmonics, and the ability to include variable composition is typically limited. The work in this thesis thus aims to provide novel, user-friendly modeling tools capable of predicting kinetic and thermodynamic shapes. Indeed,

kinetic growth control is becoming an important synthetic tool, and the analytical kinetic growth model developed in Chapter 8 provides a way to understand and predict the outcome of twinned nanoparticle synthesis. Additionally, a new thermodynamic model for alloys (Chapter 7) in alloys provides a new, more complete approach yielding novel understanding of segregation effects on particle shape.

## CHAPTER 2

### Materials and Methods

## 2.1 Synthesis

Nanoparticle syntheses were performed by a network of expert collaborators: the Huang group (Au cubes, Northwestern University), the Mirkin group (Ag bipyramids, all other Au structures, Northwestern University), and the Xia group (Ag cubes, at Georgia Tech, although the collaboration was active during their tenure at Washington University in St. Louis).

### 2.1.1 Au Cubes

Cetyltrimethylammoniumbromide (CTAB)-capped Au cubes were synthesized by reducing an aqueous solution of  $\text{HAuCl}_4$  with ascorbic acid.<sup>176</sup> Side lengths ranged from 50-110 nm and many heavily truncated and triangular particles were present, as shown in Figure 2.1. Aggregation upon deposition on a substrate was noticeably worse than for PVP-capped nanoparticles. The cubes were stable in solution for at least a year. Attempts to obtain larger cubes failed.

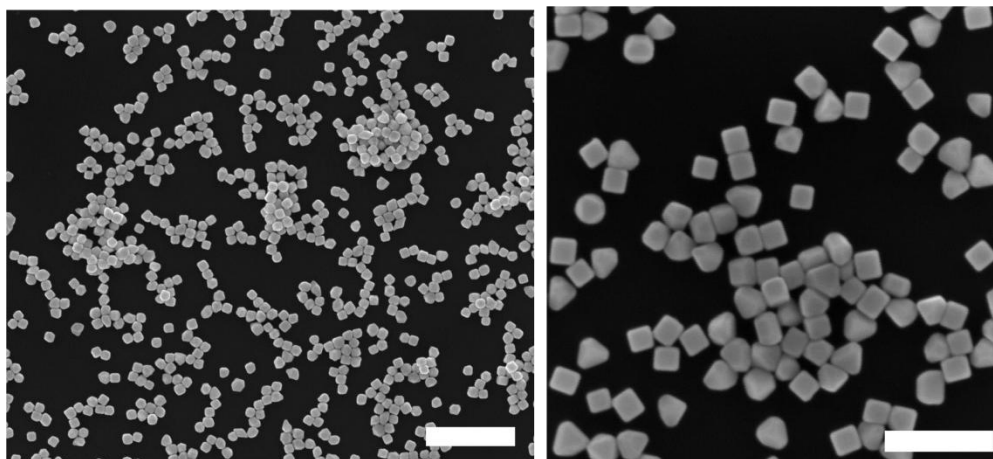


Figure 2.1. SEM images of Au nanocubes. Scalebars, 1  $\mu\text{m}$  (left) and 300 nm (right).

### 2.1.2 Au Decahedra, Au Truncated Bitetrahedra, Au Icosahedra

Poly(vinylpyrrolidone) (PVP)-capped Au decahedra were produced by reduction of hydrogen tetrachloroaurate ( $\text{HAuCl}_4$ ) following a previously reported method.<sup>129,177</sup> Icosahedra and triangles (truncated bitetrahedra) were obtained as reaction by-products (Figure 2.2)

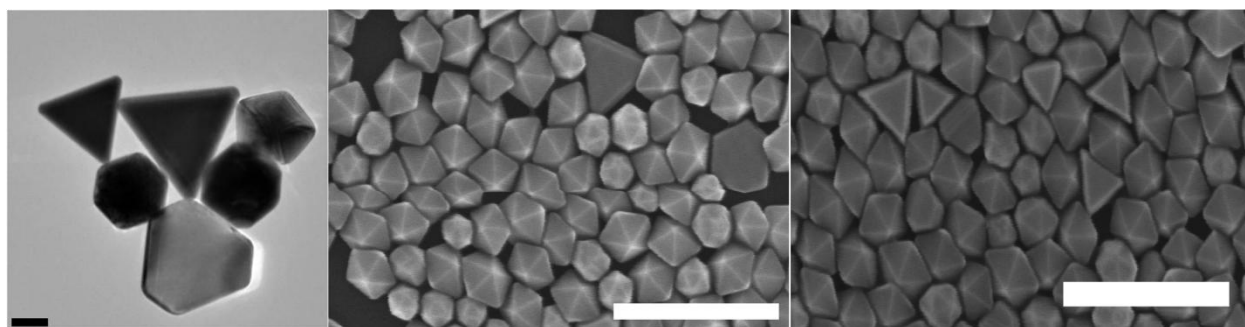


Figure 2.2. TEM and SEM images of Au decahedra synthesis products, containing flat hexagons, truncated bitetrahedra, and icosahedra. Scalebars, 50 nm (TEM) and 300 nm (SEM).

### 2.1.3 Au Octahedra

Poly(diallyldimethylammonium) (PDDA)-capped Au octahedra were synthesized following a previously reported procedure<sup>178</sup> based on the reduction of  $\text{HAuCl}_4$  in acidified ethylene glycol.

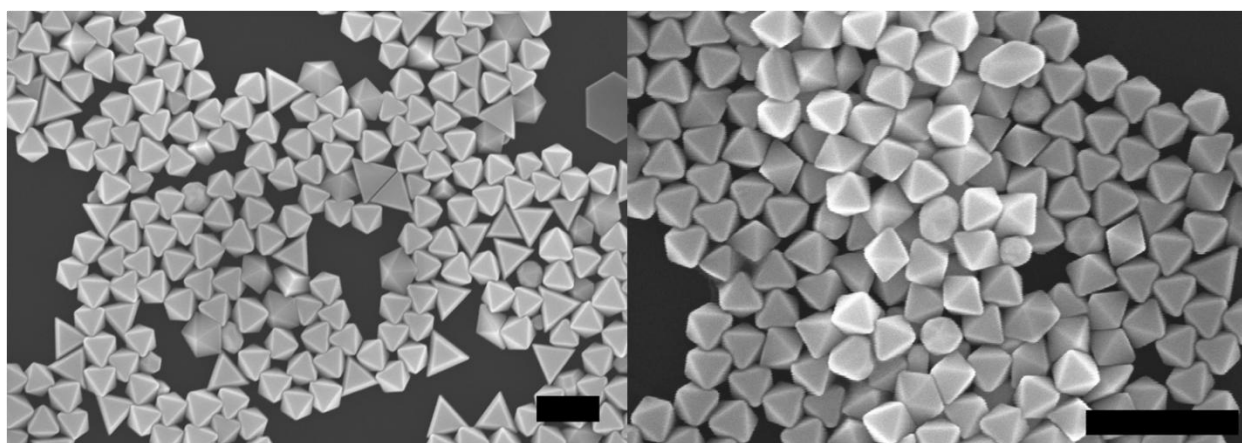


Figure 2.3. SEM images of Au octahedra synthesis products. The particles on the left have an average side length of  $\sim 145$  nm, the particles on the right have an average side length of  $\sim 80$  nm. Scalebars, 300 nm.

### 2.1.4 Ag Cubes

Poly(vinylpyrrolidone) (PVP)-capped single-crystalline Ag nanocubes were synthesized using a previously reported method,<sup>95,125</sup> where trace amounts of hydrochloric acid are added to a typical polyol reduction of  $\text{AgNO}_3$  in order to preferentially etch the twinned seeds, leading to a high yield of nanocubes, as seen in Figure 2.4.

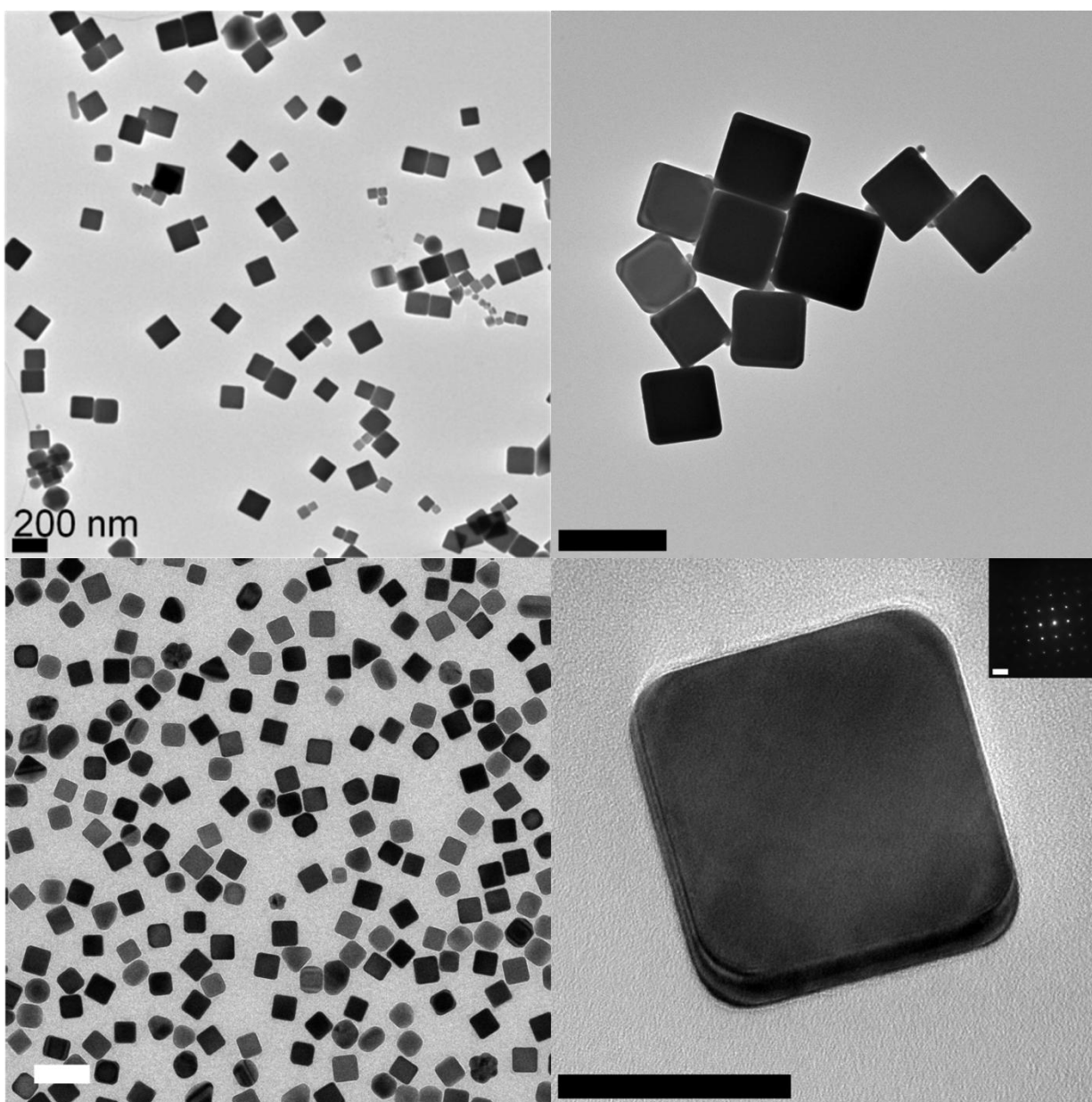


Figure 2.4. TEM images of Ag nanocubes. Top left: large (100-200 nm side length) Ag cubes. Scalebar, 200 nm. Top right: large Ag cubes. Scalebar, 200 nm. Bottom left: small Ag cubes (<100 nm side length). Scalebar, 100 nm. Bottom right: small Ag cube. Scalebar, 50 nm. Bottom right inset: Nanodiffraction pattern of single cube showing (100) zone axis. Scalebar, 5 nm<sup>-1</sup>.

### 2.1.5 Ag Bipyramids

Bis(p-sulfonatophenyl)-phenyl phosphine (BSPP)-capped Ag right bipyramids were produced by a photomediated synthesis. A basic aqueous solution of  $\text{AgNO}_3$ , sodium citrate, and BSPP was illuminated for 8 h using a 150-W halogen lamp and a bandpass filter. Optical bandpass filters (550, 600, and 650 nm) controlled the excitation wavelength and the final particle size.<sup>131,132</sup> Severe aggregation problems were observed when depositing the bipyramids on TEM grids. The solutions were stable for less than 3 weeks.

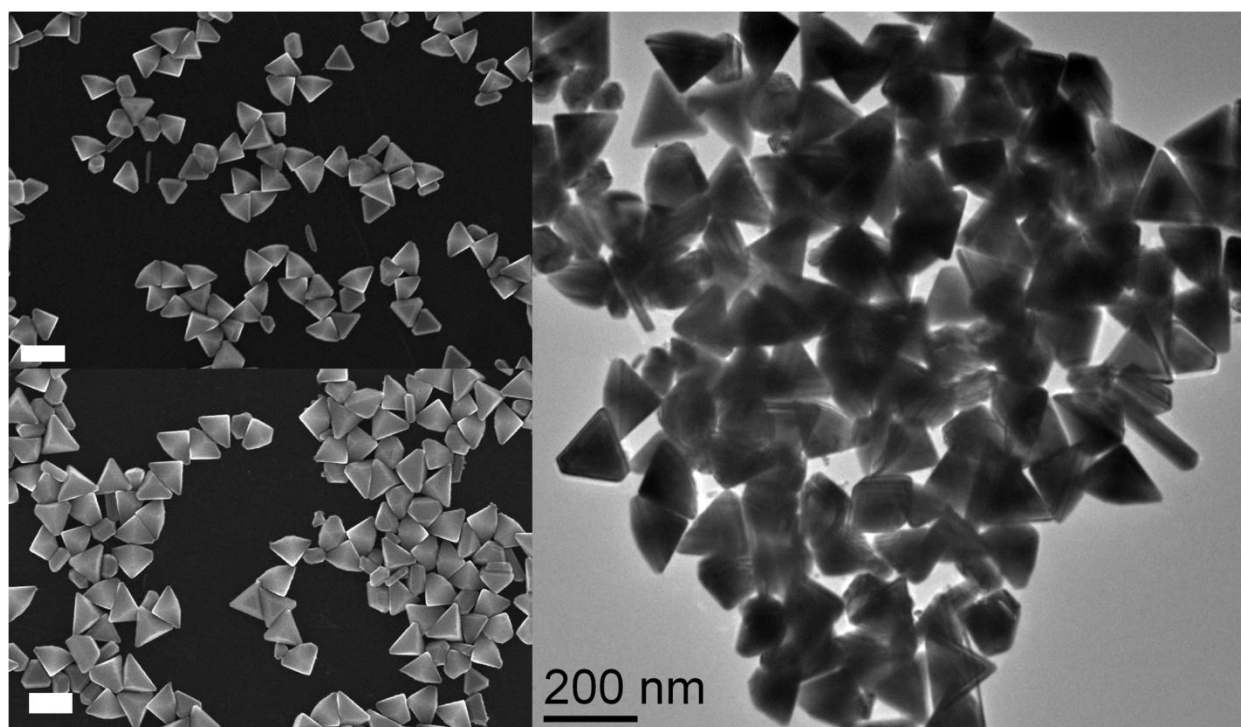


Figure 2.5. SEM and TEM images of Ag bipyramids. Top and bottom left: SEM images. Right: TEM image. Scalebars, 200 nm.

### 2.1.6. Ag-Coated Au Nanorods

The starting material for the synthesis of Ag-coated Au nanorods was a solution of Au nanorods prepared from a standard seed-mediated growth in CTAB.<sup>179</sup> CTAB was then exchanged with mPEG-SH, and a Ag shell was grown at room temperature from reduction of  $\text{Ag}^+$  with hydroquinone in slightly basic solution, following a previously reported procedure.<sup>141</sup> This synthesis was performed at the University of Melbourne by the group of Paul Mulvaney. A representative TEM image is presented in Figure 2.6.

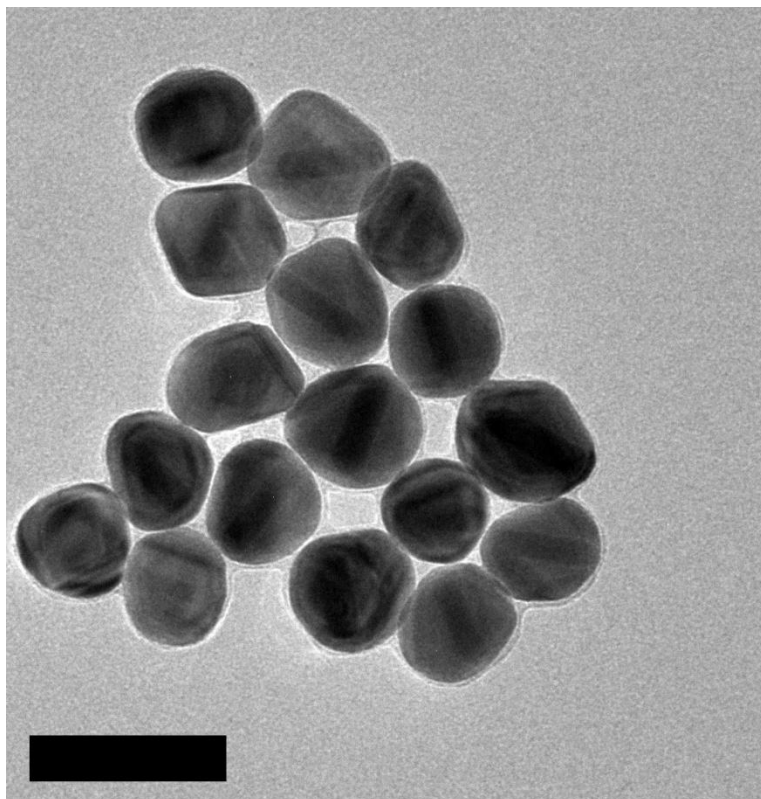


Figure 2.6. TEM image of Au rods @ Ag shell. The image was taken slightly out of focus to increase the visibility the rod cores. Scalebar, 100 nm.

### 2.1.7 Ag Colloids for SMSERS

Ag colloids were synthesized according to the Lee and Meisel procedure, in which  $\text{AgNO}_3$  is reduced by sodium citrate in a boiling aqueous solution.<sup>180</sup> Extreme care was taken to use clean (Aqua Regia) and dry glassware to avoid contamination.

## 2.2 Instrumental Methods: Single Particle Structure-Function Measurements

Through this work, a variety of single particle optical measurements were performed and correlated with structural data obtained from electron microscopy. Section 2.2.1 describes the basic method of correlated dark field microscopy and TEM, while Sections 2.2.2-2.2.7 provide details on variations of and additions to this technique, from refractive index sensitivity measurements to polarization. Related experimental/instrumental notes are presented in Section 2.2.8. Unless otherwise stated, the experiments were performed at Northwestern University.

### 2.2.1 Correlated LSPR/TEM

A 1-5 $\mu\text{L}$  drop of an aqueous suspension of nanoparticles was put on the support film, which was held by a self closing pair of tweezers. The drop was dried in air, large drops were partially removed with a filter paper or lint-free cloth (Kimwipe). For carbon/Formvar (polyvinyl formal)

grids (type B or ultrathin type A), the particles were deposited such that they were in direct contact with the Formvar because amorphous carbon is hydrophilic and lossy, which leads to enhanced aggregation and plasmon damping,<sup>147</sup> respectively. For  $\text{Si}_3\text{N}_4$  grids and other etched membrane windows, the particles were deposited inside the etch pit and extreme care was taken to avoid breaking the thin membrane. Once dry, the excess surfactant present on the grids was rinsed by gently pouring a small amount of water from a wash bottle across the grid held by tweezers. Analogous procedures were followed for the preparation of nanoparticles on glass coverslips.

TEM support films were placed particles facing up on 25 mm diameter no. 2 glass coverslips cleaned with piranha solution (sulfuric acid ( $\text{H}_2\text{SO}_4$ ) and hydrogen peroxide ( $\text{H}_2\text{O}_2$ )). Samples prepared directly on coverslip were inserted instead of a clean coverslip, particles facing up. A custom-made sample holder was used to flow nitrogen in the sample chamber closed on top and bottom by coverslips.

A video camera was used to obtain large area pictures ( $\sim 60 \times 50 \mu\text{m}$ ) of scattering, which serve as maps for both the dark field and electron microscopy; examples can be found in Figures 2.7-2.8. For standard carbon/Formvar grids, the asymmetric grid center (see top of Figure 2.7) was used as the origin an x-y coordinate system, following a previously reported procedure.<sup>147,181</sup> For c-flat grids (used in correlated LSPR/SPIM/TEM, Figure 2.8), each letter was used as the center of a x-y coordinate system. Large area pattern-matching and corner referencing were used to retrieve particles for membrane windows such as  $\text{Si}_3\text{N}_4$  (Figure 2.8).

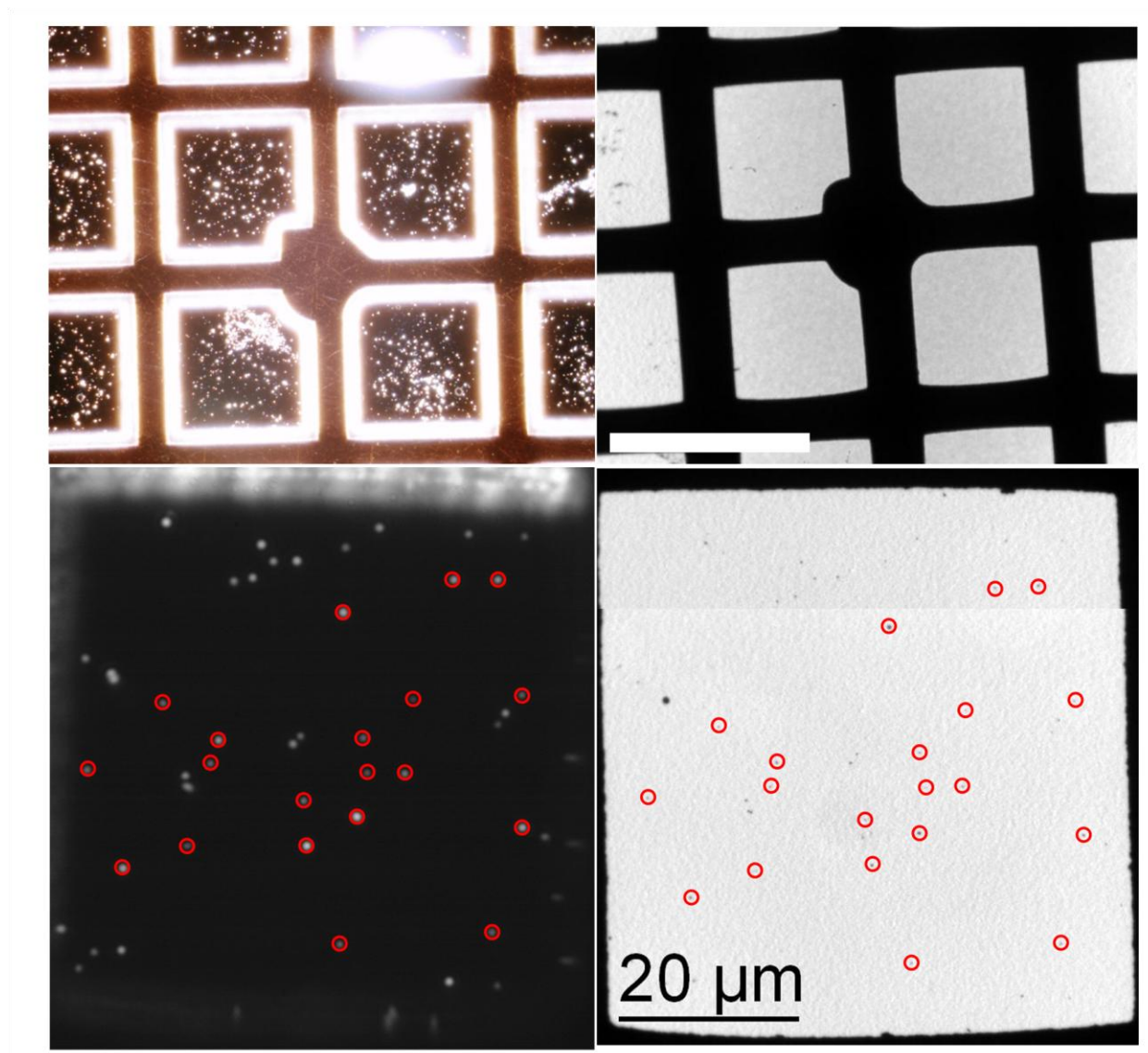


Figure 2.7. Correlated dark field microscopy and transmission electron microscopy performed on standard carbon/Formvar grids. Top: asymmetric center, as seen in an optical (left) and electron (right) microscope. Scalebar, 100  $\mu\text{m}$ . Bottom left: dark field scattering image (shown in black and white) of a grid square. Bottom right: low magnification TEM image of the same grid square.

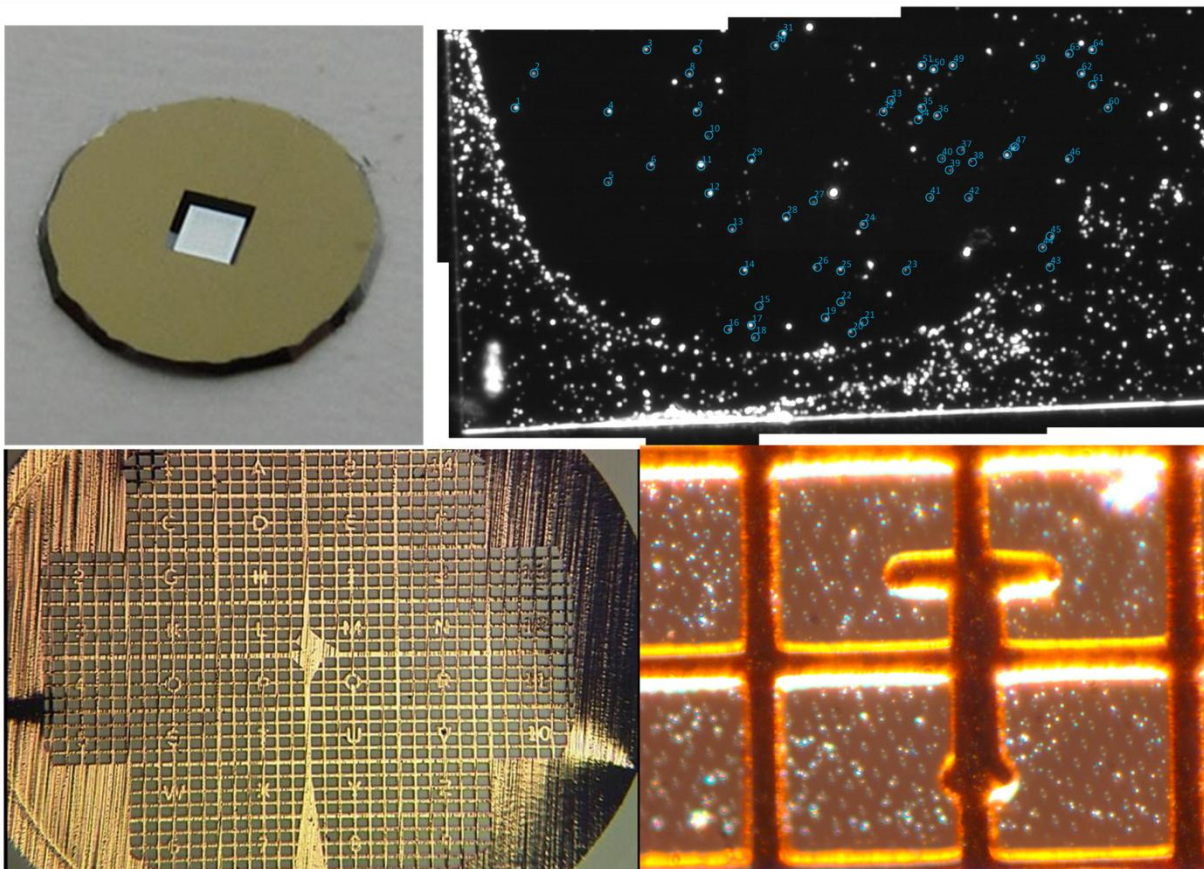


Figure 2.8. Example of non-traditional TEM support films and their use in correlated optical/structural measurements. Top left: 500 X 500  $\mu\text{m}$   $\text{Si}_3\text{N}_4$  window support film. The chip is 3 mm wide. Top right: scattering map composed of multiple images from the black-and-white video camera. The image dimensions are approximately 150 X 100  $\mu\text{m}$ . Bottom left: c-flat substrate (carbon-based, Protochips, Inc) deposited on an indexed copper grid measuring 3 mm across. Bottom right: real color scattering from a  $\sim$  150 X 100  $\mu\text{m}$  region. The equally spaced circular features are holes fabricated in the support film, white the bright blue and red spots are nanoparticles.

Single particle scattering spectra were obtained using dark field optical microscopy.<sup>52,84,92,103,106,108,109,121,147,182</sup> In this technique, white light from a halogen lamp is sent through a high numerical aperture (NA) dark-field condenser, and used to illuminate the sample. The NA is defined as  $NA = n \cdot \sin\theta$ , where  $n$  is the refractive index of the medium and  $\theta$  is the half-angle of the maximum cone of light (Figure 2.9). The dark-field condenser is equipped with a circular block at the lens such that a hollow cone of light is transmitted and focused at the sample. The scattered light from the nanoparticles is collected through a variable NA 100X oil immersion objective (set to a lower NA than the dark-field condenser) and sent to a charge coupled device (CCD) detector coupled to a spectrometer (Figure 2.10). Because the light illuminated through the condenser is at an angle higher than that prescribed by the NA of the objective, the illumination light is not collected—only the light scattered by the nanoparticle is; therefore, this is a “darkfield” configuration.

To ensure single nanoparticle spectroscopy, a single diffraction-limited spot was isolated in the center of the slit of the spectrometer such that no other particles were in the field of view. This process was repeated for each subsequent nanoparticle of interest. Acquisition times ranged from 1 to 10 seconds, spectral accumulation was set between 5 to 10, for a total accumulation time typically in the 10-60 seconds range. Winspec, a software provided by Princeton Instruments, was programmed to acquire a background spectrum at the same time as a particle’s spectrum; typically they were separated by 10 pixels and each had a height of 12 pixels. The output files, converted from .SPE to .TXT (ASCII) had 2 columns (energy and intensity) and  $n \times 2$  rows,  $n$  being the number of horizontal pixels in the detector (1340 for the visible detector used).

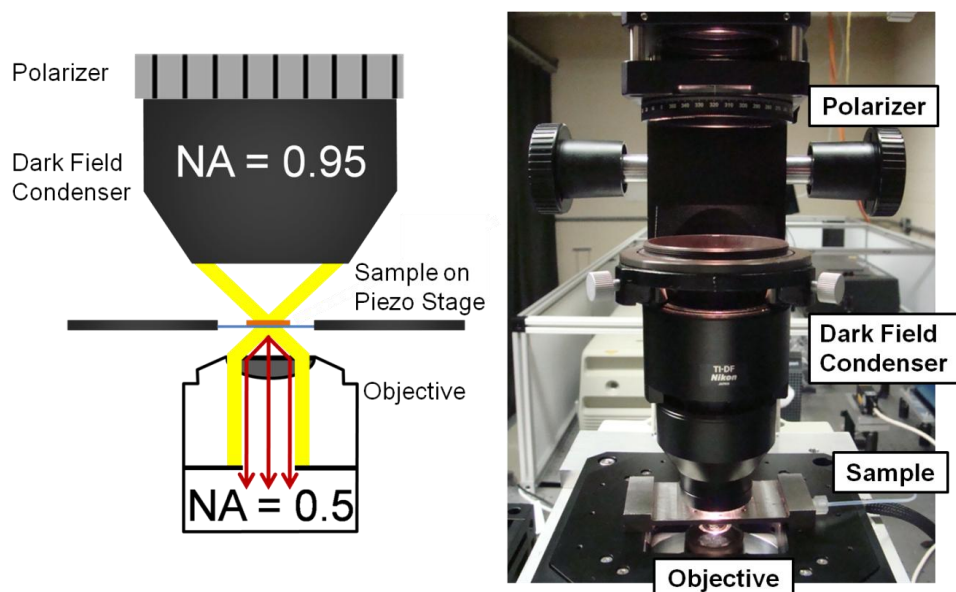


Figure 2.9. Dark field microscopy setup. Right: diagram showing the conical illumination. Left: picture of apparatus.

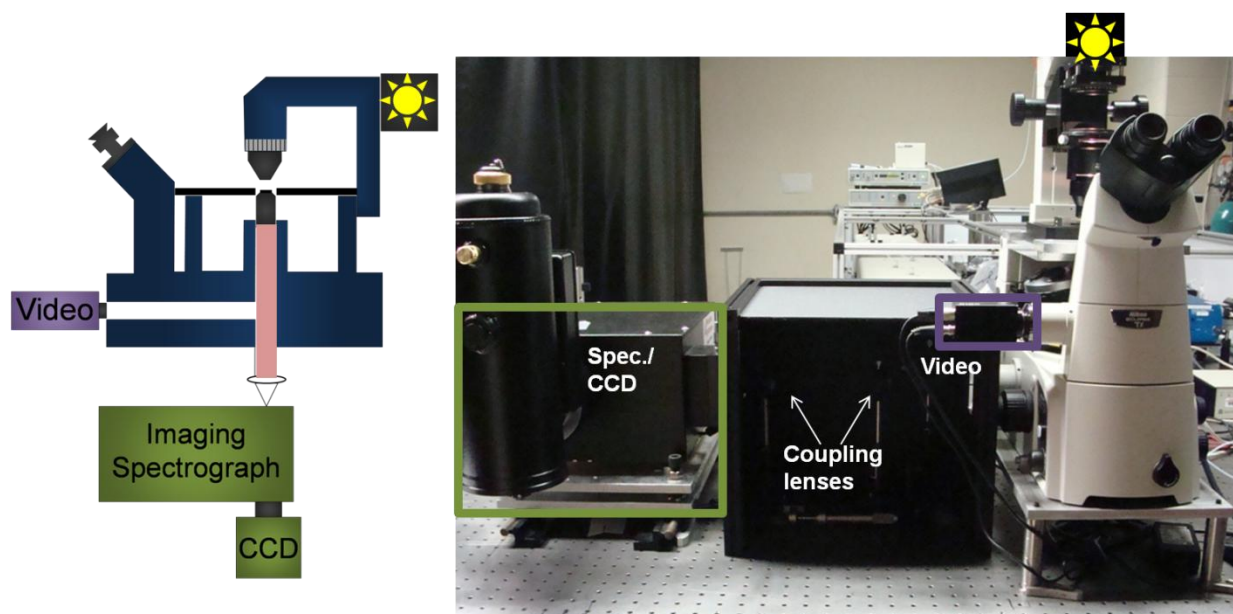


Figure 2.10. Inverted optical microscope with coupling to the video camera as well as the spectrograph/CCD. Left: diagram showing the scattered light directed in the spectrograph/CCD. Right: picture of apparatus.

The raw single particle spectra collected are not the final spectra presented here. Indeed, contributions from the wavelength-dependence of the lamp intensity ("lamp profile") and the detector readout current must be accounted for. To do so, a background spectrum, collected in the same way as the particle spectrum except from an area where no particles were present, was first subtracted from the raw particle spectrum. Then, this result was divided by the difference between the lamp spectrum and the detector dark current. The lamp and detector dark spectra must have the same acquisition parameters, but these parameters may be different than that of the particle and background spectra. For the lamp spectra, the objective NA was open (increased) such that the illuminating light was sent to the detector. Care must be taken to not saturate the detector; to this end, short acquisition times (0.007 seconds, 200 accumulations) were used. A neutral density filter can also be inserted between the objective and the detector during the lamp spectrum acquisition to allow a higher illumination intensity for weakly scattering particles. Of course, the lamp spectrum must be subsequently corrected for the presence of this filter. The detector dark current was collected with the microscope light output pointed away from the detector (e.g., in the eyepiece). An illustration of the spectral processing is presented in Figure 2.11. The MATLAB codes developed to automate this process and further notes can be found in Appendix A1.

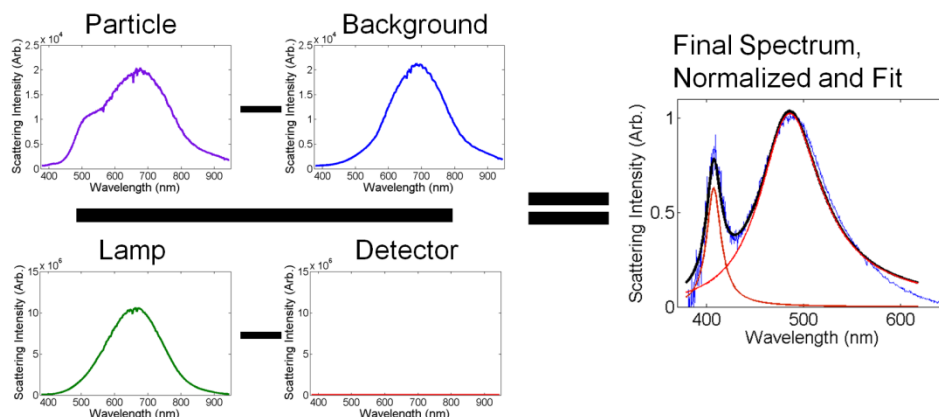


Figure 2.11. Spectral processing for single particle dark field scattering experiments. Note that normalization is optional.

TEM images were obtained within days of the optical characterization (to minimize oxidation) on either a JEOL JEM2100 FAST TEM or a Hitachi HD-2300A STEM, both operated at 200kV. The TEM was preferred to the STEM as it consistently gave better images and less contamination.

The possibility of performing TEM before dark field microscopy was explored for both Au and Ag systems, as shown in Figure 2.12. Shifts greater than 100 nm were observed for Au decahedra, while a complete loss of optical activity was observed for small Ag cubes. The former is likely due to amorphous carbon deposition, surfactant decomposition, and contamination, while the latter results from oxidation and degradation. Based on these highly reproducible results, it was concluded that TEM could only be performed after optical characterization.

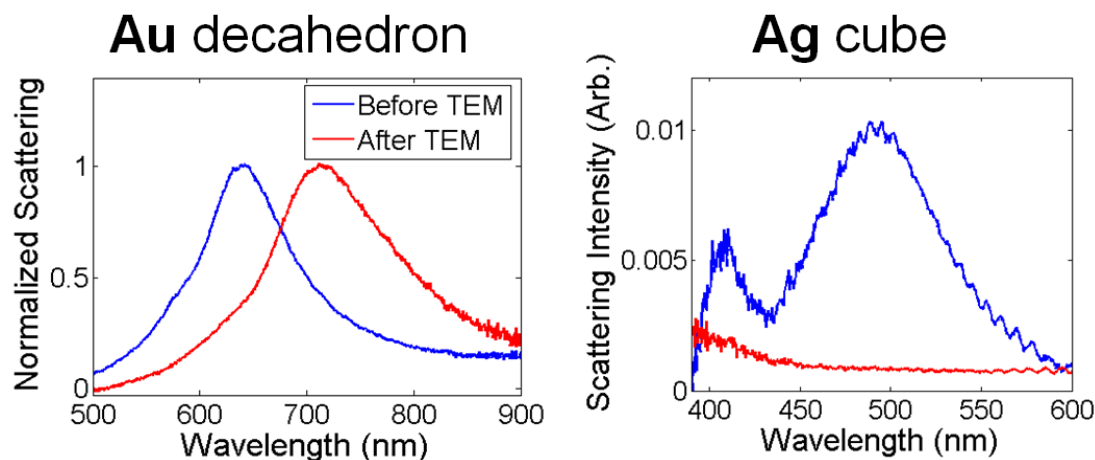


Figure 2.12. Representative single particle scattering spectra before and after TEM analysis. Right: Au decahedron. Left: Ag cube.

### 2.2.2 Polarization Experiments

A polarizer was added to the dark field scattering setup to obtain polarization-dependent spectra. At the University of Melbourne, the polarizer was loosely placed directly on top of the dark field condenser, causing instabilities, as discussed in Chapter 6. At Northwestern University, the polarizer was solidly positioned between the light source and the dark field condenser by means of a 60 mm cage mount screwed on the microscope head, as depicted in Figures 2.9-2.10. The polarization efficiency of the setup was studied by using two identical visible light polarizers, placed at different positions in the beam path. The finding most relevant to this study, presented in Figure 2.13, is that the dark field condenser partially scrambles the polarization of the incoming beam. This effect is expected to be identical at the University of Melbourne, as the same model of polarizer and dark field condenser were used. Further studies, not shown here,

suggest that some objectives may also scramble polarization; caution should thus be taken to characterize the instrument used prior to obtaining polarization data in this geometry.<sup>183</sup>

Despite the lower polarization of the excitation light, good results could be obtained using correlated pol-LSPR/SEM. Validation data was obtained on Ag chains at the University of Melbourne, showing the expected polarization anisotropy, perfectly aligned with the interparticle axis.

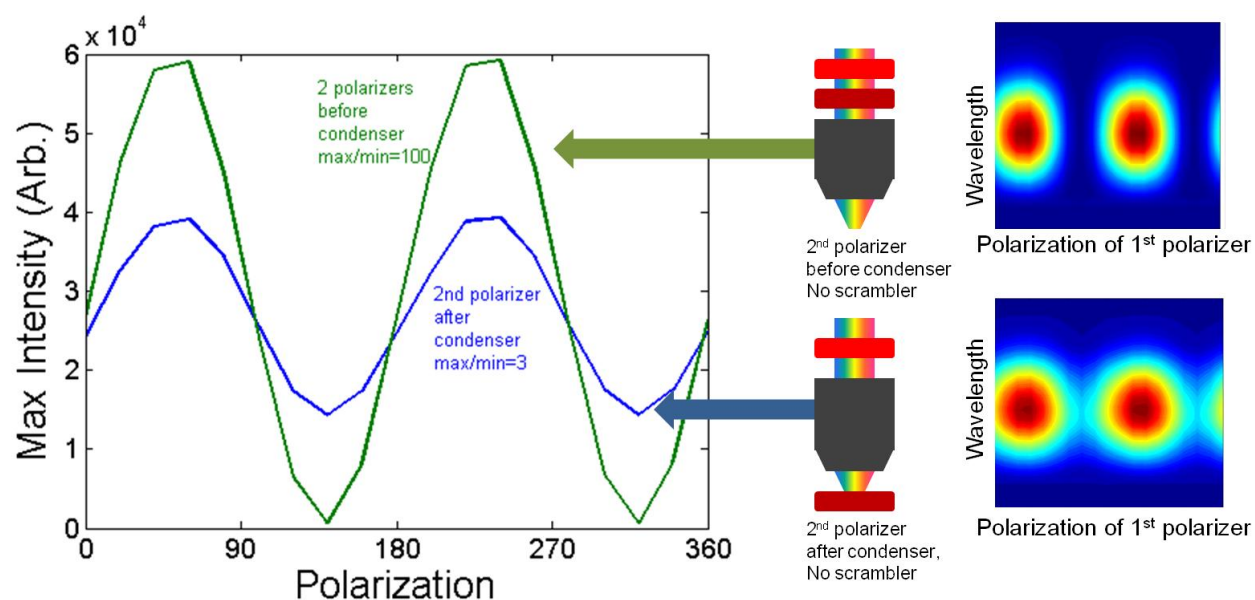


Figure 2.13. Partial polarization scrambling due to the dark field condenser. The color on the right is an arbitrary intensity scale, the wavelength scale is from 400 to 900 nm, and the polarization ranges from 0 to 360 degrees.

Since orientation in the TEM and the optical microscope are not necessarily identical, the orientation was calibrated with pictures of the support grid, and the polarization data was adjusted accordingly for the figures presented in this work. For example, if the TEM image was

tilted  $114^\circ$  from the grid orientation during LSPR measurements,  $246$  ( $360-114$ ) $^\circ$  was added to the x-axis for the polarization plot, until  $360^\circ$ , then  $360^\circ$  was subtracted from the x-axis, followed by addition of  $246^\circ$ . This was performed to make figures more easily interpretable.

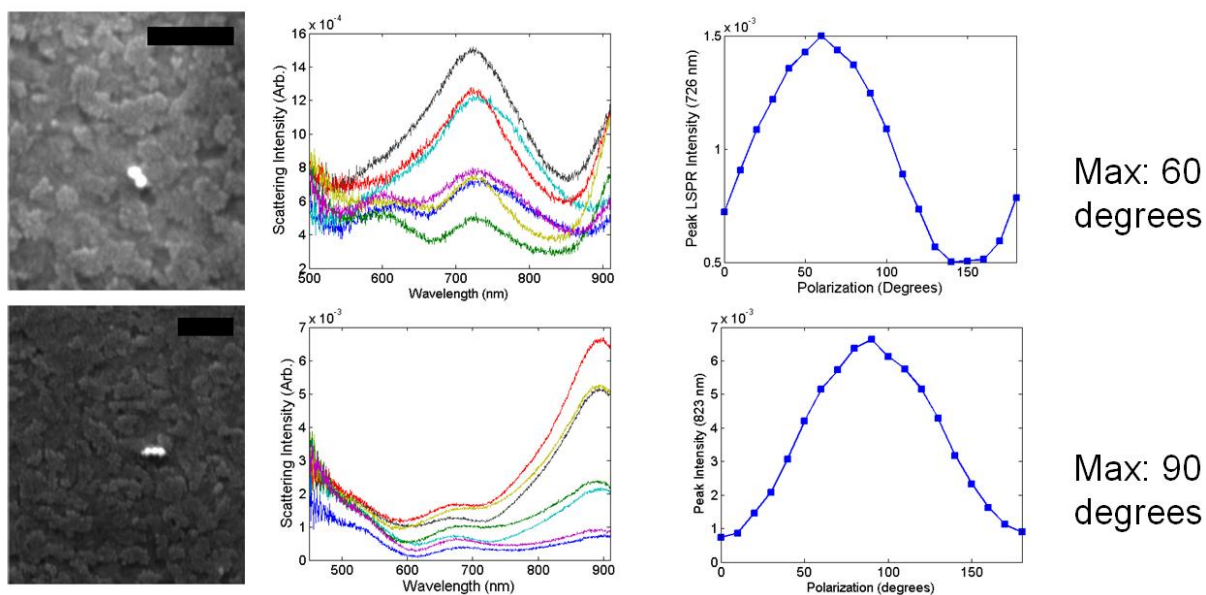


Figure 2.14. Correlated LSPR/SEM validation of the polarization experiments performed at the University of Melbourne. Left: SEM images, where the  $0^\circ$  orientation is vertical. Scalebars, 500 nm. Middle: scattering spectra shown at  $30^\circ$  intervals to highlight the large intensity variation of the lowest energy peak. Right: peak intensity maximum as a function of polarization.

### 2.2.3 Correlated SEM/LSPR and SEM/LSPR/TEM

Due to the large, irreversible sample damage caused by TEM imaging (Figure 2.12), it is impossible to identify the shape or aggregate state of nanoparticles prior to the optical characterization. Thus, many spectra collected are typically discarded because they result from

aggregates or undesired shapes. A way to overcome this challenge is to use a structural characterization technique which minimizes damage to screen the sample and identify particles of interest. SEM is a prime candidate, as it can be performed at a variety of low voltages and current and gives reasonably good resolution. Note that AFM could also be used to this end. To maintain electron transparency and ease of retrieval (x-y coordinate system), TEM grids were used for most SEM studies, except the validation data presented in Figure 2.14, performed on indium tin oxide (ITO)-coated coverslips. A TEM grid holder compatible with SEM sample mounts was available at the University of Melbourne; a 4-grid holder was purchased for Ted Pella, Inc. at Northwestern University.

The effect of SEM imaging on the optical response of Au and Ag nanoparticles was investigated. Noisy before/after SEM results for Ag particles show retention of plasmonic activity (not shown); the strong response shown in Figure 2.14 for particles investigated by SEM prior to dark field microscopy also support the hypothesis of minimal damage in Ag. However, Ag nanoparticles are prone to oxidation and care must be taken to characterize and minimize oxidation effects. On the other hand, Au particles seem to withstand short imaging in SEM very well: results for Au decahedron and icosahedron showing no damage are presented in Figure 2.15. Note that the degree of damage could be surfactant-specific, as some molecules may react differently to the electron beam. It is recommended to test every new system and not assume that it is not damaged by SEM imaging.

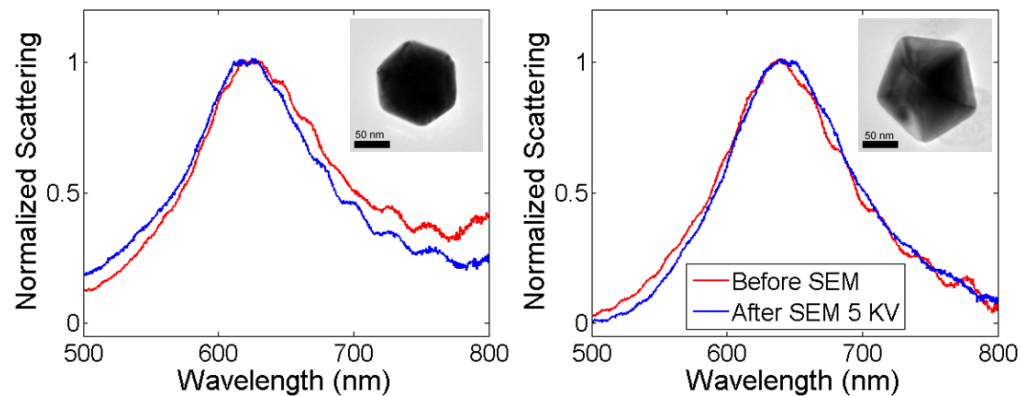


Figure 2.15. Optical response of Au particles before and after shape identification by SEM, showing no noticeable damage. Left: icosahedron. Right: decahedron.

Pre-screening with SEM allows the identification of particles of interest, which can be particularly useful for the investigation of rare shapes, in cases where aggregation is a problem, for weak scatterers as well as for complex aggregates. Note that the electron beam dwell time must be kept to a minimum; SEM performed prior to LSPR is a screening and not an imaging technique (as shown in Figure 2.16) because long exposure results in the formation of a contamination layer that alters the optical response.

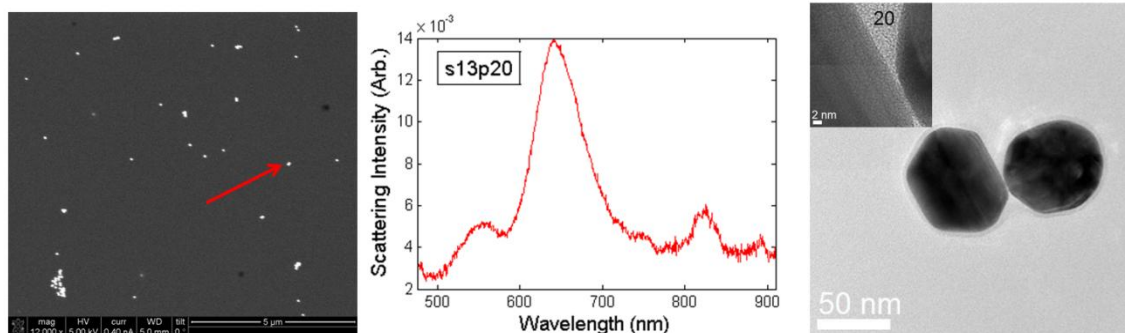


Figure 2.16. Example of correlated SEM/LSPR/TEM. Left: an aggregate of interest is observed in SEM and its position recorded in a low-magnification image. Middle: a single particle scattering spectrum is obtained in dark field microscopy. Right: high resolution TEM images provide information about interparticle distance and particle size and shape.

#### 2.2.4 Correlated LSPR/SERS/TEM

Adding single particle SERS measurements to the LSPR/TEM approach was relatively straightforward. A laser was coupled in epi illumination geometry with the appropriate optics, as described elsewhere.<sup>184</sup> SERS-active particles were deposited on electron-transparent carbon/Formvar support films, although other substrates can be used if SEM is used as the structural characterization tool. A scattering map was obtained to guide dark field scattering, SERS experiments, and TEM imaging. The SERS spectra of active particles/aggregates were first collected, followed by dark field scattering, to prevent the superfluous acquisition of LSPR spectra of inactive particles. The grids were then transferred to a TEM and the SERS-active aggregates were characterized.

### 2.2.5 Correlated ALD/LSPR/TEM

Atomic layer deposition (ALD) of Alumina ( $\text{Al}_2\text{O}_3$ ) was performed on c-flat and  $\text{Si}_3\text{N}_4$  grids, both well-known for their thermal stability. Particles were deposited, dried, and studied by single particle dark field microscopy. The grids were then placed in a custom-built ALD reactor run by Natalie Ray. The ALD precursors used for  $\text{Al}_2\text{O}_3$  growth were trimethylaluminum (TMA) and water, carried by nitrogen gas in a custom made reactor kept at 1-2 Torr. The following cycle was performed: dose TMA 2 s, purge 10 s, dose water 2.5 s, purge 30 s. A total of 10 cycles were deposited, yielding  $\sim 1.1$  nm  $\text{Al}_2\text{O}_3$ . The deposition was performed at 50 or 100 °C, as discussed in the text. The samples were allowed to cool and their post-ALD optical response was analyzed with single particle dark field microscopy.

### 2.2.6 Correlated LSPR/SPIM/TEM

To correlate particle shape, orientation, and optical response to their photoelectron emission behavior, a collaboration with Andrej Grubisic in the group of David Nesbitt at U. Colorado Boulder was established. Special TEM grids, coated with a c-flat membrane (Figure 2.8) instead of carbon/Formvar were used as they gave a low photoemission background. Samples were prepared and characterized with dark field microscopy at Northwestern University, the mailed overnight in a desiccated, triple enclosed,  $\text{N}_2$ -filled Ziploc bag. Scattering maps were provided with the samples. Grids were analyzed by SPIM, a technique described in ref. and Figure 2.17. The grids were then returned promptly (overnight, in dry, inert atmosphere) to Northwestern

University, where post-SPIM dark field microscopy and transmission electron microscopy were immediately performed.

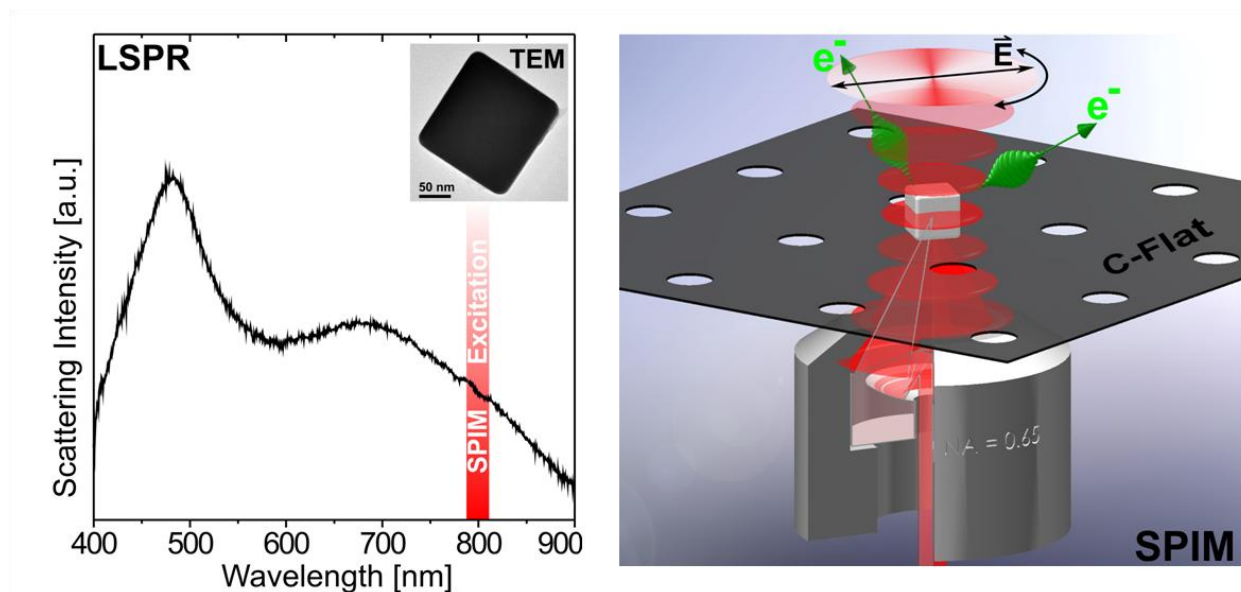


Figure 2.17. Schematic of the correlated LSPR/SPIM/TEM experiment. Left: scattering spectrum of an individual Ag nanocube ( $d \sim 160$  nm) on a c-flat substrate. Inset: TEM image of the Ag nanocube responsible for the scattering spectrum. Right: scanning photoionization microscopy (SPIM) setup, where electron emission following ultrafast laser excitation of a single Ag nanocube is monitored as a function of the laser polarization in the substrate plane.

## 2.2.7 Refractive Index Sensitivity Measurements

### 2.2.7.1 Non-Correlated RIS Measurements

Single particle refractive index sensitivity measurements were performed by depositing a drop of nanoparticle solution on a 25 mm no. 2 glass coverslip. The particles were dried and rinsed with

water. Then, the coverslip was glued on the sample holder with silicone glue. A top coverslip was also glued, and left overnight to form a watertight seal. Tubes were attached on both sides of the sample holder to deliver nitrogen or solutions of water and glycerol (up to 75 % glycerol). After each measurement, the solution was emptied, the cell was washed three times with the next solution, filled, and then measurements were carried out. The seal broke early on in ~20 % of experiments, otherwise the cell could be used with up to 8 different solutions, followed by water and a final measurement in nitrogen. The coverslips on which the particles were deposited were carefully scratched in a half-filled martini glass shaped pattern for easy retrieval over a large area; scattering maps obtained with the video camera were used for particle retrieval. Because of the very low scattering background (i.e. the absence of scattering from Cu grid bars), the NA of the objective could be open (high NA) more than usual, increasing the signal and decreasing acquisition times. SEM correlation would be possible, but was not carried out. For high resolution SEM, ITO-coated coverslips can be used, although their roughness tends to produce an dim, inhomogeneous scattering background.

#### 2.2.7.2 Correlated RIS/TEM

Correlating the structure of a nanoparticle with its refractive index sensitivity, at the single particle level, has traditionally been done using SEM.<sup>108</sup> However, since the initial reports, very few studies have been published on the subject, despite its importance for sensor development. The main challenges for TEM coupling is to find and immobilize an electron transparent substrate which can withstand the flow of multiple viscous solutions. Recently, this problem was

solved by a commercial product from the manufacturers of the  $\text{Si}_3\text{N}_4$  windows previously described (Figure 2.8). This product is TEMVu, a glass coverslip fitted with soft silicone holders securing a silicone-based chip in which a TEM membrane is etched (Figure 2.18). The distance between the bottom of the coverslip and the electron-transparent membrane in the as-provided construct is, however, too large for dark field scattering measurements with an oil immersion 100X objective. The product was thus specially requested "membrane down", i.e. etch pit facing away from the glass coverslip, and a 50X extra-long working distance (ELWD) objective was used. Particles could be clearly seen (Figure 2.18), albeit this technique may be difficult for low scatterers. Note that unlike all the other results presented in this work, the spectra for the RIS measurements were not typically fit with Lorentzian line shapes. Rather, MATLAB was used to obtain the numerical maxima of the smoothed spectra. This was implemented because of the prohibitively large data sets (hundreds of spectra) obtained for each particle, and because the shift can be well captured with numerical peak retrieval.

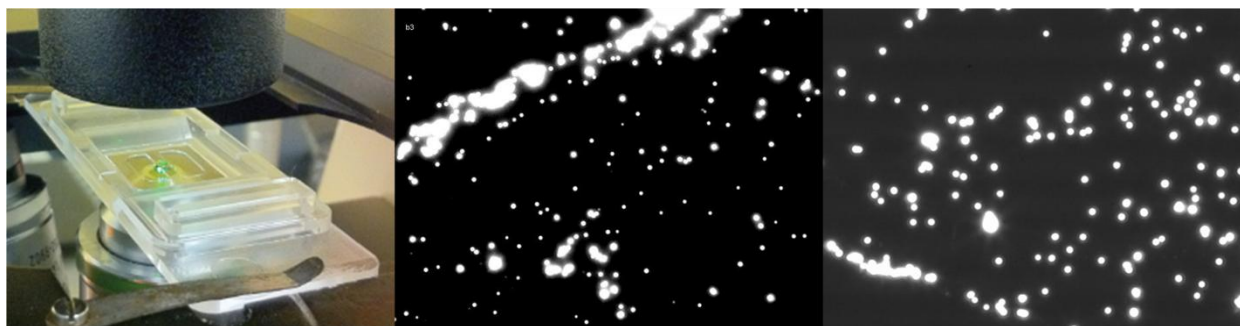


Figure 2.18 Scattering maps and grid sample holder for RIS measurements. Left: TEMVu cell showing the immobilized membrane window, image provided by TEMWindows.com. Middle: Au decahedra on a  $\text{Si}_3\text{N}_4$  membrane in a TEMVu cell, observed with a 50 X ELWD objective. Right: Au decahedra on a glass coverslip, observed with a 100 X oil immersion objective. The images in the middle and on the right have the same size, approximately  $60\ \mu\text{m}$  in width.

## 2.2.8. Other Experimental Observations and Notes

### 2.2.8.1 Reactive Ion Etching

Typical colloidal synthesis products consist of nanoparticles covered with a near-monolayer of surfactants, which can be bound more or less tightly. Such molecules are necessary to direct the growth and/or stabilize the final product in solution, however their presence on the surface of nanoparticles can be detrimental to fundamental studies as well as applications. A difference in refractive index due to the variability in surfactant amounts or chemical nature can, in principle, alter the plasmon resonance frequency of plasmonic particles. The presence of capping ligands may prevent or modify surface availability, influencing catalysis and sensing. Given such potential effects of surfactants, a reliable, simple way to remove them without affecting the

plasmonic properties would be very valuable. The use of reactive ion etching (RIE) was suggested based on previous work in the Van Duyne group. RIE cannot be performed on Formvar/carbon grids as it destroys the support film.

Tests were performed by depositing either small Au decahedra or octahedra (two very homogeneous reaction mixtures) on glass coverslips and performing oxygen RIE for 5 minutes at standard pressure settings. A significant blueshift was observed for both structures, as can be seen in Figure 2.19. This may be due to the removal of ligands (lowering of the average refractive index around the particle). The larger shift for Au decahedra could be due to their larger RIS. However, rounding of the particle corners may also play a role. Further investigation to optimize ligand removal while ensuring that no shape change occur would add a much-needed tool to the nanoplasmonics toolbox. Further, the development of surface decontamination via RIE would allow RIS measurements before and after removal; it is thought that ligand removal could improve RIS in colloidal nanoparticles by freeing some of the sensing volume. Of course, oxygen RIE cannot be applied to Ag or Cu particles due to their tendency to oxidize.

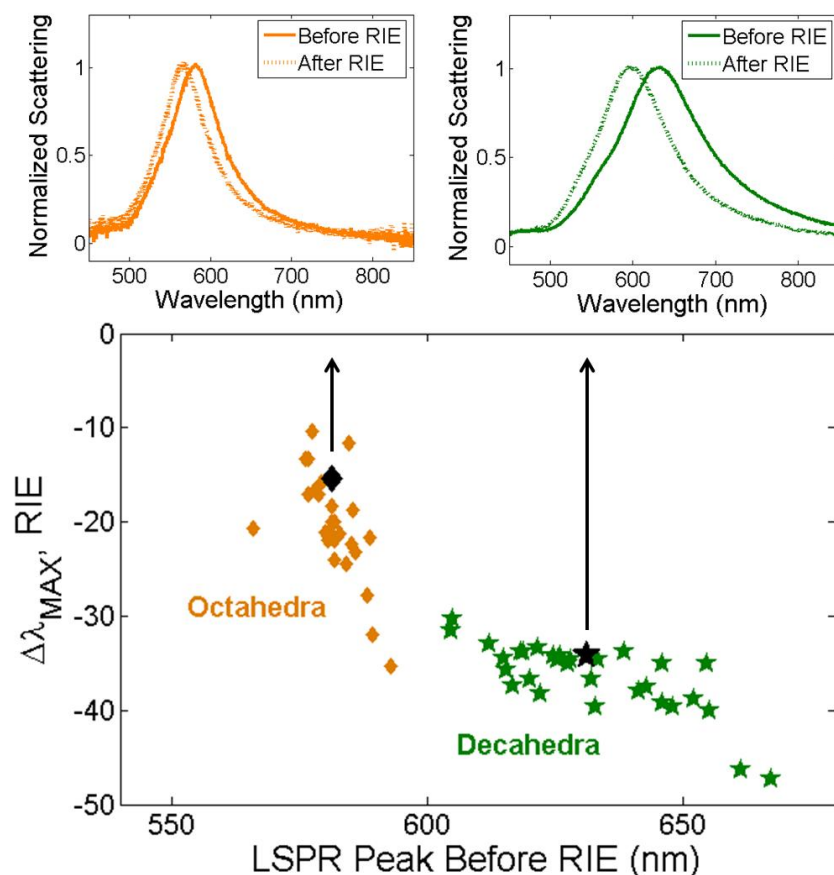


Figure 2.19. Reactive ion etching effect on single Au nanostructures. A blue shift is observed for both shapes.

### 2.2.8.2 Size and Corner Rounding Measurements from TEM Images.

Two methods can be employed to determine the size of nanoparticles from TEM images, as illustrated in Figure 2.20. Lines can be drawn in Microsoft Paint and the coordinates of their intersections recorded; this provides information about orientation, size, and aspect ratio. Alternatively, ImageJ can be used to quickly determine the projected surface area of a particle, a process that requires calibration and homogeneous corner rounding.

Similarly, corner rounding can be either fit manually or with ImageJ. In the former, Microsoft PowerPoint is used to draw a circle matching the radius of curvature of a cube (Figure 2.20) or a triangle corresponding to the truncation height of a bipyramid (Figure 4.6). In the later, the size is determined through the coordinate system approach, and the difference between the actual area (imageJ) and the idealized area (coordinate system) represents the rounding. All measurements presented here used the coordinate system and circle fitting; future experiments may benefit from the ImageJ approach.

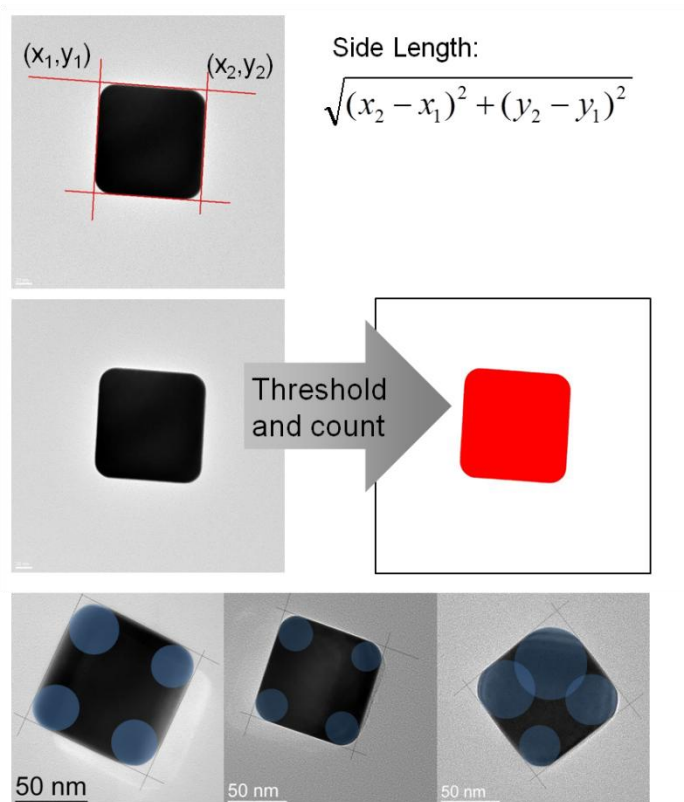


Figure 2.20. Size and corner rounding measurement approaches. Top: coordinate system in Microsoft Paint. Middle: projected surface area measurement with ImageJ. Bottom: circle fitting in Microsoft PowerPoint.

## 2.3 Computational Methods

### 2.3.1 Alloy Wulff Construction Code Overview

A MATLAB code was written and used to calculate the value of  $\Lambda$ ,  $h_{100}$ ,  $h_{111}$ , bulk concentration, surface concentration, and total energy for a given range of initial (homogeneous) composition, cycling through each initial composition and each possible surface composition. The inputs were the number of atoms, an initial guess on  $\Lambda$ , the range and step size desired for the surface and initial concentration, as well as the parameters and functions describing the surface free energy, the bulk free energy, and the unit cell composition-dependence.

Since the surface concentration was fixed in each loop, the bulk concentration could be calculated by knowing the shape, i.e. the number of surface atoms. In the code,  $h_{111}$ , and  $h_{100}$ , and the first approximation for  $\Lambda$  (after the initial guess input) were calculated by solving the basic Wulff model. Then, the  $\Lambda$  in the alloy Wulff model was twice solved for and all concentrations and shape parameters were recalculated at each step. It was found that this number of repetition was sufficient to reach convergence. Concentrations above unity or below zero were set to unity and zero, respectively, and parameters were calculated with those fixed concentrations.

The lowest energy configuration for each initial concentration was found from the energy matrix output of the previous step by finding the numerical energy minimum. Similarly,  $h_{111}/h_{100}$  ratios could be calculated from the output  $h_{111}$  and  $h_{100}$  matrices by knowing the lowest energy configuration.

Graphics were produced by creating an isosurface plot from a basic Wulff model, given the  $h_{111}/h_{100}$  parameter.

Most calculations were performed on a laptop or desktop computer. Using a computational cluster would speed the calculations, but a personal computer can handle them.

All the MATLAB codes used are reported in appendix A2. The details of their usage is clearly outlined in Chapter 7.

### 2.3.2 Kinetic Twinned Wulff Construction Code Overview

All the calculations necessary to produce publication-quality figures were performed in MATLAB with the codes supplied in Appendix A3. The codes consist of the single twinned code, the five-fold twinned code, and the graphical user interface (GUI) code that contains both singly and penta-twinned codes.

In kinetic Wulff modeling, a 3D (xyz) grid is first defined with the meshgrid function, and the growth front value ( $E_{xyz}$ ) is calculated for each point according to the following equation:

$$E_{xyz} = e^{-\beta([h,k,l] \cdot G - G \cdot G)^2} \quad (2.1)$$

Where

$$G = (1 + \varphi) \frac{V_{hkl}}{\sqrt{h^2 + k^2 + l^2}} [h, k, l] \quad (2.2)$$

$$\varphi = \varphi_{re-entrant} + \varphi_{twin} + \varphi_{disclination} \quad (2.3)$$

As explained in Chapter 8,  $\varphi$  is a face-specific enhancement factor and  $V_{hkl}$  is the growth velocity of the hkl face. The parameter  $\beta$  is a smoothing factor to soften the edges of the faces, lowering the number of mesh points needed to produce a reasonably smooth figure. Finally, an isosurface plot, i.e. a surface connecting mesh points with the same value, in three dimensions, is used to render the nanoparticle shape. Additional smoothing can be performed in MATLAB (and in the GUI provided) through box kernel smoothing, but care has to be taken not to round the nanoparticle edges with too aggressive smoothing.

A personal computer was used for calculations with step size larger than 0.1; clusters were used for smaller step sizes and for the initial rendering of the isosurface. Once saved as a ".fig" file, the isosurface of a small step size data set can be easily manipulated on a personal computer.

## CHAPTER 3

### Unraveling the Effects of Size, Composition, and Substrate on the LSPR Properties of Au and Ag Nanocubes: A Systematic Single Particle Approach

### 3.1 Introduction to Size, Composition, and Substrate Effects

As previously discussed (Chapter 2), size, shape, composition, dielectric environment, and aggregation affect the plasmon resonance frequency and linewidth of metal nanoparticles.<sup>2,8,31,52,60,62,66,74,79,81,84,86,89,91-94,97,98,101-103,105,106,109,112,129,185-190</sup> Amongst those, the latter two can be exploited in detection schemes,<sup>54,55,63,64,191</sup> while size, shape, and composition can be used to tune the resonance frequency for optimized applications in, for example, surface-enhanced spectroscopies<sup>192-194</sup> and sensors based on molecular resonance interactions.<sup>195,196</sup> Despite recent synthetic advances that have allowed the production of a wide range of nanoparticle sizes and shapes,<sup>62,74,85,119,122,127,129,132,134,138,187,197-199</sup> very few rules exist to quantitatively predict the effects of such factors on the plasmonic behavior.

One of the structures for which significant synthetic progress has been made are nanocubes:<sup>62,102,122,127,187</sup> increasingly monodisperse and size-controlled products can be obtained, allowing their use as SERS substrates<sup>200-203</sup> and plasmonic sensors,<sup>57,61</sup> for example. Indeed, cubic structures are interesting building blocks for supported devices, as they can sit flat on a substrate, their right angles and flat faces allowing them to be closely stacked next and on top of each other, in a random<sup>200</sup> or directed fashion.<sup>123</sup>

For such supported devices, substrate selection is part of the design process; transparency, conductivity, and robustness are only a few of the attributes that may be required for a given application. Changing these properties may alter the density, i.e. refractive index of the support film, which in turn can affect the plasmon resonance frequency of the deposited particles.

In an effort to provide a predictive tool for easy tuning of the plasmonic properties of supported nanocubes, Au and Ag nanocubes were obtained and analyzed using single particle correlated LSPR/TEM. The effects of size, shape (i.e. corner rounding), composition, and substrate refractive index were addressed and quantified.

### 3.2 Previous Studies on Au Nanocubes

Previous work on supported Ag nanocubes highlighted the presence of a high-energy, sharp plasmon peak not prominent in solution.<sup>106,147</sup> The spectra and structure of a single Ag nanocube was obtained and a good agreement with Finite-difference time-domain (FDTD) results could be achieved by using a size and corner rounding close to what was observed experimentally (TEM: 85.6 X 80.9 nm, 11 and 12 nm rounding, best FDTD fit: 83 X 83 nm, 13 nm rounding). While limited experimental data were reported (only one cube), the extensive computational results provided the trends to be expected in a future, more complete study. In particular, the plasmon resonance frequency of both peaks was shown to shift to longer wavelengths for larger or sharper cubes, with the higher energy peak appearing to shift less, at least in the (non-linear) wavelength scale presented.

Other calculations on the properties of plasmonic nanocubes have been published, predicting the occurrence of Fano resonances,<sup>57</sup> and describing high order modes,<sup>96</sup> for example. The wide-ranging, burgeoning literature on nanocubes<sup>52,57,61,86,92,106,123,125,138,147,200-204</sup> (both fundamental

and applied) testifies of the scientific interest in such regular, sharp-cornered, and easily stackable shape.

### 3.3 Experimental Results and Discussion

To probe the effect of size, corner rounding, composition, and substrate dielectric constant on the localized surface plasmon resonance frequency and linewidth of Ag and Au nanocubes, particles with size (side length) ranging from 60 to 100 nm were obtained from synthesis collaborators (see Chapter 2). The two substrates studied were polyvinyl formal, i.e. Formvar, a polymer typically used as TEM grid membrane (refractive index of 1.5<sup>205</sup>), and the semiconductor silicon nitride, of approximate composition Si<sub>3</sub>N<sub>4</sub> and refractive index 2.05.<sup>206</sup> The cubes on different substrates were analyzed using single particle correlated LSPR/TEM, as described in Chapter 2. A total of 42 (Ag, Formvar), 58 (Ag, Si<sub>3</sub>N<sub>4</sub>), 52 (Au, Formvar), and 23 (Au, Si<sub>3</sub>N<sub>4</sub>) nanocubes with a projected aspect ratio between 0.90 and 1.11, isotropic rounding, and average relative rounding ( $r/c$ ) of less than 0.22 were obtained.

Representative TEM image and spectra for nanocubes with  $c \sim 78$  nm and  $r \sim 12$  nm are presented in Figure 3.1. In the Ag spectra, two peaks are observed: a sharp resonance near 400 nm and a broader one in the 500 nm region. The high-energy peak is a quadrupolar resonance that becomes prominent when a Ag cube is in a relatively high RI medium, i.e. as low as 1.33 (water).<sup>106</sup> Considering the fact that the configuration of a nanocube lying on a surface is a non-symmetric, the resonance is not a true quadrupole, just as the dipole is not a true dipole. Figure

3.2 shows a simulated spectrum of a single nanocube on a dielectric substrate. The higher-energy peak (quadrupolar in origin) has strong correlations with enhanced electric fields away from the surface whereas the lower-energy peak (dipolar in origin) correlates with fields towards the substrate. Note that this quadrupolar resonance is not observed in Au nanocubes because of the onset of interband transitions at energies above 500 nm, as discussed in Section 3.3.2.

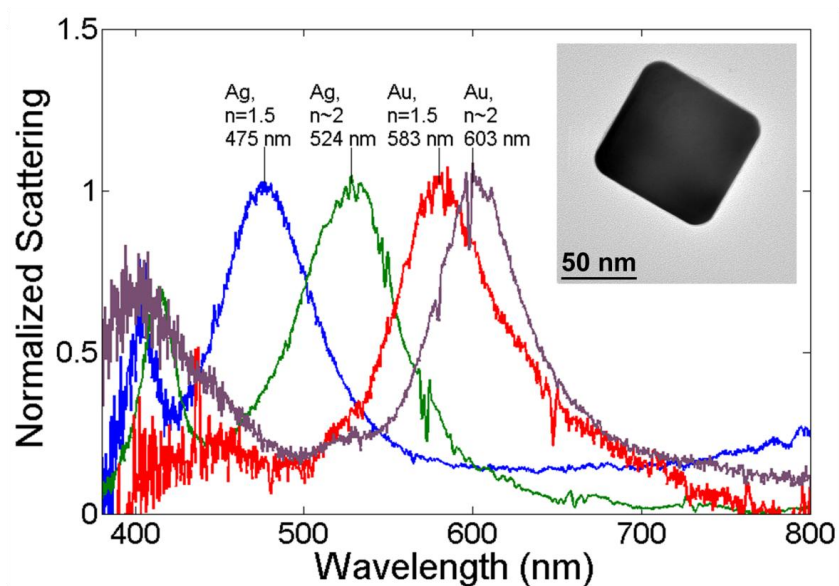


Figure 3.1. Representative single particle LSPR spectra and TEM image of single Ag and Au nanocubes with  $c \sim 78$  nm and  $r \sim 12$  nm. Blue trace: Ag on Formvar. Green trace: Ag on Si<sub>3</sub>N<sub>4</sub>. Red trace: Au on Formvar. Purple trace: Au on Si<sub>3</sub>N<sub>4</sub>. Inset: TEM image of Ag nanocube on Formvar.

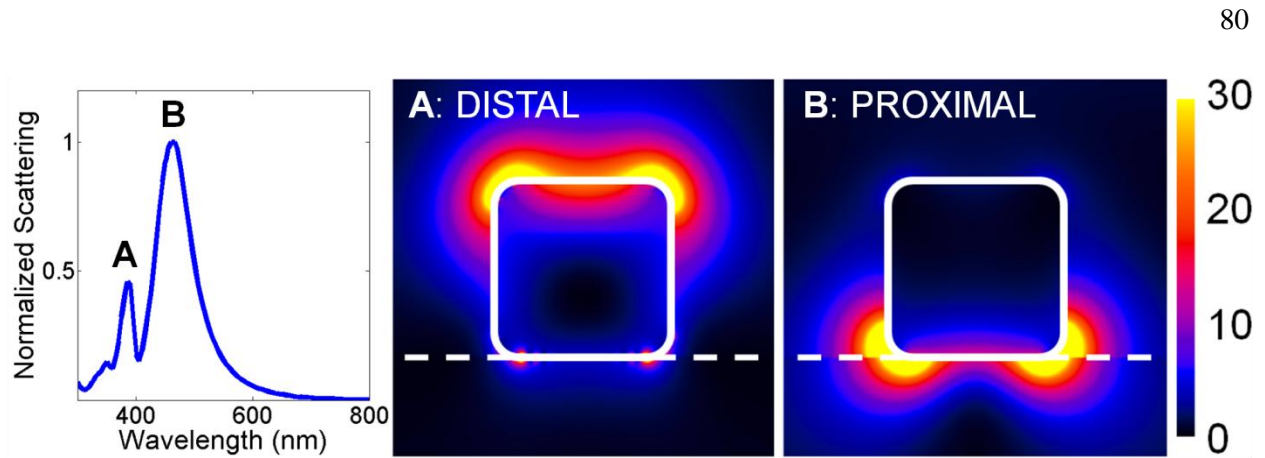


Figure 3.2. FDTD calculated optical response and electric field intensities for a  $c = 78$  nm and  $r = 12$  nm Ag nanocube on Formvar. Left: calculated scattering spectrum. Middle: Field profile for the quadrupolar (A) resonance at 388 nm. Right: field profile for the dipolar (B) resonance at 467 nm. In the field profiles, the nanocube is outlined in solid white, and the substrate position is indicated using a dashed white line.

### 3.3.1 Effect of Size

Size is a powerful handle on plasmonic properties: generally, a redshift of the LSPR frequency is observed with increasing particle size because of retardation effects, a phenomenon described in Chapter 1.

To quantify the effect of size on the plasmonic properties of nanocubes, 175 single particle spectra were obtained and fit to Lorentzian line shape function(s) (one per mode), yielding plasmon energy and FWHM as a function of particle size for different compositions (Ag and Au) and different substrates (Formvar and  $\text{Si}_3\text{N}_4$ ), see Figure 3.3 and 3.4. From this correlated LSPR/TEM data, statistics related to the fit and the error for both plasmonic attributes were extracted. A statistically significant linear relationship between the LSPR position and the

nanocube side length (Figure 3.3) was found for all three resonances under consideration (Ag quadrupole, Ag dipole, and Au dipole). Statistics were obtained using analysis of covariance, a tool for analyzing groups of data which may have different slopes. The slope of the LSPR positions as a function of size was found to not be statistically different for a given peak on either substrate, having p-values of 0.37, 0.63, and 0.65 for Au proximal, Ag distal, and Ag proximal, respectively (Table 3.1). Note that a p-value is related to the probability that the difference between two groups is the result of chance, which goes from zero (not likely, or in other words a real effect) to one (extremely likely). A model constraining the slopes to be the same (parallel lines) was thus used for subsequent analysis. The results obtained, together with their standard deviations, are presented in Table 3.1. It can be seen that the resonance energy dependence on nanocube size is greatest for the Ag dipole, followed by the Ag quadrupole, and the Au dipole. An interesting feature of these results is that the redshifts due to the substrate are independent of nanocube size for a given plasmon mode (parallel lines), suggesting that an heterogeneous collection of nanocubes would not affect their performance if used in an application based on the sensitivity to substrate RI, investigating phase transitions, for example.

While quantitative, predictive rules could be extracted from the size dependence of the LSPR energy, the relationship between plasmon decay (measured in terms of FWHM) and side length is not as conclusive (Figure 3.4). The effect of inhomogeneous corner rounding, the limited size range available, and small local changes in dielectric environment are likely responsible for the scatter in the FWHM data. Analysis of covariance (not shown) yielded large errors, with the 95% confidence intervals on the slopes ranging from negative to positive values (i.e. no statistically

significant relationships). Successful attempts at correlating the plasmon FWHM with size for wider particle size ranges and different shapes are presented in Chapter 4.

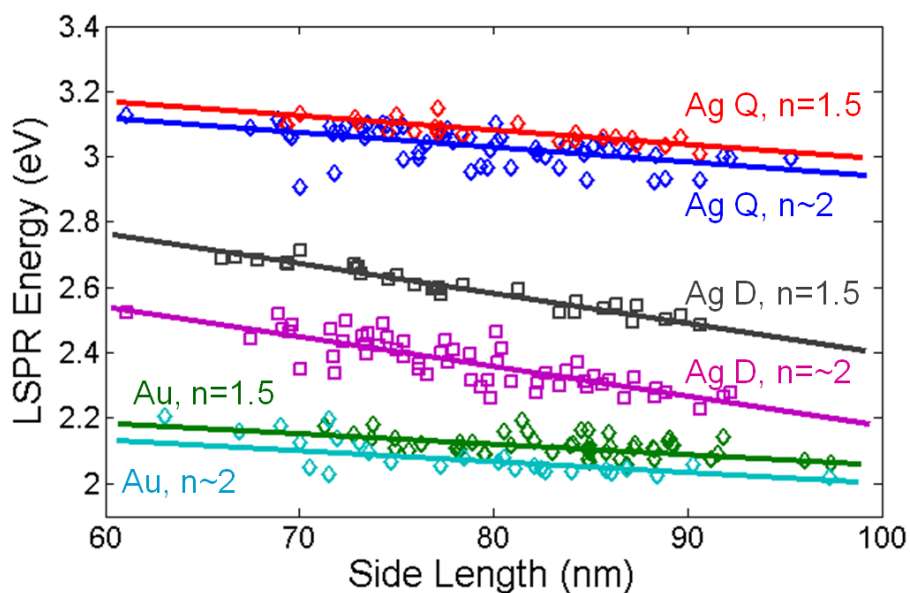


Figure 3.3. Effect of nanocube composition, plasmon mode, and substrate RI ( $n$ ) on the LSPR energy for Ag and Au nanocubes. The difference in LSPR positions on Formvar and  $\text{Si}_3\text{N}_4$  are 0.23 and 0.057 eV for the dipolar (D) modes of Ag and Au, respectively; it is 0.053 eV for the Ag quadrupolar (Q) mode. Parallel slopes fit shown (see Table 3.1 for values and text for discussion).

Table 3.1. Fit parameters and p-values for the size dependence of the resonance energy of Ag and Au nanocubes. The data is presented in Figures 3.3.

Sample (LSPR)	Substrate	Slope meV/nm	Intercept eV	p-value
Au (proximal)	Si <sub>3</sub> N <sub>4</sub>	-3.9 (0.6)	2.39 (0.05)	0.37
Au (proximal)	Formvar		2.44 (0.05)	
Ag (distal)	Si <sub>3</sub> N <sub>4</sub>	-4.2 (0.6)	3.36 (0.05)	0.63
Ag (distal)	Formvar		3.41 (0.05)	
Ag (proximal)	Si <sub>3</sub> N <sub>4</sub>	-8.9 (0.5)	3.07 (0.04)	0.65
Ag (proximal)	Formvar		3.30 (0.04)	

Note: Standard deviation on the last digit shown in parentheses.

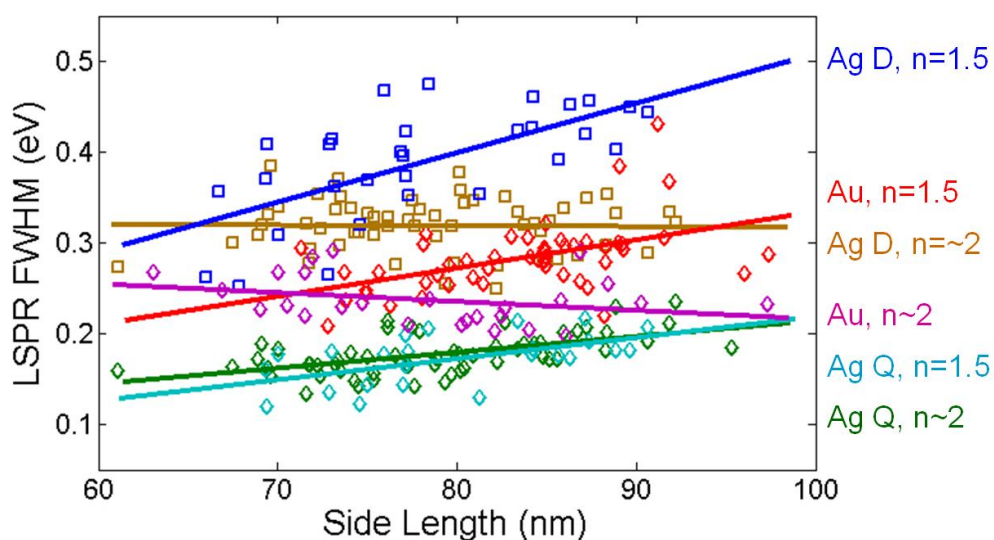


Figure 3.4. Effect of nanocube composition, plasmon mode, and substrate RI on the LSPR FWHM for Ag and Au nanocubes. Separate slopes fit shown.

### 3.3.2 Effect of Composition

Ag and Au have, as discussed previously, strikingly different spectra, most notably the presence of a sharp quadrupole-like mode for Ag below 400 nm. Such resonance is absent of the Au

spectra because of the onset of interband transitions at energies higher than 500 nm, resulting in a damping of all plasmon resonances at such frequencies. This resonance nonetheless exists in Au, and is expected to redshift and become more noticeable upon increase of the surrounding RI. Indeed, a shoulder around 525 nm was consistently observed for Au nanocubes on Si<sub>3</sub>N<sub>4</sub>. Work with a support film of high refractive index (Si, RI ~ 4), aimed at shifting the quadrupolar plasmon mode away from the interband transitions, was inconclusive: only very thin (15 nm) Si films were available, such that the dielectric medium probed by the plasmon extends beyond the film, reducing the effective refractive index. This RI was further lowered by the presence of a thin, low density native oxide (SiO<sub>x</sub>, RI ~ 1.5) on both sides of the support film.

While it remains impossible to compare the quadrupolar modes of Ag and Au, both dipoles are prominent in their spectra. The dipolar plasmon of Au is located at significantly lower energies than that of Ag (600 and 500 nm region, respectively), as predicted by their different dielectric constants; this effect can be modeled by Mie theory<sup>2,91</sup> and has also been observed experimentally.<sup>79</sup> The energy gap between Ag and Au depends on the size of the cubes and the substrate (Section 3.3.1, Figure 3.3); typical values for  $c = 85$  nm are 0.43 eV and 0.26 eV on Formvar and Si<sub>3</sub>N<sub>4</sub>, respectively.

Beyond understanding the effects of structure and composition on the LSPR energy, it is interesting to study the plasmon decay, i.e. the peak FWHM for the various resonances. Despite the noise in this data (Figure 3.4), it is clear that the dipolar mode of Au is sharper (lower FWHM) than the dipolar mode of Ag for a given substrate. Lower losses in the red region for Au are most likely responsible for this effect. Additionally, the quadrupolar mode in Ag is the

sharpest amongst the studied resonances; higher order modes tend to have sharper plasmon widths.<sup>57,82,96,106</sup>

### 3.3.3 Effect of Substrate

The resonance frequency of small metal particles is highly sensitive to the immediate dielectric environment surrounding them, as expected from basic models, e.g., Mie theory.<sup>2</sup> This sensitivity, in fact, has been exploited in a number of biological and chemical sensors.<sup>54,55,61,63-66,68,69,73,207,208</sup> While modifying the substrate only alters the environment immediately adjacent to one of the six equivalent faces of a nanocube, this change nevertheless expected to have noticeable effects on its plasmonic properties.<sup>57,186</sup> Substrate effects are indeed observed for all the plasmon modes of nanocubes, as shown in Figure 3.3. The difference in dielectric properties between Ag and Au, in particular the different absolute value of the real part of the dielectric constant in the visible region (they have a similar slope),<sup>50,59</sup> give rise to their different sensitivities to the surrounding dielectric medium.<sup>50,59,68,79,102</sup> This is reflected, in the present study, by the different degree of spacing between the parallel lines in Figure 3.3. The Ag dipolar resonance is about five times as sensitive as its Au analogue, with plasmon shifts of 0.23 and 0.057 eV between Formvar and Si<sub>3</sub>N<sub>4</sub>, respectively. This finding is important for sensing applications relying on substrate-induced optical shifts (e.g., sensing of phase transitions or surface segregation), where Ag nanocubes should be favored due to their higher sensitivity.

### 3.3.4 Quadrupole and Dipole Modes in Ag Nanocubes

Silver nanocubes supported on a substrate display two plasmon resonances, a sharp quadrupole around 400 nm and a dipole around 500 nm, as discussed above. The dipolar resonance is about five times as sensitive to the change in substrate refractive index than the quadrupolar resonance (0.23 and 0.053 eV), as expected from their different local environment correlations (Figure 3.2): the electric fields of the dipolar mode extend into the substrate, leading to high substrate RI sensitivity; the quadrupolar fields are concentrated away from the substrate, suggesting a higher sensitivity to the dielectric properties of the medium above the substrate (a property of interest for sensing applications). Additionally, the width of the quadrupolar peak is significantly less than that of the dipolar peak (Figure 3.4, another property interesting for sensing).

### 3.3.5 Effect of Corner Rounding

Due to the effects of corner rounding on plasmonic properties,<sup>81,85,97,103,105,106,147,209</sup> only cubes with average relative rounding ( $r/c$ ) of less than 0.22 were used for the statistical analysis of the effects of size, composition, and substrate RI (Figures 3.3 and 3.4). While the majority of Ag cubes fulfilled this requirement, a number of Au particles had to be rejected. Such particles can now be used to investigate, rather qualitatively, the influence of shape on the plasmonic properties. A total of 66 Au cubes, 14 rounded ( $r/c > 0.25$ ) and 52 sharp ( $r/c < 0.22$ ) were investigated; their plasmon energy and FWHM are reported in Figure 3.5. As expected,<sup>106,147</sup> a shift to higher resonance energy is observed for more rounded cubes. The average shift obtained

between the sharp and rounded group was 0.1 eV. Refractive index sensitivity measurements were not performed, but comparing sharp and rounded cubes, without bulk inhomogeneities, would certainly provide insight on the effect of tip sharpness on sensing performance, as was determined for their SERS activity.<sup>201,202</sup> Additionally, no effect of rounding was found on the FWHM of the nanocubes; it is unclear whether, in this shape range, any broadening is expected as previous calculations did not directly address this issue.<sup>106,147</sup>

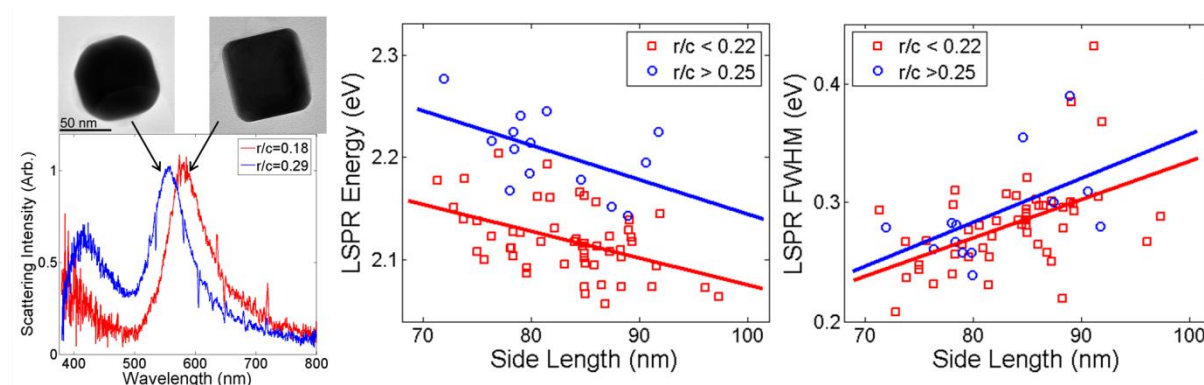


Figure 3.5. Effect of corner rounding on the plasmonic properties of Au nanocubes. Left: example of single particle LSPR spectra and TEM pictures for sharp ( $r/c = 0.18$ ) rounded ( $r/c = 0.29$ ) nanocubes of 78 nm side length ( $c$ ). Middle: effect of rounding on the dipolar resonance energy. Right: effect of corner rounding on the dipolar resonance FWHM. Separate slopes fit shown.

### 3.4 Computational Results and Discussion

A collaboration with the Schatz group at Northwestern University was established to study the plasmonic behavior of nanocubes with FDTD.<sup>52,147,210</sup> Effects difficult or impossible to probe

experimentally were targeted, as numerical results typically yield qualitative results; reproducing large data sets such as that in Figures 3.3-3.5 are beyond the current computational capabilities.

Previous calculations showed good agreement between the experimental and FDTD calculated spectra of Ag nanocubes on Formvar.<sup>147</sup> To validate the technique with Au structures, calculations were performed (see ref.<sup>52</sup> for details) for a variety of experimental nanocube sizes and rounding. The agreement between numerical and experimental spectra was typically acceptable: the energy matched within 50 nm, and the width and symmetry of the peaks was moderately well reproduced computationally. Two representative spectra, for Au on Formvar and Si<sub>3</sub>N<sub>4</sub>, are presented in Figure 3.6. Discrepancies are noticeable, and many factors and computational assumptions can be invoked to explain the mismatch, some of which are discussed below.

The disparities in the interband transition region (energy above 500 nm) can be attributed to the low intensity of the white light at short wavelengths in the experiments, rendering the results in that region less reliable. Another mismatch is obvious in the Si<sub>3</sub>N<sub>4</sub> spectra: the calculations show a sharp dip to zero intensity near 720 nm, not seen experimentally. This feature is believed to arise from an optical mode in the Si<sub>3</sub>N<sub>4</sub> layer, which does not occur in the experiments due to substrate inhomogeneities (in particular thickness variations). Further calculations confirmed this assignment (see ref.<sup>52</sup> and Section 3.4.1). While the optical response of the cube on Si<sub>3</sub>N<sub>4</sub> is moderately well modeled with FDTD, both the peak shape and energy are inadequately reproduced for the Au nanocube on Formvar (Figure 3.6). The 10 nm shift between theory and experiment may be due to the clean surface assumption in FDTD, i.e. the presence of surfactants and contaminants around the particle was neglected. Such molecules would create a higher local

dielectric environment, leading to a blueshift of the plasmon resonance. This effect is expected to be more pronounced for Formvar than  $\text{Si}_3\text{N}_4$ , as the substrate RI is already high in the latter.

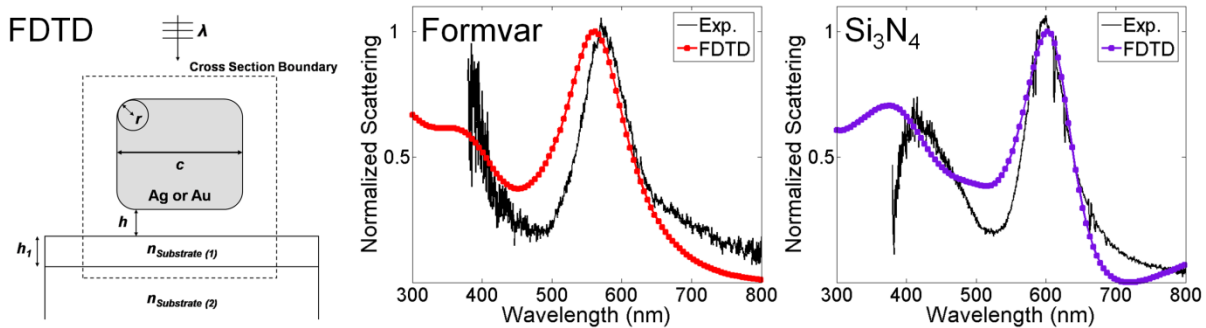


Figure 3.6. Computational and experimental Au nanocube spectra. Right: geometry used for FDTD calculations. Middle: comparison of FDTD calculated and experimental scattering for a  $c = 84.0$  nm and  $r = 15.2$  nm cube on Formvar. Left: comparison of FDTD calculated and experimental scattering for a  $c = 74.2$  nm and  $r = 12.7$  nm cube on  $\text{Si}_3\text{N}_4$ .

### 3.4.1 Effect of Substrate Composition and Layering Morphology

Experimental parameters such as the substrate thickness (100 nm) and its distance from the glass coverslip were fixed, such that to study the effect of substrate thickness and layering, FDTD calculations were performed. Following the computational geometry presented in Figure 3.6, the optical response of a Au nanocube with  $c = 72$  nm and  $r = 11$  nm placed directly ( $h = 0$ ) on  $\text{Si}_3\text{N}_4$  layers of varying height ( $h_l = 25 - 200$  nm), all atop infinite glass substrates, were calculated (Figure 3.7). Note that for these calculations, grid spacing of 1.0 nm were used to save computational time, as only qualitative trends were sought. As soon as the  $\text{Si}_3\text{N}_4$  layer is added

( $h_l = 25$  nm), the proximal LSPR shifts from 557 nm to 607 nm, equivalent to that found when changing the RI of an infinite layer from  $n = 1.5$  to  $n = 2$  (see below). Further increasing  $h_l$  does not affect the position of the proximal LSPR, showing that only the RI of the material in the very near-field ( $\sim 25$  nm) of the nanoparticle is important for the dipolar response. Further calculations varying the layer thicknesses between 0 and 25 nm would be of interest, as they would unravel the form of substrate thickness dependence of the plasmon shift (linear? exponential?), and may help explain the results for Au cubes on thin (15 nm) Si layers.

A minimum going to zero around 800 nm, the optical mode in the  $\text{Si}_3\text{N}_4$  layer previously described, becomes apparent at  $h_l = 75 - 100$  nm. Confirmation of the nature of this mode comes from its behavior with changing  $h_l$ . As  $h_l$  is increased, the optical mode redshifts, eventually leaving the spectral range considered. Note that for thicknesses of both 100 nm and 200 nm, a peak near 400 nm is observed, which is likely unrelated to interband transitions, but could be attributed to a LSPR, or possibly another optical mode altogether.

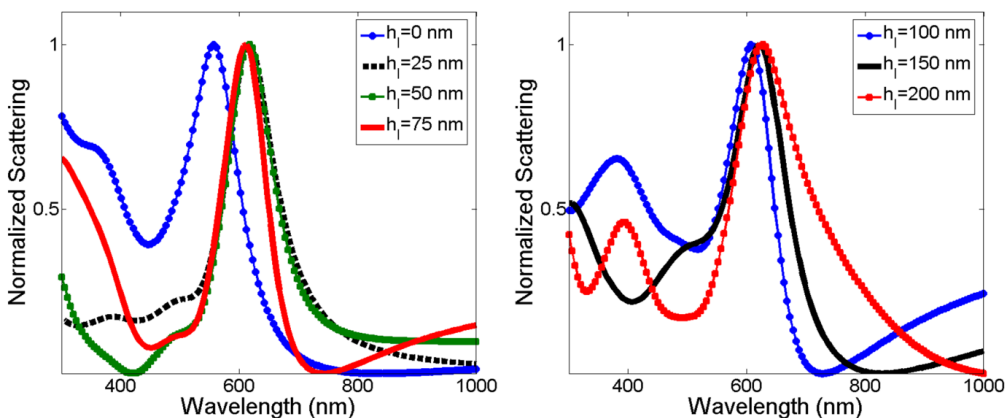


Figure 3.7. Effect of substrate thickness on the optical response of a Au nanocube calculated using FDTD. The nanocube is directly atop a  $\text{Si}_3\text{N}_4$  substrate on an infinite glass medium. Right: redshift of the dipolar LSPR due to the introduction of a high RI substrate ( $\text{RI} = 2$ ), and the buildup of an optical mode with increasing thickness. Left: redshift of the optical mode with a further increase of thickness.

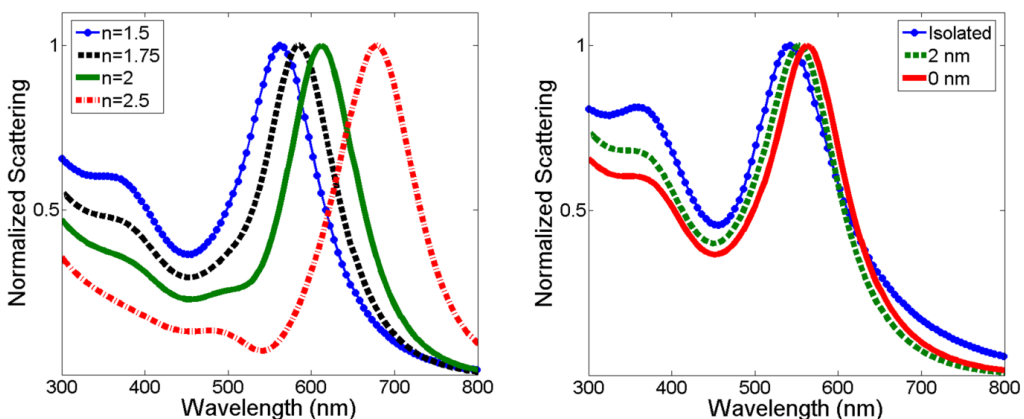


Figure 3.8. Effect of the substrate on the optical response of a Au nanocube, calculated using FDTD. Left: optical responses for various substrate RI values, with nanocube resting directly atop the substrate. Right: optical responses of a nanocube as a function of the distance from a Formvar substrate.

The optical response (scattering) of a  $c = 84.0$  nm and  $r = 15.0$  nm (i.e. the parameters of the cube in Figure 3.6) nanocube on a infinite slabs of material of different refractive indices were also calculated. As expected and observed experimentally, the plasmon resonance shifts towards lower energies in a high refractive index medium. However, the main goal of this exercise was not to extract this well understood phenomenon, but rather to predict the magnitude of the shift and probe the appearance of the quadrupolar band on high RI substrate. Both questions were left half-answered. The magnitude of the FDTD calculated shift between Formvar (RI = 1.5) and  $\text{Si}_3\text{N}_4$  (RI  $\sim 2$ ) is 50 nm, while the value obtained experimentally was 16 nm. A variety of factors can be invoked to explain this difference, most prominently the presence of surfactant molecules around the particle, however it remains that the calculation performed are not adequate to predict the effect of substrate on the LSPR of Au nanocubes. The spectra shown in Figure 3.8 do suggest a small shoulder in the 500 nm region, which could be the Au analogue of the sharp Ag mode. However, no field distribution computation at this wavelength were performed, thus it is unclear whether this is indeed a quadrupole-like resonance.

### 3.4.2 Effect of Particle-Substrate Distance

Another factor that is both difficult to probe experimentally and important for plasmonic properties is the particle-substrate distance. The presence of surfactant molecules around the nanocubes is expected to create some separation from the underlying support film; however, this distance is difficult to measure or control experimentally. FDTD was thus used to calculate the

optical response of a Au nanocube with  $c = 84.0$  nm and  $r = 15.0$  nm (i.e. the parameters of the cube in Figure 3.6) at different distances  $h$  from a Formvar substrate. As can be seen in Figure 3.8, The dipolar mode shifts to lower energy as the nanocube is brought closer to the substrate, from 542 nm when infinitely separated (isolated in air), to 552 nm when  $h = 2$  nm, to 562 nm when directly in contact with it ( $h = 0$ ). The results obtained are in agreement with previous studies on Ag nanocubes without corner rounding<sup>106</sup> as well as with the discussion above, further suggesting that only the near-field proximity of a material, often just a few nanometers, is influential on the proximal LSPR.

### 3.5 Conclusions

The systematic study of Ag and Au nanocubes on different support films performed using correlated LSPR/TEM provided quantitative and predictive rules for the effects of size, composition, and substrate on the plasmon resonance energy. Qualitative trends were also obtained using FDTD, specifically about factors difficult to control experimentally such as the substrate layering morphology and the particle-substrate distance. The results presented suggest that nanocubes could be very good optical RI sensors. In particular, the quadrupolar mode of Ag nanocubes is a prime candidate, as it is sharp, and has a relatively weak dependence on position with nanocube size, meaning slight heterogeneities would be insignificant. Additionally, based on its field correlations, this mode is expected to have a high sensitivity to change in RI above the substrate, while having a low sensitivity to the substrate itself.

## CHAPTER 4

### Plasmon Length: a Universal Parameter for the Size Dependence of Plasmonic Phenomena

#### 4.1 Correlated LSPR/TEM of Sharp Au Nanostructures

Shape is often cited as a potent handle to tune the optical properties of metal nanoparticles, such that many research groups focus on developing ways to synthesize novel nanostructures, understand their growth, and improve size and shape control.<sup>62,74,85,104,107,119,122,127,129,132,136,138,140,141,143,145,187,197-199,211</sup> Over the past twenty years, a number of increasingly effective synthesis strategies such as seed-mediated and plasmon-assisted growth have appeared.<sup>62,119,122,126,127,129,132,179,187</sup> While plasmonics is not the sole applications of metal nanoparticles, many synthesis publications also include basic information about the LSPR behavior of the products. However, the optical response of nanoparticle solutions is blurred by size and shape heterogeneity.

The high throughput correlated single particle spectroscopy and electron microscopy methods developed in this work has shown to be an invaluable technique that can overcome this ensemble-averaging difficulty and provide quantitative data from inhomogeneous reaction mixtures.<sup>52,86,87,92</sup> Indeed, single particle analysis can yield unparalleled information about linewidths and precise effects of various structural factors on the LSPR behavior of nanostructures. Increasingly refined single particle correlated approaches have been used for the last ten years, to answer, either qualitatively or quantitatively, questions about the effects of various structural factors on the LSPR energy, and, in few cases, linewidth.<sup>52,82,84,87,91,108,109,117,147,149,212</sup>

However, systematic shape comparisons have not been carried out, despite its leading importance in guiding the choice of particles for a wide range of

applications.<sup>132,148,149,192,201,213,214</sup> To address the effect of shape on optical properties, in particular LSPR energy and linewidth, five Au shapes were obtained: cubes, decahedra, octahedra, truncated bitetrahedra, and icosahedra. Synthesis details can be found in Chapter 2. Different shapes of the same metal (Au) were chosen because composition plays a major role in determining the plasmon energy, plasmon width, and their dependence on size (Chapter 3 and ref.<sup>52,68,76,79,92</sup>). Correlated dark field optical spectroscopy (performed with unpolarized light) and transmission electron microscopy was performed on the particles deposited on either the Formvar side of ultrathin carbon type A grids or on 100 nm thick Si<sub>3</sub>N<sub>4</sub> windows. Representative scattering spectra and electron micrographs of single Au nanoparticles on Formvar are presented in Figure 4.1. Each spectrum was fit to one or more Lorentzian line shape functions (one per mode present). The peak positions and linewidths of the dipolar resonances (lowest energy peak) were used for the analysis of covariance presented below.

#### 4.1.1 Side Length as a Size Parameter: Shape-Dependent Descriptor, Shape Dependent Retardation Effects

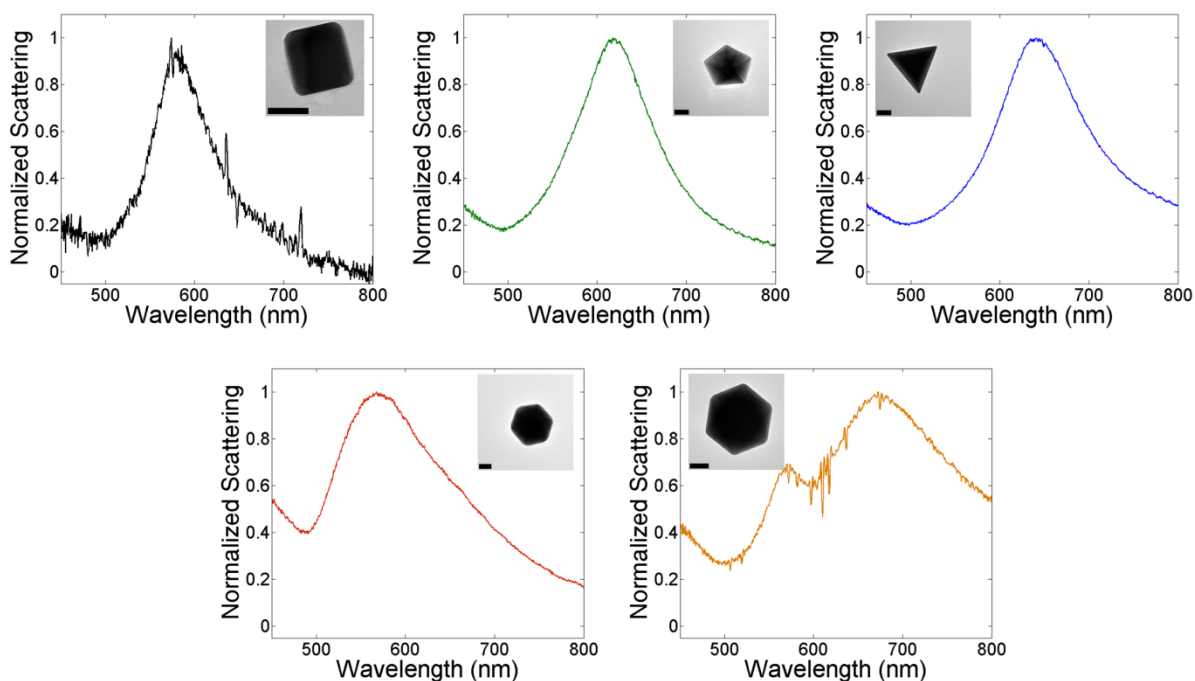


Figure 4.1. Representative TEM images and LSPR spectra for Au nanostructures on Formvar. Clockwise from top left: cube, decahedron, truncated bitetrahedron, octahedron, and icosahedron.

As a first attempt to compare plasmonic nanoparticles of different shapes, the spectral differences of five Au structures of the same size can be examined. However, before proceeding with such comparison, size must be defined. How will the size of different shapes be measured? For some structures, an obvious parameter exists, such as the side length for cubes and diameter for spheres. Characterizing more complex structures is not as straightforward, however. Decahedra have been measured using both the pentagonal base edge length<sup>199</sup> and the pentagonal base "apex to apex"<sup>137</sup> distance, while triangles can be measured edge to corner (height), or

corner to corner (edge length).<sup>103,143,149</sup> The most commonly used parameters, referred to as side lengths from now onwards, were chosen for this analysis (Figure 4.2 and 4.3), however there remain subjectivity in this assignment. Not surprisingly this parameter is also the easiest to measure experimentally from TEM images (Figure 4.2).

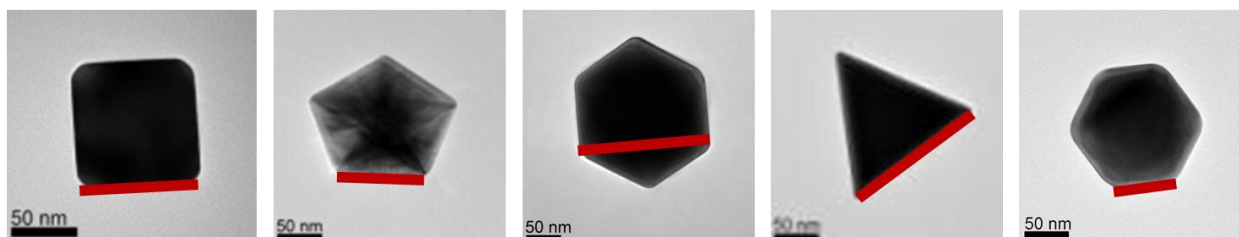


Figure 4.2. Representative TEM images and side length measurements for, from left to right, a cube, decahedron, octahedron, truncated bitetrahedron, and icosahedron.

Comparing particles of the same size using this arbitrary side length parameter does not provide much information, however. As one might expect, particles of different shapes have different spectra, as illustrated for a truncated bitetrahedron (triangle), decahedron, and icosahedron in Figure 4.3. Shape-specific LSPR behavior can be obtained, however, and may prove useful. In fact, quantitative values for the size-dependence of plasmon energy and linewidth can be extracted for all the five shapes studied, as shown in Figure 4.4 and Table 4.1. Analysis of covariance was performed in MATLAB, using the correlated single particle scattering/TEM data obtained on 50 cubes, 245 decahedra, 40 icosahedra, 139 triangles, and 200 octahedra. Note that the error for cubes is significantly higher than that of other structures because of the small size range available. P-values are also reported in Table 4.1: they indicate whether the difference between two groups is the result of chance (with 0 being a real difference and 1 being a chance,

or random, event). Two of the five p-values for the side length dependence of energy and linewidth are below 0.05 (Table 4.1), indicating that size effects are significantly different for different shapes when described by the side length. While such quantitative rules can be useful for specific shapes, the disparity of values for the various shapes makes this study a case-by-case analysis, where predictive rules will be empirical.

Table 4.1. Fit parameters for the side length fit to dipolar LSPR energy and full width at half maximum (analysis of covariance).

Shape	Energy Dependence on Side Length				FWHM Dependence on Side Length			
	Slope (meV/nm)	p- value	Intercept (eV)	p- value	Slope (meV/nm)	p- value	Intercept (eV)	p- value
Cubes	-2.4 (9)	0.082	2.32 (7)	0.10	3.1(13)	0.64	0.02 (11)	0.64
Triangles	-2.8 (2)	0	2.41 (2)	0.23	2.4 (4)	0	-0.10 (3)	0.047
Icosahedra	-6.3 (4)	0	2.53 (4)	0.0093	5.0 (6)	0.027	0.03 (5)	0.27
Decahedra	-3.9 (3)	0.96	2.40 (3)	0.12	3.8 (4)	0.90	-0.02 (3)	0.68
Octahedra	-4.2 (2)	0.26	2.53 (2)	0	4.4 (4)	0.075	-0.09 (3)	0.090

Note: standard error on last digit(s) in parentheses. When the standard error has two digits, it represents the error on the last two digits. P-values less than 0.0005 are reported as 0.

#### 4.1.2 Plasmon Length: a Universal Parameter to Describe Size Effects

Figure 4.3 and 4.4, as well as the analysis discussed above show that using an arbitrary size parameter to characterize the size of Au nanostructures leads to arbitrary values for the size-dependence of plasmonic properties. Such relationships may of course be useful to predict the plasmonic behavior of nanoparticles of a given shape; however, they do not improve our understanding of shape effects, the ultimate goal of this study.

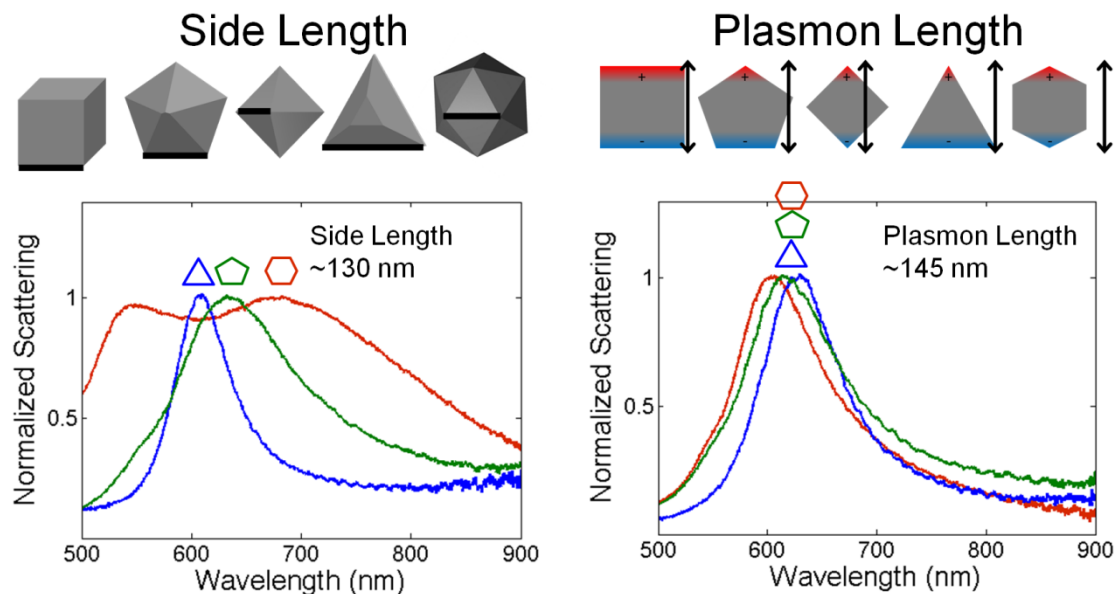


Figure 4.3. Side length and plasmon length as descriptors of nanoparticle size. Top left: side length definition. Top right: plasmon length definition. Bottom panels: representative single particle spectra for Au triangles (blue), decahedra (green) and icosahedra (red). Bottom Left: particles of similar side length. Right: particles of similar plasmon length.

Another way to approach the study of shape effects is to use a size parameter that reflects the plasmon resonance of the particle rather than the length of some repeating geometric unit. Because the electron oscillation frequency is expected to depend on the separation between charges for a dipolar mode, the distance relevant to characterize particle size is the distance between poles of inverse charge, as depicted in Figure 4.3. To determine this length for specific shapes, results from numerical calculations and experimental plasmon mapping experiments were used, and the regions of opposite charges were deduced from visual inspection. The computed vector plots of the induced polarization in octahedra presented by Li *et al.*<sup>178</sup> clearly show apex to apex oscillation for the dipolar mode. A number of groups have published field

maps for triangles (a good review can be found in ref.<sup>143</sup>), the work of Kelly *et al.*<sup>214</sup> and Brioude and Pileni<sup>215</sup> was most useful. The face-to-face mode of nanocubes (i.e. edge length and plasmon length are equivalent) is obvious in the work of McMahon *et al.*,<sup>147</sup> Sherry *et al.*,<sup>106</sup> and Ringe *et al.*<sup>52</sup> The plasmon length for decahedral particles, from edge to apex of the decahedral base, was assigned following a number of publications from the Liz-Marzán group.<sup>67,82,199</sup> No information was found on the plasmonic properties of icosahedra, as this seems to be the first systematic structure-function analysis for this shape. Its plasmon length was deduced by analogy to octahedral and spherical particles, i.e. taken to be apex to apex.

Table 4.2. Fit parameters for the plasmon length fit to dipolar LSPR energy and full width at half maximum (analysis of covariance, unconstrained slopes).

Shape	Energy Dependence on Plasmon Length				FWHM Dependence on Plasmon Length			
	Slope (meV/nm)	p-value	Intercept (eV)	p-value	Slope (meV/nm)	p-value	Intercept (eV)	p-value
Cubes	-2.4 (9)	0.50	2.32 (7)	0.10	3.1 (13)	0.87	0.02 (11)	0.64
Triangles	-3.2 (2)	0.31	2.41 (2)	0.23	2.8 (3)	0.79	-0.10 (3)	0.047
Icosahedra	-3.3 (3)	0.21	2.53 (4)	0.009	2.6 (4)	0.46	0.03 (5)	0.27
Decahedra	-3.0 (2)	0.89	2.40 (2)	0.12	2.9 (4)	0.97	-0.02 (3)	0.68
Octahedra	-3.0 (2)	0.97	2.53 (2)	0	3.1 (3)	0.58	-0.09 (3)	0.089

Note: standard error on last digit(s) in parentheses. P-values less than 0.0005 are reported as 0.

Table 4.3. Fit parameters for the plasmon length fit to dipolar LSPR energy and full width at half maximum (Analysis of Covariance, slope set equal for all shapes).

Shape	Energy Dependence on Plasmon Length			FWHM Dependence on Plasmon Length		
	Slope (meV/nm)	Intercept (eV)	p-value	Slope (meV/nm)	Intercept (eV)	p-value
Cubes	3.08 (4)	2.374 (6)	0	2.96 (6)	0.036 (9)	0
Triangles		2.384 (4)	0		-0.122 (6)	0
Icosahedra		2.485 (6)	0		-0.035 (9)	0.56
Decahedra		2.411 (3)	0		-0.023 (5)	0
Octahedra		2.550 (4)	0		-0.058 (5)	9*10 <sup>-4</sup>

Note: standard error on last digit(s) in parentheses. P-values less than 0.0005 are reported as 0.

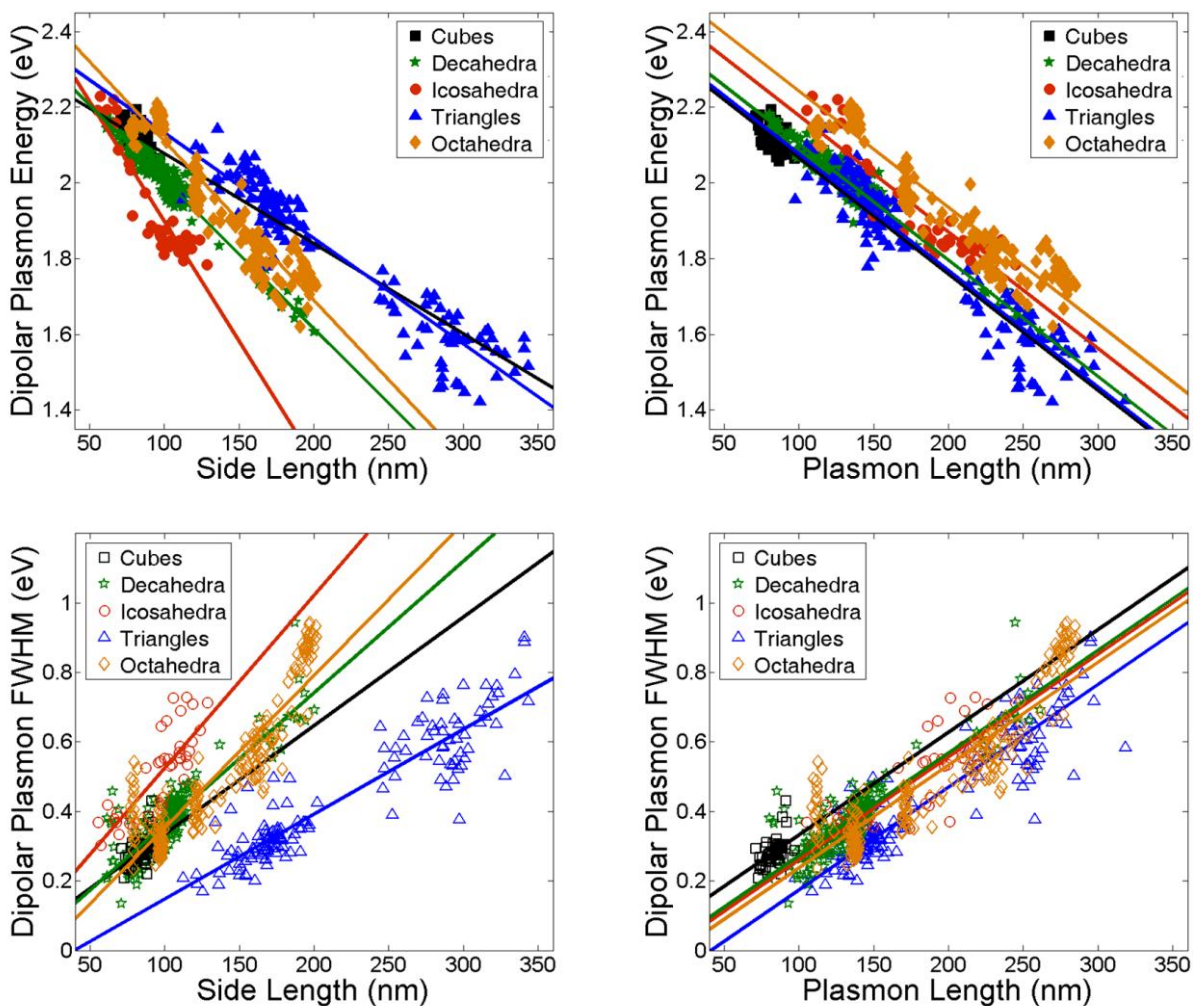


Figure 4.4. Statistical analysis of size effects using side and plasmon length for Au cubes (black squares), decahedra (green stars), icosahedra (red circles), triangles (blue triangles), and octahedra (orange diamonds). Clockwise from top left: dipolar plasmon energy dependence on side length, dipolar plasmon energy dependence on plasmon length, full width at half maximum (FWHM) dependence on side length, FWHM dependence on plasmon length. Parallel slopes in the right panels were obtained from analysis of covariance.

The results presented in Figure 4.3 show that particles with different shapes, but comparable plasmon lengths, have similar LSPR spectra. Analysis of covariance, performed for the 674 single Au nanoparticles using the plasmon length as size descriptor (Tables 4.2-4.3), yields a homogeneous size-dependence of the dipolar plasmon energy and linewidth. The size-dependence of energy and linewidth now all have p-values over 0.2 (Table 4.2), i.e. the slopes are not significantly different, in sharp contrast with the side length analysis presented above. This phenomenon can be understood by considering that retardation effects are mostly determined by the increase in distance between regions of opposite oscillation-induced charge, i.e. increase in plasmon length. A model constraining the slopes to be the same (parallel lines), the statistically relevant model for this system, was used to compute the universal size-dependence of plasmon energy and linewidth shown in Table 4.3. Note, however, that the intercepts obtained for constrained slopes are significantly different (p-values less than 0.0005 for all structures, Table 4.3).

Linear trends for the dipolar plasmon energy variation with size can also be extracted from previously published data on fixed aspect ratio structures, obtained experimentally for structures such as silver cubes and decahedra,<sup>52,96,137</sup> and computationally for silver truncated tetrahedral.<sup>143</sup> However, the experimental data commonly used to obtain such trends are based on bulk measurements; the assumption of constant shape composition, aspect ratio and corner rounding between the reaction mixtures producing different sizes must be perfectly obeyed to make bulk trends quantitative. This is rarely the case: a good example can be found for the corner rounding of Ag nanocubes, Section 4.3. Therefore, these trends cannot be claimed to be quantitative or predictive. Another major drawback of bulk measurements is the inherent inability to obtain

information about the plasmon linewidth because of inhomogeneous broadening, i.e. broadening due to the shape and size inhomogeneity of the particles in the sample. The current results are truly a first in this field; never before has such large sample size been so successfully used to provide quantitative, statistically significant relationships between size, shape, and plasmon linewidth such as those presented in Figure 4.4.

#### 4.1.3 Substrate Effects on Au Nanostructures

While size effects seem to be independent of shape for dipolar modes, given that the plasmon length is used, other factors known to influence LSPR behavior may affect the size- and shape-dependence of the plasmon energy and linewidth. Amongst those, the effect of substrate can be readily probed by acquiring data on different electron-transparent support films, in this case Formvar (RI = 1.5<sup>205</sup>) and Si<sub>3</sub>N<sub>4</sub> (RI ~ 2<sup>206</sup>). This study was performed, such that in addition to the 26 Au nanocubes already discussed in Chapter 3, the plasmon response of 69 Au decahedra, 7 Au icosahedra, and 10 Au truncated bitetrahedra on the Si<sub>3</sub>N<sub>4</sub> were obtained.

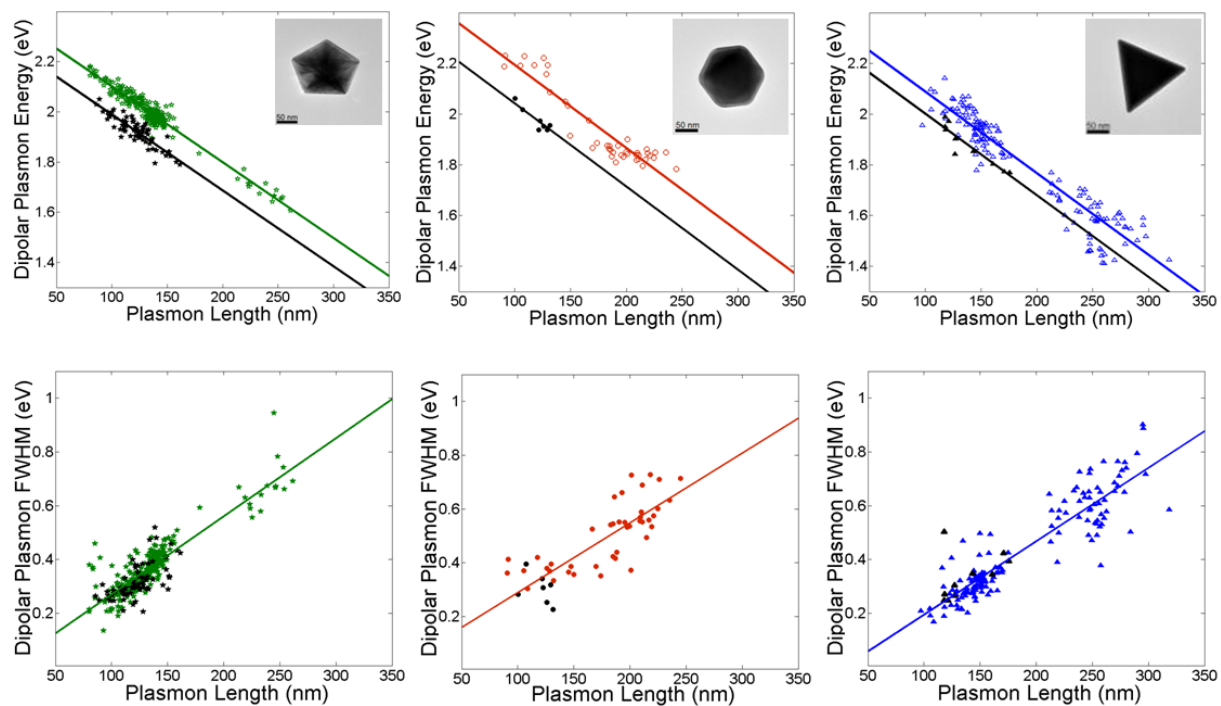


Figure 4.5. Effect of substrate refractive index on the plasmon energy and FWHM of Au nanostructures. Colored data points are for a substrate with RI = 1.5 (Formvar), while black symbols are for particles on Si<sub>3</sub>N<sub>4</sub> (RI ~ 2). From left to right, decahedra, icosahedra, and truncated bitetrahedra. Top row: dipolar plasmon energy. Bottom row: dipolar plasmon FWHM. The statistically relevant fit is shown, i.e. a parallel line fit for the LSPR energy and a same line fit for the FWHM.

Table 4.4. Fit parameters for the plasmon length fit to dipolar LSPR energy and full width at half maximum for Au nanostructures on Formvar (RI = 1.5) and Si<sub>3</sub>N<sub>4</sub> (RI ~ 2) (pair wise analysis of covariance, unconstrained slopes).

Shape	N	Energy Dependence on Plasmon Length				FWHM Dependence on Plasmon Length			
		Slope (meV/nm)	p-value	Intercept (eV)	p-value	Slope (meV/nm)	p-value	Intercept (eV)	p-value
Cubes Formvar	52	-2.4(5)	0.011	2.31(4)	0.053	0.0031(5)	0.07	0.02(4)	0.001
Cubes Si <sub>3</sub> N <sub>4</sub>	23	-5.2(5)	0.011	2.49(4)	0.053	-0.0011(5)	0.07	0.33(4)	0.001
Decahedra Formvar	245	-2.95(9)	0.58	2.403(11)	0	0.0029	0.10	-0.02(2)	0.29
Decahedra Si <sub>3</sub> N <sub>4</sub>	69	-3.05(9)	0.58	2.279(11)	0	0.0023	0.10	0.03(2)	0.29
Icosahedra Formvar	40	-3.3(9)	0.84	2.53(11)	0.63	0.0025(9)	0.31	0.05(11)	0.43
Icosahedra Si <sub>3</sub> N <sub>4</sub>	7	-3.7(9)	0.84	2.42 (11)	0.63	0.0007(9)	0.31	0.23(11)	0.43
Triangles Formvar	139	-3.3(4)	0.93	2.41(6)	0.53	-0.09(8)	0.21	0.0027(6)	0.29
Triangles Si <sub>3</sub> N <sub>4</sub>	10	-3.3(4)	0.93	2.33(6)	0.53	0.13(8)	0.21	0.0015(6)	0.29

Note: standard error on last digit(s) in parentheses. P-values less than 0.0005 are reported as 0.

Table 4.5. Fit parameters for plasmon length fit to dipolar LSPR energy and full width at half maximum for Au nanostructures on Formvar (RI = 1.5) and Si<sub>3</sub>N<sub>4</sub> (RI ~ 2) (pair wise analysis of covariance, constrained slopes).

Shape	N	Energy Dependence on Plasmon Length				FWHM Dependence on Plasmon Length			
		Slope (meV/nm)	p-value	Intercept (eV)	p-value	Slope (meV/nm)	p-value	Intercept (eV)	p-value
Cubes, Formvar	52	-3.1(5)	0	2.37(4)	0	1.1(6)	0.078	0.194(4)	0
Cubes, Si <sub>3</sub> N <sub>4</sub>	23			2.31(4)	0			0.1536(4)	0
Decahedra, Formvar	245	-3.00(5)	0	2.402(6)	0	2.90(10)	0	-0.009(3)	0.0002
Decahedra, Si <sub>3</sub> N <sub>4</sub>	69			2.291(6)	0			-0.035(3)	0.0002
Icosahedra, Formvar	40	-3.3(2)	0	2.532(13)	0	2.5(3)	0	0.02(2)	0.27
Icosahedra, Si <sub>3</sub> N <sub>4</sub>	7			2.376(13)	0			0.04(2)	0.27
Triangles, Formvar	139	-3.20(9)	0	2.411(17)	0	2.80(11)	0	-0.046(12)	0.10
Triangles, Si <sub>3</sub> N <sub>4</sub>	10			2.324(17)	0			-0.086(12)	0.10

Note: standard error on last digit(s) in parentheses. P-values less than 0.0005 are reported as 0.

Table 4.6. Fit parameters for plasmon length fit to dipolar LSPR energy and full width at half maximum for Au nanostructures on Formvar (RI = 1.5) and Si<sub>3</sub>N<sub>4</sub> (RI ~ 2) (global analysis of covariance).

Shape	N	Energy Dependence on Plasmon Length, Unconstrained Slopes				Energy Dependence on Plasmon Length, Constrained Slopes			
		Slope (meV/nm)	p-value	Intercept (eV)	p-value	Slope (meV/nm)	p-value	Intercept (eV)	p-value
Cubes, Formvar	52	-2.6(9)	0.50	2.34(7)	0.54	-3.20(5)	0	2.382(6)	0.25
Cubes, Si <sub>3</sub> N <sub>4</sub>	23	-3.6(10)	0.68	2.36(8)	0.73			2.318(8)	0
Decahedra, Formvar	245	-3.0(3)	0.46	2.40(3)	0.52			2.422(4)	0
Decahedra, Si <sub>3</sub> N <sub>4</sub>	69	-2.9(4)	0.40	2.28(4)	0.011			2.309(5)	0
Icosahedra, Formvar	40	-3.3(3)	0.72	2.53(4)	2			2.500(7)	0
Icosahedra, Si <sub>3</sub> N <sub>4</sub>	7	-3.7(12)	0.69	2.42(15)	0.80			2.355(13)	0.13
Triangles, Formvar	139	-3.2(3)	0.997	2.41(3)	0.37			2.399(5)	0
Triangles, Si <sub>3</sub> N <sub>4</sub>	10	-3.3(6)	0.89	2.33(7)	0.50			2.315(11)	0

Note: standard error on last digit(s) in parentheses. P-values less than 0.0005 are reported as 0.

As observed in Chapter 3, the plasmon resonance energy decreases with an increase in the refractive index of the underlying substrate. The shift for cubes, decahedra, icosahedra, and truncated bitetrahedra, obtained for the pair wise constrained slope analysis of covariance (Table 4.5) are 0.06, 0.11, 0.16, and 0.087 eV, respectively; for the global constrained slope analysis of covariance, the difference in LSPR energy are 0.06, 0.11, 0.14, and 0.084 eV. To evaluate the error on this substrate effects, standard error propagation methods were employed, where the error of a sum (or difference) is the square root of the sum of the square of the individual errors. This approach applied to the global analysis of covariance results yields the following 95 % confidence intervals: 0.06(2), 0.114(13), 0.14(3), and 0.084(2) eV for cubes, decahedra,

icosahedra, and truncated bitetrahedra, respectively. The latter three do not have a significantly different shift, while the cubes do. Differences are indeed expected as refractive index sensitivity is strongly shape-dependent (as seen in Chapter 5).

Despite having a variance larger than that of the energy data, the FWHM information obtained for the different substrates is worthy of statistical analysis, results of which are presented in Tables 4.4-4.5. The constrained slopes pair wise fit for the FWHM dependence on size show mixed results for the substrate effects. On one hand, icosahedra and triangles have no significant differences between their intercept for the particles on Formvar and Si<sub>3</sub>N<sub>4</sub>, suggesting no effect of substrate on plasmon decay under these conditions. On the other hand, cubes and decahedra, the particles with the largest data set on Si<sub>3</sub>N<sub>4</sub>, have significantly different FWHM for the different substrate, with a shift of 0.040(8) and 0.026(8) eV, respectively (95 % confidence interval in parentheses). Further experiments would clarify this finding.

Another interesting result, obvious in Figure 4.5 and Table 4.4, is that the substrate does not have a statistically significant effect on the size dependence of the LSPR energy and width (i.e. the slope in Figure 4.5). However, numerical analysis (e.g., ref.<sup>81</sup>) that a shift in the size-dependence of the plasmon energy is expected for different dielectric environments. The change in the surrounding medium in the current experiments must thus be too small to produce effects other than a size-independent plasmon shifts; this is probably true for most sensing applications as well. This results suggest that for Au nanostructures subjected to a small change in refractive index, one can neglect the change in the slope of the LSPR energy as a function of size.

#### 4.1.4 Important Findings, Advantages and Limitations of the Plasmon Length Parameter

The concept of plasmon length, an intrinsic property of the nanoparticle, offers the opportunity to predict the dipolar plasmon energy and linewidth dependence on size without having to rely on experiments or detailed calculations; it also provides a powerful framework to compare various shapes, real or hypothetical. The data presented in this Section demonstrated and explained how plasmon length describes size effects in a assortment of Au nanoparticles shapes, yielding shape-independent variations of the plasmon energy and linewidth. Also, both size and FWHM dependence on size were found to be substrate-independent for rather large substrate refractive index change (1.5 to 2), implying that this effect can be neglected in practical sensor applications.

However, the validity of the plasmon length approach was only shown for the dipolar mode of particles with fixed aspect ratio, well-formed vertices, and with homogeneous, small corner rounding for all sizes. For large corner rounding heterogeneities, other parameters are needed in order to fully describe the simultaneous effects of size and rounding on the plasmon energy and decay (Section 4.2). Higher order modes, beyond the dipolar resonance, can be modeled with some variation of the plasmon mode concept (Section 4.3).

A possible extension of this work is the study of Ag shapes, as shape and size effects have not yet been systematically studied for this material. Because of the different absolute values of the real part of the dielectric constant in the visible range (slopes are similar),<sup>50,59</sup> plasmon resonance frequencies in Ag nanoparticles are expected to have a more acute size dependence than their Au counterparts (as is observed in Chapter 3). Studies have been performed on size effects in Ag

nanoparticles,<sup>31,84,85,103,109,132,143,149</sup> however the vast differences in experimental conditions (in solution/air, bulk/single particle, etc) in the published data severely limits our ability to perform any comparison.

#### 4.2 Effective Plasmon Length: Going Beyond a Single-Parameter Model to Describe Corner Rounding and Size Effects

Amongst the many factors affecting the plasmon frequency, shape has been shown to be an important one. Albeit it does not affect the size-dependence of the dipolar plasmon energy and width, as seen in the previous section, it influences their absolute values<sup>84,103,106,209</sup> as well as changing the electric field distribution around the particle.<sup>90,147,216</sup> It has been shown using EELS mapping that the field intensity at sharp triangular corners is higher than at rounded ones,<sup>216</sup> and numerical results revealed that the field at the tips of ellipsoids acutely depends on their tip geometry and aspect ratio.<sup>213</sup> Such near-field changes typically result in significant far-field effects; examples exist in the literature for, amongst others, cubes,<sup>106,147</sup> triangles,<sup>31,84,103,143,215</sup> and bipyramids.<sup>132</sup>

While it is well known that varying the corner rounding affects the LSPR position,<sup>52,87,103,106,147,149,214</sup> it remains unclear how the corner rounding affects the size dependence of plasmon energy and width. This effect is difficult to properly probe computationally, because of the need to sample a large range of sizes and shapes. High throughput correlated experiments such as the ones pioneered in this work provide an efficient tool to address this question.

#### 4.2.1 Correlated LSPR/TEM on Ag Bipyramids

BSPP-capped silver right bipyramids<sup>132</sup> (see Chapter 2 for synthesis details) were deposited on the Formvar side of carbon type B grids (Ted Pella, Inc) and analyzed using correlated dark field optical and transmission electron microscopy. Right triangular bipyramids are a planar {111} twinned structure with six equivalent triangular {100} faces and an equilateral triangular base,<sup>132</sup> as can be seen in the SEM picture and model in Figure 4.6. The side length of the equilateral triangular base and the truncation of the equatorial corners for each bipyramid were obtained by drawing a perfect bipyramid overlay and corner fillings on top of the 2-dimensional projection obtained in TEM, as depicted in Figure 4.6. Note that the relationship between  $a$  and  $a'$  (and  $t$  and  $t'$ ) is  $a = \sqrt{3}a'/2$ .

Typical bipyramid spectra, showing two main resonances, are presented in Figure 4.7. Previous calculations have assigned the origin of such peaks based on their shift upon corner truncation.<sup>132</sup> In short, the high energy peak around 420 nm is the transverse dipolar resonance, an electron oscillation perpendicular to the equilateral pyramid base, while the low energy peak in the 600 nm region is the longitudinal (or equatorial) dipolar resonance, an electron motion parallel to the equilateral triangular base (the {111} twin plane). The spectra in Figure 4.7 are in excellent agreement with previously calculated spectra for truncated bipyramids.<sup>132</sup>

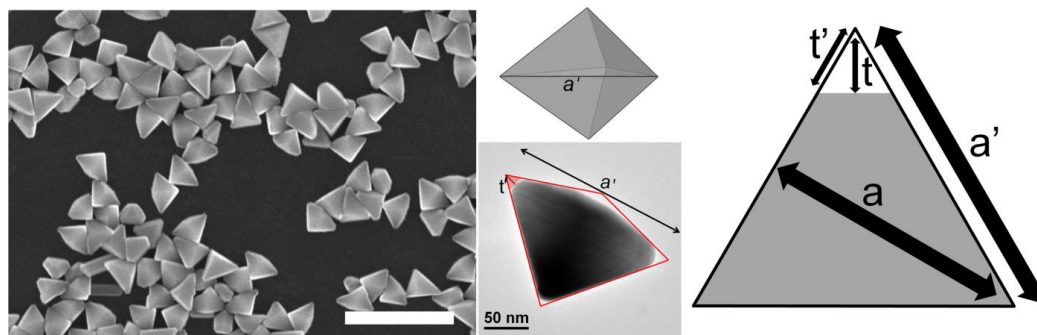


Figure 4.6. Representative images and structural parameters of Ag bipyramids. Left: SEM image. Scalebar, 500 nm. Top Middle: 3D model of a right bipyramid showing the measured edge length as  $a'$ . Bottom middle: example of structural measurements on a TEM image where  $a'$  is the measured edge length and  $t'$  is the measured corner truncation. Right: view of the equilateral base, i.e. the  $\{111\}$  twin plane, and depiction of the structural parameters used in the paper: the height of the triangle  $a$ , the measured side length  $a'$ , the corner truncation  $t$ , and the measured corner truncation  $t'$ .

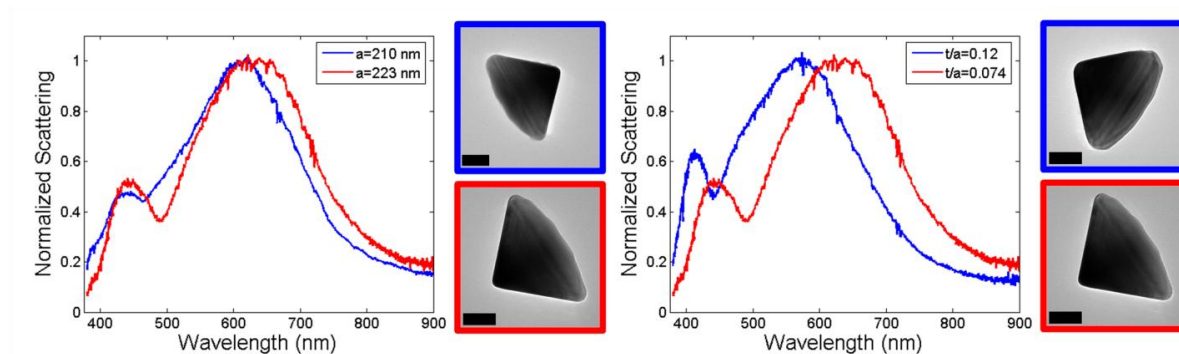


Figure 4.7. Effect of size and corner rounding on the spectra of individual Ag bipyramids. Left: redshift of the equatorial plasmon with size increase for bipyramids with equivalent relative corner rounding. Right: redshift of both plasmon modes with increased corner sharpness for particles of the same size. Scalebars, 50 nm.

#### 4.2.1.1 Single Particle Comparisons

Comparing a few single particle data obtained through correlated optical/structural measurements can provide trends on the effect of various structural factors on the LSPR resonances in those particles. In fact, many of the early papers<sup>108,109</sup> and practically all of the published numerical approaches<sup>82,97,103,106,132,143,147,149,214</sup> compare a few spectra to deduce qualitative yet useful trends. In the current data set, such qualitative relationships can also be obtained. As shown in the left panel of Figure 4.7, a size increase results in a lowering of the plasmon resonance energy (redshift). This can be explained by retardation effects, as discussed in Chapter 1 and observed in the previous Section. The effect of corner rounding can be deduced from comparing the two spectra in the right panel of Figure 4.7; an increase in LSPR energy (blueshift) is observed for increasing corner rounding, as suggested in Chapter 3.

#### 4.2.1.2 Single Parameter Fits

While the qualitative trends presented in Figure 4.7 may be useful, they are rather obvious and do not provide the quantitative guidance useful in the plasmon tuning that is so critical in applications such as surface-enhanced spectroscopies<sup>192-194,217-219</sup> and resonant interaction-based sensors.<sup>195,196</sup> To obtain such trends, an approach similar to that used in the previous Section and in Chapter 3 can be applied to the large (123 particles) data set obtained on Ag bipyramids. The correlation between LSPR frequency and FWHM with corner truncation and particle size is presented in Figure 4.8, note that relative truncation is defined as  $t/a$ . The results from linear

regression on single parameter effects are reported in Table 4.7. Clearly, the fit for the plasmon energy is superior to that of the decay. The latter indeed has no significant relationship to the corner truncation, but its value increases, as understood through retardation effects, with increased particle size. No further, 2-parameter analysis, was performed on the FWHM because the data can only be used to correlate it to a single parameter, the size of the particle. The plasmon energy, however, convincingly depends on both the size and corner truncation (Figure 4.8, top panels). A very basic way to quantify how much a factor explains the variation of the dependent variable is the R-square value. While R-square is not a measure of error, it is a useful number in that it assesses what fraction of the variation in the data set is due to a given parameter (here, size or truncation). A R-square of 1 (or 100 %) means that there are no other parameters to consider, and a R-square of 0 means that this parameter has no effect on the results. The R-square values for the plasmon energy are 75 % for the size effect, and 49 % for the truncation effect. This clearly indicates that both parameters have a significant contribution yet neither parameter alone is sufficient to describe the variation in plasmon energy.

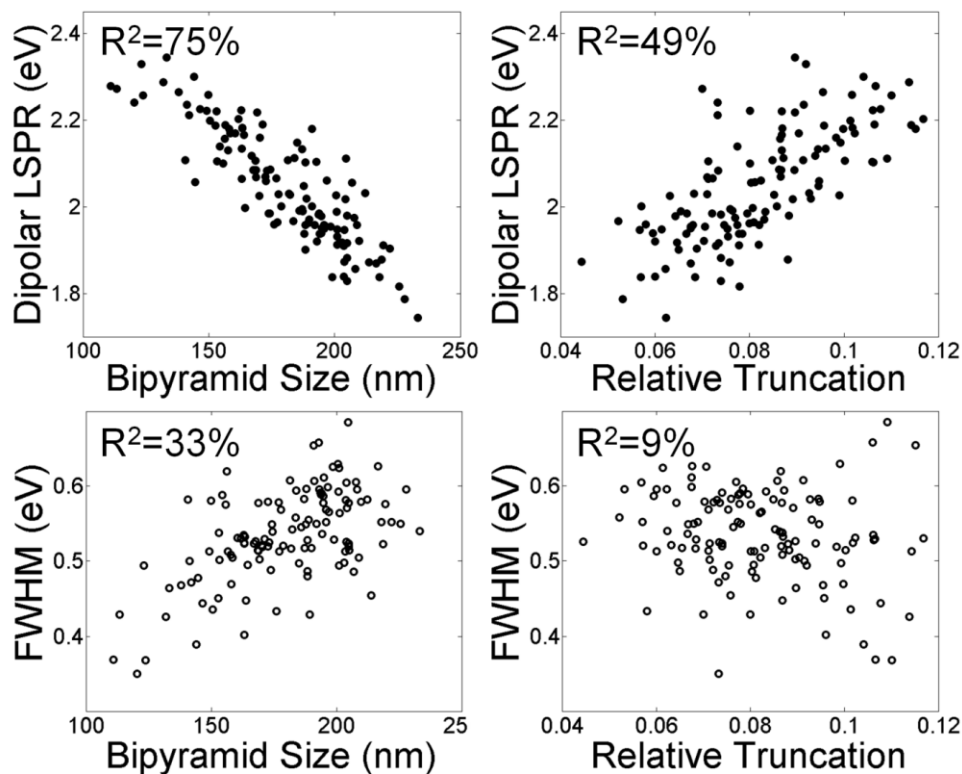


Figure 4.8. Single parameter effects on the longitudinal dipolar resonance energy and FWHM of Ag bipyramids, showing the inadequacy of either parameter to truly describe the variation. Top left: effect of size on the LSPR energy. Top right: effect of truncation on the LSPR energy. Bottom left: effect of size on the plasmon FWHM. Bottom right: effect of truncation on the plasmon FWHM.

Table 4.7. Linear fit parameters for the effect of size and corner truncation on plasmon energy and FWHM.

Relationship	Slope	Intercept (eV)
Size effect on energy	-4.4(5) meV/nm	2.84(8)
Truncation effect on energy	6.0 (11) eV	1.56(9)
Size effect on FWHM	1.4(4) meV/nm	0.29(6)
Truncation effect on energy	-0.7(7) eV	0.59(6)

Note: The fits follow the equation  $y = mx+b$ ; size is in nm; relative truncation is used ( $t/a$ ); FWHM and energy are in eV; 95 % confidence intervals on the last digit(s) are shown in parentheses.

Single parameter data can also be used to extract distribution information; such analysis may be the end goal of the study<sup>83</sup> or some sanity check on the sample.<sup>91</sup> For the current analysis the latter is appropriate; the histograms of size, relative rounding, plasmon energy, and FWHM are reported in Figure 4.9. A distribution close to normal is present, despite the particles being synthesized in multiple batches. Of course, correlated data is not required to obtain such histograms, but a more reliable correspondence can be made between histograms if they report the same data set. For example, the small asymmetry towards larger sizes in the top left panel of Figure 4.9 correlates well with the plasmon FWHM and energy asymmetry. The relative rounding does not show this feature, pointing towards a size-independent distribution of edge sharpness amongst the samples (as is obvious in Figure 4.11).

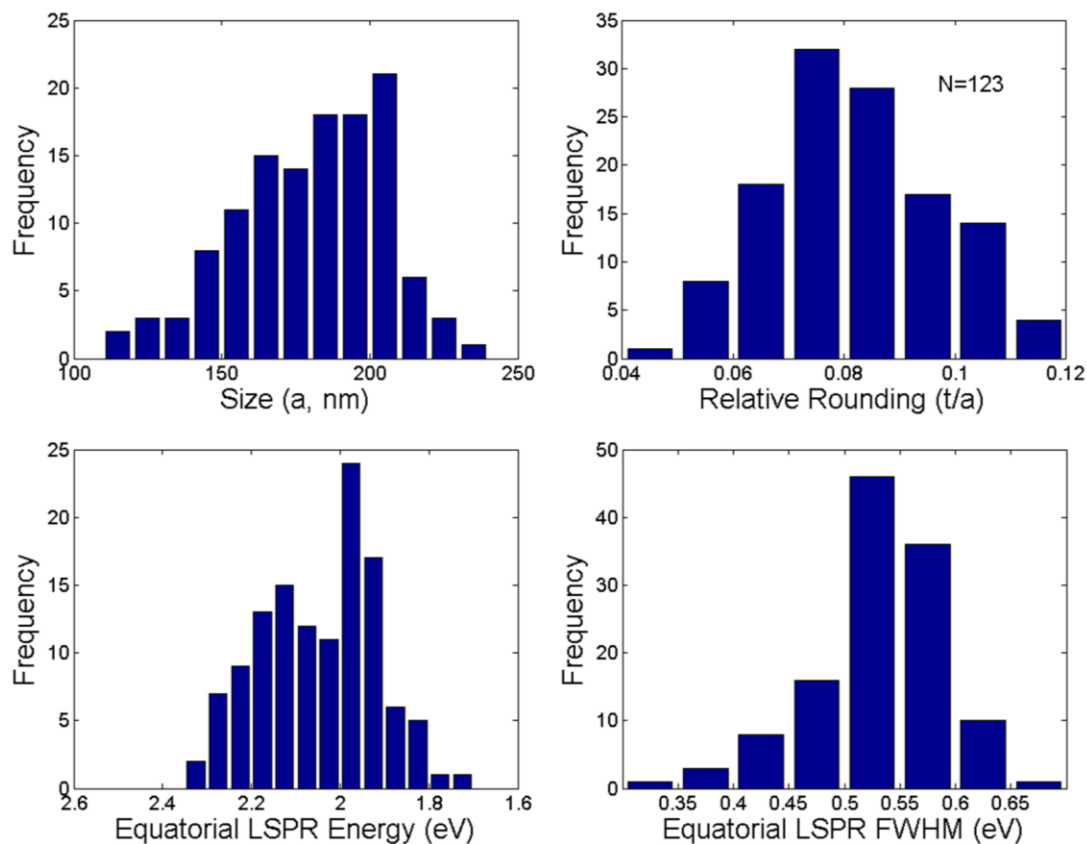


Figure 4.9. Single parameter distribution for the 123 bipyramids studied. Clockwise from top left: size, relative rounding, LSPR FWHM, and LSPR energy.

#### 4.2.1.3 Multiple Parameter Fits

While the correlation observed between size, corner rounding, and the longitudinal plasmon resonance energy presented in Figure 4.8 is rather convincing, a significant amount of “noise” remains present in both top panels.

Given the large number of experimental data points (123), it is possible to go beyond a single parameter model and answer questions otherwise impossible to address. However, as the number

of parameters in the model increases, so does the number of ways to represent the fit. For completeness, three ways will be used and discussed here; note that all lead to the same general conclusions but different people may better understand them from one of the given representations.

#### 4.2.1.3.1 Grouped Fit

A simple way to understand the simultaneous effects of two parameters (x and y) is through a simple linear plot for parameter x, with the data grouped according to parameter y. This has been done for the plasmon linewidth of triangles<sup>84</sup> and the plasmon energy of cubes with different degrees of rounding (Chapter 3). To use this model on the current data set, bipyramids were divided into three groups on the basis of relative corner truncation.

Two approaches were taken to group the sample into three rounding categories. The first approach, published previously,<sup>92</sup> selects the groups by an arbitrary round number for the relative corner truncation, setting the group boundaries at  $t/a = 0.08$  and  $0.095$ . As can be seen in Table 4.8 and Figure 4.10, the slope of the sharp group is significantly different than that of the rounded group, pointing to an effect of corner rounding on the size-dependence of the LSPR energy. This simple grouping approach indicates an interesting phenomenon, but cannot quantify it. Furthermore, shifting the group boundaries does not change the different slopes trend, but it may annihilate the statistical relevance of such differences, leading to a potential type II error (the null hypothesis being that the slopes are all the same). Given the qualitative nature of this approach and its potential pitfalls, it is not recommended except as an initial analysis of the

experimental data. Note that for numerical data, this is the approach of choice when multiple variables are under consideration: it has been employed to analyze the effect of size, corner rounding, and aspect ratio on the optical response nanorods, for instance.<sup>99,209</sup>

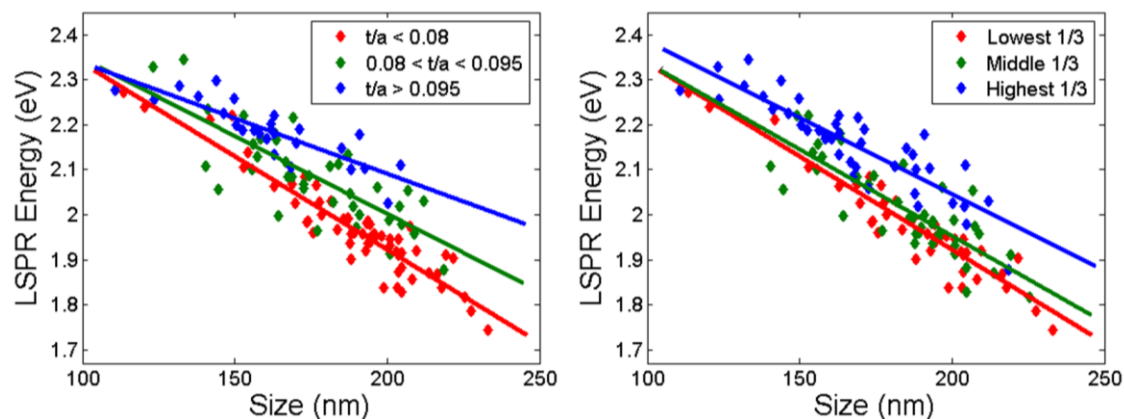


Figure 4.10. Grouped fits for the analysis of the simultaneous effect of size and truncation on the equatorial LSPR energy of Ag bipyramids.

Table 4.8. Ag bipyramids fit parameters for the grouped approaches presented in Figure 4.10.

Sharpness grouping by value	N	Slope (meV/nm)	Intercept (eV)
Sharp ( $t/a < 0.08$ )	60	-4.2(4)	2.76(8)
Average ( $0.08 < t/a < 0.095$ )	38	-3.5(9)	2.70(16)
Rounded ( $t/a > 0.95$ )	25	-2.4(7)	2.58(10)
Sharpness grouping by counts	N	Slope (meV/nm)	Intercept (eV)
Sharp ( $t/a < 0.073$ )	41	-4.1(5)	2.75(9)
Average ( $0.073 < t/a < 0.087$ )	41	-3.9(9)	2.72(16)
Rounded ( $t/a > 0.87$ )	41	-3.4(6)	2.71(10)

Note: The second set of boundaries represents an equal number of particles in each group. The fits follow the equation  $y=mx+b$ ; 95% confidence intervals on the last digit(s) in parentheses. The average relative truncation of the data set is 0.082, with a standard deviation of 0.015; the average size is 180 nm with a 26 nm standard deviation (Figure 4.9).

#### 4.2.1.3.2 Plane Fit

A rigorous, and perhaps an obvious (at least statistically), way to fit a variable that depends on two independent variables is a plane fit, i.e. a regression analysis. This can be easily performed in MATLAB using the surface fitting tool. Any equation relating the variables can be input, although in this case the simplest first-order formula gave the best results. The longitudinal plasmon energy was found to be related to the size and corner truncation following the equation:

$$\text{LSPR}_{(\text{eV})} = -0.0051(3) \cdot a_{(\text{nm})} + 0.019(3) \cdot t_{(\text{nm})} + 2.69(6) \quad (4.1)$$

The tight 95 % confidence bounds on the fit coefficients (in parenthesis, on the last digit) indicate low errors associated with the model, while the R-square value of 0.88 signify that this planar fit explains 88 % of the variation in the experimental data. The rigor of this model, its attractive visual representation in three dimensions, as well as the easy visualization of pair wise interactions (Figure 4.11) make the planar fit an interesting way of displaying and analyzing large data sets involving multiple parameters. Surprisingly, only one example of such simultaneous 2-parameter analysis has been carried out, to our knowledge and that of our reviewers; the system studies in that case was core-shell Ag-Ag<sub>2</sub>O particles, where the optical properties are influenced by both the core radius and the shell thickness.<sup>220,221</sup>

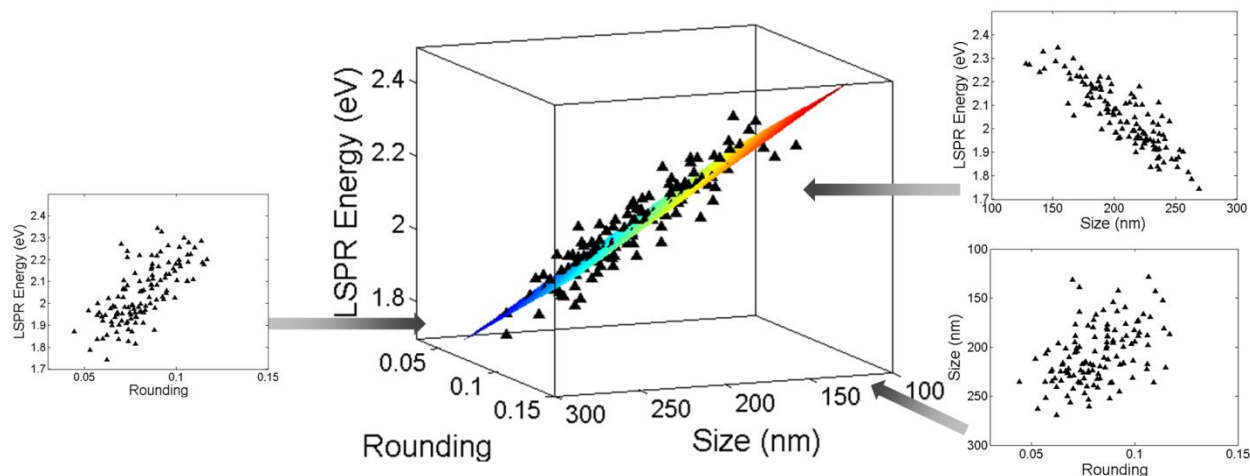


Figure 4.11. Planar fit approach to describe the simultaneous LSPR energy dependence on size and corner rounding, fit described by equation 4.1. The two dimensional plots show pair wise correlations between energy and rounding, energy and size, and size and rounding.

#### 4.2.1.3.3 Effective Plasmon Length Fit

While the planar fit (Section 4.2.1.3.2) represents a quantitative improvement over the grouping approach (Section 4.2.1.3.1), the former is not as intuitive as the latter. Indeed, the lower slope of the LSPR energy for more rounded particles, seen as an incline of the plane, could easily remain unnoticed after a quick glance. The third fitting approach aims at re-establishing the intuitiveness of the grouped model while preserving the rigor of the planar fit. As mentioned earlier, regression can be performed on any type of mathematical equation, i.e. it is not limited to the basic  $z = a*x+b*y+c$ . Inspired by the concept developed in Section 4.1, a modified plasmon length was sought, which must account for both size and corner truncation. A linear relationship, akin to those of Section 4.1, is then expected between the effective plasmon length

( $PL_{\text{eff}}$ ) and the LSPR energy. The following equations, with 95% confidence levels in parenthesis, describe this fit (Figure 4.12):

$$LSPR_{(\text{eV})} = -0.0051(3)PL_{\text{eff}} + 2.69(6) \quad (4.2)$$

$$PL_{\text{eff}} = a_{(\text{nm})} - 3.7(6)*t_{(\text{nm})} \quad (4.3)$$

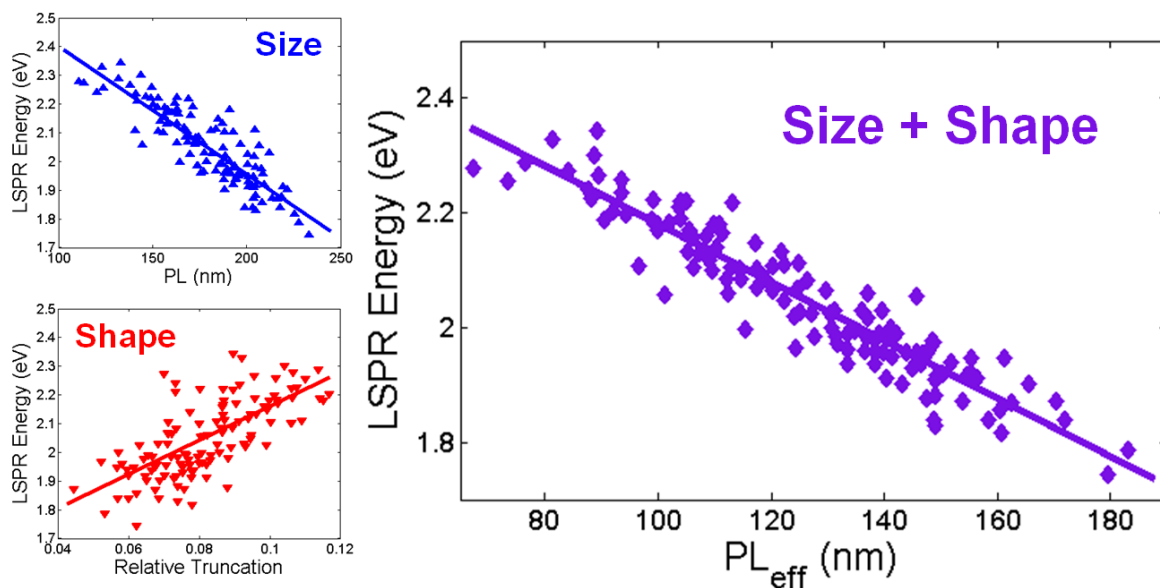


Figure 4.12. Effective plasmon length approach describing the simultaneous size and shape effects in Ag bipyramids. The left panels are identical to Figure 4.8. Right panel: fit described by Equations 4.2 and 4.3.

The effective plasmon length approach provides an intuitive way, akin the plasmon length, to linearize the size effects on LSPR energy, while taking corner truncation into account. It is obvious from the fit parameters that the effect of truncation is not only geometric. Indeed, if it

were the case, and truncation would simply lower the plasmon length value, the coefficient of  $t$  in equation 4.3 would be 1 (and the coefficient of  $t$  in Equation 4.2 would be equal in magnitude and opposite in sign to the coefficient of  $a$ ), i.e. a fit relating the plasmon energy to the truncated height ( $a-t$ ) would be best. Clearly, variations in tip sharpness also change the charge distribution, such that for rounded particles opposite charges become even closer than from this geometrical argument only. This field distribution difference is responsible for the difference in size-dependence of the plasmon energy for different truncation groups (obvious in Figure 4.10).

#### 4.2.1.4 Bipyramids Fits Discussion

The high R-square value of the planar and  $PL_{\text{eff}}$  fits indicate that size and corner rounding comprehensively dictate the position of the plasmon resonance frequency. The remaining noise in Figures 4.11 and 4.12 can be attributed to variation in the transverse corner truncation; calculations have shown that the geometry of these tips can slightly affect the transverse plasmon,<sup>132</sup> and was not accounted for in this study because of the experimental difficulties associated with obtaining accurate structural information on the transverse tips. The plasmon FWHM was not as effectively modeled by size or shape; in fact no statistically significant relationship between the FWHM and relative corner truncation was obtained, albeit one might be expected due to the change in the near field electric charge distribution.<sup>106,116,147</sup> The larger variance in the FWHM data, leading to larger uncertainties in the fit, may be due to a number of factors such as small changes in the dielectric environment, surface oxidation, transverse tip truncation, and the possible apparition of higher order modes (not included in the peak fitting).

## 4.2.2 Correlated LSPR/TEM on Nanocubes

### 4.2.2.1 Au Nanocubes

Another structure with a large range of corner rounding is Au nanocubes (Chapter 3). Figure 3.5 is in fact a grouped fit analysis where the nanocubes were divided in "sharp" and "rounded" groups. Without rejecting the rounded cubes (as was done in Chapter 3), the R-square value for the size and relative corner rounding effect on the LSPR energy is 12 and 40 %, respectively. The fit in Figure 3.5 qualitatively indicates an effect of corner rounding on the LSPR energy. Could more information of the simultaneous effects of size and corner rounding be extracted from this data using the multiple parameter fits that were successful with Ag bipyramids?

To answer this question, the nanocubes data were analyzed using a planar fit and a effective plasmon length fit. The parameters for the single factor fits (Figure 4.13, left panels) are reported in Table 4.9. The plasmon energy data was adequately described by a plane fit ( $R^2 = 49\%$ ) following the equation:

$$\text{LSPR}_{(\text{eV})} = -0.0039(15) \cdot a_{(\text{nm})} + 0.007(2) \cdot t_{(\text{nm})} + 2.34(12) \quad (4.4)$$

The effective plasmon length fit (Figure 4.13, right panel), followed the equations

$$\text{LSPR}_{(\text{eV})} = -0.0039(15) \cdot \text{PL}_{\text{eff}} + 2.34(12) \quad (4.5)$$

$$\text{PL}_{\text{eff}} = a_{(\text{nm})} - 1.8(8) \cdot t_{(\text{nm})} \quad (4.6)$$

Note that due to the large variance (Figure 3.5) and small size range probed, the plasmon decay of Au nanostructures was not included in this analysis.

Table 4.9. Size and shape effect on the LSPR energy of Au and Ag nanocubes.

Composition, Parameter, Mode	N	Slope	Intercept (eV)	R-Square
Au, Size, Dipole	64	-2.8(19) meV/nm	2.37(16)	12%
Au, Relative Rounding, Dipole	64	0.6(2) meV	2.01(4)	40%
Ag, Size, Dipole	119	-10.8(5) meV/nm	3.48(7)	93%
Ag, Relative Rounding, Dipole	119	10.3(13) meV	0.84(16)	68%
Ag, Size, Quadrupole	118	-6.5(5) meV/nm	3.64(6)	87%
Ag, Relative Rounding, Quadrupole	118	6.2(8) meV	2.04(10)	66%

Note: 95 % confidence intervals on the last digit(s) in parentheses.

Table 4.10. Size and shape effect on the LSPR FWHM of Ag nanocubes.

Composition, Parameter, Mode	N	Slope	Intercept (eV)	R-Square
Ag, Size, Dipole	119	7.0(14) meV/nm	0.04(19)	44%
Ag, Relative Rounding, Dipole	119	-6.4(18) meV	1.7(2)	30%
Ag, Size, Quadrupole	118	5.5(6) meV/nm	-0.26(8)	76%
Ag, Relative Rounding, Quadrupole	118	-4.9(9) meV	1.05(11)	49%

Note: 95 % confidence intervals on the last digit(s) in parentheses.

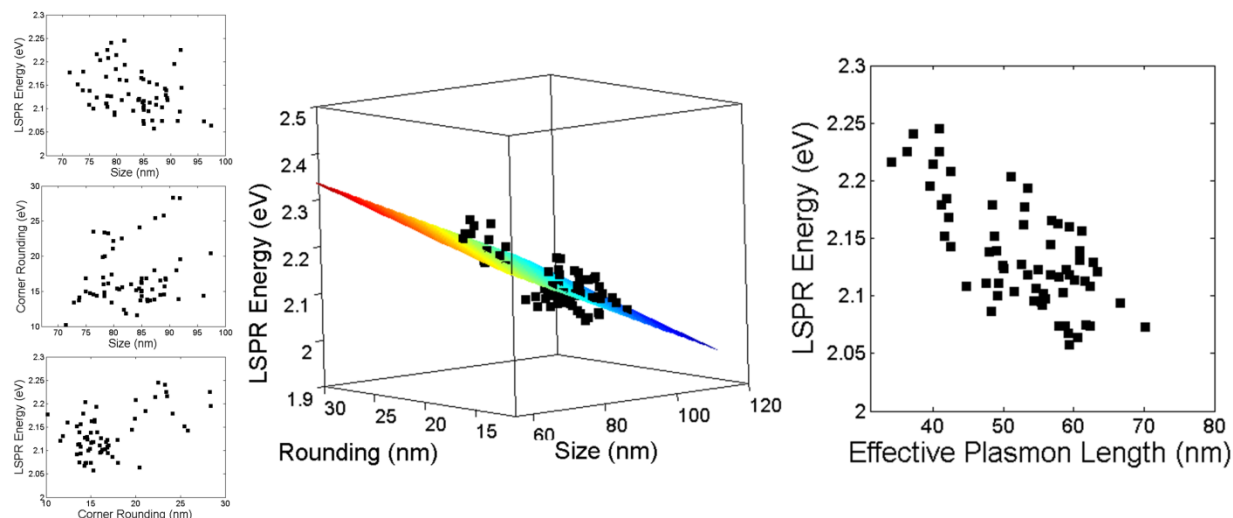


Figure 4.13. Effect of size and corner rounding on the LSPR energy of Au nanocubes. Left: single parameter effects. Top left: Size effect on LSPR energy. Middle left: Size and corner rounding correlation. Bottom left: Rounding effect on LSPR energy. Middle: plane fit, described by Equation 4.4. Right: Effective plasmon length fit, described by Equations 4.5 and 4.6.

#### 4.2.2.2 Ag Nanocubes

A very large size range was available for Ag nanocubes (some results have already been discussed in Chapter 3, some will be discussed in Section 4.3), such that a multiparameter fit akin that performed for Au cubes and Ag bipyramids is possible. Such analysis is interesting as it would provide an interesting comparison with other structures on the basis of shape (Ag cubes and bipyramids) and composition (Ag and Au cubes).

#### 4.2.2.2.1 Single Parameter Fits on the Energy and FWHM of the Dipolar and Quadrupolar Resonances

The single parameter fits for the energy and FWHM of both dipolar and quadrupolar resonances are presented in Figure 4.14 and Tables 4.9-4.10. The correlation between energy and edge length ( $R^2 = 93\%$  and  $87\%$ ) and energy and relative rounding ( $R^2 = 68\%$  and  $66\%$ ) is remarkable for both the dipolar and quadrupolar plasmon modes. The plasmon decay of the quadrupolar mode also correlates well with side length and relative rounding ( $R^2 = 76\%$  and  $49\%$ ). However, the width of the dipolar resonance is noisier and does not appear to vary linearly with size. Experimental differences between the small ( $< 100$  nm) and large cubes may be responsible; indeed, the data on large cubes was acquired over a year after that of the small cubes, and they were produced in two different batches, such that experimental and synthetic differences may be present. For example, the dielectric environment (critical to plasmon decay) may vary between the two samples, as rinsing was not performed on the small cubes, leaving a larger number of surfactant molecules on the particles, and the cubes were deposited on the Formvar side of different types of grids, small ones on carbon type B and large ones on ultrathin carbon type A. The former contains significantly more plasmon-damping amorphous carbon.<sup>106,147</sup> Also, measurements for small cubes were performed in air and not carried out particularly efficiently, while larger cubes were kept under dry nitrogen and measured quickly. The refractive index difference between air and nitrogen is not expected to significantly affect the optical response but surface oxidation is; in addition to these experimental differences, small cubes are intrinsically more prone to oxidation. Because of these effects and their implications on

the significance of the statistical analysis, the FWHM of the dipolar resonance will not be analyzed further.

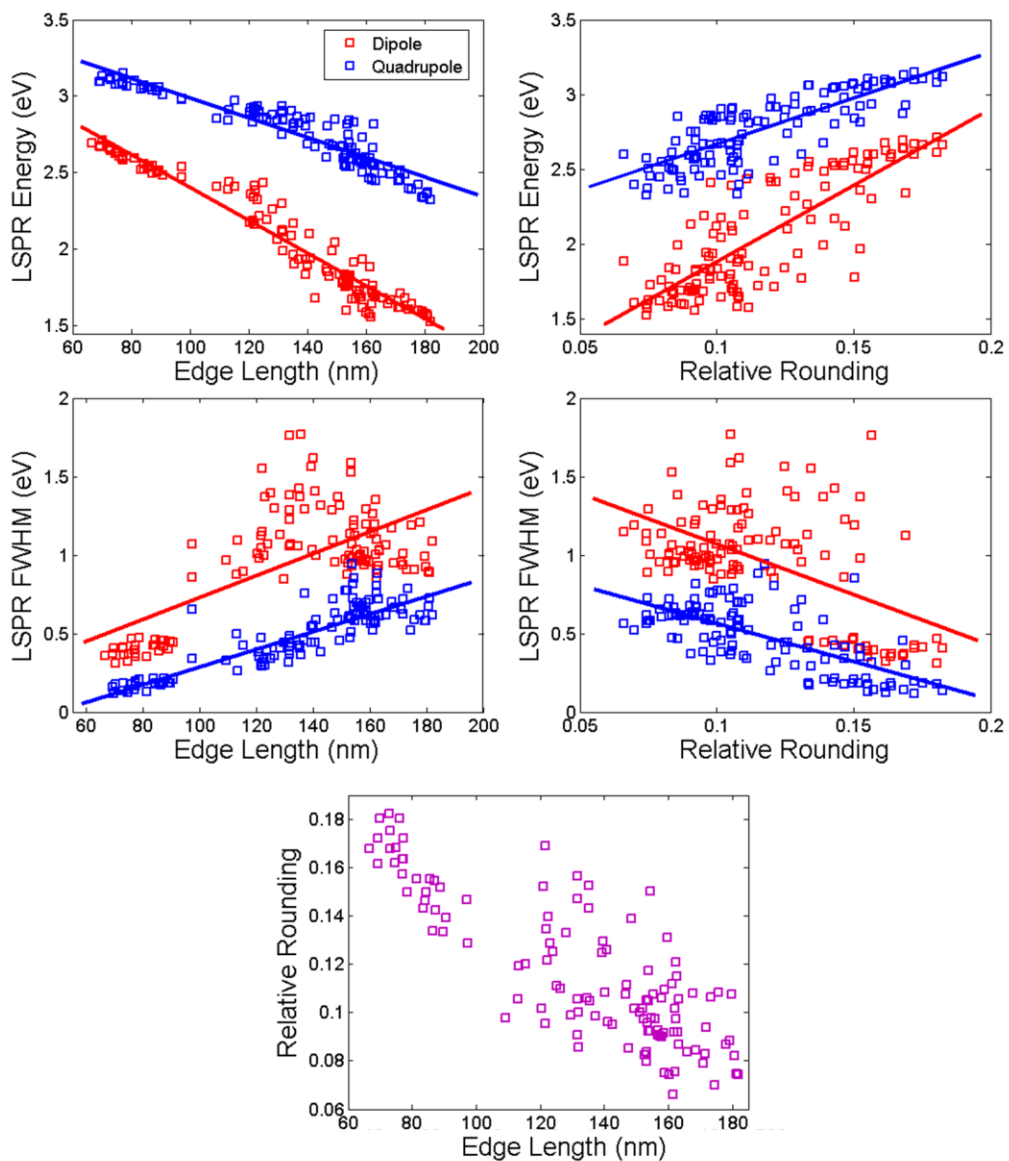


Figure 4.14. Correlation between size, corner rounding, dipolar energy and the dipolar (red) and quadrupolar (blue) LSPR energy and FWHM of Ag nanocubes. Clockwise from top left: size effect on LSPR energy, rounding effect on LSPR energy, correlation between rounding and size, size effect on LSPR FWHM, rounding effect on LSPR FWHM.

#### 4.2.2.2.2 Multiparameter Fits: Planar and Effective Plasmon Length Approach

The data presented thus far provide insight on the effect of size and shape on the optical response of Ag nanocubes, however the graphical representation in Figure 4.14 hides a trend that invalidates this single parameter analysis. As can be seen in the bottom panel of Figure 4.14, there is a correlation between cube size and relative rounding, large cubes being sharper than small ones. Thus, pair wise correlations are flawed and do not provide predictive information on size or shape effects as the rules obtained are sample-specific. For example, the sharper large cubes in the current data set skew the slope of the LSPR energy as a function of size towards a larger value than it would be for homogeneous rounding. In such cases, a multiparameter fit is the best approach. Despite the unequal sampling of the parameter space (e.g., there are few very rounded large cubes), a multiparameter fit provides quantitative, predictive equations relating optical response and structural parameters for any combination of size and corner rounding.

##### 4.2.2.2.2.1 LSPR Energy

The dipolar and quadrupolar modes can be well described by a plane fit (Figure 4.15), according to the equations (95 % confidence levels on the last digit(s) in parenthesis;  $a$  is the cube side length,  $t$  is the absolute corner rounding)

$$\text{Energy}_{(\text{Dipole, eV})} = -0.0112(6)*a_{(\text{nm})} + 0.011(7)*t_{(\text{nm})} + 3.38(10); R^2 = 94 \% \quad (4.7)$$

$$\text{Energy}_{(\text{Quadrupole, eV})} = -0.0070(5)*a_{(\text{nm})} + 0.014(5)*t_{(\text{nm})} + 3.49(8); R^2 = 89 \% \quad (4.8)$$

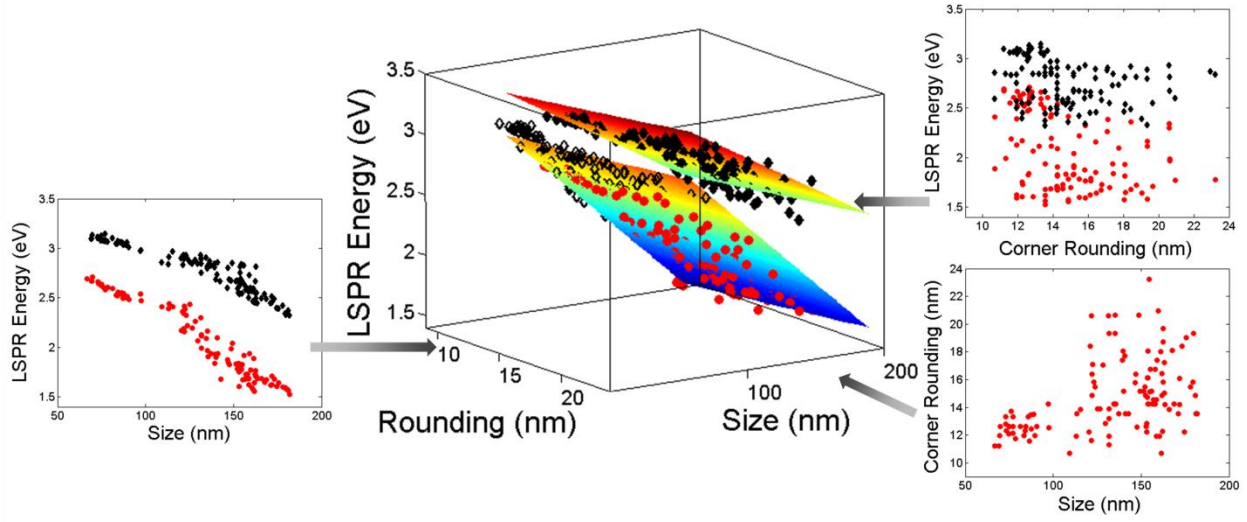


Figure 4.15. Planar fit on the simultaneous effects of size and corner rounding on the dipolar (red circles) and quadrupolar (black diamonds) plasmon energy of Ag nanocubes. The two dimensional plots show pair wise correlations between energy and rounding, energy and size, and size and rounding. The empty black diamonds are the quadrupolar resonance analyzed with a size equal to the half of the side length, see Section 4.3 for discussion of higher order modes.

The effective plasmon length fit (Figure 4.16), follows the equations

$$\text{Energy}_{(\text{Dipole, eV})} = -0.0112(6) \cdot (\text{PL}_{\text{eff}}) + 3.38(10); R^2 = 94 \% \quad (4.9)$$

$$\text{PL}_{\text{eff}} = a_{(\text{nm})} - 1.0(6) \cdot t_{(\text{nm})} \quad (4.10)$$

$$\text{Energy}_{(\text{Quadrupole, eV})} = -0.0070(5) \cdot (\text{PL}_{\text{eff}}) + 3.49(8); R^2 = 89 \% \quad (4.11)$$

$$\text{PL}_{\text{eff}} = a_{(\text{nm})} - 2.1(8) \cdot t_{(\text{nm})} \quad (4.12)$$

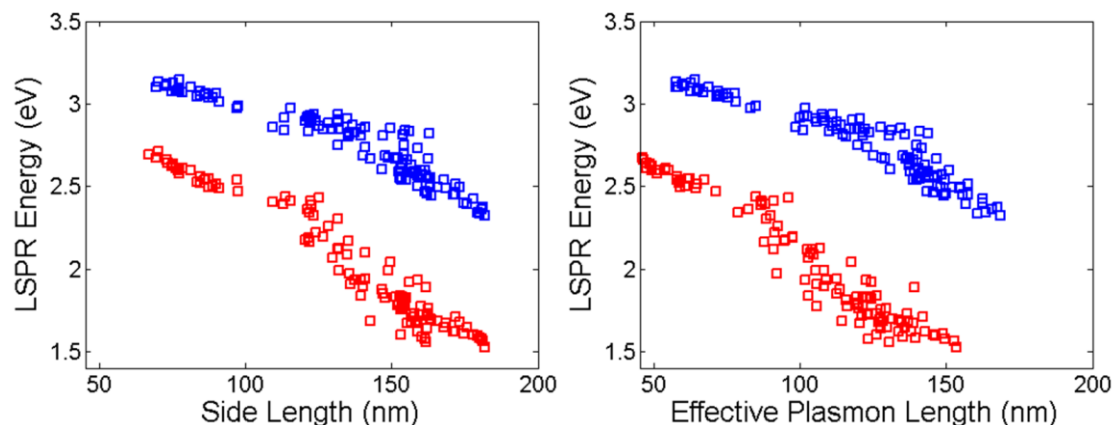


Figure 4.16. Simultaneous effects of size and corner rounding on the dipolar (red) and quadrupolar (blue) plasmon energy of Ag nanocubes. Left: single parameter fit (side length). Right: effective plasmon length fit described by Equations 4.9-4.12. The increase in correlation is modest, but the effective plasmon length approach provides sample-independent predictive rules, as discussed in the text.

Corner rounding plays a statistically significant role in determining the position of both the dipolar and quadrupolar resonance of Ag nanocubes. However, it may be tempting to dismiss its effect due to the minimal increase in R-square obtained with the plane fit. As shown in Table 4.9, the correlation between plasmon energy and size is very high, with R-square of 93 % and 87 % for the dipolar and quadrupolar resonances. One may wonder if it is worth perform multidimensional analysis to gain a mere 1 % and 2 %. In this case, the modest gain in R-square is not the motivation for including multiple parameters. Rather, the more rigorous analysis is mandatory to circumvent the correlation between size and corner rounding present in the sample analyzed.

#### 4.2.2.2.2 Plasmon Linewidth

Multiparameter fits on the FWHM of the dipolar mode yield the following plane equation

$$\text{FWHM}_{(\text{Quadrupole, eV})} = 0.0055(6)*a_{(\text{nm})} + 0.003(7)*t_{(\text{nm})} - 0.29(11); R^2 = 76 \% \quad (4.13)$$

Alternatively, this can be expressed as the effective plasmon length

$$\text{FWHM}_{(\text{Quadrupole, eV})} = 0.0055(6)*(PL_{\text{eff}}) - 0.29(11); R^2 = 76 \% \quad (4.14)$$

$$PL_{\text{eff}} = a_{(\text{nm})} + 0.5(1.4)*t_{(\text{nm})} \quad (4.15)$$

In the above Equation, the 95 % confidence interval on the corner rounding coefficient is larger than the coefficient itself; i.e. no statistically significant relationship exists between corner truncation and FWHM for the quadrupolar mode of Ag nanocubes. In other words, one can say with 95 % confidence that the coefficient of  $t$  is between -0.0048 and 0.010 eV/nm: zero being part of this interval, no significant relationship exists; the same is true for the effective plasmon length equation, of course.

This is a prime example of two common traps of statistical data analysis. First, the single parameter study (middle right panel of Figure 4.14) showed a seemingly valid correlation between truncation and FWHM, which broke down when analyzed more rigorously. Second, the R-square value of Equations 4.14-4.15, 76 %, seems rather satisfactory, yet this multiparameter fit is not the relevant one to use. The correct way to describe the quadrupolar FWHM of Ag nanocubes is that it has no statistically significant dependence on corner rounding, and thus size effects can accurately be described in a single parameter model as presented in the bottom left

panel of Figure 4.14. Of course, this lack of observed corner rounding effect does not necessarily imply that such effect does not exist for any size or shape. Rather, it indicates that the linewidth variance is high and that the small range of corner rounding in the current sample is not a significant contributor to this variance.

#### 4.2.2.3 Multiparameter Modeling in Nanocubes: Effect of Composition and Discussion

Nanocubes of both Ag and Au have been analyzed using single particle spectroscopy and TEM. Single and multiparameter fits were performed to better understand the simultaneous effects of size and corner rounding on the LSPR energy and FWHM. The LSPR energy of both structures have a statistically significant relationship to both the size and the corner rounding. Because of differences in dielectric constants, Au and Ag have significantly different slopes for the size-dependence of LSPR frequency,  $-0.0039(15)$  and  $-0.0112(6)$  eV/nm from the planar fits, respectively. An interesting and novel analysis the experimental data allows is the comparison of the effects of corner rounding for the two metals. The coefficient of  $t$  in the effective plasmon length equations (Equations 4.6 and 4.10) gives the ratio between size and corner rounding effects, regardless of the magnitude of the size effects; its value is  $-1.8(8)$  and  $-1.0(6)$  eV/nm for Au and Ag, respectively. These parameters are not significantly different, suggesting that corner rounding may play an equivalent effect for both compositions. Of course, since the magnitude of size effects are higher in Ag, the absolute value of the rounding effects are higher as well, as is suggested by the plane fit parameters in Equations 4.4 and 4.7 (Au:  $0.007(2)$  eV/nm, Ag:  $0.011(7)$  eV/nm).

The simultaneous effects of size and corner rounding on the plasmon resonance frequency of cubes can be compared to what has been calculated for rods of aspect ratio 2, based on the  $L_{\text{eff}}$  values calculated by Prescott & Mulvaney<sup>209</sup> and the dielectric constant for Ag and Au reported by Johnson & Christy.<sup>50</sup> Using these inputs, Mie-Gans theory was used to calculate the plasmon energy for a range of rod length ( $L$ ) and corner rounding ( $b$ ) (values reported in Table 4.11 and Figure 4.17). Note that only the longitudinal plasmon mode (along the rod long axis) was considered.

Table 4.11. Calculated LSPR energies for the longitudinal plasmon mode of rounded Ag and Au rods.

L (nm)	b (nm)	E (eV)	
		Ag Rods	Au Rods
10	4.3	2.76	2.18
10	3.0	2.71	2.16
10	1.6	2.64	2.13
20	8.7	2.71	2.16
20	6.0	2.66	2.13
20	3.1	2.58	2.10
30	13.0	2.64	2.13
30	9.0	2.58	2.10
30	4.7	2.50	2.06
40	17.3	2.54	2.07
40	12.0	2.50	2.04
40	6.2	2.41	2.00

The correlation between the rod length  $L$ , the height of ellipsoidal cap  $b$ , and longitudinal plasmon energy can be expressed as (95 % confidence intervals on the last digit(s) in parentheses):

Ag Rods:

$$\text{Energy}_{(\text{eV})} = -0.012(2) * L_{(\text{nm})} + 0.016(6) * b_{(\text{nm})} + 2.79(4), R^2 = 97 \% \quad (4.16)$$

$$\text{Energy}_{(\text{eV})} = -0.012(2) * (PL_{\text{eff}}) + 2.79(4), R^2 = 97 \% \quad (4.17)$$

$$PL_{\text{eff}} = a_{(\text{nm})} - 1.3(5) * t_{(\text{nm})} \quad (4.18)$$

Au Rods:

$$\text{Energy}_{(\text{eV})} = -0.0063(11) * L_{(\text{nm})} + 0.008(3) * b_{(\text{nm})} + 2.20(2), R^2 = 96 \% \quad (4.19)$$

$$\text{Energy}_{(\text{eV})} = -0.0063(11) * (PL_{\text{eff}}) + 2.20(2); R^2 = 96 \% \quad (4.20)$$

$$PL_{\text{eff}} = a_{(\text{nm})} - 1.3(5) * t_{(\text{nm})} \quad (4.21)$$

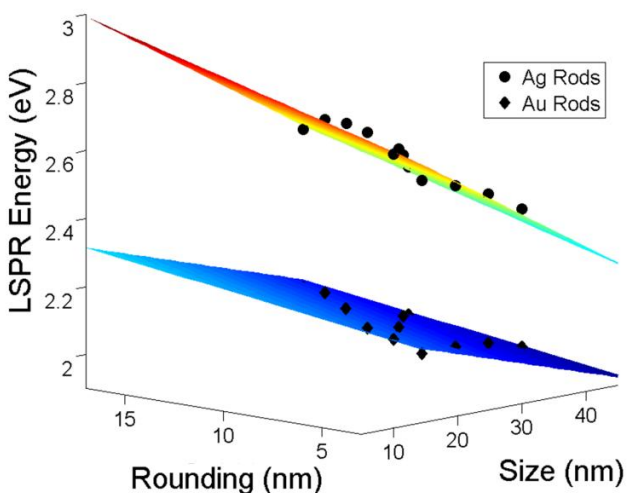


Figure 4.17. Effect of size and corner rounding on the longitudinal dipolar resonance of ellipsoidally capped Ag (circles, top plane) and Au (diamonds, bottom plane) nanorods<sup>209</sup> (fits described by Equations 4.16-4.17).

Interestingly, the coefficient of  $t$  in the effective plasmon length fits for short rods (Equations 4.18 and 4.21) are not significantly different than that obtained experimentally for nanocubes (Au cubes: -1.8(8) eV/nm, Ag cubes: -1.0(6) eV/nm, both rods: -1.3(5) eV/nm). The size

dependence of the LSPR energy for nanocubes and nanorods are also not significantly different for Ag (cubes:  $-0.0112(6)$  eV/nm, rods:  $-0.012(2)$  eV/nm) and Au particles (cubes:  $-0.0039(15)$  eV/nm, rods:  $-0.0063(11)$  eV/nm). The structural dependence of the calculated optical response of short rods is thus comparable to that of cubes, supporting the experimental findings on retardation and corner rounding effects. Note that experimental studies on short rods would be very interesting to cement this claim; their feasibility, however, depends on the ability to synthesize a large size range of particles with fixed aspect ratio.

This analysis also enables the comparison of the size-dependence of the energy of the dipolar and quadrupolar resonances of Ag nanocubes. The size-dependence of the latter is almost half of the former, with values, from Equations 4.9 and 4.11, of  $-0.0112(6)$  and  $-0.0070(5)$  eV/nm. This interesting effect will be discussed in detail in the next section. The relative contributions of size and corner rounding to the LSPR energy for the two modes are also within a factor of two of each other, although they are not statistically different: the coefficient of  $t$  in Equations 4.10 (dipole) and 4.12 (quadrupole) is  $-1.0(6)$  and  $-2.1(8)$  eV/nm, respectively. A true difference is expected to exist because of the dissimilar electric field distribution around the particle, in particular in the corner regions, for the dipolar and quadrupolar modes.

#### 4.2.3 Origin of Simultaneous Rounding and Size Effects and Shape Comparisons

The analysis above clearly points to cooperative effects between size and corner truncation going beyond simple geometric arguments. The work of Prescott and Mulvaney<sup>209</sup> and Bryant *et al.*,<sup>99</sup> and Slaughter *et al.*<sup>222</sup> have observed similar effects on the calculated optical response of Au

nanorods. Indeed, each report hints, in different ways and with different degree of completeness, at a smaller decrease of the plasmon resonance energy with size for more rounded nanorods. Note that, as previously mentioned, the low scattering and the experimental difficulties associated with producing a large size range of rods of the same aspect ratio make this cooperative effect challenging to probe experimentally. The latter could, however, be surmounted by adding a third parameter to the fit, i.e., modeling the simultaneous effects of size, aspect ratio, and corner rounding on optical response. A new generation of high throughput measurements would be needed to obtain enough data for this fit.

This multi-parameter, cooperative effect of size and corner rounding on the size dependence of the plasmon energy can be partially understood from a simple geometric argument. Indeed, for a bipyramids of edge length  $a$  and truncation  $t$ , the tip-to-edge distance (real height) is  $a-t$ , i.e. smaller for more rounded particles. Retardation effects (phase differences between the particle tips) are responsible for the size-dependence of plasmon frequency. Retardation is less present in a more round particle because of the shorter real height, explaining the blue shift observed with increased truncation. Additionally, as  $a$  is doubled, the idealized height is also doubled, but the true (truncated,  $a-t$ ) distance is not: the absolute increase is smaller for more rounded bipyramids. However, if this effect was solely responsible for the observed trend, the coefficient of  $t$  in the planar fit equations would be equal in magnitude and opposite in sign to the coefficient of  $a$ , such that a fit relating the plasmon energy to the truncated height ( $a-t$ ) would be best. Clearly, variations in tip sharpness also change the charge distribution, such that for rounded particles opposite charges become even closer than from this geometrical argument only. The phase difference between the tips (geometric size effect) and the charge distribution not changing

equivalently thus leads to dissimilar increase in retardation for the same (idealized) size increase in rounded and sharp particles. Consequently, the plasmon frequency of rounded particles is less dependent on size than that of sharp particles, as experimentally observed.

Shape may not affect the size-dependence of the plasmon energy and FWHM (Section 4.1 and ref.<sup>86</sup>), but it does change the relative contribution of corner rounding and size. Indeed, the coefficient of  $t$  in the effective plasmon length equations, expressing the relative contribution of the two parameters, is significantly different for Ag cubes and bipyramids, with values of -1.0(6) and - 3.7(6), respectively. This disparity arises from the geometry of the plasmon oscillation path, in other words the electric field distribution. Indeed, the bipyramid equatorial plasmon is an oscillation along the equilateral triangle base, from apex to edge. The plasmon path passes by the apex, thus the plasmon mode energy is significantly more influenced by tip geometry than for a mode oscillating from face to face such as the dipolar resonance in cubes. Unlike the effects observed for homogeneously sharp Au particles in Section 4.1, shape does seem to affect the plasmon dependence on size for Ag particles, although the corner truncation are very large and different for cubes and bipyramids. Further studies of Ag shapes are needed to draw any conclusions on the universality of size effects for this metal.

#### 4.3 Plasmon Length Applications to High Order Modes in Ag and Au Nanoparticles

As plasmonic particles become larger, they can support an increasing number of resonance modes beyond the low energy dipole, such that in spheres larger than 100 nm, for example, the quadrupole tends to dominate the spectra. For large Ag cubes (> 120 nm plasmon length), up to

four modes can be present, as shown in Figure 4.18. Gold particles typically do not support as many high order modes because of the interband transitions at energies above 500 nm, such that large decahedra have up to three prominent modes.

#### 4.3.1 High Order Modes in Ag Nanocubes

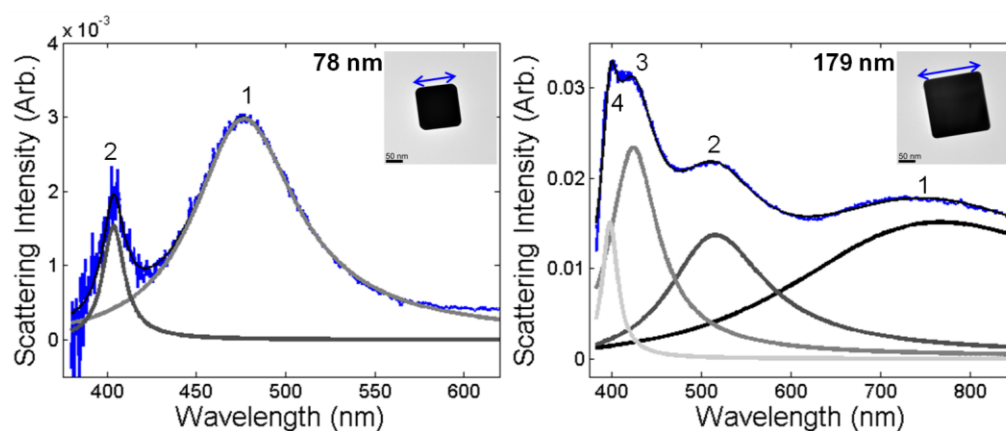


Figure 4.18. Plasmon modes in Ag cubes. Left: small Ag cube with 2 plasmon modes, the dipole (lowest energy, peak 1) and the quadrupole (highest energy, peak 2). Right: large Ag cube showing all four plasmon peaks, labeled 1 to 4.

The size dependence of the plasmon energy of the four resonant modes of Ag nanocubes is presented in Figure 4.19. As expected, the plasmon energy decreases with increasing particle size for all modes because of retardation effects. However, a large difference in the slope of this decrease exists between the modes, as reported in Table 4.12. Interestingly, the slope seems to halve between each mode. This observation lead us to the analysis presented in Table 4.13 and Figure 4.19, where the plasmon length is defined as side length/mode number; the mode double

for each peak, i.e. dipole = mode number 1, quadrupole = 2, peak 3 = 4, peak 4 = 8. The plasmon length of the dipole is thus equal to the side length, and that of the quadrupole, to half of the side length, etc. Physically, this implies that for a quadrupole, the plasmon goes through a “node” akin that of a resonant string mode (in which the length of each oscillator becomes the length of the string divided by the number of node plus one), and likewise for higher orders.

Table 4.12. Fit parameters for the plasmon energy dependence on side length for the four plasmon modes of Ag nanocubes. (unconstrained slopes, analysis of covariance).

Peak #	Slope (meV/nm)	p-value	Intercept (eV)	p-value
1 (Dipole)	-10.6(3)	0.89	3.46(5)	0
2 (Quadrupole)	-6.5(3)	0.0008	3.62(5)	0
3	-2.8(4)	0.66	3.42(6)	0
4	-1.3(8)	0.26	3.31(13)	0

Note: standard error on last digit(s) in parentheses. P-values less than 0.0005 are reported as 0.

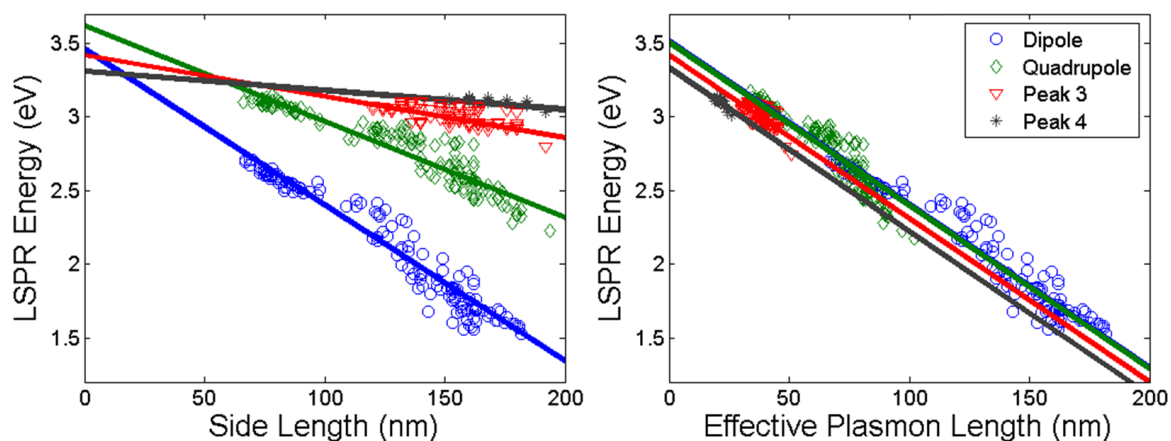


Figure 4.19. Statistical analysis of size effects on the plasmon energy of Ag nanocubes using side length (left) and plasmon length (right) for peak 1 (dipole, blue circles), peak 2 (quadrupole, green diamonds), peak 3 (red triangles), and peak 4 (grey stars). Parallel slopes in the right panels were obtained from analysis of covariance; the parameters are reported in Table 4.13.

Table 4.13. Fit parameters for the plasmon energy dependence on plasmon length (side length/(mode number)) of Ag nanocubes (unconstrained and constrained slopes, analysis of covariance).

Shape	Energy Dependence on Plasmon Length, Unconstrained Slopes				Energy Dependence on Plasmon Length, Constrained Slopes			
	Slope (meV/nm)	p-value	Intercept (eV)	p-value	Slope (meV/nm)	p-value	Intercept (eV)	p-value
Peak 1 (Dipole)								
Mode 1	-12(2)	0.89	3.46(5)	0.90	-11.1(16)	0	3.518(12)	0
Peak 2 (Quadrupole)								
Mode 2	-9(2)	0.42	3.62(5)	0.0008			3.507(6)	0
Peak 3								
Mode 4	-11(2)	0.98	3.42(7)	0.66			3.419(8)	0.003
Peak 4								
Mode 8	-10(6)	0.84	3.31(13)	0.27			3.333(12)	0

Note: standard error on last digit(s) in parentheses. P-values less than 0.0005 are reported as 0.

While some caution is required when interpreting the result in Figure 4.19 and Table 4.13 because of the correlation between size and rounding in the sample used, the data strongly suggest that the effective plasmon mode approach can be applied to the experimental analysis of high order modes. Some previous work by Zhou *et al.*<sup>96</sup> calculated the plasmonic behavior of untruncated Ag nanocubes in vacuum over a large size range between 15 and 200 nm: an almost linear relationship between plasmon energy and cube size was found for cubes larger than 80 nm, although the data is presented in wavelength, a non-linear energy unit. The slope of the dipole was roughly half of that of the quadrupole, consistent with the current results. Surprisingly, Zhou *et al.* found no size-dependence of the energy of the peak located around 400 nm. This peak may be equivalent to either peak 3 or 4 in this work; the field distribution calculated in the Zhou *et al.* paper clearly shows 3 nodes of in the plasmon oscillation. While this may help assigning the mode to peak 4, any comparison must be done cautiously, as the calculations were performed for perfect cubes in an homogeneous vacuum environment. Developing analytical models for the

optical response of nanocubes, which should be achievable due to their high symmetry, would greatly advance the field by providing easy, intuitive modeling.

#### 4.3.2 High Order Modes in Au Decahedra

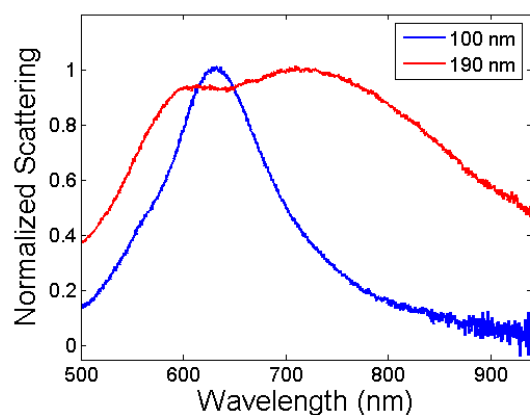


Figure 4.20. Plasmon modes in Au Decahedra. Red: small decahedron (100 nm side length) scattering spectrum, dominated by the equatorial dipolar resonance (the quadrupole appears as a shoulder around 560 nm). Blue: large Au decahedron (190 nm side length) showing a broad equatorial dipolar and a strong quadrupolar resonance.

Large Au decahedra can be efficiently synthesized by reduction of  $\text{HAuCl}_4$  in PVP and diethylene glycol (see Chapter 2 for details), such that a large size range between 50 and 300 nm was available for experiments. Previous work by the Liz-Marzàn group showed that the lowest energy resonance is the equatorial dipole (along the pentagonal plane), followed by the equatorial quadrupole and the weak transverse dipole (perpendicular to the pentagonal plane).<sup>67</sup> The latter appears as a shoulder for large decahedra, the quadrupole is obvious in all but very

small particles, and the equatorial dipole is typically broad and well separated from the other modes, as can be seen in Figure 4.20.

Table 4.14. Fit parameters for the plasmon energy dependence on dipolar plasmon length for the dipolar and quadrupolar resonances in Au decahedra on Formvar and  $\text{Si}_3\text{N}_4$  (unconstrained slopes, analysis of covariance).

Peak, Substrate	N	Slope (meV/nm)	p-value	Intercept (eV)	p-value
Dipole, Formvar	245	-3.02(10)	0	2.403(13)	0
Quadrupole, Formvar	22	-1.20(12)	0	2.39(2)	0.10
Dipole, $\text{Si}_3\text{N}_4$	69	-2.92(16)	0	2.28(2)	0
Quadrupole, $\text{Si}_3\text{N}_4$	44	-1.0(2)	0	2.35(3)	0.84

Note: standard error on last digit(s) in parentheses. P-values less than 0.0005 are reported as 0.

Statistical analysis results on the size-dependence of the energy of the dipolar and quadrupolar modes of Au decahedra are presented in Table 4.14 and Figure 4.21. A total of 245, 22, 69, and 44 particles were studied for the dipolar resonance on Formvar, quadrupolar resonance on Formvar, dipolar resonance on  $\text{Si}_3\text{N}_4$ , and quadrupolar resonance on  $\text{Si}_3\text{N}_4$ , respectively. The plasmon FWHM dependence on size for the dipolar and quadrupolar modes are not statistically different, with respective values of 2.90(10) and 3.2(4) meV/nm on Formvar, as can be seen in Figure 4.21. This result is reminiscent of the behavior of Ag cubes (Figure 4.14), as is the significantly lower absolute value of the slope of the quadrupolar resonance energy dependence on size compared to the dipolar resonance. This finding agrees with previous experimental and numerical results for Au decahedra with side length ranging from 40 to 170 nm.<sup>82</sup> Only qualitative comparisons can be made, however, because of the lack of statistical analysis in the previous reports. Unlike the plasmon resonances of nanocubes, the effective plasmon length for the quadrupolar mode of Au decahedra is not 1/2 but 0.37 times the dipolar plasmon length

(average between Formvar and  $\text{Si}_3\text{N}_4$  substrates). Of course, not all particle shapes have a symmetry as high as nanocubes, hence not all quadrupolar modes will have the same relative plasmon length. In the case of decahedra, 0.37 may be consistent with the decahedral symmetry and the oscillation mode depicted in ref.<sup>199</sup> However, the latter numerical analysis, was performed on bicones, and further computational work using accurate shapes and substrates would more precisely reveal the symmetry of the mode involved. This knowledge could also be gained experimentally through plasmon field mapping, as can be done with, e.g., EELS.<sup>216</sup> This would yield a more accurate understand the geometric origin of the quadrupole plasmon length obtained from the current far-field approach.

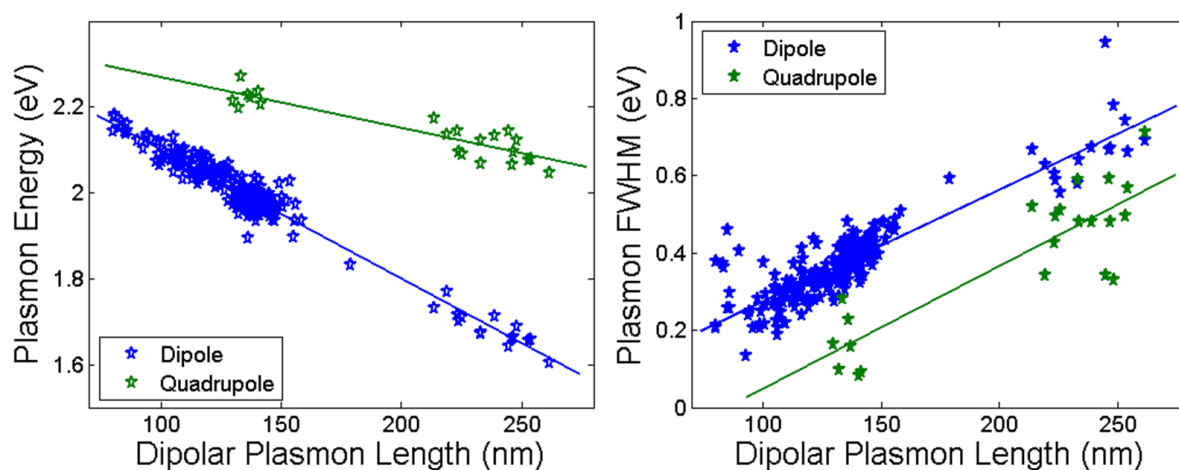


Figure 4.21. Size-dependence of the energy and width of the equatorial dipolar (blue) and quadrupolar (green) resonances in Au decahedra on Formvar. Left: plasmon energy. Right: plasmon FWHM.

### 4.3.3 Higher Order Modes and Sensing Applications

Because of the different size-dependence of plasmon modes, quantitative, predictive rules can help determine the degree of separation between the different modes, an important parameter for sensor design and harnessing of the plasmon-induced electric fields around the particle. This higher order mode analysis, performed here on cubes, an exceptional high symmetry structure, and decahedra, may prove useful for a variety of other shapes. However, as seen in the decahedra case, it may not be straightforward because of lower symmetry, ill-defined quadrupolar resonance field distributions and potential coupling with the substrate. Additionally, the possibility of multiple modes of the same order may complicate the analysis; transverse and longitudinal modes in nanorods, and equatorial and transverse modes in bipyramids are all dipolar resonances, for instance.

### 4.4 Conclusions

The plasmon length concept has been used in both basic and modified forms to describe the size-dependence of plasmonic properties of metal nanoparticles. When the plasmon length, the distance between region of plasmon-induced opposite charge, is used for Au nanostructures, the size-dependence of LSPR energy and FWHM was found to be shape-independent (Section 4.1). For shapes with larger corner rounding inhomogeneities, the concept of effective plasmon length has been developed to provide a platform to compare the relative effects of rounding and size on various shapes, in this case Ag bipyramids, Ag nanocubes, and Au nanocubes (Section 4.2). It

was found that Ag bipyramids were more affected by corner rounding than nanocubes and that the composition of the latter did not influence the relative contribution of size and corner rounding to the plasmon energy. Furthermore, a higher order plasmon length parameter was used to analyze the plasmonic behavior of Ag nanocubes, yielding mode-independent size effects (Section 4.3).

Both the plasmon energy and FWHM for all the particles studied vary linearly with plasmon length. The latter is surprising, as radiative damping, the dominant decay mechanism in large particles, is generally expected to depend on size such that the FWHM varies linear with volume, not side length.<sup>84,110,116,117</sup> This work consistently finds the latter over large sizes ranges for multiple different shapes, different plasmon modes, and two different compositions. A likely explanation of this phenomenon is simultaneous size-dependence of radiative damping and the dielectric function; the large redshift of the plasmon energy with size modifies the imaginary part of the metal dielectric function, i.e. other plasmon damping phenomenon such as interband transitions are reduced.

Overall, the plasmon length approach to size characterization, taking into account the plasmon mode, provides a useful tool to describe the linear dependence of LSPR energy and width with particle size. These findings are expected to make a significant impact in the plasmonic community because of the prevalence of LSPR tuning through size and shape control.<sup>31,54,67,82,84,104,107-109,122,130,132,133,143,187,198,199,223</sup>

## CHAPTER 5

### Sensing Using Plasmon Resonances and Plasmon-Enabled Spectroscopy

## 5.1 Au and Ag Nanostructures for Localized Surface Plasmon Resonance Sensors

As seen in previous chapters, many factors influence the localized surface plasmon resonance frequency in noble metal nanoparticles. In Chapters 3 and 4, the effect of size, composition, and shape on the plasmonic properties was systematically analyzed. Another critical factor, the refractive index of the surrounding medium, was studied via a substrate change in Chapters 3 and 4. The plasmon frequency sensitivity to the dielectric environment (as predicted by Mie theory, see Chapter 1) provides a sensing mechanism that has been exploited in a range of biological and chemical detection schemes.<sup>54,55,61,63,64,69,73,208</sup>

The efficiency of a plasmonic sensor depends on the magnitude of the optical signal change induced by the presence of the analyte. For a LSPR-based technique, this parameter is the bulk refractive index sensitivity  $m$ , the plasmon resonance frequency shift per refractive index unit. This relationship is linear over the typical RI range of interest (for aqueous solution, between 1.33 and 1.5,<sup>54,64,66</sup> for gases, between 1 and 1.1<sup>53</sup>). Values of  $m$  range from 70 to 500 nm/RUI,<sup>53,58,59,61,63-67,108,224</sup> although ever larger ones have been reported for hollow, core-shell, star-shaped, and irregular structures.<sup>58,63-67,72,73,103,105,106,108,224</sup>

Despite its importance, the refractive index sensitivity ( $m$ -value or RIS) is not the only factor to consider when determining potential usefulness for sensing applications: the sensing figure of merit, RI sensitivity divided by peak FWHM (both in eV),<sup>106</sup> is a better parameter to describe sensing capacity, as shifts are easier to detect for sharp peaks. Since both sensitivity and peak width generally increase with particle size, a maximum in the figure of merit for a given shape should exist at the size where peak widening overcomes the benefit of increased RI sensitivity. Because of its reliance on FWHM, the intrinsic FOM for a particle of a given shape and size can

only be determined by single particle analysis. Indeed, as discussed in Chapter 1, the linewidth of a bulk sample is a convolution of homogeneous and inhomogeneous broadening, the latter due to the unavoidable variety of shapes and sizes in the sample.

### 5.1.1 Single Particle Refractive Index Sensitivity

#### 5.1.1.1 Correlated Single Particle Refractive Index Sensitivity Measurements of Au Decahedra, Au Truncated Bitetrahedra, and Ag Colloids

To study the relationships between size, shape, refractive index sensitivity, and sensing FOM, single particle correlated RIS/TEM was performed with  $\text{Si}_3\text{N}_4$  TEMVu grids. The decahedra reaction mixture was chosen because of the stability and high scattering efficiency of the Au structures. Particles were immersed in glycerol-water solutions (refractive indices shown in Table 5.1) and a total of 42 single decahedra and 5 single truncated bitetrahedra were analyzed. Representative spectra and TEM images are reported in Figures 5.1 and 5.2. The size-dependence of the decahedra RIS and FOM is presented in Figure 5.3. There is no statistically significant relationship between RIS or FOM and size in the range studied. More data is needed to draw conclusions, as will be discussed in Section 5.1.1.2.

Table 5.1. Refractive indices of glycerol-water solutions, from ref.<sup>225</sup>

Glycerol %	Refractive Index (RIU)
0	1.33303
6.25	1.34209
8	1.34238
12.5	1.35142
16	1.35233
25	1.36404
40	1.38413
50	1.39809
75	1.43534
80	1.44290
100	1.47399

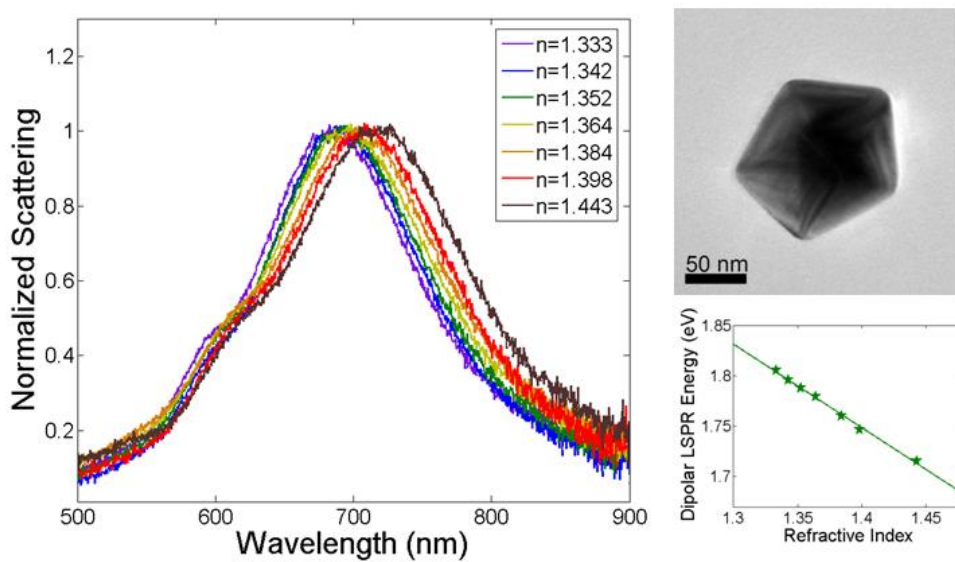


Figure 5.1. Refractive index sensitivity measurements of a single Au decahedra. Left: spectra in different glycerol/water solutions. Top right: TEM picture. Bottom right: linear relationship between the RI and LSPR energy; the  $m$ -value for this particle is  $-0.89$  eV/RIU (350 nm/RIU).

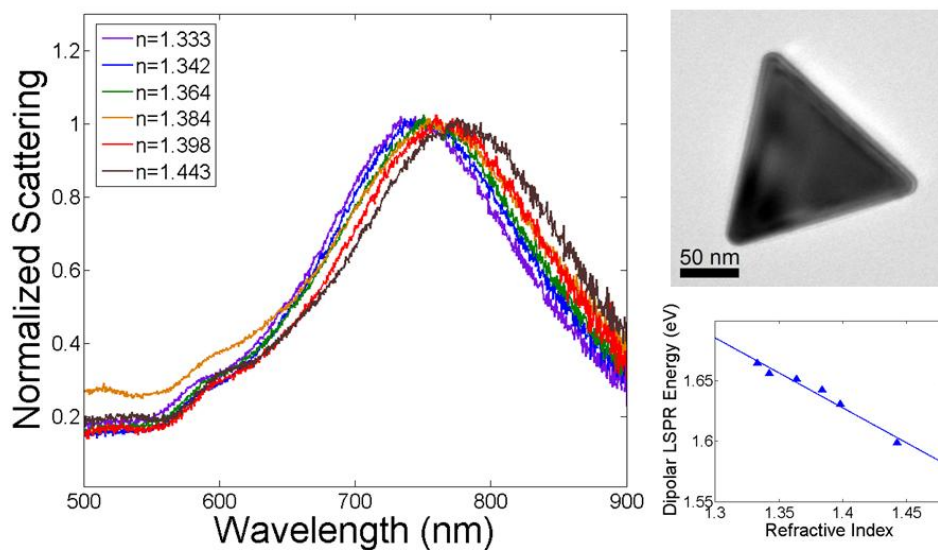


Figure 5.2. Refractive index sensitivity measurements of a single Au truncated bitetrahedra. Left: spectra in different glycerol/water solutions. Top right: TEM picture. Bottom right: linear relationship between the RI and LSPR energy; the  $m$ -value for this particle is  $-0.60$  eV/RIU (270 nm/RIU).

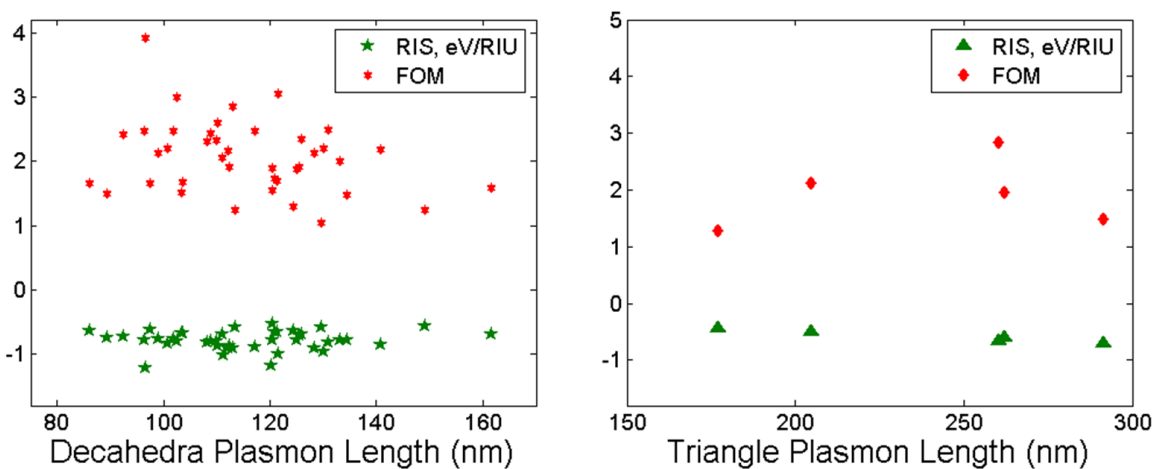


Figure 5.3. Refractive index sensitivity values ( $m$ ) and figures of merit (FOM) for single decahedra (left) and triangles (truncated bitetrahedra, right) obtained from correlated RIS/TEM.

The large amount of data obtained on single particles in different media can also be used to study retardation effects. Indeed, calculations on spheroids predict that the plasmon energy size dependence will be more acute for particles in a higher refractive index media.<sup>81</sup> This effect was not observed for particles on different substrates (Chapters 3 and 4). The effective refractive index change between air and water immersion is much larger than for the substrates previously studied, providing a better testing ground for this theory. As expected, the size dependence of the LSPR energy was statistically different for the two media. As shown in Table 5.2, the plasmon energy variation with particle size for single Au decahedra in air is  $-3.1(3)$  meV/nm, a value significantly different than that of any of the glycerol-water mixtures (p-value: 0.0042). No statistically significant slope differences were observed for the glycerol-water mixtures, likely due to the similarity of their RI (1.33 to 1.44); as can be seen in Table 5.3, the p-values for these slopes are all over 0.4. A constrained slope model was thus applied to the water-glycerol mixtures; results are reported in Table 5.4. As expected from the refractive index dependence of the LSPR energy, the intercept of the energy vs. size lines, in a constrained slopes model, are statistically different (Table 5.4). These intercepts can be used to calculate the average  $m$  value for Au decahedra,  $-0.99$  eV/nm. This value may seem like a bulk result; it is not. Actually, it would be impossible to obtain it from bulk measurements because of the shape inhomogeneities and the presence of aggregates in the reaction mixture (Figure 2.2).

This shape inhomogeneity can be useful for fundamental research: in this case it allowed the most common by-product in the decahedra synthesis, truncated bitetrahedra, to be studied. Data on five nanoparticles, suggesting lower  $m$ -values (range:  $-0.42$  to  $-0.70$  eV/RIU) and FOM (range: 1.3-2.8) than for decahedra, are presented in Figures 5.2-5.3. This lower sensitivity is

attributed to the positioning of the particle on the substrate and the tip geometry. Indeed, decahedra sit at an angle with respect to the substrate, fully exposing three equatorial tips and a pyramid apex to the surrounding medium. Also, the decahedra obtained were very sharp, with well-defined facets and corners, allowing a high field intensity at all the exposed tips. However, these are qualitative observations, and due to the small data set on truncated bitetrahedra, no statistical analysis was performed.

Table 5.2. Fit parameters for the plasmon energy dependence on plasmon length for various refractive index environments (unconstrained slopes, analysis of covariance).

Glycerol %	Slope (meV/nm)	p-value	Intercept (eV)	p-value
0 %, air	-3.1(3)	0.0042	2.30(3)	0.42
0 %, water	-4.1(3)	0.20	2.39(3)	0.0001
8 %	-3.9(3)	0.60	2.29(3)	0.68
16 %	-3.9(3)	0.60	2.28(3)	0.87
25 %	-3.9(3)	0.83	2.26(3)	0.66
40 %	-3.8(3)	0.98	2.24(3)	0.27
50 %	-3.9(3)	0.78	2.24(3)	0.24
80 %	-3.8(3)	0.93	2.20(3)	0.044

Note: standard error on last digit in parentheses.

Table 5.3. Fit parameters for the plasmon energy dependence on plasmon length for various refractive index environments, excluding air (unconstrained slopes, analysis of covariance).

Glycerol %	Slope (meV/nm)	p-value	Intercept (eV)	p-value
0 %, water	-4.1(3)	0.40	2.39(3)	0.0001
8 %	-3.9(3)	0.89	2.29(3)	0.61
16 %	-3.9(3)	0.88	2.28(3)	0.79
25 %	-3.9(3)	0.85	2.26(3)	0.76
40 %	-3.8(3)	0.73	2.24(3)	0.34
50 %	-3.9(3)	0.93	2.23(3)	0.29
80 %	-3.8(3)	0.68	2.20(4)	0.063

Note: standard error on last digit in parentheses.

Table 5.4. Fit parameters for the plasmon energy dependence on plasmon length for various refractive index environments, excluding air (unconstrained slopes, analysis of covariance).

Glycerol %	Slope (meV/nm)	p-value	Intercept (eV)	p-value
0 %, water	-3.90(11)	0	2.362(4)	0
8 %			2.284(4)	0.008
16 %			2.276(4)	0.39
25 %			2.268(4)	0.38
40 %			2.252(4)	0
50 %			2.241(4)	0
80 %			2.220(5)	0

Note: standard error on last digit(s) in parentheses.

Single particle refractive index sensitivity measurements on Ag colloids were also performed, on the same type of substrate used for the decahedra studies ( $\text{Si}_3\text{N}_4$  TEMVu). Difficulties due to their very low scattering intensity, which was worsened by the use of a 50 X objective (instead of the usual 100 X, see Chapter 2 for RIS measurements details), and possible oxidation rendered the results unusable. Most particles investigated were large aggregates, with complex spectra showing little trend in the different refractive index environments. Typical results are presented in Figure 5.4, for completeness.

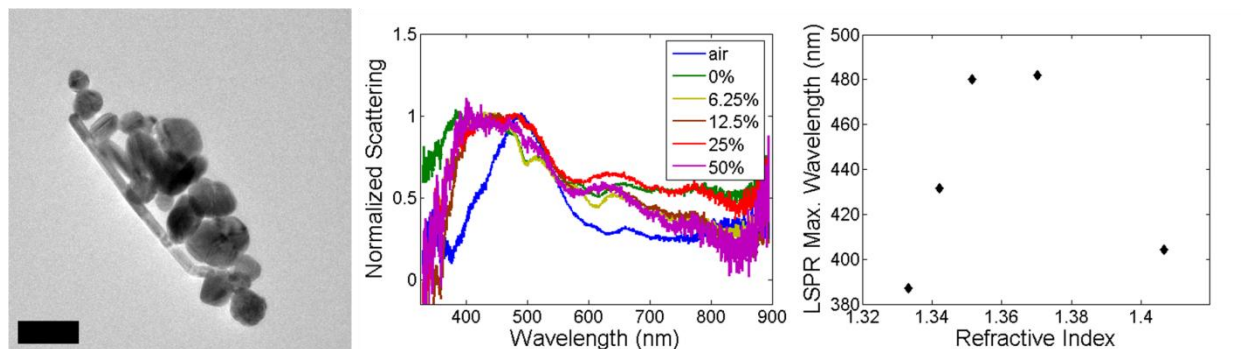


Figure 5.4. Correlated RIS/TEM measurement of Ag nanoparticles aggregates. Left: TEM image. Scalebar, 100 nm. Middle: spectra acquired in various concentrations of aqueous glycerol. Right: peak position as a function of refractive index.

#### 5.1.1.2 Uncorrelated Single Particle Refractive Index Sensitivity Measurements of Au Decahedra

To obtain more information on the refractive index sensitivity of decahedra over a large size range, measurements were performed on glass coverslips and were not correlated with structural analysis. Other structures and aggregates were present in the reaction mixture, albeit they were identified by their spectral signature and rejected from the data set. The dipolar resonance of very large decahedra was typically, once immersed in water, outside the range of the detector. In such cases, the RIS of the dominant quadrupole peak was recorded. Figure 5.5 reports the refractive index sensitivity of single Au decahedra as a function of their plasmon energy in water. A statistically significant relationship between RIS and LSPR energy is present, in contrast with the lack of relationship in Section 5.1.1.1; the latter is due to the large variance in the data, which obscures relationships over small size ranges. Note that there is no sensitivity

difference between the decahedra studied on  $\text{Si}_3\text{N}_4$  (Section 5.1.1.1, dotted circles in Figure 5.5) and those on glass (this section), thus they are both included in Figure 5.5.

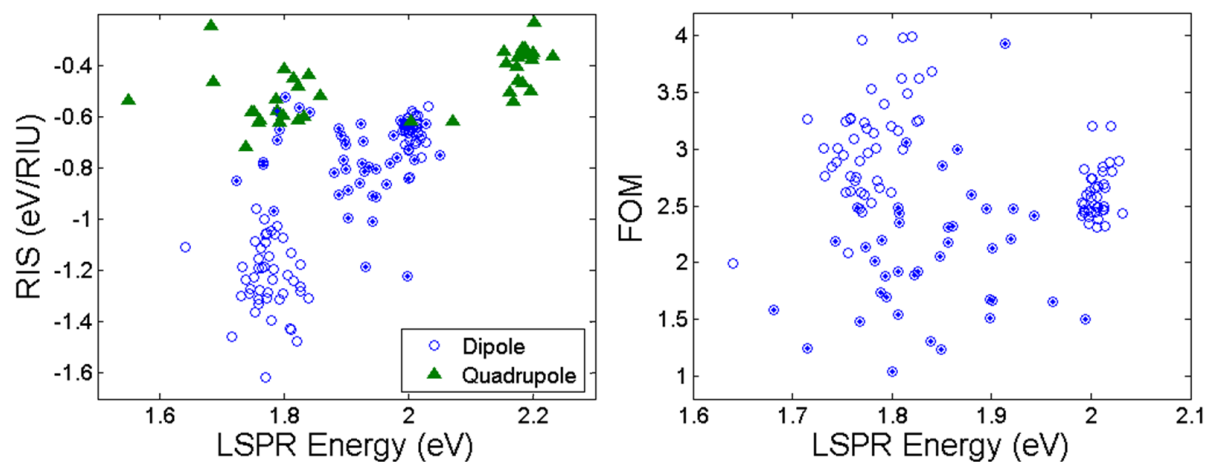


Figure 5.5. Refractive index sensitivity ( $m$ -values) and sensing figures of merit (FOM) of single Au decahedra as a function of the LSPR energy in water. Dotted circles represent the particles studied in Section 5.1.1.1. Left: RIS, note that the majority of the data points in the 2 eV/-0.6 eV/RIU region are from measurements on glass. Right: FOM, defined by  $\text{RIS}/\text{FWHM}$  (both in eV), note the lower FOM for the particles on  $\text{Si}_3\text{N}_4$ .

### 5.1.1.3 Guidelines for Sensor Applications Based on Single Particle Studies

Figure 5.5 clearly shows that decahedra with lower dipolar resonance energies, i.e., larger particles, are more sensitive to the surrounding dielectric environment than smaller ones. However, as previously discussed, the performance of a sensor depends on both the RIS and the FWHM of the plasmon peak. FOM values for single particles, calculated with the FWHM of the peak in water, are thus also reported in Figure 5.5. Interestingly, the suggestion that larger

particles are better sensors (because of their larger  $m$ -values) is not supported by the FOM values. When considering only particles on glass (empty circles), the FOM have similar values for all LSPR energies, with more variance for the larger decahedra. Given this similarity, other factors must be used to choose the ideal sensing platform; in this case the superior size control achieved in the synthesis of small decahedra and their simpler, singly-peaked spectra make them more desirable.

A unexpected feature observed in Figure 5.5 is the consistently lower FOM for particles on  $\text{Si}_3\text{N}_4$ . These particles have similar or lower RIS for a given plasmon energy than those on glass, such that the redshift caused by the substrate is likely the main factor giving rise to such effect. Smaller, less sensitive particles would thus have the same LSPR energy on  $\text{Si}_3\text{N}_4$  as larger, more sensitive particles on glass, yielding higher FOM for the latter. However, corner rounding effects cannot be ruled out, as the decahedra were from different batches and no structural data is available for the particles on glass.

The quadrupolar resonance, which becomes dominant in large particles, has a much lower RIS ( $m \sim -0.5$  eV/RIU, Figure 5.5), but it is much narrower than the dipole by a factor of three; typical FWHM values are around 0.3 eV. Despite this small width, the quadrupole FOM are around unity, a value much smaller than the dipole FOM. Based on this analysis, the quadrupolar resonance is a poor candidate for RI sensors, although its different field distribution may be useful in specialized applications such as surface-enhanced spectroscopy.

### 5.1.2 Alumina Coating on Single Nanoparticles

Au and Ag particles have proven useful as plasmonic sensors in chemical and biological systems;<sup>53-55,61,63,64,66,69,73,207,226</sup> however, their surface chemistry is limited by their metallic composition, and their stability in solvents, air, or oxidizing media can be an issue. An efficient way to provide new surface anchoring capabilities and improve stability is by covering the particle with a thin (few nm) metal oxide layer deposited via atomic layer deposition (ALD), a layer-by-layer, self-limiting growth technique.<sup>70,227,228</sup>

To investigate the effects of an inorganic coating on the optical response of Au decahedra and Ag nanocubes, a series of experiments were performed, focused on characterization of the plasmon energy, refractive index sensitivity, and long-term stability of Al<sub>2</sub>O<sub>3</sub>-coated particles. Control experiments were performed with bare particles.

#### 5.1.2.1 Effect of Alumina Coating on LSPR Energy

##### 5.1.2.1.1 Au Decahedra

Ten cycles of alumina (Al<sub>2</sub>O<sub>3</sub>) with a well-characterized typical thickness of 1.1 nm, was deposited on Au nanoparticles supported on c-flat grids. The ALD process was performed at 100°C; further experimental details are available in Chapter 2. The scattering spectra of single Au decahedra were recorded before and after ALD; their structure was confirmed by TEM analysis. A heat control experiment was performed to characterize the effect of heating the

particles for 5 minutes at 100 °C in nitrogen atmosphere, in the ALD chamber (conditions equivalent to the ALD deposition). No significant shift was observed: the average for 162 Au decahedra is -2 nm, with a standard deviation of 2 nm (Figure 5.6).

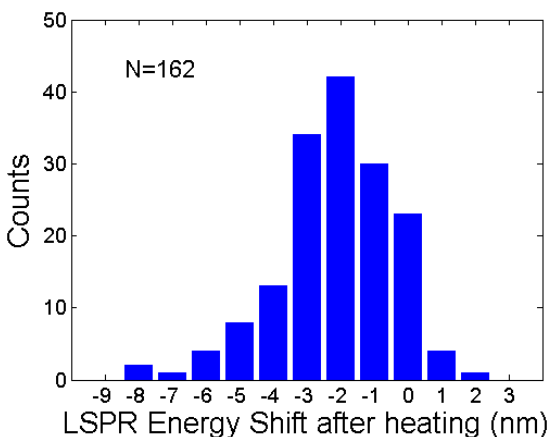


Figure 5.6. Effect of heating Au decahedra for 5 minutes at 100 °C in conditions equivalent to ALD deposition. The average shift is -2 nm, standard deviation of 2 nm.

A thin layer of alumina is expected to redshift the LSPR frequency of nanoparticles because its refractive index is larger than that of air ( $1.57^{70}$  vs.  $1.0003^{229,230}$ ). This shift is indeed observed, as shown for a small fraction of the data in Figure 5.7 (complete data set reported in Table 5.5). The heat control experiments (Figure 5.6) confirm that this shift is due to alumina and not other factors. The average LSPR shift induced by the deposition of 1.1 nm  $\text{Al}_2\text{O}_3$  is 15 nm for small decahedra and 67 nm for larger ones (Table 5.5). The shift difference for different sizes can be attributed to the higher RIS of large particles (studied in Section 5.1.1). However, the same shift was unexpectedly observed for particles with side length  $\sim 65$  and  $\sim 105$  nm, despite their strikingly different RIS (65 nm particles:  $m = -0.65$  eV/RIU,  $N = 39$ , standard deviation = 0.05,

105 nm particles:  $m = -1.22$  eV/RIU,  $N = 46$ , standard deviation = 0.14, data from Section 5.1.1). A possible reason for this effect is the degradation of one of the two reaction mixtures, although ALD and RIS were investigated in the same few months. A different PVP coverage may be responsible, lowering the RIS of the smallest particles while not contributing to the ALD-induced shift. Indeed, it is believed that the highly reactive aluminum precursor (trimethylaluminum) effectively removes the surfactants and start  $\text{Al}_2\text{O}_3$  growth directly on the metal surface.

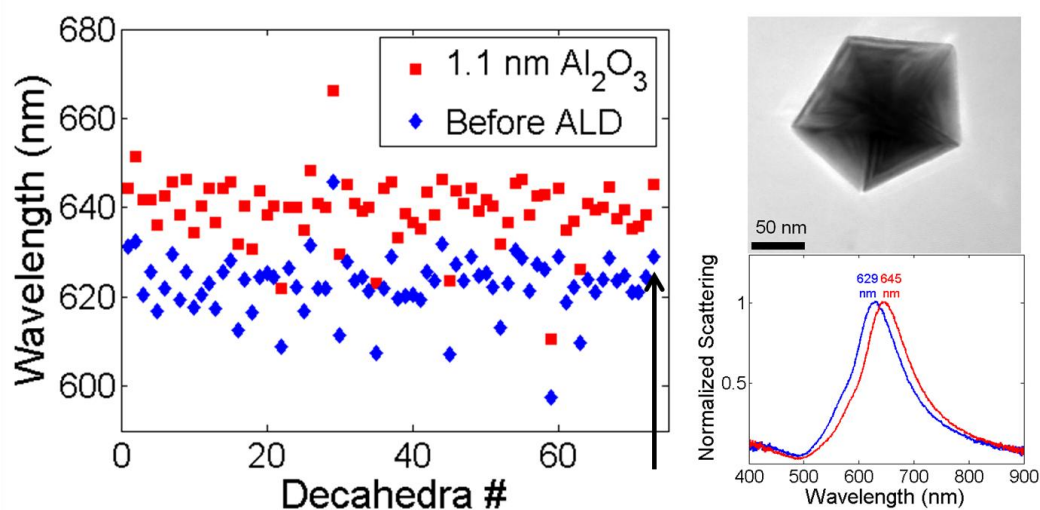


Figure 5.7. Example of the plasmon redshift observed following the deposition of 1.1 nm  $\text{Al}_2\text{O}_3$  on Au decahedra (partial data). The TEM picture and single particle LSPR spectra on the right are marked with the arrow on the left.

Table 5.5. Effect of 10 layers Al<sub>2</sub>O<sub>3</sub> ALD (1.1 nm) on the dipolar plasmon resonance of Au decahedra deposited on c-flat grids.

Approximate Side Length (nm)	N	Pre-ALD peak Energy (nm)	Peak Shift (nm)
65	9	576(5)	15(2)
105	193	628(12)	16(3)
150-210	15	728(19)	67(15)

Note: standard deviation on the last digit(s) in parentheses.

A common equation used in plasmonic sensing relates the plasmon shift ( $\Delta\lambda_{max}$ ) to the particle's refractive index sensitivity ( $m$ ), the change in refractive index induced by the adsorbate (Al<sub>2</sub>O<sub>3</sub> in this case,  $\Delta n$ ), the effective adsorbate layer thickness ( $d$ ), and the plasmon field decay length ( $l_d$ ):

$$\Delta\lambda_{max} = m\Delta n \left[ 1 - e^{-2d/l_d} \right] \quad (5.1)$$

Due to the large data set on the ~105 nm particles, they will be used in the following analysis. The RIS ( $m$ ) for this batch of particles was found to be 510 nm/RIU ( $N = 46$ , standard deviation = 62 nm/RIU). The layer thickness  $d$  is 1.1 nm (10 Al<sub>2</sub>O<sub>3</sub> ALD cycles). This leaves  $\Delta n$  and  $l_d$  as variables. Assuming a  $\Delta n$  of 0.57 RIU (1.57-1.00) yields a rather large  $l_d$  of 39 nm (a value of 5 - 6 nm was previously deduced for nanotriangles<sup>71</sup>). An analogous analysis for the small (65 nm) particles yields  $l_d = 16$  nm; a  $l_d$  value could not be obtained for the large particles due to high variations in both  $\Delta\lambda_{max}$  and RIS. The obvious flaw in this analysis is to assume that  $\Delta n$  is 0.57: the particles are covered with a thin layer (0.5 nm? 1nm?) of PVP (of unknown refractive index), which is replaced by Al<sub>2</sub>O<sub>3</sub> in the ALD chamber. The range of guesses that can be made for the PVP thickness and RI would allow any reasonable value of  $l_d$  to be obtained; however, these would still remain pure guesses. If the shift values for the 65 nm and 105 nm decahedra agreed

better with their RIS, they could provide the 2 data points needed to solve simultaneously for  $l_d$  and  $\Delta n$ ; however, their values are too disparate to allow such analysis.

#### 5.1.2.1.2 Ag Nanocubes

Ag nanocubes are heavily studied for their LSPR sensing and SERS capabilities<sup>52,57,61,92,106,123,147,200-203,231-233</sup> despite being prone to oxidation, a phenomenon limiting their practical applications. A stable and protective layer of metal oxide can be applied to protect plasmonic nanoparticles, a strategy previously demonstrated for, e.g., nanotriangles.<sup>234</sup> The effect of alumina coating on Ag nanocubes was thus studied to demonstrate its feasibility and provide an additional tool for robust device design.

On the first ALD trial, small (50 - 100 nm side length) nanocubes were coated with 10 layers of alumina in a custom-built reactor at 100 °C. The cubes displayed major spectral changes after oxide deposition, beyond the expected shift, accompanied with loss of the high energy peak, as shown in Figure 5.8. Subsequent ALD depositions were performed at 50 °C to avoid any possible oxidation or heat-induced transformations; at this temperature no spectral changes other than a shift were observed (Figure 5.8), and the average particle shape was confirmed to remain cubic.

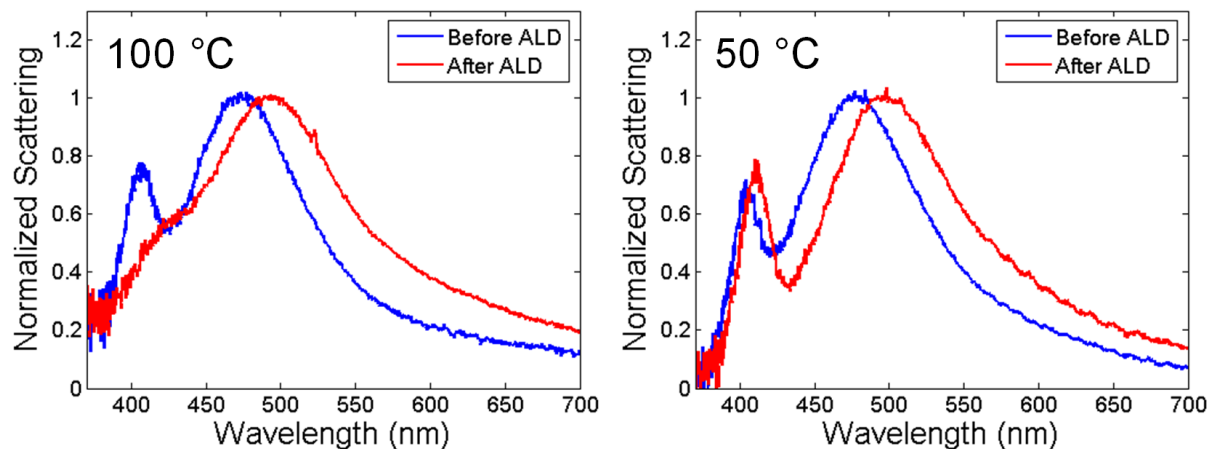


Figure 5.8. Representative spectra of single Ag nanocubes on c-flat grids before and after 10 layers of alumina ALD deposition. Left: deposition performed at 100°C resulting in damage to the particle. Right: spectral shift observed for the deposition performed at 50°C.

A total of 73 single Ag nanocubes were optically characterized before and after coating 1.1 nm  $\text{Al}_2\text{O}_3$  at 50 °C. Cubic morphology was confirmed by TEM analysis. The average (standard deviation in parenthesis) shift for the quadrupolar and dipolar resonance was 8(3) nm and 15(5) nm, respectively. Their pre-ALD resonance energy was 403(4) nm and 473(11) nm, respectively. The quadrupolar resonance sensitivity to the small layer of alumina was thus roughly half of that of the dipolar resonance sensitivity (also half when considered in eV: 0.03 and 0.06 eV). This lower quadrupolar shift disagrees with early calculations,<sup>106</sup> but is supported by recent experimental results on the RIS of cubes,<sup>231</sup> as well as that of other shapes such as prisms<sup>235</sup> and decahedra (Section 5.1.1).

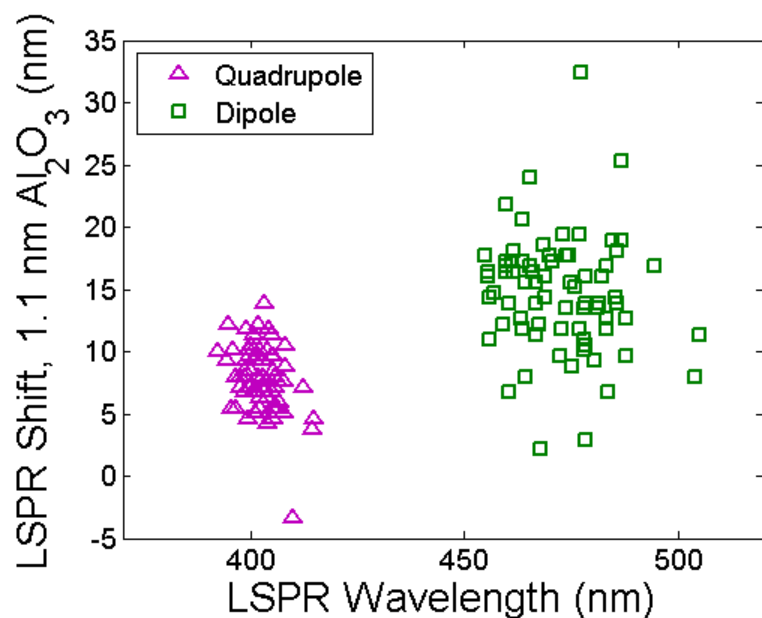


Figure 5.9. Plasmon resonance shift caused by the deposition of 10 cycles (1.1 nm) Al<sub>2</sub>O<sub>3</sub> on ~80 nm side length Ag nanocubes.

As shown in Figure 5.9, there is no correlation with ALD-induced plasmon resonance energy shift and LSPR energy (i.e., cube size) over the narrow range of size studied. However, larger cubes are expected to have larger RIS ( $m$ -values), yielding a larger plasmon shift when coated with a high refractive index material such as alumina.

A representative scattering spectrum from a single Ag cube coated with alumina left in air for a month is presented in Figure 5.10. The cubes appear to fully retain their plasmonic activity when protected with a thin layer of metal oxide; without it, large spectral changes are observed after less than a day for 50-100 nm cubes. Alumina ALD is thus successful at preventing oxidation in the studied Ag nanoparticles, and constitutes a useful addition to the nanoplasmonics toolbox.

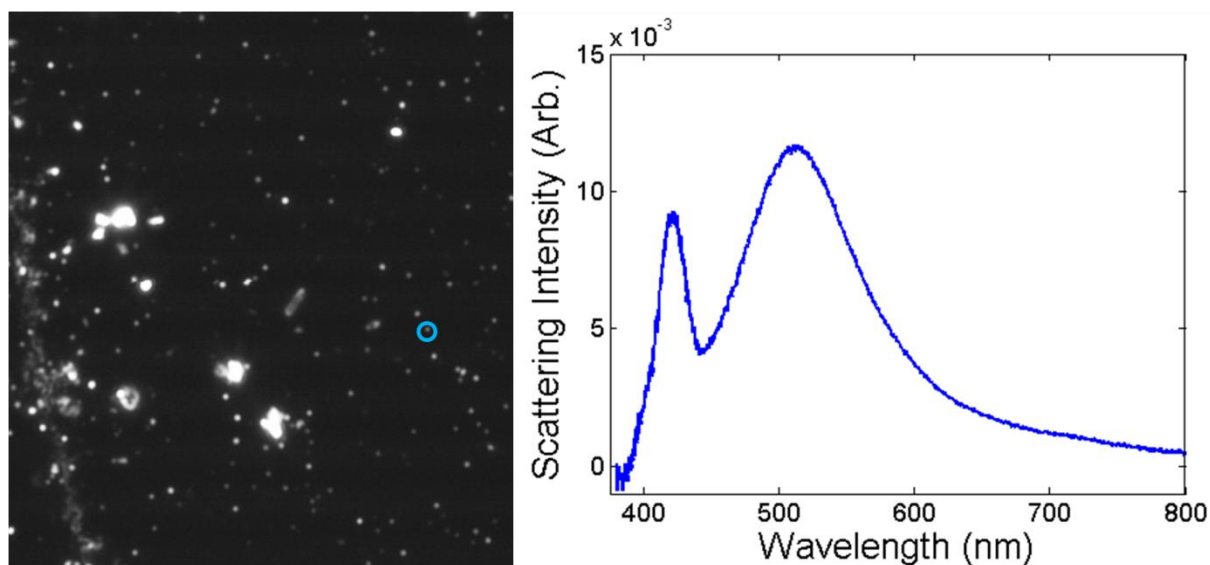


Figure 5.10. Representative spectrum and black and white scattering map of ALD-coated Ag nanocube after 1 month in moist air. The scattering spectrum on the right is from the particle circled on the map shown on the left. Note that the majority particles with the same scattering intensity as the circled one were plasmonically-active single Ag nanocubes.

#### 5.1.2.2 Effect of Alumina Coating on Refractive Index Sensitivity

Plasmonic particles such as Au decahedra and Ag cubes are potential refractive index sensors; the effects of covering them with a thin layer of alumina, to diversify anchoring chemistry and improve stability, has been explored to aid in device development. Further studies assessing the RIS of ALD-coated and bare Au decahedra on glass are presented in this section; all decahedra used were from the same batch. The RIS of coated Au decahedra is significantly lower than for uncoated ones, with average (standard deviation) RIS of  $-0.75(10)$  and  $-1.23(14)$  eV/RIU, respectively (Figure 5.11). The corresponding average FOM decreases from 3.0 to 1.9. The

plasmon energy shift due to ALD deposition is also clearly visible from the horizontal offset between the two groups in the right panel of Figure 5.11; the dipolar resonance FWHM does not change significantly.

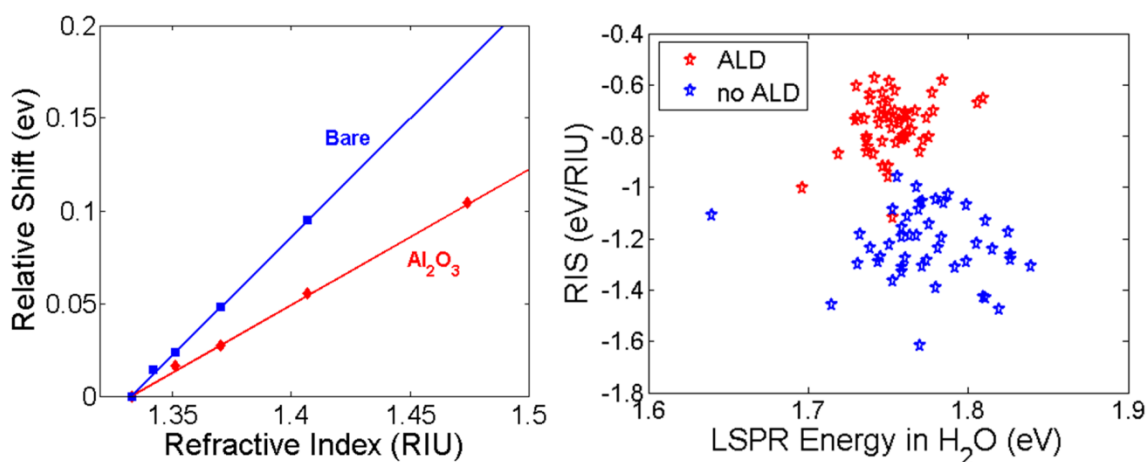


Figure 5.11. Refractive index sensitivity of Au decahedra with and without 1.1 nm Al<sub>2</sub>O<sub>3</sub>. Left: example of the linear relationship between RI and LSPR energy for two single Au decahedra. Right: RIS of 54 (with ALD) and 46 (without ALD) single Au decahedra on glass.

## 5.2 Plasmon-Enabled Sensing: Single Molecule, Single Particle Surface-Enhanced Raman Spectroscopy of Crystal Violet

Single molecule SERS (SMSERS) has been a subject of intense research and debate in the last 15 years,<sup>26,27,184,236-242</sup> during which most SMSERS signals have been observed from random aggregates of Ag colloids. A number of SMSERS studies have been performed in the Van Duyne group<sup>237-239</sup> and are beyond the scope of this thesis. The current contribution to this wide research effort is the large data set of correlated SMSERS/LSPR/HRTEM obtained on SM-active

aggregates. For this work, SMSERS spectra were obtained for crystal violet (CV) or deuterated CV adsorbed on Ag aggregates deposited on standard TEM grids, followed by dark field microscopy and high resolution transmission electron microscopy (as described in Chapter 2).

Representative data from correlated SMSERS/LSPR/TEM are presented in Figure 5.12. One of the two aggregates is a dimer, while the other is composed of at least 10 nanoparticles, demonstrating the structural variety of SMERS-active nanoparticle clusters. This can also be seen in Figure 5.13, where additional SMERS-active TEM images (without spectra) are reported.

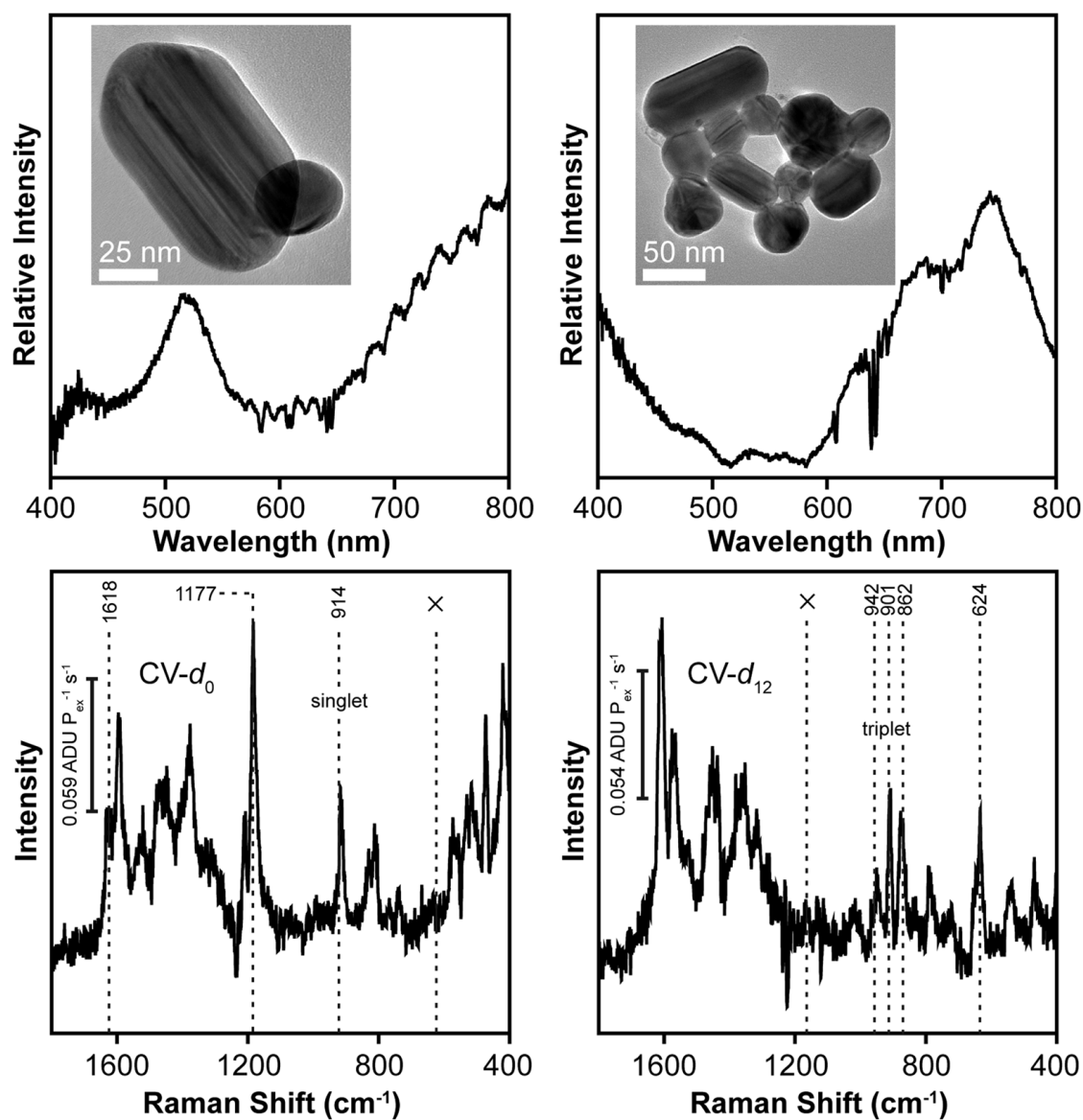


Figure 5.12. Representative data from correlated SMSERS/LSPR/TEM from aggregates of Ag colloids. Top right: TEM image and scattering spectrum of the dimer giving rise to the crystal violet SMSER spectrum in the bottom left panel. Top left: : TEM image and scattering spectrum of the large aggregate giving rise to the deuterated crystal violet SMSER spectrum in the bottom right panel. SMER spectra were obtained with  $75.9 \text{ W/cm}^2$  power, 532 nm laser excitation wavelength, and acquisition time of 30 s.

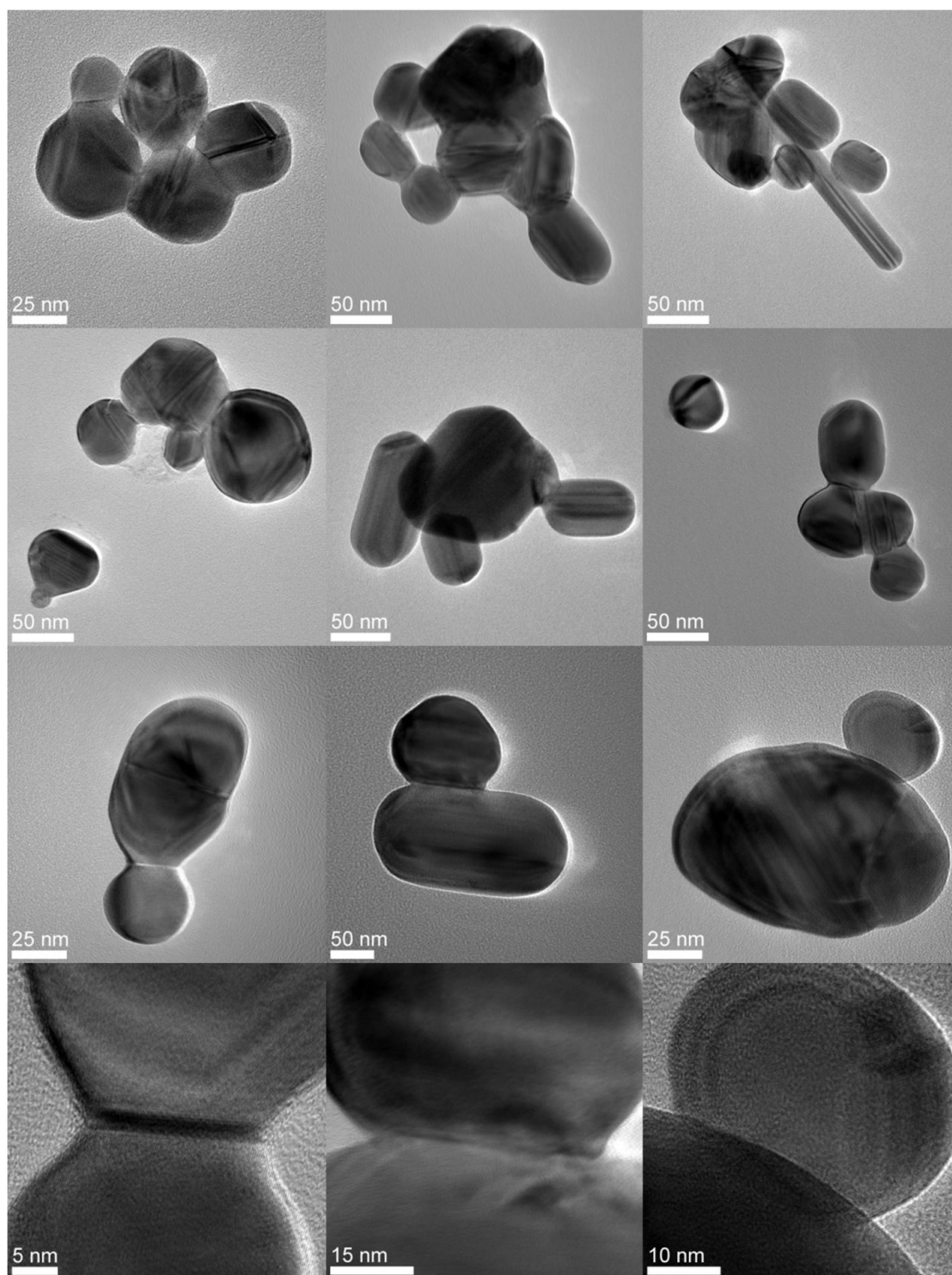


Figure 5.13. SMSERS-active Ag colloid aggregates. The bottom row are high magnification images of the region between nanoparticles for the dimers in the third row.

The data acquired show no evidence of a relationship between aggregate morphology (number of particles and arrangement) and identity of the isotopologue observed in SMERS. Previous reports suggest that all SMERS-active clusters are multiparticle aggregates, necessary to create “hot spots” of high electric field enhancements in the interparticle region. Consistent with those results, SMSERS was not observed from single particles; the smallest aggregates giving rise to SMSERS signal were composed of two particles (four dimers observed out of ~ 40 SMSERS-active aggregates), and all of them were heterodimers, i.e. of disparately sized nanoparticles (> 10 % difference in radius of individual particles). However, it was more common to find SMSERS-active clusters composed of three or more Ag nanoparticles because clusters composed of 3 or more nanoparticles are more common than dimers in the sample studied, and there are on average more molecules in larger aggregate, thus a greater chance of exhibiting SMSERS.

Another interesting finding that could be unraveled by correlated structural measurements is the lack of relationship between SMSERS signal intensity and number of nanoparticles in an SMSERS-active cluster. Additionally, correlating scattering and Raman spectroscopy revealed no correlation between the location, shape, or breadth of the scattering peaks associated with SMSERS-active clusters and SMSERS signal intensity, consistent with previous work.<sup>243</sup>

This first example of a large collection of correlated structure, SMSERS, and scattering spectra provides a tool to study, characterize, and rationally design SERS and SMSERS substrates to be used in chemical and biological sensing.

## CHAPTER 6

### Single Particle Studies of Polarization Effects in Plasmon Resonances

## 6.1 Polarization Phenomena in Localized Surface Plasmon Resonances

Plasmon energy and linewidth can be controlled by changing the size, shape, composition, and environment of a plasmonic nanoparticle (Chapter 3-5 and references herein). Such tuning tools allow optimization of the plasmonic properties for use in sensors and devices such as refractive index sensors,<sup>30,33,53-68,70-73,77,207,208,226,231,235</sup> substrates for surface-enhanced spectroscopies,<sup>26,27,148,184,192-194,201-203,218,219,236-239,241,243,244</sup> and optical signal transducers.<sup>36,39,41-43,49,245</sup> However, plasmonic control is not necessarily simple or straightforward, as an increase in the particle size typically leads to the appearance of higher order modes,<sup>67,82,92,96,139,199</sup> while an increase in anisotropy (particle shape) commonly lifts the degeneracy of the dipolar resonances.<sup>97,126,132,144,179,246</sup> A well-known example of the latter is the presence of a transverse and a longitudinal mode in nanorods<sup>68,179</sup>. Both higher order modes and degeneracy splitting lead to spectral broadening, a undesirable effect in sensing. On the positive side, new modes may be sharper or more sensitive to their surroundings, improving the sensing potential. Additionally, the position and number of modes can be used to spectrally identify nanoparticle shape.<sup>87,100,106</sup> Selective excitation of plasmon modes is achieved using polarized light; excitation profiles are expected to reflect the particle shape and the symmetry of the oscillation modes probed. For example, the longitudinal plasmon mode in a nanorod is excited by light polarized along the long axis of the particle, while the transverse mode is excited by light polarized perpendicular to the long axis.<sup>68,81,209,222</sup> It is thus possible to determine the orientation of single particles or aggregates based on their polarization-dependent spectra. Polarization studies, which reveal mode symmetry and particle anisotropy, cannot typically be performed on ensembles because of

the random particle orientation. It is possible, however, to obtain polarization-dependent spectra from templated or oriented particles.<sup>104</sup> Yet to study the magnitude of the intrinsic polarization-induced scattering intensity variation, mode selectivity, and orientation dependence of the plasmon resonance, single particle studies are arguably a superior approach as they overcome all heterogeneous effects (from size and shape to orientation and composition). Methods to correlate the polarization-dependent spectrum and the structure and orientation of single nanoparticles were developed (details in Chapter 2), and the results are presented in this Chapter. Single particles, bimetallic particles, particle chains, and random aggregates are discussed, followed by the correlated, polarization-dependent scattering and 2-photon photoemission of silver nanocubes. Through this work, polarization effects on individual plasmon modes is quantified as the polarization anisotropy,  $(I_{\max,\lambda} - I_{\min,\lambda})/I_{\text{average},\lambda}$ ,<sup>100</sup> where  $I_{\max,\lambda}$ ,  $I_{\min,\lambda}$ , and  $I_{\text{average},\lambda}$  are the maximum, minimum, and average polarization-dependent peak intensity, respectively.

## 6.2 Plasmon Polarization in Isolated Au Nanostructures

Polarization-dependent scattering spectra of single Au decahedra and truncated bitetrahedra were obtained by adding a polarizer to a typical dark field microscopy setup (details in Chapter 2). Both structures were present in the same reaction mixture, and thus were studied in the same experimental manipulation. Representative spectra and TEM images of Au decahedra and truncated bitetrahedra are presented in Figures 6.1 and 6.2, respectively.

### 6.2.1 Au Decahedra

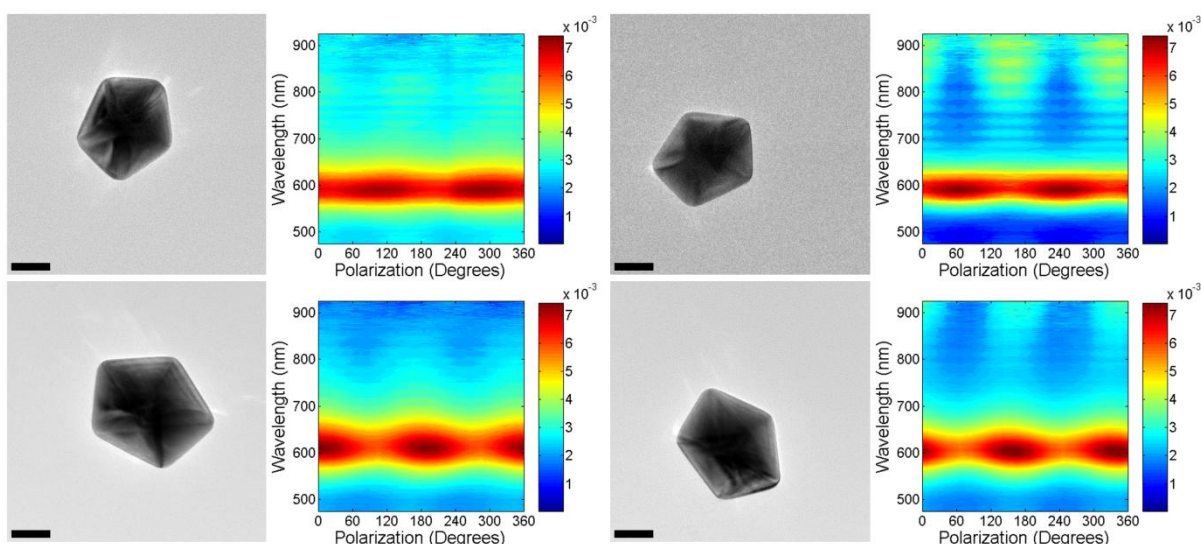


Figure 6.1 Representative correlated polarization-dependent scattering spectra and TEM images of single Au decahedra. Clockwise from top left, the polarization anisotropy is 17, 15, 35, and 29 %. The average polarization anisotropy for the nine decahedra measured was 21 %. The vertical axis in the picture corresponds to  $0^\circ$  polarization. Scalebars, 50 nm.

Computational results on the effects of the angle of incidence on the plasmonic behavior of single decahedra have been published previously,<sup>82</sup> although the calculation geometry and the current experimental setup are not equivalent. Rodríguez-Fernández *et al.*<sup>82</sup> calculated the spectral variation, at constant polarization, for angles of incidence starting from apex to apex and ending along the plane of the pentagonal base (from corner to edge). Their fixed polarization was perpendicular to one of the pentagonal base edge. The current experiments differ in that they have a constant range of simultaneous angles of incidence and a variable polarization. The former is defined by the particle tilt,  $35.3^\circ$  from the surface (laying flat on a  $\{111\}$  face), and the

orientation of the geometry of illumination (the hollow cone of light formed by the dark field condenser is oriented  $\sim 60^\circ$  from the surface normal). Simultaneous angles of incidence ranging from  $(60-35)$  to  $(60+35)^\circ$  (from the apex-apex orientation) are thus formed, unlike the single angle of incidence in the calculations of Rodríguez-Fernández *et al.*. Despite such differences, a  $180^\circ$ -period (peak repeats twice within  $360^\circ$ ) was observed in both cases, as is expected for a uniaxial dipolar resonance (as in nanorods). The dipolar plasmon resonance of the nine decahedra studied peaked around 600 nm (average: 608 nm, min: 591 nm, max: 633 nm, st. dev.: 15 nm); this peak resonance energy was very stable against polarization changes, with an average maximum energy difference ( $\lambda_{\max}-\lambda_{\min}$ ) of 3.4 nm (min: 1.8 nm, max: 6.7 nm, st. dev.: 1.54 nm, determined by numerical maximum value finding in MATLAB). A total of nine decahedra were studied, yielding a non negligible polarization anisotropy average of 21% (min: 10 %, max: 35 %, st. dev.: 7 %). This is in quite good agreement with boundary element method (BEM) calculations performed by Rodríguez-Fernández *et al.*<sup>82</sup>

As for many other plasmonic attributes, size is expected to contribute to the degree of polarization anisotropy, with larger polarization anisotropy associated with increased decahedra size;<sup>82</sup> this effect was not observed in the current work due to the limited range of sizes studied. An interesting future experiment involves studying the size-dependence of polarization anisotropy. Smaller step sizes ( $10^\circ$  or  $5^\circ$ , compared to the current  $20^\circ$ ) are not expected to reveal different patterns, but likely would reduce the polarization anisotropy variation between particles of comparable sizes.

### 6.1.2 Au Truncated Bitetrahedra

Truncated bitetrahedra were also studied with correlated pol-LSPR/TEM. Two dipolar modes have been proposed for a similar structure, flat nanoprisms: one oscillating from edge to apex, and one from apex to apex.<sup>100,149</sup> In this context, a peak corresponding to the edge to apex mode should appear every  $120^\circ$ , and a peak corresponding to the apex to apex mode should appear every  $120^\circ$ , offset from the other mode by  $60^\circ$ . A total of 6 peaks should thus be observed, one every  $60^\circ$ . Given that peaks are not excited solely when the polarization is perfectly matched (but rather over a range), some overlap is expected. In addition, calculations<sup>149,214</sup> predict a rather small difference in energy between such modes, further reducing the expected polarization dependence.

The four truncated bitetrahedra studied (Figure 6.2) indeed have negligible peak wavelength fluctuations, with all the peaks for a given particle within 2 nm of each other for all polarizations. The polarization anisotropies is also very small: 3.5, 5.7, 6.1, and 4.3 %. This lack of intensity variation, unlike what is expected for thin triangular platelets, may be due to the effects of the (undetermined) thickness of the particles and the tilted illumination geometry.

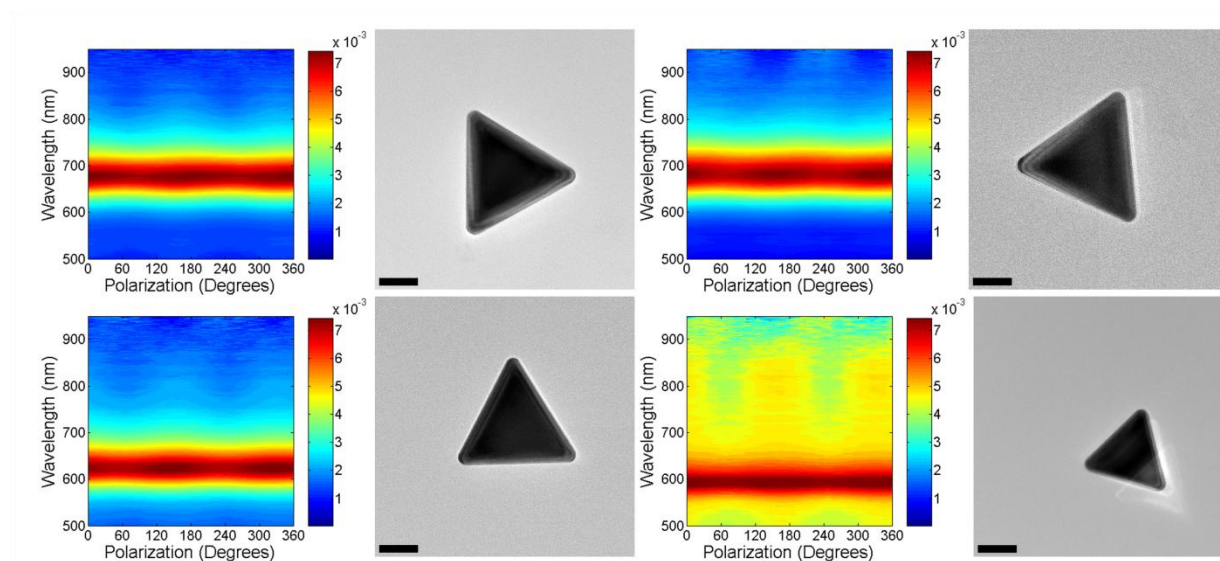


Figure 6.2 Correlated polarization-dependent scattering spectra and TEM images for the four single Au truncated bitetrahedra observed. Clockwise from top left, the polarization anisotropy is 3.5, 5.7, 4.3, and 6.7 %. The presence of a higher background signal for the particle in the lower right corner is likely due to the proximity of a strong scatterer (grid bar, small dust particle, or large nanoparticle aggregate). Scalebars, 50 nm.

Thin triangular platelets being a well-researched shape,<sup>100,103,143,149,216,247-249</sup> a number of contradicting results are present in the literature. Unlike the previously discussed predictions, the work of Schubert *et al.*<sup>100</sup> suggests that the polarization dependent spectrum should have two peaks of different energy repeating every 180°, offset by 60° from one another. This finding seems to not match the 3-fold symmetry of the particle, and no such pattern was observed, either in intensity or energy, in the current experiments on truncated bitetrahedra.

## 6.2 Plasmon Polarization in Single Bimetallic Nanostructures: Hiding Anisotropy

Polarization dependence of anisotropic nanoparticles has been studied here and elsewhere,<sup>82,100</sup> and is known to acutely depend on the symmetry of the particle shape and aggregate geometry. Recently, an interesting structure was synthesized: gold rods encapsulated in a quasi-spherical silver shell.<sup>141</sup> Such structure is similar to the well-known silica-encapsulated Au nanorods.<sup>120,250</sup> Silica is a dielectric material not participating in the plasmon oscillation, and the result of the encapsulation is a simple red-shift of the LSPR frequency due to the increased refractive index around the rod; the scattering signal retains its polarization-dependent behavior. For Ag encapsulation, whether the plasmon scattering remains anisotropic is an interesting question that was approached in this work.

The bulk solution LSPR spectrum of Au rods @ Ag shells, initially published alongside the synthesis,<sup>141</sup> shows one strong plasmon peak located between 400 and 500 nm, significantly blue-shifted from the initial uncoated rod longitudinal peak at 800 - 900 nm. Additionally, the two modes, longitudinal and transverse, slowly merge into a single intense mode as the particle becomes isotropically covered with the Ag shell. However, as discussed above, no polarization information could be obtained from such ensemble measurements.

### 6.2.1 Correlated pol-LSPR/TEM of Au rods @ Ag shells

To elucidate whether anisotropy can be hidden by an isotropic shell of plasmonic material, single Au rods @ Ag shell synthesized according to ref.<sup>141</sup> were studied using correlated pol-

LSPR/TEM using the instrumentation available at the University of Melbourne. The difference in contrast between Ag and Au in the transmission electron microscope allows the identification of the Au rod orientation within the Ag shell, as can be seen in Figures 6.3-6.4. The solution spectrum is presented in Figure 6.3; typical single particle spectra and TEM pictures are reported in Figure 6.4.

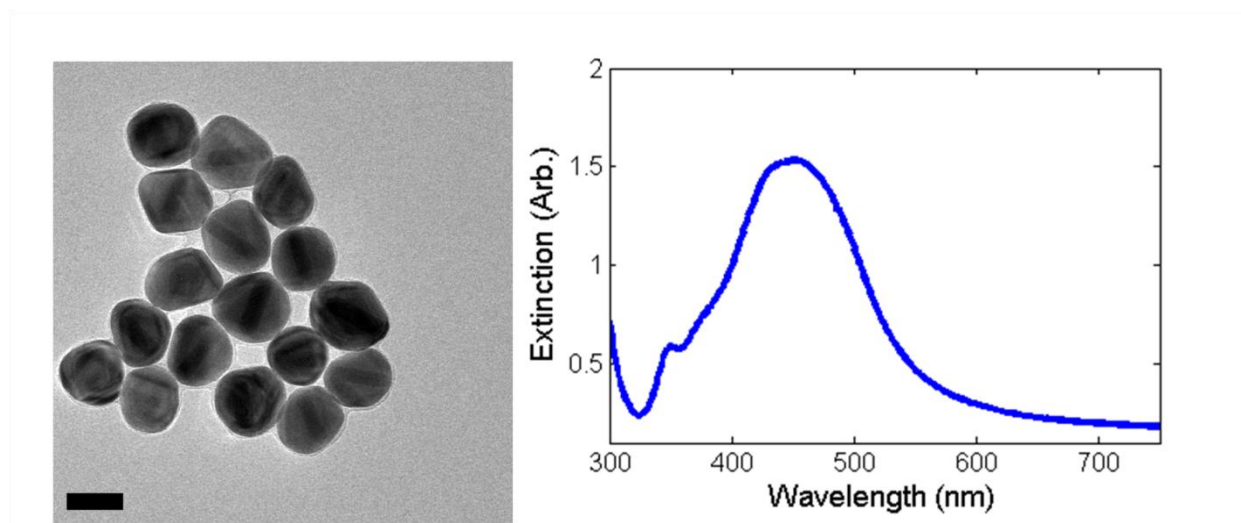


Figure 6.3. Representative TEM image (left) and solution spectrum (right) for Au rods @ Ag shell particles. Scalebar, 50 nm.

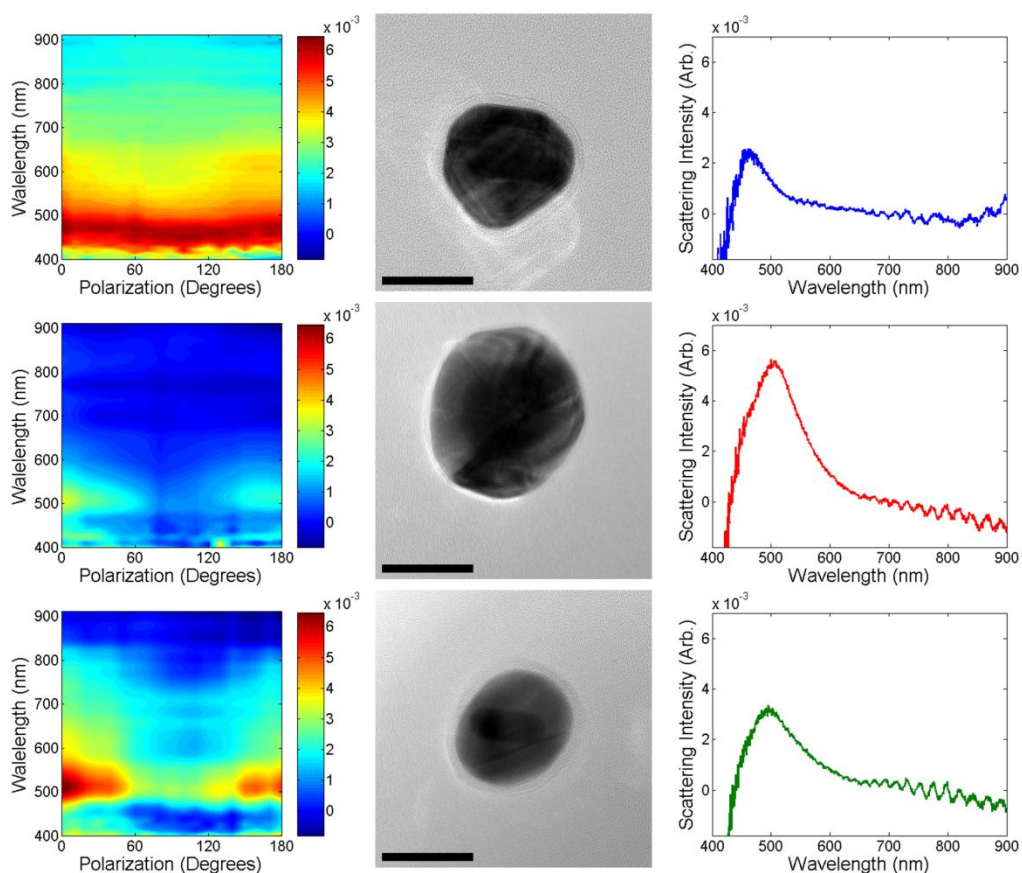


Figure 6.4. Representative single particle correlated pol-LSPR/TEM results on Au rods @ Ag shell deposited on Formvar substrate. The polarization angle in the pol-LSPR plots on the left are aligned with the TEM images in the middle, with the vertical axis corresponding to  $0^\circ$ . The polarization anisotropy is, from top to bottom, 20, 83, and 133 %. The LSPR spectra on the left were obtained with unpolarized light. Scalebar, 50 nm.

Several experimental difficulties were encountered while trying to characterize single Ag rods @ Au shell particles. The first trials, aiming to correlate the polarization anisotropy, LSPR frequency, rod orientation, and particle size, were performed on standard Formvar-coated TEM grids. However, the scattering intensity of the single particles was very low: visual alignment in

the optical microscope was rather difficult. Instrumental limitations further complicated this approach: the numerical aperture of the 60X objective used was such that an intense background from the grid scattering was collected alongside the particle signal, and the detector quantum efficiency in the blue region was low, adding to the noise. Several reasonable quality single particle spectra and TEM images were successfully acquired, yet not enough polarization data could be obtained to prove or disprove the presence of polarization anisotropy. In Figure 6.4, for example, no anisotropy is apparent for the top particle (rod aligned  $90^\circ$ ), while a strong anisotropy is surprisingly observed perpendicular to the rod axis for the middle particle. The bottom particle also shows anisotropy, although  $90^\circ$  from what would be expected from the rod orientation. Such inconclusive results prompted the acquisition of more statistics through simpler experiments.

### 6.2.2 Single Particle pol-LSPR of Au rods @ Ag shells

In order to reduce the background noise, particles were deposited and dried on glass coverslips and an oil immersion 100 X objective was borrowed from another group and used. Structural correlation was forgone, but single particles could be identified by eye because of their dim blue color. This visual identification was confirmed by comparing the spectra of known single particles with the spectra of particles obtained on glass. This approach allowed the collection of 19 single particle polarization spectra, an example of which is presented in Figure 6.5. The average polarization anisotropy of the single particles is 12.8 % with a standard deviation of 7 % (Figure 6.5). This small anisotropy (given the anisotropy of other types of particles and the

instrumental limitations) suggest that Au rods are indeed very well hidden inside the Au shell, as suggested by the presence of a plasmon resonance in the blue region.

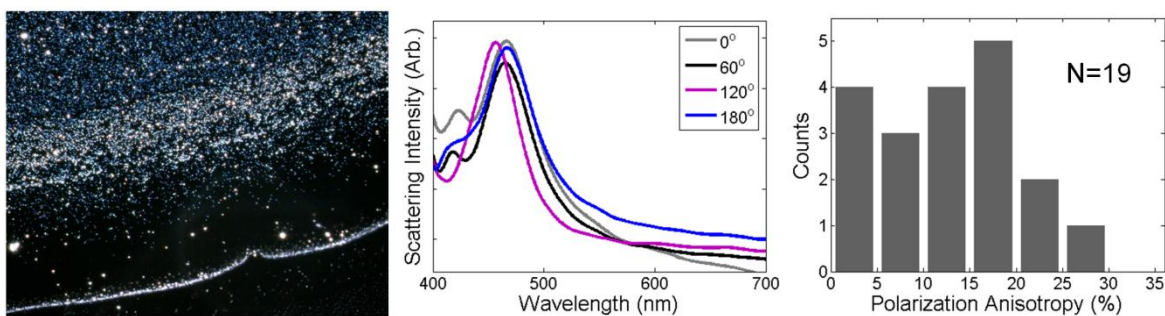


Figure 6.5. Plasmon polarization of single Au rods @ Ag shell nanoparticles. Left: particles on glass, where the dim blue spots on the bottom of the image are single particles. Middle: example of pol-LSPR data. Right: polarization anisotropy distribution.

### 6.3 Plasmon Polarization in Chains and Aggregates of Spheroid Au Particles

As a proof-of-concept for correlated SEM/LSPR/TEM of rare structures, the optical response of random particle chains deposited on standard Formvar/carbon TEM grids were studied. Au nanoparticles of approximately spherical shape with  $\sim 50$  nm diameter were deposited on a standard Formvar/carbon TEM grid. The particles were identified using low magnification SEM, which has been shown to minimally affect the plasmon resonance (Chapter 2). Scattering spectra were then obtained with dark field microscopy (LSPR and pol-LSPR), followed by detailed structural characterization in a TEM. Note that the scattering of single monomers, at  $\sim 540$  nm, was typically too weak to be observed with the current instrument. These experiments were performed at the University of Melbourne.

### 6.3.1 Plasmon Polarization in Dimers of Spheroid Au Particles

Five dimers were observed; they have, as expected, two main resonances (Figure 6.6).<sup>251,252</sup> The lowest energy resonance is red-shifted with respect to the monomer resonance, and represents the oscillation along the interparticle axis. Polarization experiments on similar Ag structures confirmed this assignment (Chapter 2). The second resonance represents oscillation perpendicular to the interparticle axis and has a higher energy due to the weaker interparticle coupling.

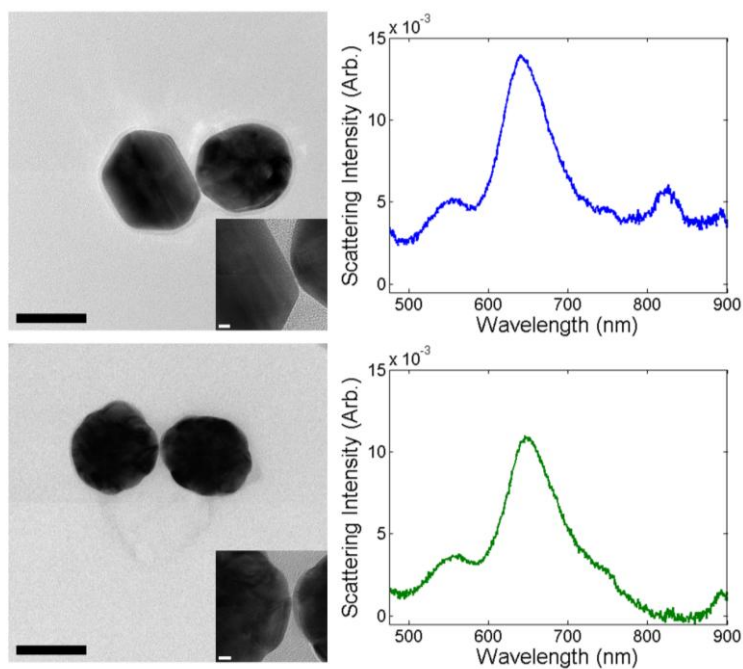


Figure 6.6. Example of correlated LSPR/TEM on Au dimers. Left: TEM images. Right: scattering spectra showing the two main plasmon resonances. Scalebars for the images and inserts, 50 and 5 nm, respectively

## 6.3.1 Plasmon Polarization in Aggregates of 3 or More Spheroid Au Particles

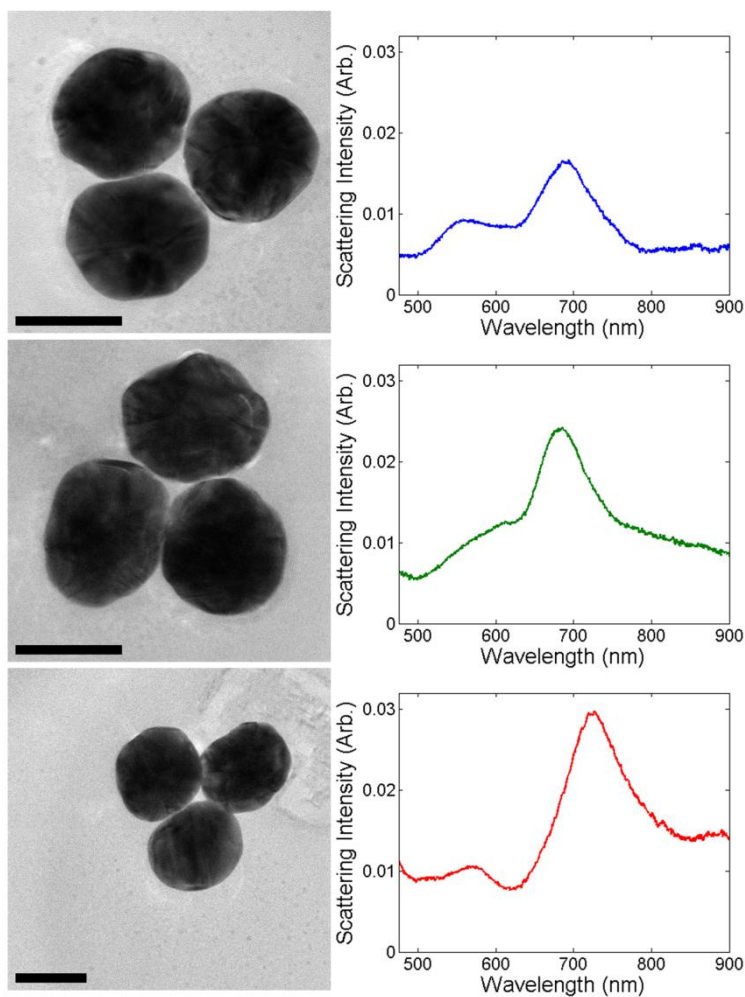


Figure 6.7. Plasmonic properties of three of the five Au T-shaped trimers studied by SEM/LSPR/TEM. An intense plasmon resonance slightly red-shifted from the dimer resonance, and a broad peak located close to the transverse mode in dimer structures can be seen. Scalebars, 50 nm.

Two types of trimers exist, linear and T-shaped aggregates; both were observed. Typical T-shaped trimer spectra and electron micrographs are reported in Figure 6.7. Two bands are present in the spectra of T-shaped trimers: the most intense peak at an energy slightly red-shifted from the dimer resonance, and a broader, less intense resonance located close to the transverse mode of the dimers ( $\sim 550$  nm, see Figure 6.6). No formal peak assignment was done because no polarization experiments were performed on those structures.

The linear trimers have various degree of interparticle spacing, making them interesting to study interparticle coupling in structures other than dimers. A strong peak is present in all the trimer spectra (Figure 6.8). The dimer + particle structure also has another weaker peak at higher energy. The most intense peak significantly redshifts when monomers are brought closer together: the lowest energy resonance decreases from 3 separated monomer (570 nm) to a monomer and a dimer (705 nm) to a nearly touching linear trimer (785 and 810 nm). Based on the polarization experiments summarized in Figure 6.9, this main peak was associated with an oscillation along the interparticle axis. The higher energy peak in the dimer + particle structure cannot be attributed to the transverse dimer mode as it does not have the expected  $90^\circ$  offset from the main resonance; it is likely a modified transverse mode that also involves the adjacent monomer. The magnitude of the polarization anisotropy for the separated monomers is non-negligible, 52 %, as expected for moderately interacting particles (interparticle distance  $\sim$  particle diameter). Dimers and trimers have much stronger polarization anisotropy, 155 % and 76 % for the chains in Figure 6.9. A linear quadramer was also observed, with a plasmon energy of 830 nm and a polarization anisotropy of 157 %; its constituent monomers were smaller than average (Figure 6.9). As expected, the polarization anisotropy increase with the number of

particles in (i.e. the length of) a near-touching linear aggregate. However, to properly compare such structures, monomers of a similar size need to be examined, which is not the case for the limited number of results presented here. Additionally, structural instabilities in the mounting of the polarizer at the University of Melbourne make quantitative analysis difficult.

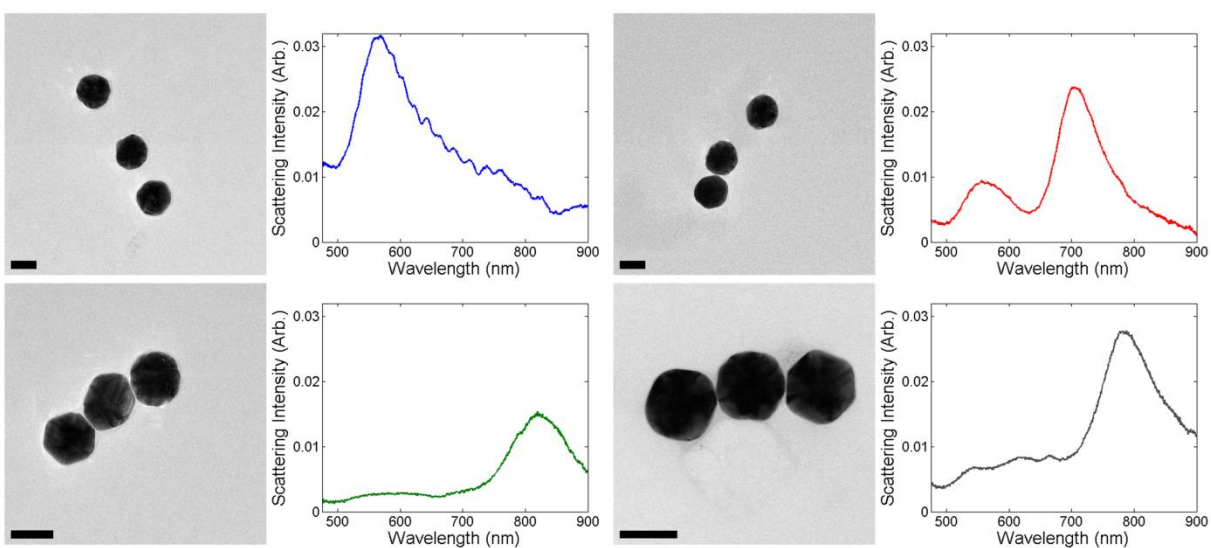


Figure 6.8 Plasmonic properties of Au linear trimers with various interparticle separation studied by SEM/LSPR/TEM. Scalebars, 50 nm.

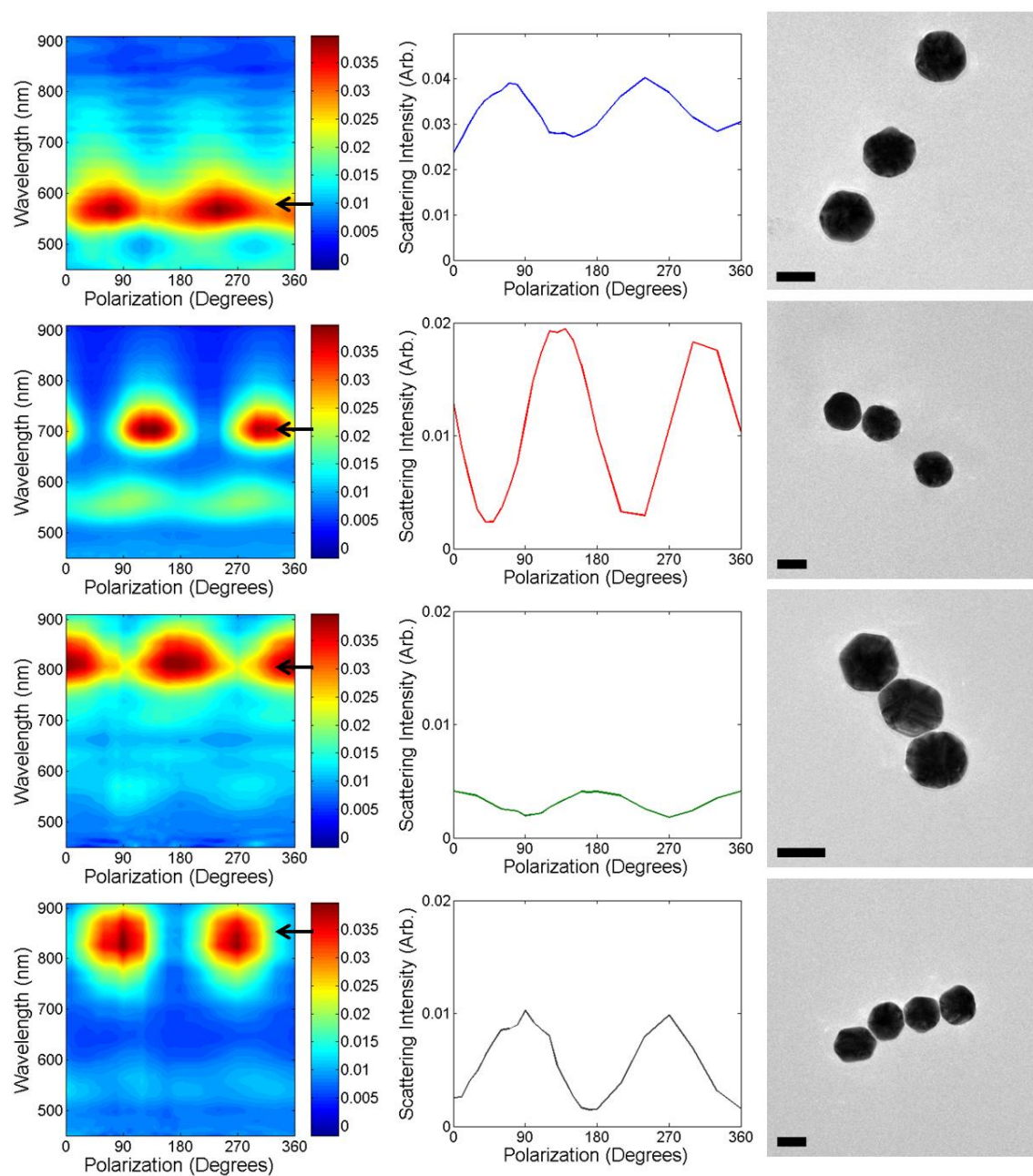


Figure 6.9 Polarization dependence of the scattering of linear Au trimers and quadrumer. The particles were rotated to match the grid orientation. The polarization anisotropy for the main mode is, from top to bottom, 52, 155, 76, and 157 %. Scalebars, 50 nm.

## 6.4 Plasmon Polarization in Aggregates of Sharp Au Particles

Nanostructure aggregates form spontaneously on substrates upon drying. While such structures were not the subject of this study, the results are nonetheless interesting and confirm the efficacy of the pol-LSPR setup used at Northwestern University. In all the observed aggregates, the most intense mode is the lowest energy oscillation, along the longest axis of the aggregate.

### 6.4.1 Plasmon Polarization in Dimers of Sharp Au Particles

In the case of a dimer, the dominant mode along the interparticle axis is typically accompanied by a weaker mode at higher energy, which has a polarization perpendicular to the interparticle axis. Such modes do repeat every  $180^\circ$  as expected.<sup>89</sup> Figure 6.10 shows the polarization dependence of the LSPR spectrum as well as TEM images of small aggregates.

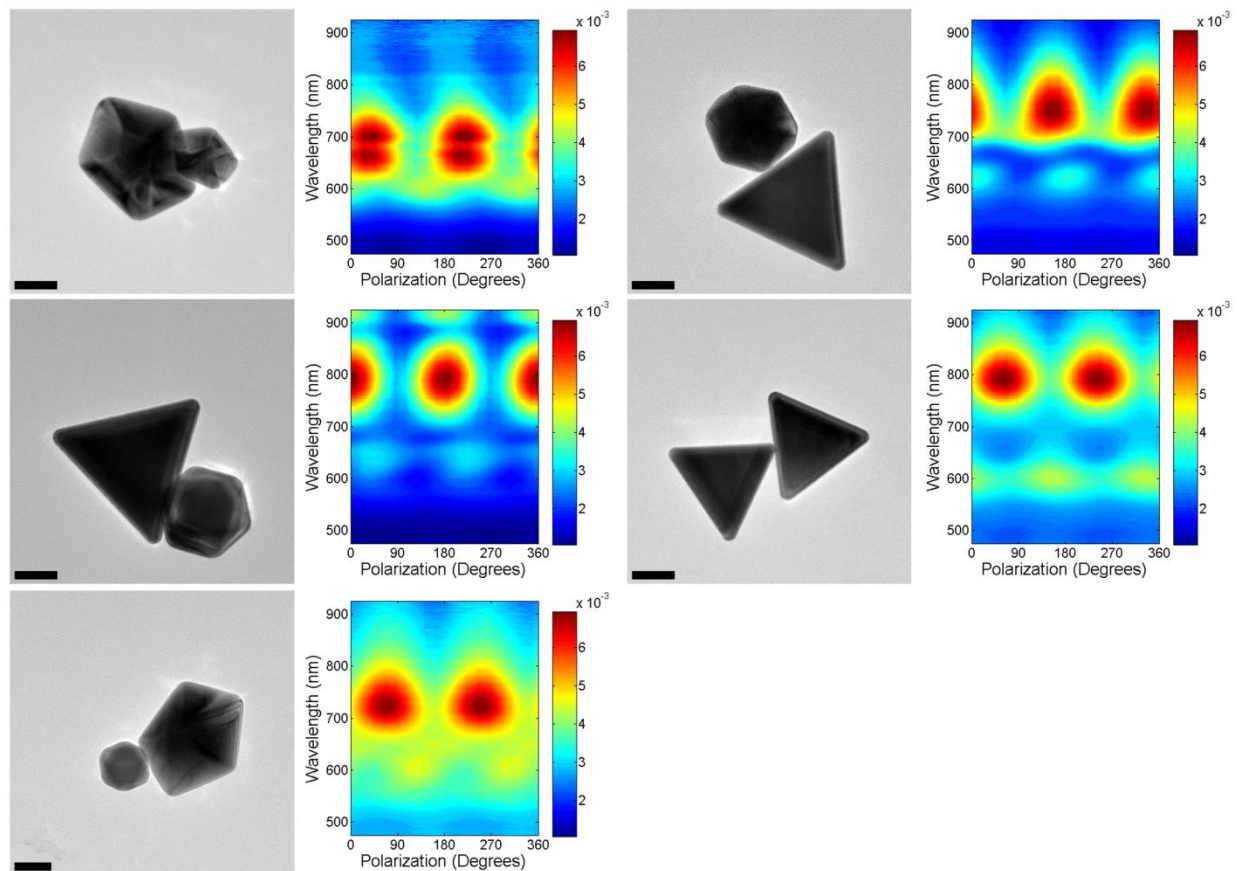


Figure 6.10 Scattering intensity dependence on incoming light polarization for Au dimer structures. The highest scattering intensity (deep red) is obtained when the polarization is approximately along the interparticle axis. Zero degree corresponds to the vertical axis. Scalebars, 50 nm.

## 6.4.2 Plasmon Polarization in Aggregates of 3 or More Sharp Au Particles

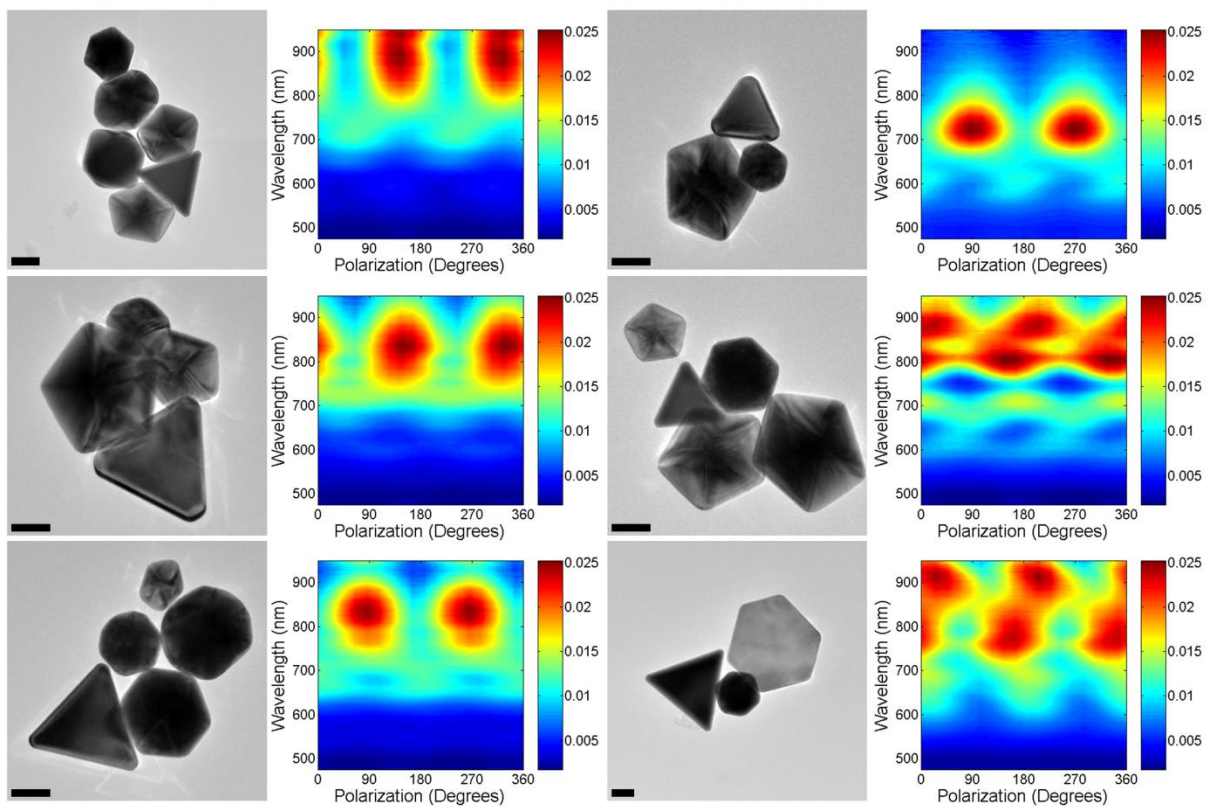


Figure 6.11 Scattering intensity dependence on incoming light polarization for Au nanoparticle aggregates. Note that the lowest energy mode present is along the interparticle axis. Scalebars, 50 nm.

## 6.5 Plasmon Polarization in Ag and Au Nanostructures: Comparison of one-Photon and Multiphoton Techniques Reveals Photoemission Mechanism

Single particle studies are a powerful tool to describe and quantify the effect of various structural factors on their optical response, in particular plasmon energy, width, and polarization-dependence. As discussed in Chapter 2, plasmon resonances lead to an enhancement of the electric field near the surface of the particle, a phenomenon at the basis of surface enhanced spectroscopies and other applications.<sup>29,184,192-194,202,218,236,237,239,243</sup> In individual nanoparticles near-field enhancement factors as much as  $|E|/|E_0| = 10^2$  can be observed, where  $|E|$  is the field intensity around the particle, and  $|E_0|$  is the applied field intensity. Values as high as  $|E|/|E_0| = 10^3$  can be attained in the interparticle junctions of specially designed nanostructures.<sup>253,254</sup>

Recently, the large local electric field enhancements provided by plasmonic phenomena have been proposed to underlie more exotic processes such as the generation of high kinetic energy (up to keV) electrons and THz radiation upon ultrafast laser illumination of metallic surfaces and metallic nanostructures, respectively.<sup>255,256</sup> In such cases the observed phenomena are necessarily accompanied by electron emission - a process poorly understood for metallic nanoparticles and nanostructures irradiated with ultrafast laser pulses at a photon energy ( $E_{ph}$ ) below the material work function ( $\Phi$ ). In particular, the exact role of the localized surface plasmon in augmenting the electron emission is presently unclear.<sup>257-263</sup>

### 6.5.1 Possible Photoemission Mechanisms

Two families of mechanisms are often invoked to explain electron emission from metallic surfaces upon ultrafast excitation with sub-work function photon energies (i.e.,  $E_{\text{ph}} < \Phi$ ). In thermionic emission models,<sup>264,265</sup> the laser momentarily heats up the conduction electrons, thus promoting a fraction of electrons in the Fermi-Dirac distribution above the metal work function, whereupon they are emitted. Alternatively, the electron emission can be described in terms of a multiphoton photoelectric effect, where a particular electron is emitted after absorbing  $n > \Phi/E_{\text{ph}}$  photons either simultaneously (i.e., a coherent/direct process) or sequentially (i.e., an incoherent/indirect process).<sup>266-270</sup>

The experimentally observed enhancement of electron emission from metallic nanoparticles upon resonant excitation of a plasmon can in principle be rationalized via either thermionic or multiphoton mechanism. For example, in thermionic emission models the plasmon could facilitate incident light absorption due to an increased particle linear absorption cross-section  $\sigma_{\text{ABS}}$ , thus leading to an increased electron gas temperature, and consequently an enhancement in thermionic emissivity. On the other hand, in multiphoton photoelectron emission (MPPE) models, the build-up of coherent oscillations could lead to near-field enhancement ( $|E|/|E_0|$ ) of the incident electric field and thus result in increased photoelectron yields.

### 6.5.2 Experimental Approach to Determine the Photoemission Mechanism in Ag Nanocubes

In the current work, we have devised an experiment that distinguishes between the two possible plasmon roles, and consequently the two mechanisms, by studying the polarization-dependence of the electron emission from individual, supported Ag nanocubes<sup>125</sup> (edge length,  $d \sim 160$  nm). The four-fold symmetry, well-defined positioning on the substrate (i.e., face down) and relatively simple scattering spectra in the visible spectral range make nanocubes ideal for this experiment. Single Ag nanocubes exhibit two main plasmon resonances, a dipolar and a quadrupolar mode, as discussed in Chapters 3 and 4. This work focuses on the dipolar resonance, as it is the sole mode excited at 800 nm, the excitation laser wavelength (intensity contribution  $> 99.9$  % for all cubes studied). Typical scattering spectra for single silver nanocubes can be found in Figures 6.12 and 4.18.

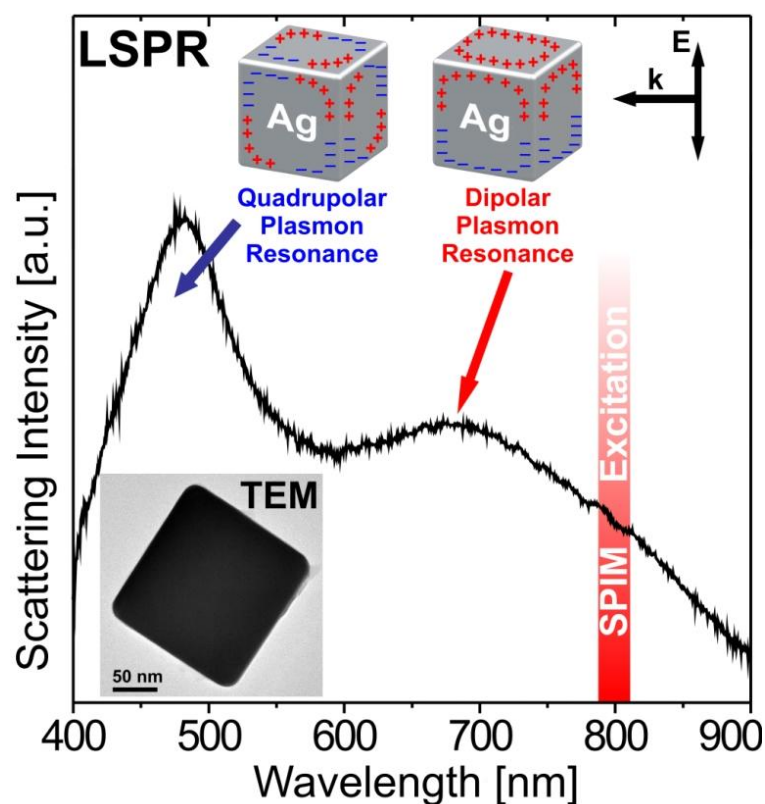


Figure 6.12. Scattering spectrum of an individual Ag nanocube ( $d \sim 160$  nm) on a c-flat substrate and SPIM excitation wavelength. The two prominent peaks correspond to a quadrupolar ( $\lambda = 480$  nm) and a dipolar ( $\lambda = 690$  nm) plasmon resonance. The charge distribution for the two resonances is schematically depicted at the top of the Figure for the indicated incident electromagnetic radiation. Inset: TEM image of the Ag nanocube responsible for the scattering spectrum.

The electron emission studies were performed in a scanning photoionization microscope (SPIM, see ref.<sup>261,262,271,272</sup> and Figure 2.17). Briefly, ultrafast laser pulses with center wavelength  $\lambda = 800$  nm are focused by an *in-vacuo* microscope objective onto a supported particle, momentarily generating high laser intensities ( $I \sim 10^9$  W/cm<sup>2</sup>) that lead to electron emission. The two models

described above predict substantially different behavior for the electron yield from Ag nanocubes as a function of the excitation laser polarization orientation in the substrate plane, such that single particle correlated experiments provide a powerful tool to differentiate between them.

In the thermionic emission case, where the electron gas temperature is of utmost importance, the electron emission pattern upon varying the laser polarization direction is expected to reflect the underlying polarization dependence of the particle's linear absorption cross-section. However any linear process (i.e., light absorption or scattering) in structures with 3-fold symmetry or higher is independent of the laser polarization, because every excited mode can be expressed as a linear combination of two (or more) degenerate modes.<sup>273</sup> Consequently, thermionic emission from symmetric structures such as cubes is insensitive to laser polarization (Figure 6.13).

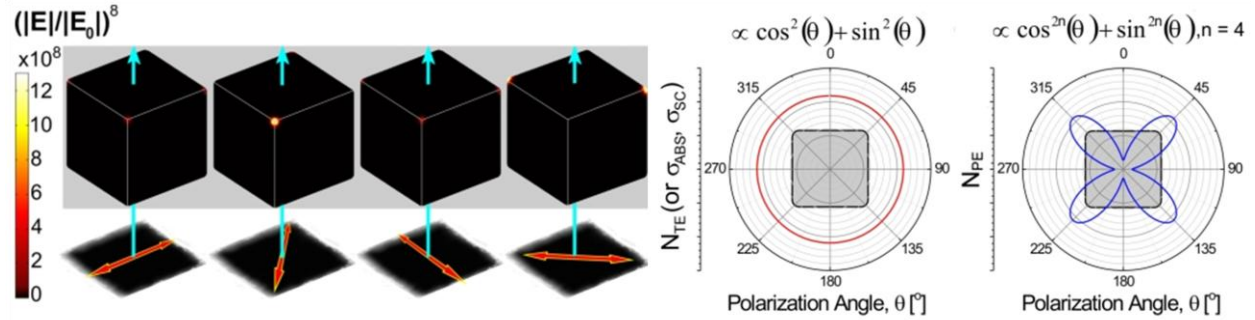


Figure 6.13. Electric field intensity and expected polarization dependence of the electron emission of Ag nanocubes. Left: Distribution of the electric near-field component normal to the particle surface (2 nm from cube surface) for four select orientations of the incident electric field vector. Due to the n-photon nature of the process ( $n = 4$ ), the enhancement factor  $|E|/|E_0|$  raised to the 8<sup>th</sup> ( $2 \times 4$ ) power is used as a metric approximating multiphoton photoelectron emissivity. Right: anticipated laser polarization dependence of the electron emission from individual nanocubes if thermionic emission ( $N_{TE}$  - red trace) or photoelectron emission ( $N_{PE}$  - blue trace) mechanism dominates

On the other hand, the multiphoton photoelectron emission rate depends on the local electric field component normal to the particle surface raised to the power  $2n$ , where  $n$  is the minimum number of photons required to overcome the material work function (i.e.,  $n > \Phi/E_{ph}$ ). Given the Ag work function,  $\Phi_{Ag} = 4.74$  eV,<sup>274</sup> a minimum of four ( $n = 4$ ) photons are thus necessary for electron emission at  $\lambda = 800$  nm ( $E_{ph} = 1.55$  eV). Since a plasmon resonance enhances the local electric-field intensity, multiphoton photoelectron emission will scale roughly with  $|E|/|E_0|$  to the 8<sup>th</sup> power. Therefore, numerical electrodynamics calculations of the quantity  $|E|/|E_0|$ <sup>8</sup>, which serves as a metric for multiphoton photoemissivity, were performed at select excitation laser

polarization orientations (Figure 6.13). From the images, the corners can be clearly identified as the dominant electron sources, in agreement with previous studies that found maximum near-field enhancements at cube corners.<sup>52,106,129,147</sup> More importantly, stronger local electric field enhancement arises at the corners when the excitation polarization aligns with the cube diagonals than when it points parallel with the square facets of the cube. This implies that multiphoton photoelectron emission will be sensitive to the laser polarization direction and resemble the four-lobe pattern shown in Figure 6.13. Moreover, the laser polarization directions resulting in maximum electron emission are thus expected to be aligned with the cube diagonals/corners. Correlated LSPR/SPIM/TEM (see Chapter 2 for details) was used to differentiate between the two mechanisms. Typical diffraction limited SPIM and DFM images, as well as low- and high-magnification TEM pictures are presented in Figure 6.14.

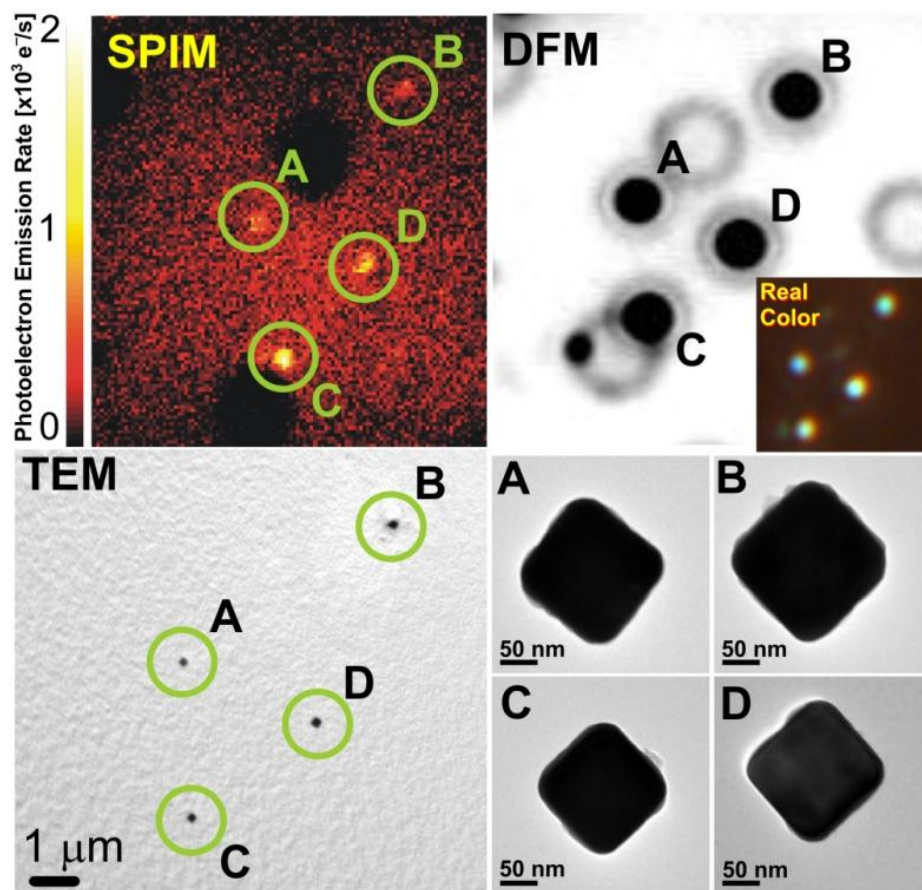


Figure 6.14. Correlated LSPR/SPIM/TEM of Ag cubes. Top left: SPIM. Top right: scattering image from dark field microscopy. The black and white image is shown with inverted colors, while the real color image is unprocessed. Bottom left: low magnification TEM image. Bottom right: high-magnification TEM images of the four nanocubes (A-D) present in the SPIM and DFM images.

### 6.5.3 Results from Polarization Experiments

The polarization-dependence of the scattering of Ag nanocubes was studied using correlated LSPR/TEM. Twenty cubes of side length 140-180 nm were studied. The peak intensity was

measured at the dipole position for each nanocube. The average polarization anisotropy, or peak intensity variation (calculated as previously,  $(I_{\max,\lambda} - I_{\min,\lambda})/I_{\text{average},\lambda}^{100}$ ) was 9 % with a standard deviation of 3 %,  $N = 20$  (Figure 6.15).

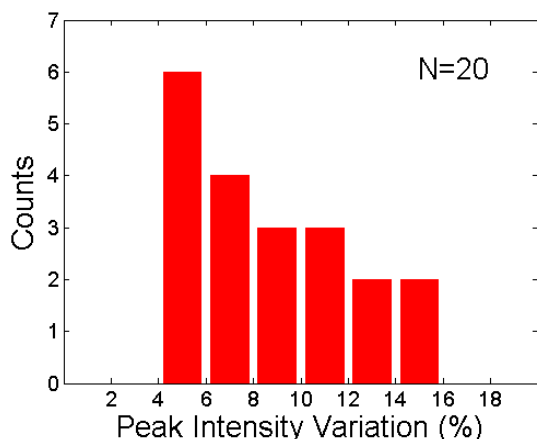


Figure 6.15. Polarization anisotropy of supported Ag nanocubes.

The small polarization-dependence of the intensity produced a pattern showing two maxima and two minima over  $360^\circ$  (Figure 6.16). The average intensity variation for cubes (9 %) was significantly smaller than for an elongated particle (71 %, Figure 6.16) found in the reaction mixture, or other anisotropic particles and aggregates studied on the same instrumental setup (previous sections). Note that this elongated particle was not included in the data presented in Figures 6.15 and 6.17.

No correlation was found between the corner orientation and the polarization giving the highest intensity (Figure 6.17). The origin of the small intensity variation with polarization remains unclear but it cannot be attributed to the cubes themselves and is likely due to instrument

positioning and other small instrumental contributions. The predominance of highest peak intensity positions between 90 and 180° also supports this claim.

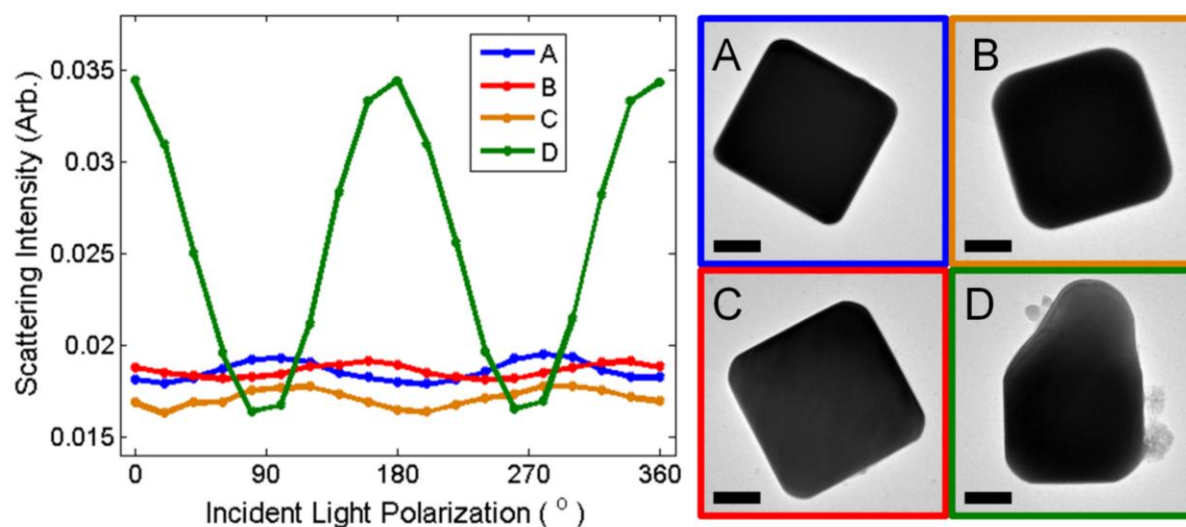


Figure 6.16. Representative polarization-dependent spectra and TEM pictures of Ag nanocubes. Left: LSPR spectra, where the polarization anisotropy for cubes a, b, c, and d is 8.7, 5.5, 8.7, and 71 %, respectively. Right: TEM images. Scalebars, 50 nm. The peak intensity maximum is 100, 160, 120, and 180°, while the corner orientation is 74, 17, 27, and 45° for cubes a, b, c, and d, respectively.

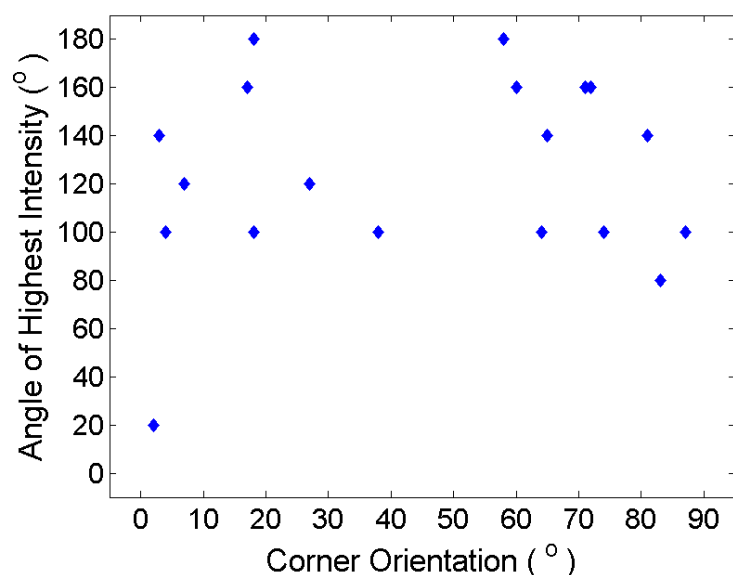


Figure 6.17. Correlation between the polarization giving the highest peak intensity and the cube corner orientation.  $N = 20$ .

The observed lack of polarization-dependence of the scattering intensity of the dipolar mode is in agreement with previous observations and calculations as well as with the expectations based on the particle symmetry.<sup>100</sup> The electron emission from Ag nanocubes, however, was observed to strongly depend on the laser polarization, as can be seen in Figure 6.18 for the same cube. Since the electron current resulting from a thermionic emission mechanism should be independent of the incident laser polarization (Figure 6.13), the finding clearly indicates that the multiphoton photoelectric effect is responsible for the observed electron emission signal. The multiphoton nature of this process was further confirmed by a power law dependence of the electron emission rate on laser intensity at  $\lambda = 800$  nm, where the expected ensemble-averaged exponent value  $n = 4.0(1)$  was measured in a sample of  $N = 7$  cubes.

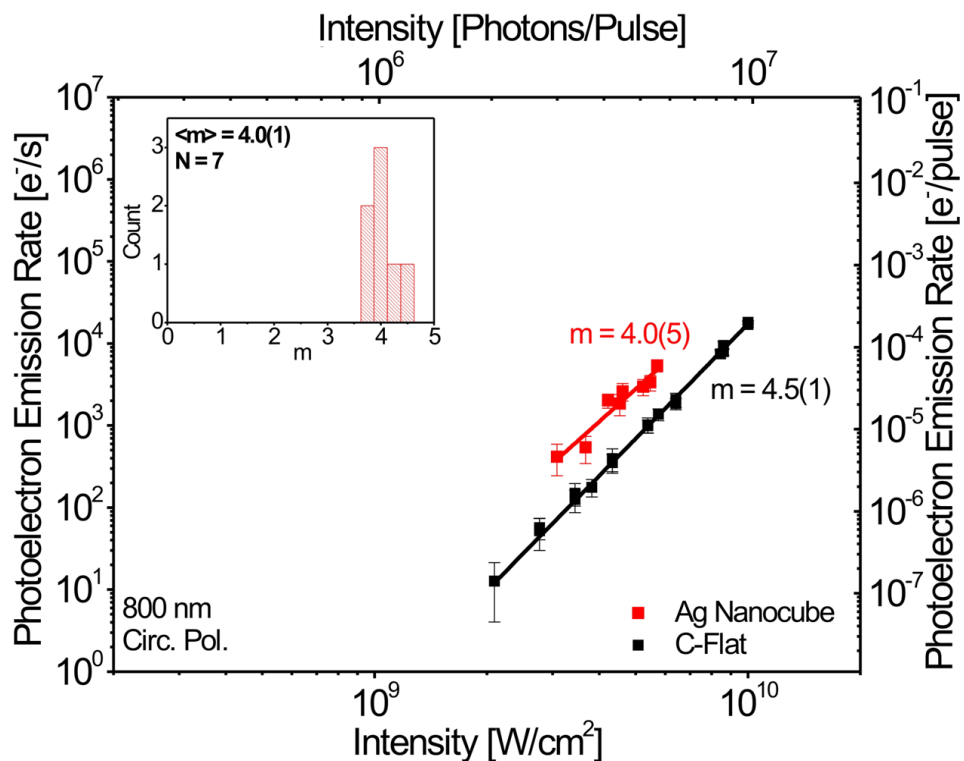


Figure 6.18. Measured photoelectron emission rate, PE, as a function of the laser intensity using circularly polarized  $\lambda = 800$  nm light. The main plot shows data for a representative Ag nanocube (red) and C-Flat substrate (black), together with a least-square fit to equation  $\text{PE} = A \times I^m$ . Inset shows a histogram of fitted  $m$  values for  $N = 7$  Ag nanocubes, yielding an ensemble-averaged value  $\langle m \rangle = 4.0 \pm 0.1$ .

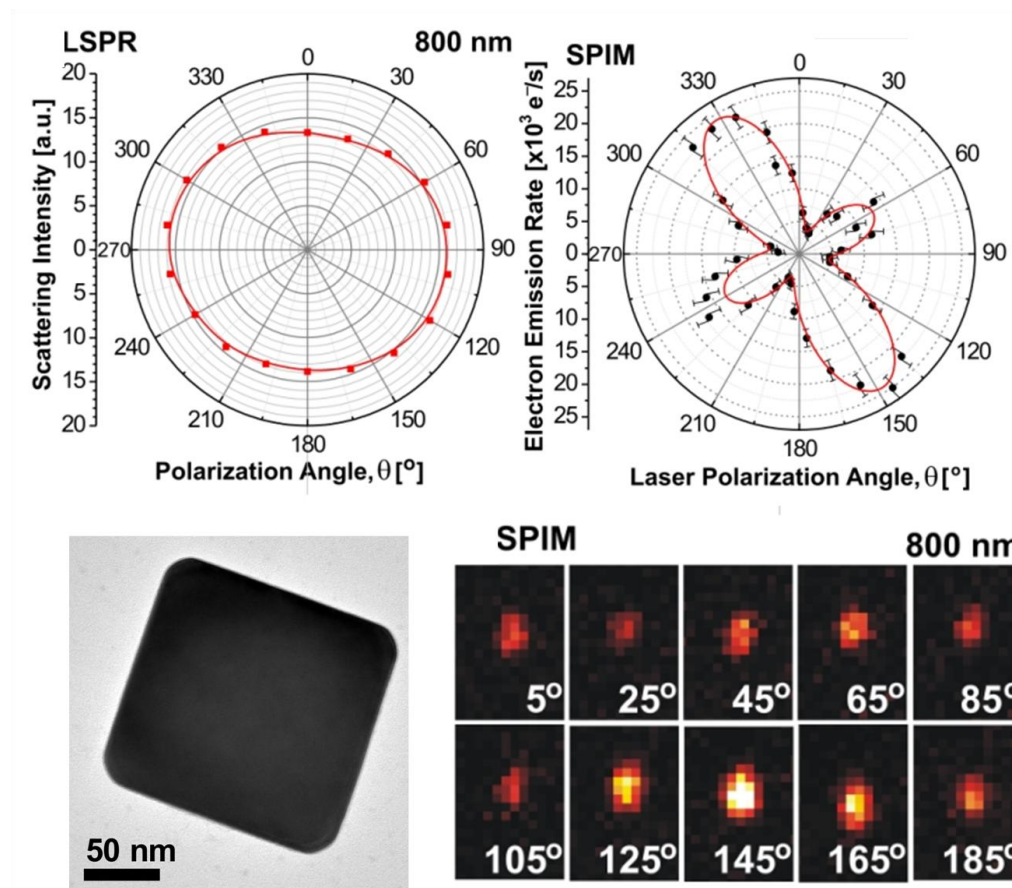


Figure 6.19. Polarization dependence of scattering and multiphoton photoemission. Top left: scattering intensity from a Ag nanocube as a function of the polarization of the illuminating light ( $\lambda = 800$  nm). Top right: electron emission from the same Ag nanocube as a function of excitation laser polarization (center wavelength,  $\lambda = 800$  nm). Bottom left: TEM image of single Ag nanocube studied. Bottom right: sequence of raw SPIM images of the nanocube recorded at indicated laser polarization angles and intensity  $I = 4.5 \times 10^9$  W/cm<sup>2</sup>.

Since photoelectron emission is strongly influenced by the local electric field at the particle surface, the electron emission yield would be expected to peak when the laser polarization aligns with the regions of highest electric field enhancement, i.e., cube corners.<sup>92,96,106,129,147</sup> This is

precisely what was experimentally observed in correlated SPIM/TEM measurements on 11 Ag nanocubes (Figure 6.20). Note that in an earlier study a marked increase in the SERS signal, which is also directly related to the local electric field intensity, was observed if the laser polarization aligns with the corners of the nanocubes.<sup>204</sup> The current finding identifies the local electric field enhancement induced by the localized surface plasmon resonance as critical for efficient electron emission, providing strong evidence for the multiphoton photoelectron emission (MPPE) mechanism.

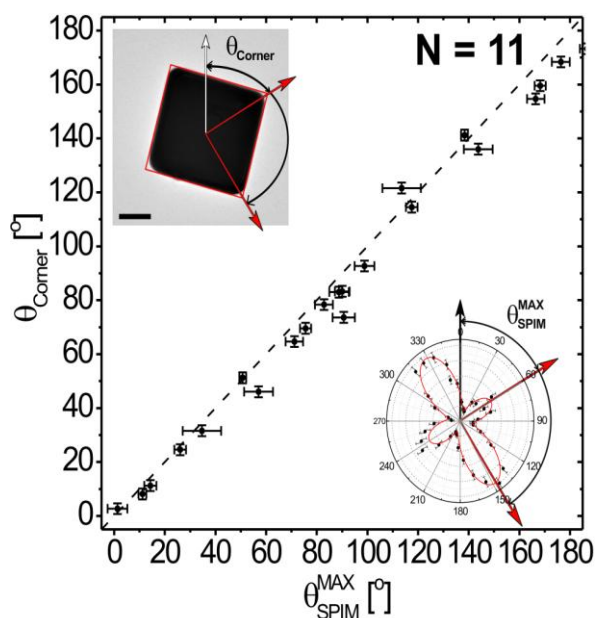


Figure 6.20. Correspondence between the direction of the cube corners ( $\theta_{\text{Corner}}$ ) and the laser polarization that results in maximum electron emission ( $\theta_{\text{SPIM}}^{\text{MAX}}$ ).

#### 6.5.4 Corner Rounding Effects on Photoemission Intensity

The MPPE signal depends sensitively on the local electric field distribution ( $|E|/|E_0|^8$ ) and consequently all factors that affect the electric near-field. For example, structure dramatically influences the particle near-field, suggesting that the MPPE yield will depend sensitively on tiny differences in topography of the particle surface. These structural variations are likely responsible for the observed imperfections in the four-lobed patterns of MPPE rate vs. excitation laser polarization (Figure 6.19), where one lobe pair is generally stronger than the other. The typically observed 3- to 5-fold differences between the adjacent lobe pairs translate into only ~ 20 % ( $\sim 5^{1/8} = 1.22$ ) variability in  $|E|/|E_0|$  for neighboring cube corners, which could easily arise due to slight topological dissimilarities between them.

Since the curvature of cube corners is a dominant structural factor influencing the local electric field enhancement in their vicinity, the inferred variation in  $|E|/|E_0|$  within the same cube implies that the roundness of neighboring corners may slightly differ. We explored the link between the observed photoelectron emission rates and the measured corner radii of 8 different cubes and interestingly found no clear correlation (Figure 6.21). This surprising result may suggest that corner features smaller than a typical HRTEM resolution of ~ 1-2 nm significantly contribute to the overall photoemission signal. Alternatively, since the corner radius was not measured directly, but rather inferred from the roundness of the edges, the dominant electron sources contributing to the observed MPPE signal could simply have been unobservable. However, they may be identifiable in HRTEM by tilting the sample, whereby the detailed corner morphology may be revealed, and will be looked at in greater detail in the future.

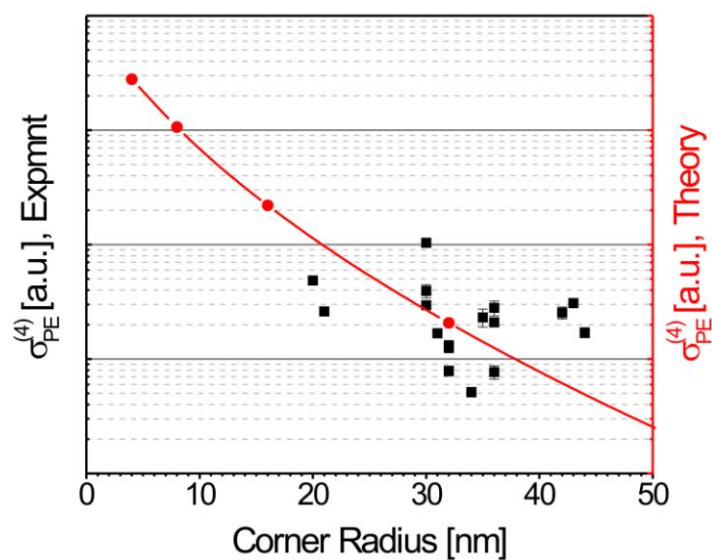


Figure 6.21. Experimental four-photon photoelectron emission cross-section for 8 Ag nanocubes as a function of measured cube corner rounding,  $r$  (black). The smallest radius value of the two aligned with a particular preferred polarization direction is used, because it is presumed to be the stronger electron emitter. The expected dependence is shown in red, where  $\sigma_{PE}^{(4)} \propto \int_{A_{NP}} (|E|/|E_0|)^8 \cdot dA$ . The surface integral of  $(|E|/|E_0|)^8$  over the particle boundary  $A_{NP}$  (2 nm away from the actual particle surface) is evaluated, see ref.<sup>272</sup> for details.

### 6.5.5 Conclusions

In summary, correlated DFM/TEM/SPIM studies of individual nanoparticles provide a unique insight into the electron emission process following excitation with high-intensity ultrashort laser pulses. By offering a well-controlled environment necessary for quantification, these studies identified multiphoton photoelectron emission as the most probable mechanism responsible for

electron emission from Ag nanocubes, and likely metal nanoparticles in general, when employing ultrafast excitation with  $E_{\text{ph}} < \Phi$ . The photoelectron emission rate depends sensitively on  $|E|/|E_0|$  by scaling approximately with  $(|E|/|E_0|)^{2n}$ , where  $n > \Phi/E_{\text{ph}}$ . The presence of a plasmon can therefore dramatically enhance the total photoelectron yield even by increasing the incident electric field near the particle surface only slightly. The strong sensitivity of the MPPE yield to the local electric field enhancement thus opens up the possibility of mapping and experimentally quantifying the local near-field enhancement factors in metallic nanoparticles and nanostructures.

## CHAPTER 7

### The Wulff Construction for Alloy Nanoparticles

## 7.1 Introduction to Alloy Nanoparticles

In the previous chapters, the effect of many different factors such as size, shape, and corner rounding, on plasmonic properties have been studied. Another handle on plasmonics is composition, as seen in Chapter 3 with the strikingly different properties of Au and Ag nanocubes, is composition. Indeed, not only do Ag and Au have different optical responses, but several studies have shown that the resonance energy varies smoothly with composition when AgAu alloys are formed.<sup>75,79,275</sup>

Additionally, alloying can drastically improve the performance of catalytic materials, where the activity rarely varies linearly with composition.<sup>11,136,276-290</sup> Examples abound, but to name a few, cyclohexane dehydrogenation on CuNi is rather insensitive to composition in the 10-80 % Cu range, with a sharp activity drops are observed for both pure metals;<sup>11</sup> CO hydrogenation produces 10 times more methanol when a 20/80 Fe/Pd alloy is used than when either pure metals are used;<sup>278</sup> Benzyl alcohol oxidation proceeds at a nearly 100 % conversion rate for any AuCu alloys, but drops to 40 - 50 % for Au or Cu alone.<sup>277,291</sup>

It is well-known, however, that shape is also a factor influencing both catalysis and plasmonics behavior.<sup>65,68,86,92,109,187,197,248,292-295</sup> Catalysis occurs on the outermost layer of a particle, hence the exact composition at the surface is absolutely critical. This composition can be different than that of the bulk due to migration of atoms to the surface, an effect called segregation.<sup>156,290,296-302</sup>

A shape-predictive model for alloys, including surface composition analysis, would thus be a useful tool for the nanotechnology community, supplementing the widely used Wulff, modified Wulff, Winterbottom, and Summertop constructions discussed in Chapter 1.

In this chapter, the analytic solution for the thermodynamic equilibrium shape and surface composition of an alloy nanoparticle is derived. The modeled nanoparticle shapes obtained when including segregation are rather different from what is found for a single component system or non-segregating alloy. Previous models and approaches are first discussed (Section 7.2), followed by a complete mathematical derivation of the alloy Wulff construction (Section 7.3). Four different alloys (AgPd, AuPd, AgAu, and CuAu) are explored, their shape and composition profiles are characterized, and some of interesting shape-dependent effects are observed in Section 7.4. Finally, in Section 7.5, results from the alloy Wulff construction are compared with published experiments, and its limitations and potential extensions are discussed.

## 7.2 Previous Modeling of Alloy Nanoparticle Shape

The shape of alloy nanoparticles is relevant to a number of properties such as catalysis and plasmonics,<sup>65,68,86,92,109,187,197,248,292-295</sup> such that many approaches have been developed to predict and understand it, with a range of simplifications and assumptions. Numerical methods such as Monte Carlo and embedded atom simulations have been used, however because of computing limitations, shapes are either fixed (with variable atomic distribution) or the particles modeled are very small.<sup>297,298,303-306</sup> While such studies can provide useful information, their limitations and approximations (on potentials, structures, and/or density functionals) reduce their applicability. In addition, analytical techniques are often more powerful than atomistic ones as they provide solutions valid for different sizes, which is often hard to extract from an atomistic calculation.

The simplest analytical model that can be used to predict the shape of alloy nanoparticles is the Wulff construction, discussed in Chapter 1. In this approach, it is assumed that no segregation occurs, and the surface energy is taken for the composition corresponding to the overall particle composition (herein referred to as homogeneous concentration). This work refers to this approach as the “basic Wulff”.

Some of the oversimplifications used in the basic Wulff model have been addressed using the “infinite reservoir approximation” (Figure 7.1). In this approach, the surface composition (hence surface free energy) is variable, while the internal composition is fixed to that of the initial (herein referred to as initial or homogeneous) concentration. Bulk composition and bulk free energy changes are neglected, and the surface free energy is computed with the initial bulk composition as underlying concentration.

For nanoparticles, the small number of atoms make the infinite reservoir approximation inapplicable. Indeed, how can one ignore the change of bulk concentration due to segregation in a 3 nm diameter (1,000 atoms) particle, in which roughly a third of the atoms are on the surface? The goal of the current effort is thus to develop a rigorous approach to alloy nanoparticle shape modeling, which include the effects of bulk and surface composition changes.

Note that the change in bulk composition due to a change in surface concentration is herein called "starvation", because segregation effectively starves the bulk of the atom(s) that preferentially go to the surface. Looking at it the opposite way, "starvation" could have also been called "enrichment", in this case enrichment of the non-segregating atom. Starvation seemed to provide a more graphic description of the phenomenon and thus was chosen.

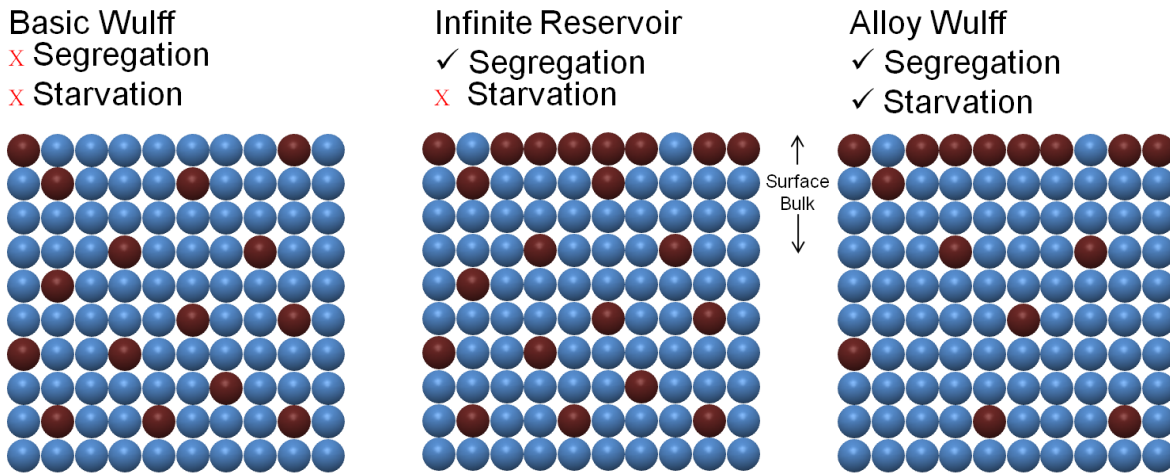


Figure 7.1. Properties of the three Wulff models discussed: the basic Wulff model, the infinite reservoir approximation, and the alloy Wulff model.

### 7.3 Mathematical Derivation of the Alloy Wulff Construction

#### 7.3.1 Parameters Definition

Surface free energy is defined as the excess energy per unit area due to the presence of a surface.<sup>307-309</sup> For the basic Wulff construction, this is a fixed number determined solely by the initial, homogeneous particle composition. For the infinite reservoir approximation and the alloy Wulff, this number depends both on the composition of the surface (variable in both models; segregation) and the underlying composition (variable only in the alloy Wulff). Indeed, a surface of composition A on bulk of composition A does not have the same energy as a surface of composition A on a bulk of composition B, if  $A \neq B$ . The amount with which it differs is represented by the last term in Equation 7.1.

Bulk free energy is defined as the material's free energy per unit volume. The term used in the alloy Wulff construction, and absent in both the basic Wulff and the infinite reservoir approximation, is the change in bulk free energy. This term is linked to starvation, i.e. the bulk energy varies because of the bulk composition changes induced by segregation.

Bulk free energy and surface free energies can be calculated or experimentally measured; the values published in ref. <sup>296,307,309-314</sup> were used in the present study, see Section 7.4.1.

### 7.3.2 Bulk and Surface Energy Definition and Derivations

The face- and concentration-dependent surface free energy must include a term correcting for the difference between bulk and surface composition, as discussed previously, i.e.

$$\gamma_{(n,c_1^S,c_1^V,c_2^S,c_2^V,\dots)} = \gamma_{(n,c_1^S,c_2^S,\dots)} + \tau \left( G_{(c_1^S,c_2^S,\dots)} - G_{(c_1^V,c_2^V,\dots)} \right) \quad (7.1)$$

Where  $\tau$  is the surface thickness,  $\gamma_{(n,c_1^S,c_2^S,\dots)}$  is the free energy of a surface of crystallographic orientation  $n$  and concentration  $C_1^S, C_2^S, \dots$  (subscript 1 = element 1, subscript 2 = element 2, etc) on a bulk of the same concentration, and  $\gamma_{(n,c_1^S,c_1^V,c_2^S,c_2^V,\dots)}$  is the free energy of a surface of concentration  $C_1^S, C_2^S, \dots$  on a bulk of concentration  $C_1^V, C_2^V, \dots$ . The bulk free energy,  $G$ , is defined as the deviation from a linear variation of bulk free energy between two pure compounds (Figure 7.2)

Expanding this term via a truncated Taylor expansion for a small change in surface composition  $x_i^S$  yields

$$\mathcal{V}_{(n, c_1^S + x_1^S, c_1^V, c_2^S + x_2^S, c_2^V, \dots)} = \mathcal{V}_{(n, c_1^S, c_1^V, c_2^S, c_2^V, \dots)} + \sum \frac{d\mathcal{V}_{(n, c_1^S, c_1^V, c_2^S, c_2^V, \dots)}}{d(c_i^S)} (x_i^S) \quad (7.2)$$

The surface chemical potential is defined as the derivative of the free energy with respect to concentration,

$$\mu_i^S = \frac{d\mathcal{V}_{(n, c_1^S, c_1^V, c_2^S, c_2^V, \dots)}}{d(c_i^S)} \quad (7.3)$$

Thus

$$\mathcal{V}_{(n, c_1^S + x_1^S, c_1^V, c_2^S + x_2^S, c_2^V, \dots)} = \mathcal{V}_{(n, c_1^S, c_1^V, c_2^S, c_2^V, \dots)} + \sum \mu_i^S (x_i^S) \quad (7.4)$$

The total surface energy of the particle,  $E^S$ , is the sum of surface free energies over the entire particle surface,

$$E^S = \int (\mathcal{V}_{(n, c_1^S, c_1^V, c_2^S, c_2^V, \dots)} + \sum \mu_i^S (x_i^S)) dS \quad (7.5)$$

Analogously, the bulk free energy can be expressed as a Taylor series for a small change in bulk composition  $x_i^V$ ,

$$G_{(C_1^V+x_1^V, C_2^V+x_2^V, \dots)} - G_{(B_1^V, B_2^V, \dots)} = G_{(C_1^V, C_2^V, \dots)} - G_{(B_1^V, B_2^V, \dots)} + \sum \frac{dG_{(C_1^V, C_2^V, \dots)}}{d(C_i^V)} (x_i^V) \quad (7.6)$$

Where the  $B_i^V$  terms refer to the initial concentration assuming equal bulk and surface composition; we refer to this as the homogeneous concentration.

The bulk chemical potential is defined as

$$\mu_i^V = \frac{dG^V_{(Cv1, Cv2, \dots)}}{dC_i^V} \quad (7.7)$$

Thus

$$G_{(C_1^V+x_1^V, C_2^V+x_2^V, \dots)} - G_{(B_1^V, B_2^V, \dots)} = G_{(C_1^V, C_2^V, \dots)} - G_{(B_1^V, B_2^V, \dots)} + \sum \mu_i^V (x_i^V) \quad (7.8)$$

The change in bulk energy,  $E^V$ , is expressed as

$$E^V = \int (\Delta G + \sum \mu_i^V (x_i^V)) dV \quad (7.9)$$

Where the bulk free energy term  $\Delta G$  is the difference between the free energy of the final bulk concentration  $C_1^V, C_2^V, \dots$  and that of the initial composition  $B_1^V, B_2^V, \dots$ ,

$$\Delta G = G_{(C_1^V, C_2^V, \dots)} - G_{(B_1^V, B_2^V, \dots)} \quad (7.10)$$

### 7.3.3 Energy Minimization and Final Equation Derivation

We first apply a conservation of mass constraint,

$$F_i = \int \tau [(C_i^S + x_i^S) - (C_i^V + x_i^V)] dS + \int (C_i^V + x_i^V) dV \quad (7.11)$$

And a constant volume constraint,

$$F_V = \int dV \quad (7.12)$$

The global problem can thus be written as minimizing via the Lagrangian multipliers  $\Lambda$  and  $\lambda_i$ ,

$$F = E^S + E^V - \Lambda(F_V - A) - \sum \lambda_i (F_i - B_i) \quad (7.13)$$

Where  $A$  and  $B_i$  are constants.

Composition conservation requires that

$$\frac{dF}{d\lambda_i} = 0 \quad (7.14)$$

Such that

$$0 = (F_i - B_i) \quad (7.15)$$

Equation 7.14 thus becomes

$$F = E^S + E^V - \Lambda(F_V - A) \quad (7.16)$$

Combining Equations. 7.5, 7.9, and 7.16 and rearranging yields

$$F = \int [\gamma_{(n, c_1^S, c_1^V, c_2^S, c_2^V, \dots)} + \sum \mu_i^S (x_i^S)] dS + \int [\Delta G + \sum \mu_i^V (x_i^V) - \Lambda] dV + \Lambda A \quad (7.17)$$

The derivative of the energy with respect to a change in composition, in the bulk or the surface, must be zero at equilibrium, i.e.

$$\frac{dF}{dx_i^S} = \frac{dF}{dx_i^V} = 0 \quad (7.18)$$

This greatly simplifies Equation 7.17, which becomes

$$F = \int \gamma_{(n, c_1^S, c_1^V, c_2^S, c_2^V, \dots)} dS + \int (\Delta G - \Lambda) dV + \Lambda A \quad (7.19)$$

Noting that the conventional Wulff problem (without alloying) is minimizing

$$F = E^S - \Lambda_c F_V \quad (7.20)$$

i.e.

$$F = \int \gamma_{(n)} dS - \int \Lambda_c dV \quad (7.21)$$

with a solution

$$\gamma = \Lambda_c h \quad (7.22)$$

We immediately obtain the solution of Equation 7.1,

$$\gamma_{(n, c_1^S, c_1^V, c_2^S, c_2^V, \dots)} = h_{(n)} \{ \Lambda - \Delta G \} \quad (7.23)$$

Rearranging gives the alloy nanoparticle Wulff construction

$$\frac{\gamma_{(n, c_1^S, c_1^V, c_2^S, c_2^V, \dots)}}{\{\Lambda - \Delta G\}} = h_{(n)} \quad (7.24)$$

Which dictates the face-dependent equilibrium surface normal  $h_{(n)}$ , i.e. the particle shape, as a function of surface composition, bulk composition, and particle size.

Neglecting change in bulk concentration due to surface segregation, i.e. setting  $\Delta G = 0$  leads as expected to a form analogous to the traditional Wulff construction,

$$\frac{\gamma_{(n, c_1^S, c_1^V, c_2^S, c_2^V, \dots)}}{\Lambda} = h_{(n)} \quad (7.25)$$

The thermodynamic equilibrium energy is then simply the sum of surface free energy and change in bulk energy,

$$E_{tot} = E^S + E^V = \int \gamma_{(n, c_1^S, c_2^S, \dots)} dS + \int \Delta G dV \quad (7.26)$$

## 7.4 Results of Shape Modeling Using the Alloy Wulff Construction: CuAu, AuPd, AgAu, and AgPd

### 7.4.1 Energy and Unit Cell Parameter Values Used

#### 7.4.1.1 Bulk Free Energy

Bulk free energy from literature values<sup>179-181,184</sup> (experimental when available, calculations otherwise) was fit by a polynomial.

For CuAu, AuPd, and AgAu:

$$G = B * [Au]^3 + C * [Au]^2 + D * [Au] \quad (7.27)$$

For AgPd:

$$G = A * [Pd]^4 + B * [Pd]^3 + C * [Pd]^2 + D * [Pd] \quad (7.28)$$

The bulk free energy of AgPd was fit by a fourth order polynomial because of the too large error introduced by a third order fit.

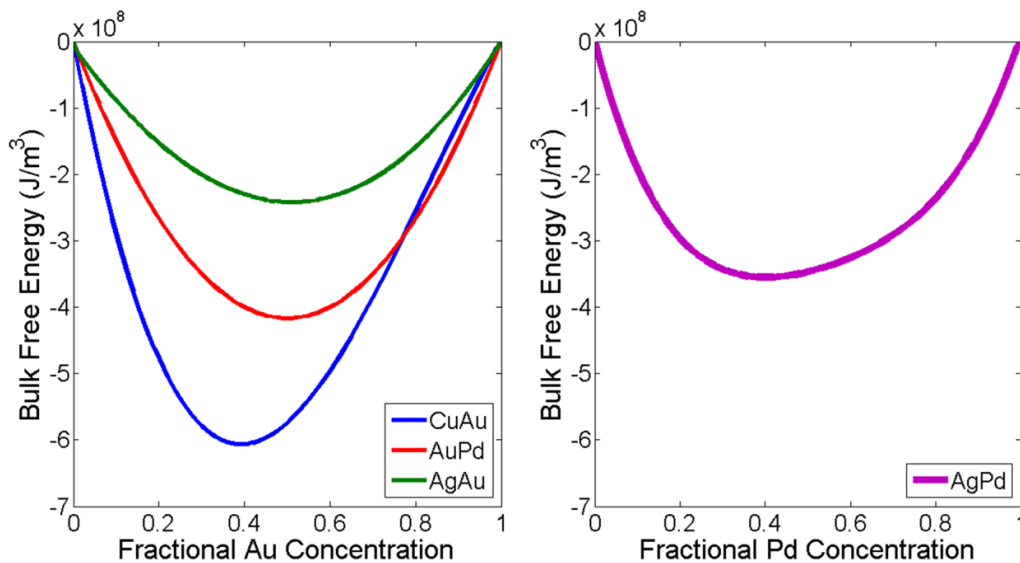


Figure 7.2 Composition-dependent bulk free energy of the studied alloys CuAu (blue), AuPd (red), AgAu (green), and AgPd (pink),<sup>309-311,314</sup> Equation 7.27-7.28.

#### 7.4.1.2 Unit Cell Parameter ( $c$ )

The unit cell parameter was assumed to vary linearly between that of pure components.

Experimental values were used.

For CuAu, AuPd, and AgAu:

$$c = E * [Au] + F \quad (7.29)$$

For AgPd:

$$c = E * [Pd] + F \quad (7.30)$$

#### 7.4.1.3 Homogeneous Surface Free Energy

Surface free energy values, taken from published material<sup>296,307,309-314</sup> (experimental when available, calculations otherwise), were assumed to vary linearly between pure components.

For CuAu, AuPd, and AgAu:

$$\gamma_{(n,c_1^s,c_2^s,\dots)} = \alpha_{(n)} * [Au] + \beta_{(n)} \quad (7.31)$$

For AgPd:

$$\gamma_{(n,c_1^s,c_2^s,\dots)} = \alpha_{(n)} * [Pd] + \beta_{(n)} \quad (7.32)$$

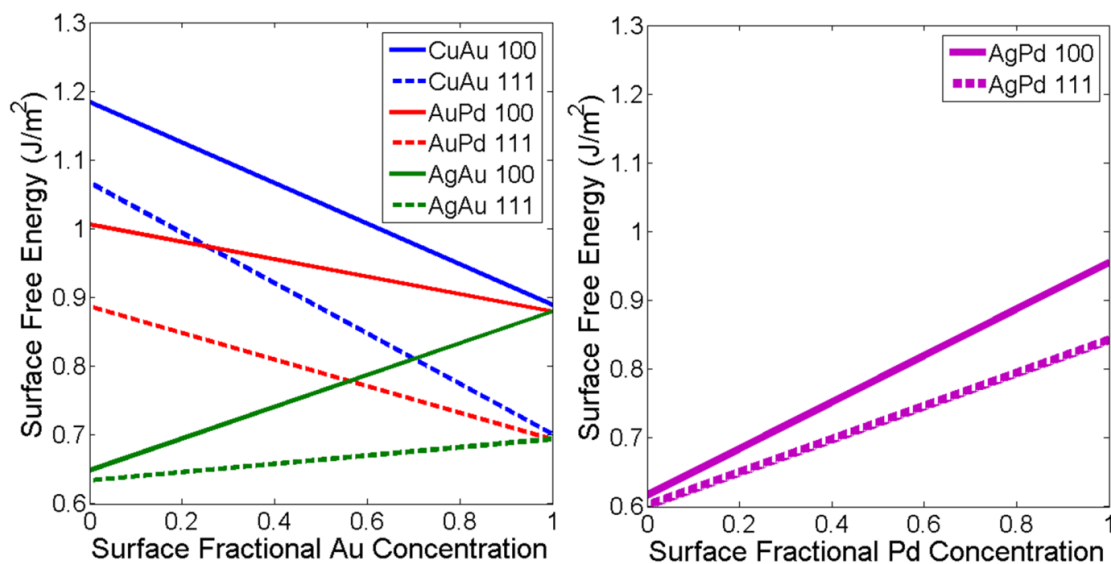


Figure 7.3 Composition and orientation dependence of the surface free energy of CuAu (blue), AuPd (red), AgAu (green), and AgPd (pink),<sup>165,177,179-184</sup> Equations 7.31-7.32.

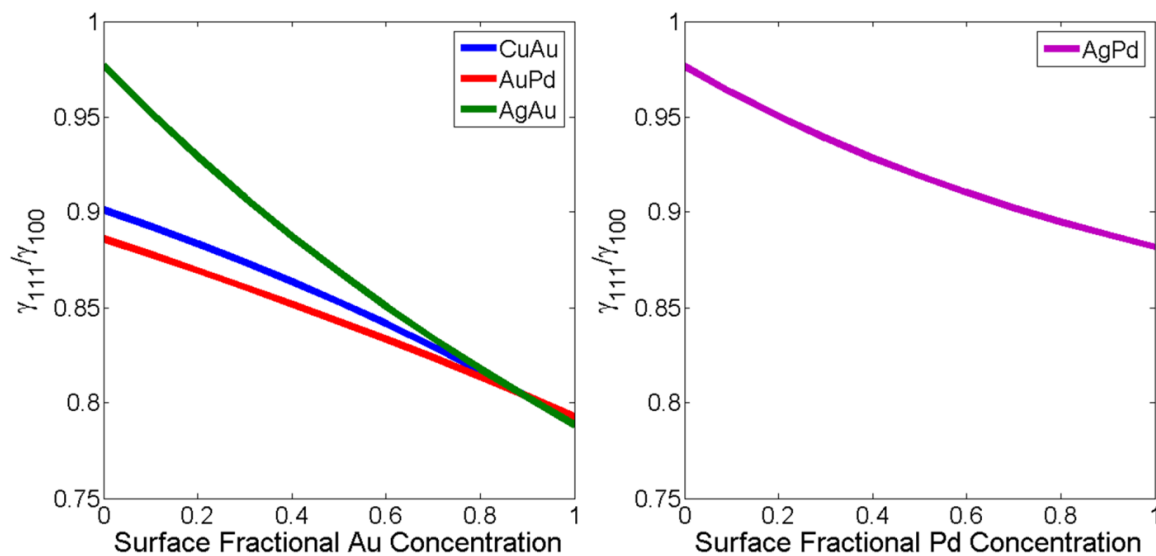


Figure 7.4 Composition-dependence of the surface energy ratio of the studied alloys CuAu (blue), AuPd (red), AgAu (green), and AgPd (pink).

Table 7.1. Parameters used for the computation of the bulk free energy (A-D, Equations 7.25-7.26) and the unit cell parameter (E-F, Equations 7.29-7.30) of CuAu, AuPd, AgAu and AgPd.<sup>296,307,309-314</sup> The concentration used are unitless fractions, thus the coefficients do not contain concentration units.

	T (K)	A ( $10^9$ J/m <sup>3</sup> )	B ( $10^9$ J/m <sup>3</sup> )	C ( $10^9$ J/m <sup>3</sup> )	D ( $10^9$ J/m <sup>3</sup> )	E ( $10^{-10}$ m)	F ( $10^{-10}$ m)
CuAu	720	-	-2.293	5.7414	-3.4458	0.4645	3.663
AuPd	600	-	0	1.667	-16.67	0.2083	3.907
AgAu	600	-	0	0.9686	-0.9705	0.01070	4.104
AgPd	915	3.194	-6.957	6.253	-2.480	-0.2089	4.133

Table 7.2. Parameters used for the computation of the surface free energy ( $\alpha$ - $\beta$ , Equations 7.31-7.32) of CuAu, AuPd, AgAu and AgPd<sup>296,307,309-314</sup>. The concentration used are unitless fractions, thus the coefficients do not contain concentration units.

	T (K)	$\alpha_{(100)}$ (J/m <sup>2</sup> )	$\beta_{(100)}$ (J/m <sup>2</sup> )	$\alpha_{(111)}$ (J/m <sup>2</sup> )	$\beta_{(111)}$ (J/m <sup>2</sup> )
CuAu	720	-0.2946	1.184	-0.3657	1.067
AuPd	600	-0.1260	1.001	-0.1931	0.8870
AgAu	600	0.2310	0.6490	0.0600	0.6339
AgPd	915	0.3390	0.6164	0.2404	0.6020

#### 7.4.2 Equilibrium Bulk and Surface Composition

Surface composition is a critical factor in catalysis, and the alloy Wulff construction can uniquely model it. To this end, the code *wulffmodel3* (see appendix A; note that functions are italicized, and matrices are underlined in the text) was used to obtain the Energy and auSout matrices. These matrices were then used as inputs to *minauS*, yielding a 2-column matrix, in which the first column is the homogeneous concentration, and the second column is the lowest-energy surface composition. For the equilibrium bulk concentration, the *minauV* function was used.

For comparison purposes, the lowest energy configurations in the basic Wulff and infinite reservoir models were obtained and are presented in Figure 7.5. The basic Wulff surface concentration is set by the model as being always equal to the homogeneous concentration, such that no calculations were necessary. For the infinite reservoir model, the *wulffmodel2noSTARvenery* code was used to obtain the Energy and auSout matrices that were then used as inputs in the *minauS* function, yielding a matrix of equilibrium surface energy as a function of homogeneous concentration.

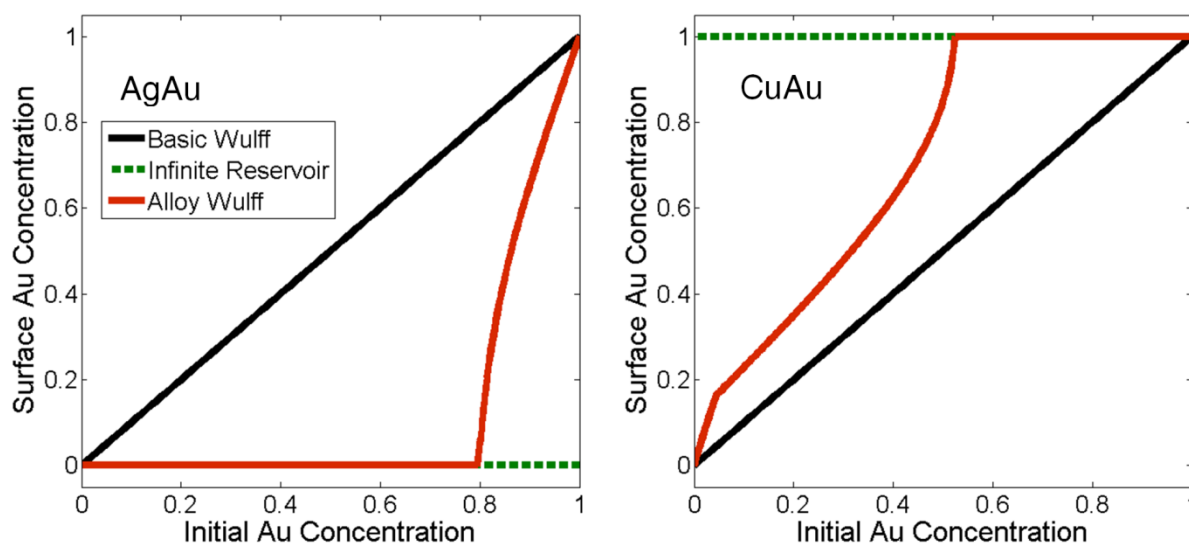


Figure 7.5 Equilibrium surface composition for AgAu and CuAu modeled using the basic Wulff construction (black line), the infinite reservoir approximation (green dashed line), and the alloy Wulff construction (red line).

The results of the equilibrium surface concentration as a function of homogeneous concentration for all 3 models are presented in Figure 7.5. Since segregation is not allowed in the basic Wulff, the surface concentration is simply a straight line of slope 1. In the infinite reservoir model, the

surface composition is always equal to the lowest energy surface, a constant. However, an issue arise in this approximation when the homogeneous concentration of the segregating component is very low: at some point the finite number of atoms present in the particle is lower than the number of atoms required to form the segregated surface. Since laws of conservation of mass are not obeyed in this approximation anyways, this effect was neglected and the surface was allowed to reach its minimum energy concentration at all times. In the alloy Wulff, the equilibrium surface concentration is neither a straight line nor a constant. In fact, the equilibrium surface concentration obtained is not even the minimum energy surface composition; it is rather, as it should be in any proper thermodynamic modeling, the minimum total energy because both bulk and surface terms are included. Segregation and starvation thus lead to a surface/bulk duality. Due to this, up 3 distinct composition-structure regimes are observed. For CuAu, at small homogeneous Au concentration ( $< 10$  atomic %), the energy gained by lowering the surface free energy overwhelms any bulk free energy changes such that all the available Au segregates to the surface, the bulk remains pure Cu, but there are never enough Au atoms to form a monolayer. As the homogeneous Au concentration increases the segregation (bulk) energy becomes of the same order as the energy gained by surface compositional changes (segregation), and regime 2 starts. While a complete surface segregation would give the lowest surface free energy, it is prohibited by the large bulk free energy change it induces. The surface and bulk energy remain in balance until the concentration at which the latter can no longer prevent the formation of a pure surface is reached. This second transition, from regime 2 to regime 3, is characterized by a very sharp change in shape and concentration. Note that with an infinite reservoir approximation the surface composition is *always* that of regime 3, a pure surface, independent of size. AuPd behave

similarly to CuAu (Figure 7.6), except that at very small sizes, the bulk free energy changes effectively prevent the formation of a full monolayer of Au on the surface. AgAu and AgPd behave differently in that there is never a balance between surface and bulk energy; a pure Ag surface is formed unless there are not enough atoms to do so (Figures 7.5 - 7.6). In other words, AgAu and AgPd do not go through regime 2.

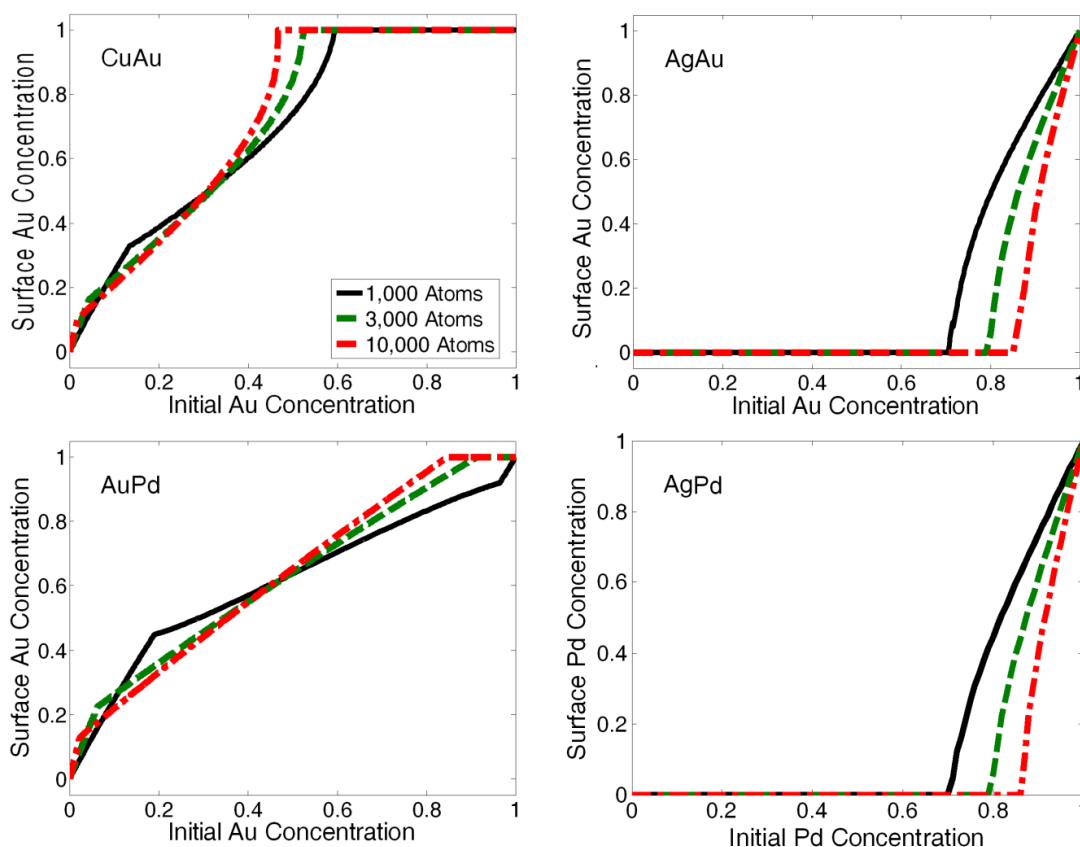


Figure 7.6 Effect of size and initial (homogeneous) composition on the equilibrium surface composition of alloy nanoparticles containing 1,000 (black solid line), 3,000 (green dashed line), and 10,000 (red dot-dashed line) atoms. Three different regimes can be seen in CuAu and AuPd, while two regimes are observed for AgAu and AgPd.

Whether an alloy will experience three or two regimes depends on the relative magnitude of its segregation and starvation energy. An empirical “rule-of-thumb” can be obtained from the four studied alloys, using the concept of “alloy strength”. The numerical “alloy strength” is defined as the largest value of the difference between the linear interpolation of bulk free energy and the actual bulk free energy. The alloy strength of AgAu, AgPd, AuPd, and CuAu is 0.65 %, 0.92 %, 1.1 %, and 1.2 %. The first two do not go through regime 2 and are thus called “weak” alloys. The last two have large enough starvation energies to sustain a bulk/surface duality, and are thus called “strong” alloys. Roughly, then, the turning point between weak and strong alloys is an alloy strength of 1 %. Of course this is just a estimate based on four data points. Note that the magnitude of the concentration-dependence of the surface free energy also matters, such that a moderately strong alloy with very large surface free energy variations could also sustain a surface/bulk equilibrium regime.

#### 7.4.3 Equilibrium Particle Shape

In addition to predicting the equilibrium surface concentration of alloy nanoparticles, the alloy Wulff construction can also model their equilibrium shape. The shape of a particle, as seen earlier (Chapters 3 - 5), is dictated by how much of each crystallographic face is present. This is particularly relevant for catalysis, as it is well-known that different crystallographic orientations have different catalytic activity and selectivity.<sup>293-295</sup>

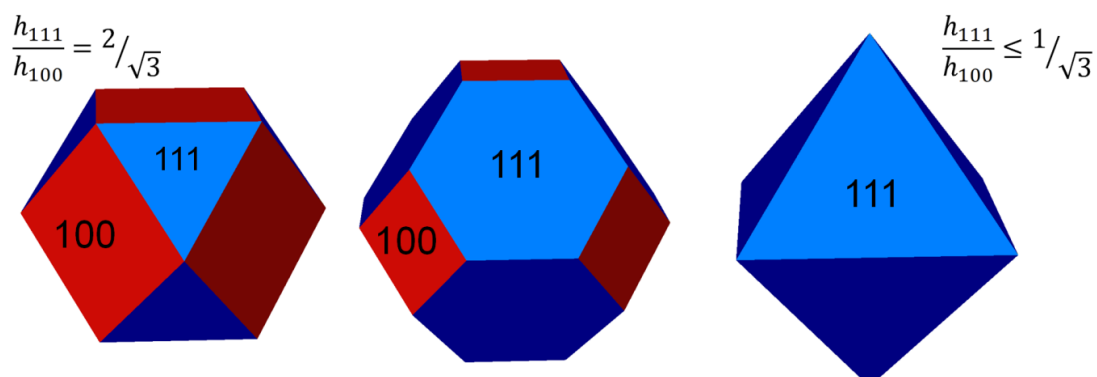


Figure 7.7 Shape of  $\{111\}$ -dominated particle and associated  $h_{111}/h_{100}$  values, from cuboctahedron to octahedron.

For the FCC materials chosen, CuAu, AgAu, AuPd, and AgPd, the surface energies at all homogeneous concentrations dictate a thermodynamic shape dominated by  $\{111\}$  faces, with small  $\{100\}$  faces and no  $\{110\}$ , yielding a structure which varies between a cuboctahedron and an octahedron (Figure 7.7). With this geometry, the only parameter necessary to describe the particle shape is the ratio of surface normals  $h_{111}/h_{100}$ . Note that a 100-dominated structure, with small 111 faces, could also be modeled, given some code changes when calculating the surface areas of  $\{100\}$  and  $\{111\}$  faces. A “if/else” statement could be included in the code to allow toggle between the two types of geometry. Also,  $\{110\}$  surfaces could be included with some additions to the surface area and energy computation; this was deemed not necessary in the studied cases because of the relatively high energy of this surface in FCC materials.

The equilibrium shape as a function of homogeneous concentration was calculated for all three models (basic Wulff, infinite reservoir, and alloy Wulff). Since no composition variation is allowed in the basic Wulff model, there is only one possible shape for each homogeneous

concentration. The  $h_{100}$  and  $h_{111}$  required to calculate the  $h_{111}/h_{100}$  were obtained using *wulffmodelbasic*. For the infinite reservoir and alloy Wulff, *wulffmodel2nostarvenergy* and *wulffmodel3* (respectively) were used to obtain  $h_{100}$ ,  $h_{111}$ , and Energy matrices for each possible combination of surface and bulk energy. These three matrices were then used as inputs in *h111\_h100nmatoms*, yielding the equilibrium values of  $h_{100}$ ,  $h_{111}$ , and  $h_{111}/h_{100}$ , as a function of homogeneous concentration.

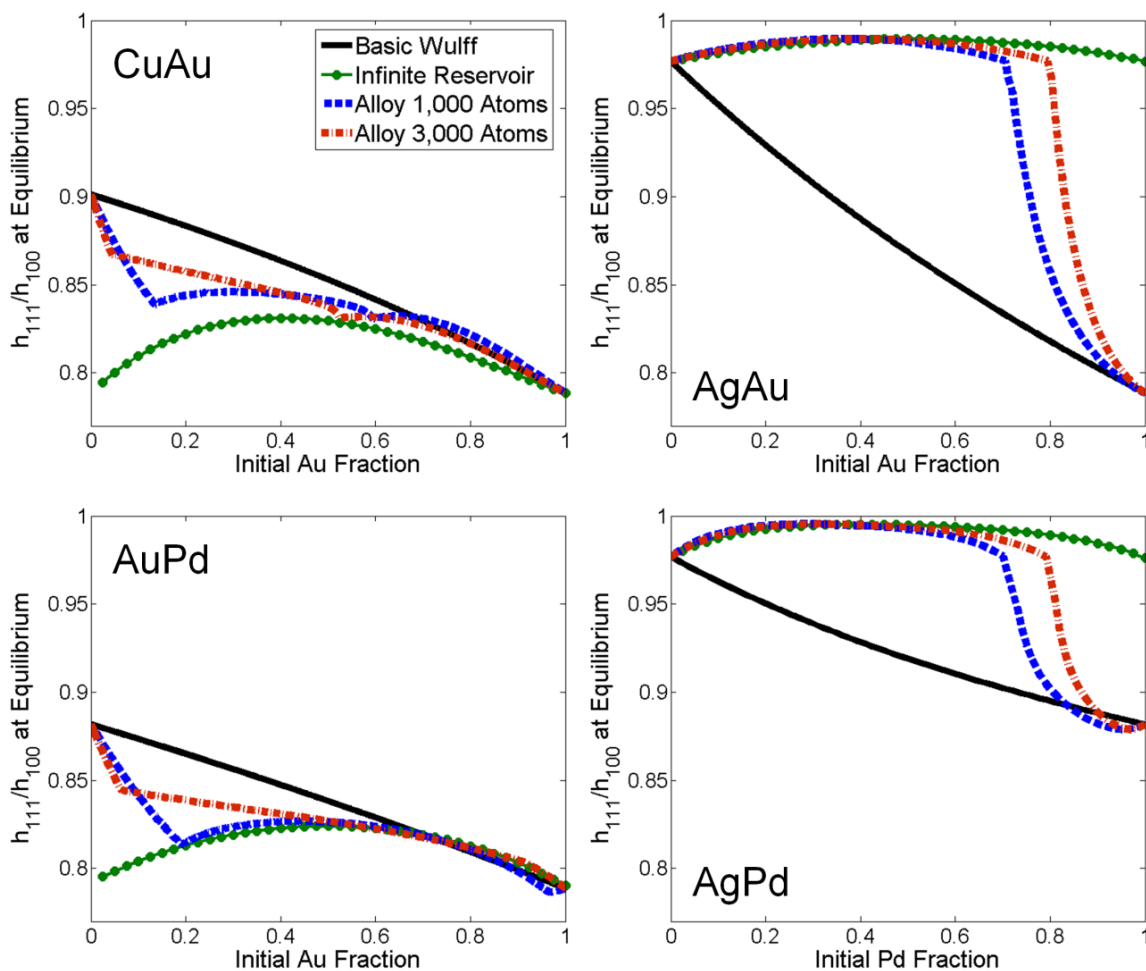


Figure 7.8 Effect of size and initial (homogeneous) composition on the equilibrium shape of alloy nanoparticles modeled using the basic Wulff (black line), infinite reservoir (green round markers), and alloy Wulff (containing 1,000 (blue dashed line) and 3,000 (red dot-dashed line) atoms). Three different regimes can be seen in CuAu and AuPd, while two regimes are observed for AgAu and AgPd.

The shape of some FCC alloys as a function of homogeneous concentration is presented in Figure 7.8. The basic Wulff and infinite reservoir approximation yield a smooth progression of

shape with composition, due to the composition-dependence of the surface energy ratio ( $\gamma_{111}/\gamma_{100}$ ), as seen in Figure 7.4. Shape modeling using the alloy Wulff construction yields rather interesting discontinuity points, much more pronounced than in the surface composition plots (Figure 7.6). Such discontinuities are due to the surface/bulk energy duality previously described; the discontinuity points correspond to regime changes. As previously observed AgAu and AgPd only goes through two regimes because of its low bulk energy variation (weak alloy).

Note that while the values of  $h_{111}/h_{100}$  seem to change only modestly, the impact on the relative surface areas ( $S_{111}/S_{100}$ ) is large, as can be seen in Figure 7.9. The  $h_{111}/h_{100}$  ratio only changes by 2 % (0.84 to 0.86) between a 1,000 and 3,000 atoms CuAu particle with homogeneous Au fraction of 0.2, but the ratio  $S_{111}/S_{100}$  changes by 26 % (1.9 to 2.4). Such changes in surface orientation are expected to make a difference in a variety of catalytic reactions.

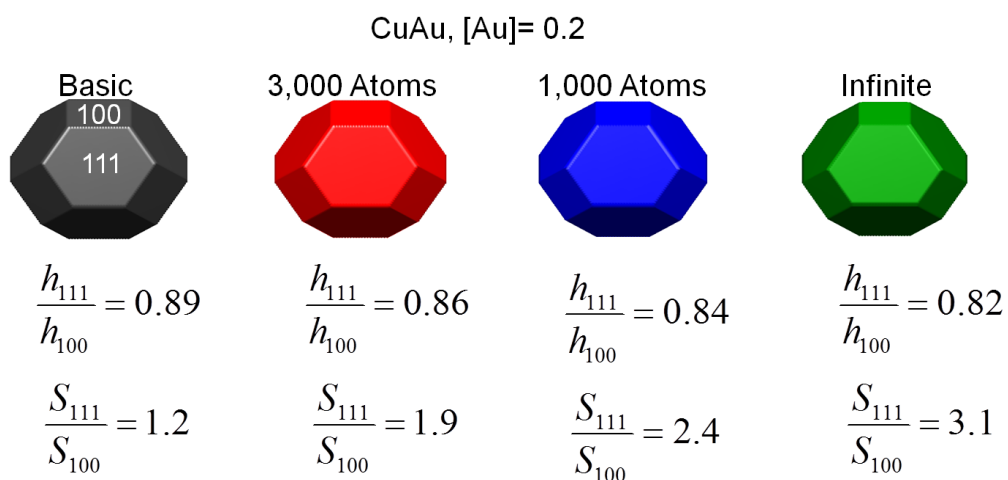


Figure 7.9 Shapes and surface area ratios predicted by different models for CuAu alloy with an homogeneous Au fraction of 0.2.

#### 7.4.4 Equilibrium Total Energy as a Function of Initial Composition

The total energy of an alloy nanoparticle can be calculated, in the alloy Wulff model, by adding the change in bulk free energy and the surface energy (Equation 7.26). Only the surface energy would be considered when calculating this value in the infinite reservoir approximation and basic Wulff models. Results for CuAu are presented in Figure 7.10, where it can clearly be seen that the presence of segregation always decreases the energy, i.e. the basic Wulff model always has the highest energy. Surprisingly, the infinite reservoir model has much lower energy than the alloy Wulff; this is due to the lack of mass conservation (no starvation) in the former.

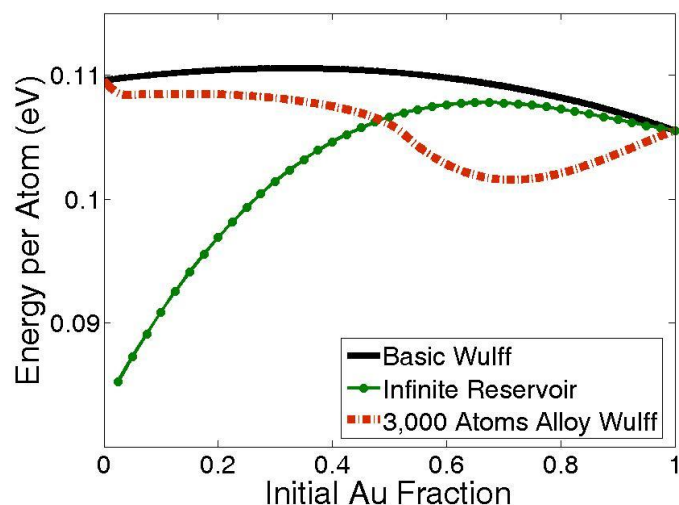


Figure 7.10. Total energy calculated for a 3,000 atoms CuAu nanoparticle, with the basic Wulff (black line), infinite reservoir approximation (green round markers), and alloy Wulff (red dot-dashed line).

#### 7.4.5 Size-Dependence of Results

The three segregation regimes encountered in alloy particle modeling result from the change in bulk concentration caused by a change in surface concentration, i.e., starvation. Nanoparticles have a size-dependent surface/bulk atoms ratio, leading to size-dependent starvation effects. This leads to the size dependence of the regime transition, and the size-dependence of particle shape for a given homogeneous composition. Note that shapes are completely size-independent for both the basic Wulff and the infinite reservoir approximation,.

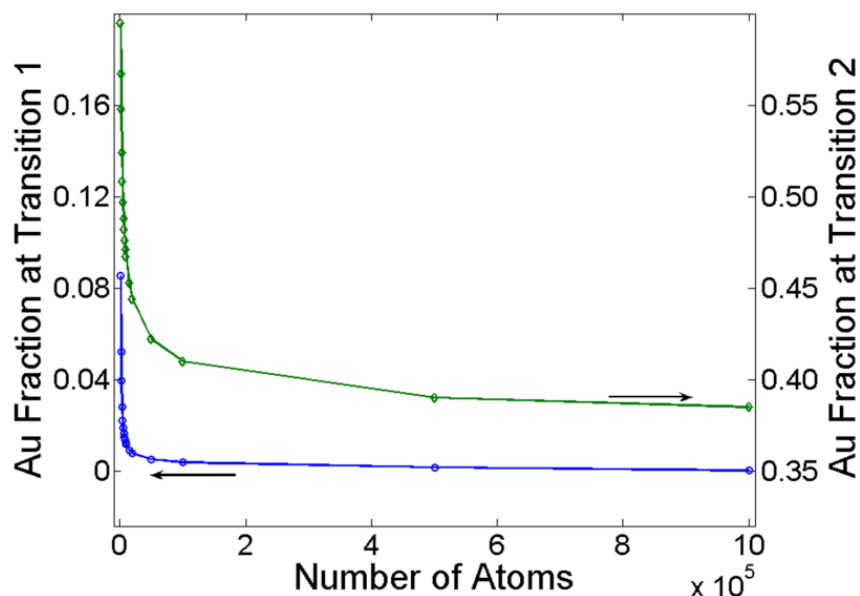


Figure 7.11 Size-dependence of transition 1 (regime 1 to 2, blue circles) and transition 2 (regime 2 to 3, green diamonds) for the strong alloy CuAu. The arrows point to the appropriate scale.

The size dependence of the regime transition was calculated by finding the exact position of the discontinuity in the composition-dependent equilibrium surface concentration. The same computational approach as in Section 7.4.2 was used, with much smaller calculation steps for

increased accuracy and calculation boundaries close to the expected transition to limit computation time. Results for the transition between de-alloying (regime 1) and bulk/surface equilibrium (regime 2), transition 1, for CuAu is presented in blue in Figure 7.11. This transition, the point at which the starvation (bulk) energy becomes comparable to the energy gained by surface compositional changes, is size-dependent up to about  $10^5$  atoms (approximately 15 nm in diameter). Transition 2, from surface/bulk equilibrium (regime 2) to monolayer formation (regime 3), occurs when starvation energy can no longer prevent the formation of a pure surface of the segregating component. This transition results in a very sharp change in shape and concentration and is size-dependent up to  $10^6$  atoms (approximately 35 nm in diameter), as shown in Figure 7.11.

## 7.5 Discussion

### 7.5.1 Comparison with Previous Models

The results of alloy nanoparticles modeling with the alloy Wulff construction are significantly different than what is obtained when using the basic Wulff construction, i.e., assuming composition homogeneity. Since lowering of energy through segregation is not allowed in the latter, the particle is practically never modeled at its equilibrium configuration. Figure 7.10 clearly shows that the total energy predicted by this simple model is always the highest. By respecting laws of conservation of mass and including energy-lowering composition changes neglected in the traditional Wulff and the infinite reservoir approximation, the current model provides a better thermodynamic description of alloy nanoparticles.

### 7.5.2 Comparison with Experimental Results

The alloy Wulff model yields size- and composition-dependent segregation and particle shape; these effects are technically observable using modern equipment, in particular with elemental mapping and structure determination in an (aberration-corrected) electron microscope. However, no systematic study was found in the literature, as no one specifically looked to validate or invalidate the current model; this may be a subject for future research.

Scattered results from multiple groups, however, provide strong evidence supporting the predictions of the alloy Wulff model. Formation of an Ag outer layer was observed in AgAu particles of diameters  $21 \pm 7$  and  $52 \pm 36$  nm, albeit the oxidizing environment also drives Ag to the surface.<sup>315</sup> Calcination at 200-400 °C of 20 nm AuPd particles of unspecified initial composition<sup>316</sup> lead to the formation of a Pd surface due to the higher affinity of Pd for O at such temperatures. Subsequent reduction at 500 °C<sup>316</sup> yielded the composition we predict, namely a Au-enriched surface. Nearly pure Ag surfaces (95-100 %) have been observed in bulk  $\text{Ag}_{33}\text{Pd}_{67}$  by STM,<sup>317</sup> while Auger electron spectroscopy of bulk  $\text{Ag}_{77}\text{Pd}_{23}$  gave mixed results, either with much Ag segregation or almost none, depending on the degree of data processing involved.<sup>318</sup>

However, morphology and composition profiles in the “strong” alloy nanoparticles uniquely modeled in the alloy Wulff construction have been barely studied. Extended x-ray absorption fine structure (EXAFS) was used to probe the environment around Cu and Au atoms in small (<10 nm) particles of the strong alloy CuAu with an homogeneous Au fraction of 0.56.<sup>319</sup> The results showed a lower average nearest neighbor for Au (11 vs. 12), consistent with partial

surface Au segregation, as predicted here (Figure 7.6). This indicates that bulk forces can indeed prevent full surface segregation, a feature the alloy Wulff construction takes into account in a unique and rigorous way. Unfortunately, the specific particle size, hence the exact degree of segregation, was not determined, leaving open questions. While the information available supports the alloy Wulff model, it also points to the lack of systematic experimental studies of alloy nanoparticle composition.

### 7.5.3 Model Limitation and Possible Extensions

Some assumptions had to be made when developing this model, most of which could be addressed by code improvements. The surface thickness  $\tau$  was taken as the distance between two equivalent planes, i.e.  $c/2$  and  $\sqrt{3}c/3$  for  $\{100\}$  and  $\{111\}$  faces, respectively, and identical segregation for all faces was assumed. These assumptions could be modified by simple code changes allowing face-dependent segregation as well as segregation gradients.

Many extensions are possible, with a range of implementing difficulty. As previously mentioned, the model can be slightly modified to accommodate  $\{100\}$ -dominated shapes, and shapes containing other facets, e.g.,  $\{110\}$ . Materials other than FCC can also be included rather easily.

An interesting and relevant extension of the alloy Wulff would be to twinned particles, in order to model segregation not only at the surface but also at the twin boundaries; both are expected to lead to significant shape changes. Segregation at the interface could also be modeled with an alloy Winterbottom or Summertop construction.

## CHAPTER 8

### The Kinetic Wulff Construction for Twinned Nanoparticles

## 8.1 Introduction: Nanoparticle Growth and Modeling

Crystal shape is important in a variety of applications, such that several modeling approaches aimed at finding the absolute minimum energy configuration have been developed. They include the Wulff construction,<sup>6,7,9</sup> the Winterbottom construction,<sup>3</sup> the Summertop construction<sup>160</sup>, the modified Wulff construction,<sup>165,320</sup> and the alloy Wulff construction.<sup>321</sup> An overview of these models can be found in Chapters 1 and 7.

Recently, advances in nanoparticle synthesis<sup>107,119,122,126,127,129,187,223,294</sup> has been driven by research in shape-dependent properties such as catalysis,<sup>124,197,292-294</sup> plasmon resonance frequency,<sup>52,62,68,100,109,122,127,183,187,198,214</sup> and field enhancement,<sup>99,213,216,322</sup> to name a few. An extensive library of possible shapes has thus been built.

Thermodynamic, Wulff-like models provide a useful understanding of several of these nanoparticle shapes, yet they cannot predict or rationalize many others. For example, the Au decahedra studied in Chapters 4 and 5 are significantly sharper than any Au decahedra (thermodynamically) modeled by the modified Wulff construction.<sup>165</sup>

The general argument used to explain the growth and relative stability of non-thermodynamic shapes is "kinetics", as in ref.<sup>223</sup>: "These results suggest that these reaction products arise from kinetic effects rather than thermodynamic effects". In the realm of particle growth, kinetics refers mainly to nucleation and to the flow of atoms from the solution to the growing particle. Hence, kinetics are responsible for a given shape if specific faces grow faster than what would be expected from their surface free energy. Such a statement, however, does not explain why a surface grows faster or how much faster it grows. Additionally, attributing a shape to "kinetics"

does not typically help understand or predict reaction outcomes. In this Chapter, the kinetic Wulff model is developed as a formal mathematical approach to growth modeling for twinned nanoparticles. Before discussing this new model, however, a short review of the modified Wulff construction is presented with examples from the recent nanoparticle synthesis literature. MATLAB codes for thermodynamic and kinetic modeling of twinned particles, as well as a graphical user interface, can be found in Appendix A.

## 8.2 The Modified Wulff Construction

The thermodynamic shape of a single crystal is defined by the ratio of its surface energies (as Discussed in Chapter 1), according to the Wulff construction,

$$h_{hkl} = Constant * \gamma_{hkl} \quad (8.1)$$

Where  $h_{hkl}$  is the length of the normal between the center of the particle and the crystallographic face  $hkl$  and  $\gamma_{hkl}$  is the surface energy of the  $hkl$  face. This model has been referred to as the basic Wulff construction in the previous Chapter, and codes to generate such Wulff shapes are available in Appendix A. This model is only valid for single crystals, such that the modified Wulff construction must be used in the presence of twinning. The simplest cases of twinned particles are when  $\alpha = 1/2$ , i.e. symmetric solutions.<sup>165</sup>

The shape of the particle is in part determined by the number of twins present and their symmetry. A single twin plane produces singly twinned particles and parallel planes produce

lamellar-twinned particles (LTP) such as the ones first observed in Argon smokes.<sup>164</sup> Higher symmetry shapes are obtained from segment assembly: five segments each bounded by two non-parallel planes give a decahedral particle (Dh), while twenty segments bounded by three non-parallel boundaries produce an icosahedral shape (Ic).<sup>13,17,24,25,165,320</sup> Note that this leads to a family of structures defined by the number of twinned segments, not by the external surface. For instance, a regular icosahedron is obtained if only  $\{111\}$  and  $\{100\}$  facets are present, but more complicated yet related structures arise if  $\{110\}$  facets are of low energy. By symmetry, it is simple to show that an equal partition is a stationary solution. Numerical calculations for a Dh yield a minimum for only  $\{111\}$  and  $\{100\}$  faceting<sup>23</sup> although it is a saddle-point for an isotropic surface free energy.<sup>165,320</sup> There is currently no analytical distinction of when a given shape is a minimum or a saddle point. Asymmetric partitioning of the twin boundary is also possible, leading to the asymmetric nanoparticle structures sometimes found experimentally.<sup>165</sup> Note that, with clean surfaces the twin-boundary energy is small compared to the surface free-energies of interest so it can be taken as zero, in which case the twin facets pass through the origin of the Wulff construction.<sup>165,320</sup> This approximation is accurate to second-order in the energy,<sup>165,320</sup> and the difference in the shape will be below experimental error for vacuum or argon smoke experiments. For solvent-based growth the surface free energies will be substantially lower, in which case they may be evident, as recently shown in large Dh structures.<sup>323</sup>

Decahedral particles are of particular interest for plasmonics because of their high refractive index sensitivity and stability. Thus, this shape will be used to illustrate the thermodynamic Wulff construction. For FCC materials, the  $\{110\}$  surface is rarely present such that it will be

omitted. Note, however, that all codes used require a {110} energy value as an input parameter; generally it was set to a number at least twice as large as the lowest surface energy. Detailed parameters for all the Figures in this Chapter can be found in Tables 8.1 and 8.2. For thermodynamic shape modeling, the kinetic functions KWulffmodelpenta (for Dh) and KWulffmodelmono (for monotwin) were used with the kinetic inputs set to zero; both functions are part of the GUI code. Assuming that the surface energies are similar to those of a broken bond model,<sup>324</sup> i.e. that the energy of {111} faces is less than that of the {100} faces ( $\gamma_{111}/\gamma_{100} = \sqrt{3}/2$ ), one gets the Marks decahedron with re-entrant surfaces at the twin boundaries (Figure 8.1, left panel).<sup>165,320</sup> If the free energy of the {100} facets is decreased such that it is lower than the energy of the {111} facets ( $\gamma_{111}/\gamma_{100} > 2/\sqrt{3}$ ), the notches disappear and the particle elongates to a rod-like shape similar to that first investigated by Ino<sup>13,17,18</sup> (Figure 8.1, middle panel). If instead the {100} energy is increased and is much larger than the {111} energy ( $\gamma_{111}/\gamma_{100} \ll 1$ ), the {100} faces no longer appear in the minimal energy shape, and the result is a star decahedron (Figure 8.1, right panel), similar to those recently synthesized by the Xia group.<sup>325</sup> Such changes in surface energy can occur in the presence of stabilizing molecules such as surfactant (in the liquid phase) or chemisorbed species (in the gas phase). Addition of {110} facets will lead to more rounded structures, as will inclusion of other higher-index surface facets if these are of low enough surface free energy. Note that all these structures are related and all will contain a wedge disclination and/or strain-relieving dislocations, as mentioned earlier they only differ in which surfaces are of lowest energy. While they may have different properties, we argue that they should all be considered as members of a class of nanoparticles, not as different entities.

While the modified Wulff construction has proved to be successful to rationalize some observations, most notably for the Dh where one has a somewhat surprising re-entrant surface in the thermodynamically lowest-energy shape, it does not explain everything. One of the simplest example is a regular decahedron with only  $\{111\}$  facets: no thermodynamic argument will give this shape as a minimum-energy configuration – that it is a minimum-energy shape is a common misconception. Other shapes which cannot be explained are sharp bipyramids which have been synthesized using various protocols<sup>126,131,132,246</sup> as well as truncated bitetrahedra, triangular platelets, and Dh rods. In many papers this has been loosely attributed to “kinetics”; we now turn to put this on a firmer foundation.

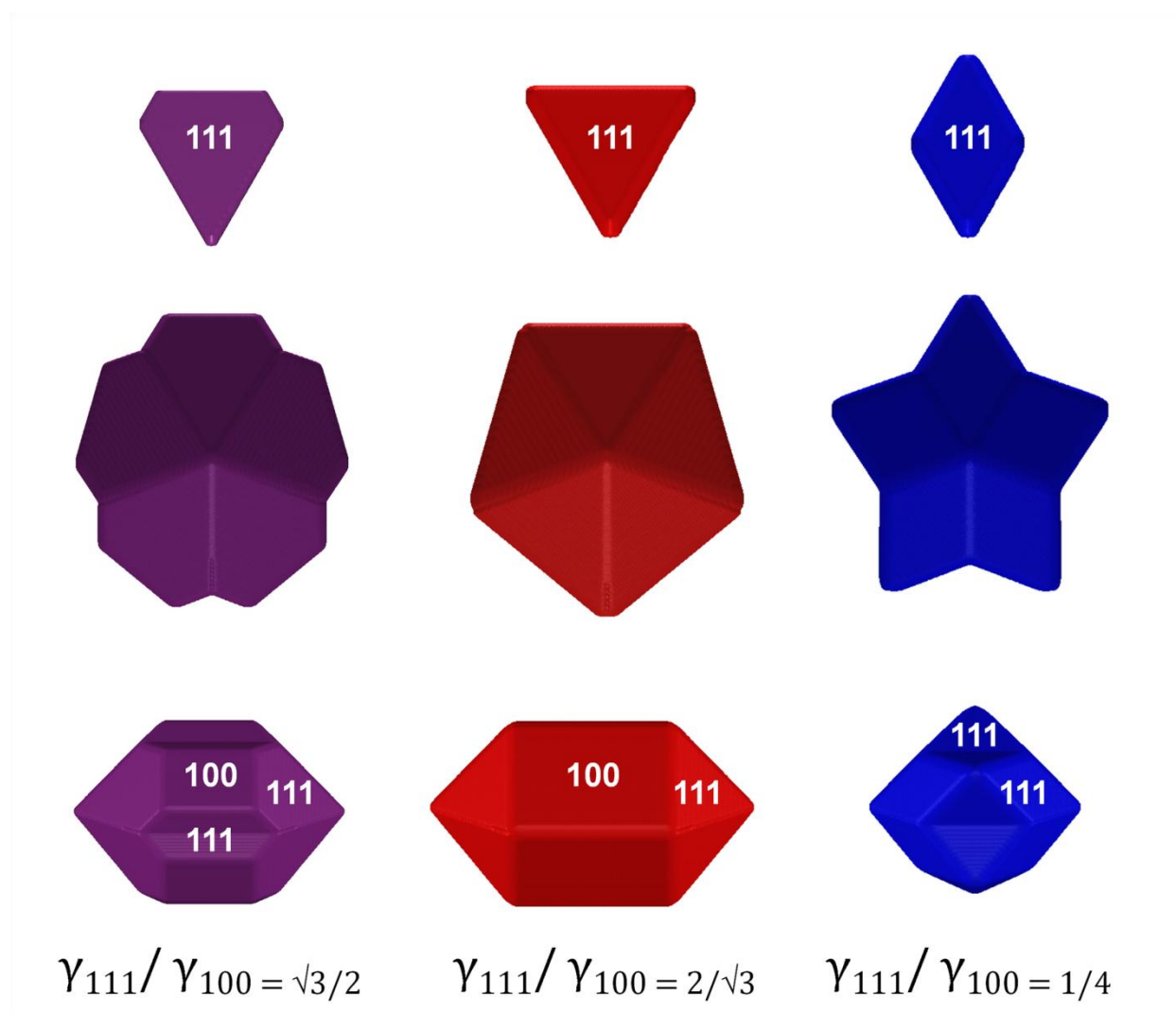


Figure 8.1. Thermodynamic Dh shape as a function of relative surface energy of {100} and {111} faces. Left: Marks decahedron, re-entrant surfaces are obtained when the energy assumed is that of the broken bond model ( $\gamma_{111}/\gamma_{100} = \sqrt{3}/2$ ). Middle: Ino decahedron, an elongated decahedron/pentagonal rod without notches, obtained by lowering the {100} surface energy to  $\gamma_{111}/\gamma_{100} = 2/\sqrt{3}$ . Right: star decahedron obtained by destabilizing the {100} faces ( $\gamma_{111}/\gamma_{100} = 1/4$ ).

Table 8.1. Parameters Used for Thermodynamic Shape Modeling (Figure 8.1).

	$\gamma_{111}/\gamma_{100}$	$\gamma_{100}$	$\gamma_{110}$	$\gamma_{111}$
Marks Dh	$\sqrt{3}/2$	10.69	20.05	9.26
Ino Dh	$2/\sqrt{3}$	5.59	27.95	6.46
Star Dh	1/4	16	20	4

Table 8.2. Parameters Used for Kinetic Shape Modeling (Figures 8.4-8.5).

	$v_{111}/v_{100}$	$v_{100}$	$v_{110}$	$v_{111}$	$\varphi_{re-entrant}$	$\varphi_{twin}$	$\varphi_{disclination}$
3a: Marks	$\sqrt{3}/2$	8	15	6.93	0	0	0
3b: Ino-like	$\sqrt{3}/2$	8	15	6.93	1	0	0
3c: Perfect Dh	7/12	10.6	13.2	6.16	1	0	0
3d: Sharp Dh Rod	$\sqrt{3}/2$	8	15	6.93	0.5	0	0.5
4a: Thermo. Bipyramid	2	5	10	10	0	0	0
4b: Sharp Bipyramid	2	5	10	10	1	0	0
4c: Thin Triangular Platelet	0.1	9.61	14.42	0.961	4	5	0
4d: Truncated Bitetrahedra	0.1	9.61	14.42	0.961	1	0	0
4e: Thin Hexagonal Plate	0.1	9.61	14.42	0.961	0	5	0

### 8.3 Mathematical Derivation of the Kinetic Wulff Construction for Twinned Nanoparticles

#### 8.3.1 The kinetic Wulff Construction for Single Crystal

An analogue of the Wulff construction for kinetic problems is well-known, often called the kinetic Wulff construction.<sup>4</sup> For solidification problems this is generally considered via a time gradient of a continuous surface, and anisotropic effects are mainly associated with temperature and compositional gradients in the liquid phase.<sup>326,327</sup> For nanoparticles, however, the anisotropy of the growth rates may be much larger and can be deliberately controlled during the synthesis by, for example, surfactants<sup>119,122,131,187,223,328</sup> or underpotential deposition.<sup>130</sup>

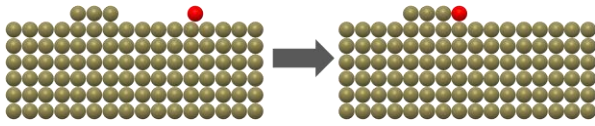


Figure 8.2. Schematic of step-flow growth. Left: initial nucleus formed on a flat surface and adatom. Right: adatom preferentially moves to step edge, providing a layer growth mechanism.

The kinetic Wulff construction implicitly assumes layer-by-layer growth; a small nucleus of atoms form on an otherwise perfectly flat surface then expands by step-flow growth as illustrated in Figure 8.2. For a particle with a set of facets each at a normal distance  $h_i(0)$  at time  $t = 0$  from the origin, given the growth velocity of each facet  $v_i$ , the shape as a function of time can be written as

$$\frac{dh_{i(t)}}{dt} = v_i \quad (8.2)$$

and this differential equation has a stationary, self-similar solution of

$$h_{i(t)} = Ctv_i \quad (8.3)$$

Where  $C$  is a constant, and  $Ct$  is analogous to the constant described in the single crystal kinetic Wulff construction by Frank:<sup>4</sup>

$$h_{hkl} = \text{Constant} * V_{hkl} \quad (8.4)$$

The vector normal to a surface facet “hkl”,  $h_{hkl}$ , is thus directly proportional to the growth velocity where  $V_{hkl}$  is the growth rate of facet “hkl”. Strictly speaking this solution and the following one (modified) are Lyapunov stable solutions. Lyapunov stability<sup>329</sup> is a way to describe a solution to a system of differential equations describing a dynamical system such as nanoparticle growth (Figure 8.3). Lyapunov stable solutions are not necessarily purely stationary. Rather, they are solutions (S) that oscillate close to the equilibrium (E), such that their distance from the equilibrium value is always less than a given (small,  $\delta$ ) value, as depicted in Figure 8.3. This means that the statistical distribution of shapes of an ensemble of many nanoparticles will be centered on the kinetic Wulff construction but with some variation about this; this is similar to the fact that water running downhill does not all go exactly along the bottom of the riverbed but oscillates about it. For completeness, we should mention that standard phase-field models for kinetics<sup>330</sup> can be used for the fine details, for instance the asymptotic convergence or oscillation about the Lyapunov solution. As a side note, not all plausible stationary solutions will be stable against perturbations (i.e. they are not Lyapunov stable), and there may be more than one such solution.

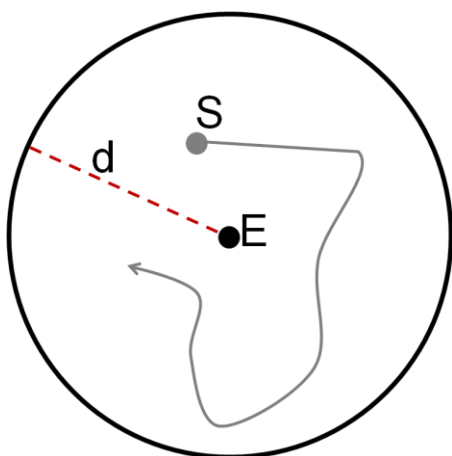


Figure 8.3. Lyapunov stability. The solution  $S$  is Lyapunov stable as it oscillates close to the equilibrium point  $E$ , within a region defined by  $d$ .

### 8.3.2 The kinetic Wulff Construction for Twinned Nanoparticles

So far the kinetic Wulff model is analogous to the traditional Wulff construction, except that kinetic inputs (growth rates) are used instead thermodynamic ones (surface free energies). For a twinned nanoparticle there is no flux of atoms to the internal twin boundary, thus zero growth velocity. Hence, as in the thermodynamic construction, we can separate the segments can be separated, a kinetic Wulff shape can be constructed for each, and then the can be reassembled into to a composite nanoparticle.

One critical addition is needed – accounting for enhanced growth associated with defects. The kinetic Wulff construction implicitly assumes layer-by-layer growth; a small nucleus of atoms form on an otherwise perfectly flat surface then expands by step-flow growth as illustrated in Figure 8.2. A significant kinetic limitation is the barrier to produce this initial nucleus. Any defects, for instance the disclination line along the 5-fold axis of a  $D_h$  or along twin boundaries

will have a smaller activation-energy barrier for this nucleation event. An enhancement term for facets adjacent to such defects need to be included, as they are more likely to form this nuclei, thus grow faster. For completeness, note that the idea of enhanced growth at defects for MTPs is not new, e.g.<sup>10</sup>, and the concept for general growth is implicit in the original work of Frank,<sup>4</sup> what is new here is mathematically coupling this with the modified Wulff construction.

This mathematical approach involves the assembly of twin segments (as in the modified Wulff construction) and the growth velocity enhancement at defect sites, parameterized via the constant  $\varphi$ , i.e.

$$G = (1 + \varphi) \frac{V_{hkl}}{\sqrt{h^2 + k^2 + l^2}} [h, k, l] \quad (8.5)$$

$$\varphi = \varphi_{re-entrant} + \varphi_{twin} + \varphi_{disclination} \quad (8.6)$$

For a re-entrant surface we enhance only the faces that form the notch {111}-type for Dh; {100}-type for LTP). Twin-enhanced growth involves enhancing any facet adjacent to the twin boundary, for example both {111} and re-entrant {100} in a LTP. Disclination-assisted growth involves facets adjacent to the central disclinations in a Dh, i.e. the 10 {111} facets present in a perfect Dh. Note that disclination assisted growth for an Ic is also possible, but in general will not give anything more than a regular Ic so will not be discussed further here. The twin boundary energy was set to zero, but this could be modified given a few generalizations of the code.

## 8.4 Examples of Shape Modeling Using the Kinetic Wulff Construction for Twinned Nanoparticles

### 8.4.1 Singly Twinned Particles

Lamellar twinned particles (LTP) are commonly found in seeds as well as final synthesis products;<sup>126,132,246,247</sup> particles containing a single twin plane or a closely spaced set of planes can be modeled using the function KWulffmodelmono or the GUI available in Appendix A. As shown in Figure 8.4, a plethora of related shapes can be obtained depending on the growth conditions, described in Table 8.2. Note that except for the top left shape, none of the structures in Figure 8.4 can be obtained from the thermodynamic Wulff construction; they all require kinetic growth enhancement.

As Shown in the top panel of Figure 8.4, the thermodynamic shape for a LTP with low  $\{100\}$  surface free energy becomes a sharp bipyramid when modeled with fast  $\{111\}$  growth (slow  $\{100\}$  growth) and enhanced growth at the re-entrant surfaces. When modeled with fast  $\{100\}$  growth (slow  $\{111\}$  growth, equivalent to low  $\{111\}$  surface free energy), a flat hexagon, truncated bitetrahedron, or flat triangular platelet is obtained depending upon whether the enhancement is applied at the twin plane, the re-entrant surface, or both, respectively (Figure 8.4, bottom). These structures can all be obtained experimentally.

Sharp Ag bipyramids (Figures 2.5 and 8.4) have been synthesized in both PVP, a  $\{100\}$ -stabilizing surfactant<sup>95,122,126,127</sup> for Ag and BSPP, a surfactant without strong preferential stabilization,<sup>131,132</sup> confirming the importance of kinetic control of the reaction.

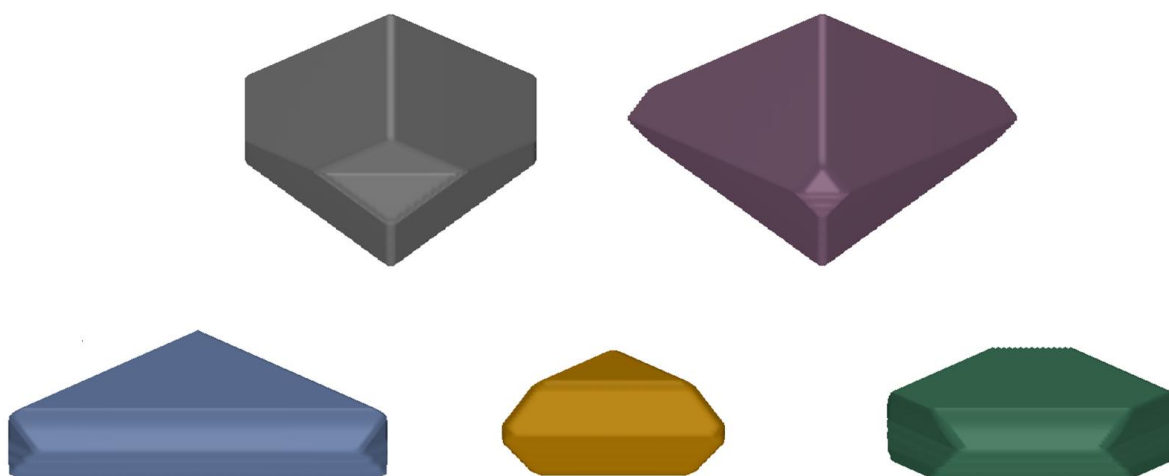


Figure 8.4. Singly twinned particle shape as a function of relative surface energy and kinetic growth enhancement. Top left: particle with fast  $\{111\}$  growth and no kinetic enhancement (thermodynamic structure). Top right: sharp bipyramid obtained with fast  $\{111\}$  growth and kinetic enhancement at the re-entrant surfaces. Bottom left: thin triangular platelet obtained with fast  $\{100\}$  growth and enhancement at both re-entrant surfaces and twin plane. Bottom middle: truncated bitetrahedron obtained with fast  $\{100\}$  growth and enhanced growth at the re-entrant surfaces. Bottom right: thin hexagonal platelet obtained with fast  $\{100\}$  growth and enhanced twin growth

The  $\{111\}$ -dominated LTP modeled with the kinetic modified Wulff construction (Figure 8.4, bottom) have also been widely observed in reaction products. Thick triangular structures, i.e. truncated bitetrahedra (Figures 2.2, 2.3, and 4.2, amongst others) are produced under weak kinetic control, with only a small enhancement at re-entrant surfaces, as is the case for perfect Dh (Figure 8.5, see Section 8.4.2).

In fact, truncated bitetrahedra and perfect Dh (pentagonal bipyramids) are abundantly obtained in similar experimental growth conditions.<sup>139</sup> Interestingly, such PVP-based synthesis also yields icosahedra and hexagonal plates, as shown in Figure 2.2. Indeed, PVP has been shown repeatedly to yield {111}-terminated Au particles,<sup>82,122,127,129,139,187,198,331</sup> unless Ag underpotential deposition is also present.<sup>122,129,130,187,198,331</sup> Ic emerge from seeds with 20 twin segments, as discussed earlier. The origin of hexagonal plates is not as straightforward, however. In our model, we can obtain this structure with fast {100} growth and enhanced twin growth (Figure 4, bottom right), meaning that all faces adjacent to the twin plane are growing equally fast. Following Lofton and Sigmund's framework for understanding re-entrant surfaces in thin plates,<sup>332</sup> this isotropy can occur in a particle with an even number of parallel twin planes; see also the earlier work on Argon smokes<sup>164</sup> for a larger database of simple twins and more crystallographies. Finally, thin triangular platelets (Figure 8.4, bottom left) have been known and studied for over a decade,<sup>20,84,90,103,107,133,143,149,216,247,332</sup> and kinetic control has been invoked repeatedly to explain their formation and fast degradation; in our model, strong kinetic enhancement (both at the twin and re-entrant surfaces) is indeed needed to obtain this shape.

#### 8.4.2 Decahedral (5-Fold Twin) Nanoparticles

Decahedral particles, containing five non-parallel {111} twin boundaries, can be modeled with the KWulffmodelpenta code or the Modified Wulff Construction GUI, both provided in Appendix A. As illustrated in Figure 8.5, if the growth rate of {100} is fast (expected for FCC particles) and there is enhanced growth at the re-entrant surfaces, a sharp analogue of the Marks

decahedron is formed (Figure 8.5, top right). If, in addition to re-entrant growth enhancement, the  $\{111\}$  facets grow more slowly (due to surfactants for example), sharp pentagonal bipyramids are formed (Figure 8.5, middle right), similar to that commonly obtained experimentally (Figures 2.2, 2.3, and 4.2, amongst others).<sup>67,82,139,177</sup> With enhanced re-entrant and disclination growth, rods are formed (Figure 8.5, bottom right) and depending upon which faces grow fast and slow there will be a range of different end results, which is consistent with the many different reports in the literature.<sup>67,82,94,128,137,139,333-337</sup> Note that similar to the thermodynamic shapes, these are not fundamentally different particles, just different end results that one can obtain by varying the kinetics of growth.

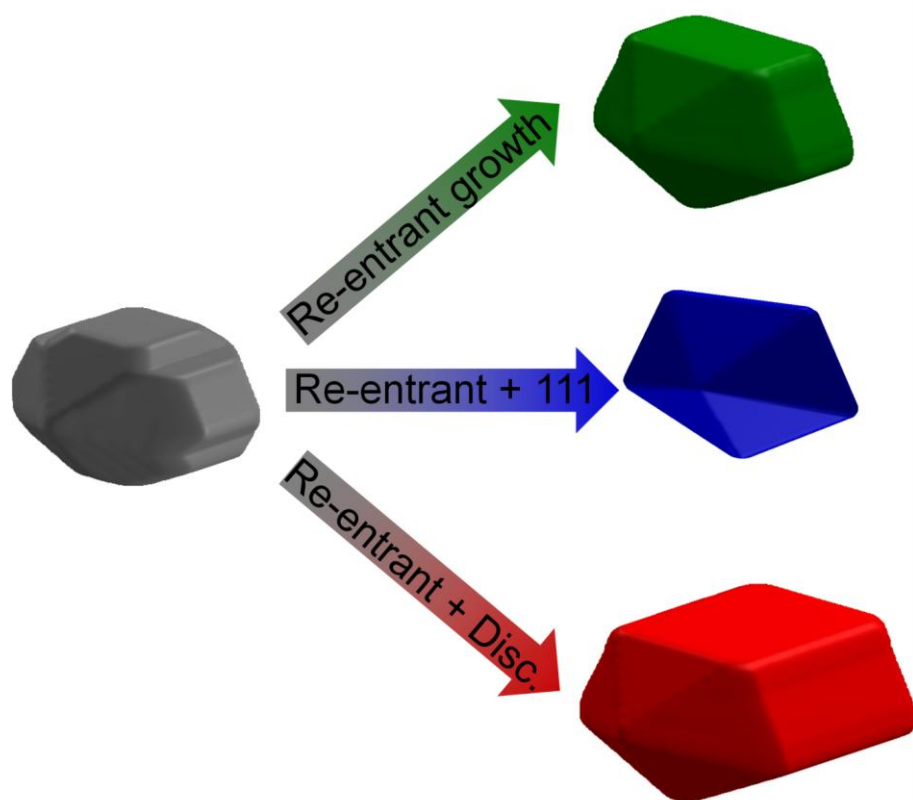


Figure 8.5. Effect of kinetic growth on Dh modeled with the Kinetic Modified Wulff construction. All particles except the blue shape in the middle right have identical  $V_{hkl}$  parameters equivalent to  $\gamma_{111}/\gamma_{100} = \sqrt{3}/2$ . Left: Marks decahedron, the thermodynamic shape. Top right: sharp Ino-like decahedron produced with re-entrant surface growth enhancement ( $\varphi_r > 0$ , b). Middle right: a pentagonal bipyramid obtained with re-entrant growth and  $\{111\}$  surface stabilization occurs ( $\varphi_r > 0$ ,  $v_{111}/v_{100} = 7/12$ ). Bottom right: a perfect pentagonal rod obtained with both kinetic enhancements active ( $\varphi_d > 0$ ,  $\varphi_r > 0$ ).

## 8.5 Graphical User Interface for Thermodynamic and Kinetic Wulff Modeling.

To aid scientists curious about the Wulff model, a simple graphical user interface (GUI) was created using the MATLAB tool GUIDE. For completeness, the GUI includes modeling of single crystals, monotwins, and pentatwins. The current version does not include substrate effect (Winterbottom construction<sup>3</sup>) or icosahedral shapes, and is limited to FCC materials. The user notes and code are available in Appendix A and Chapter 2, respectively.

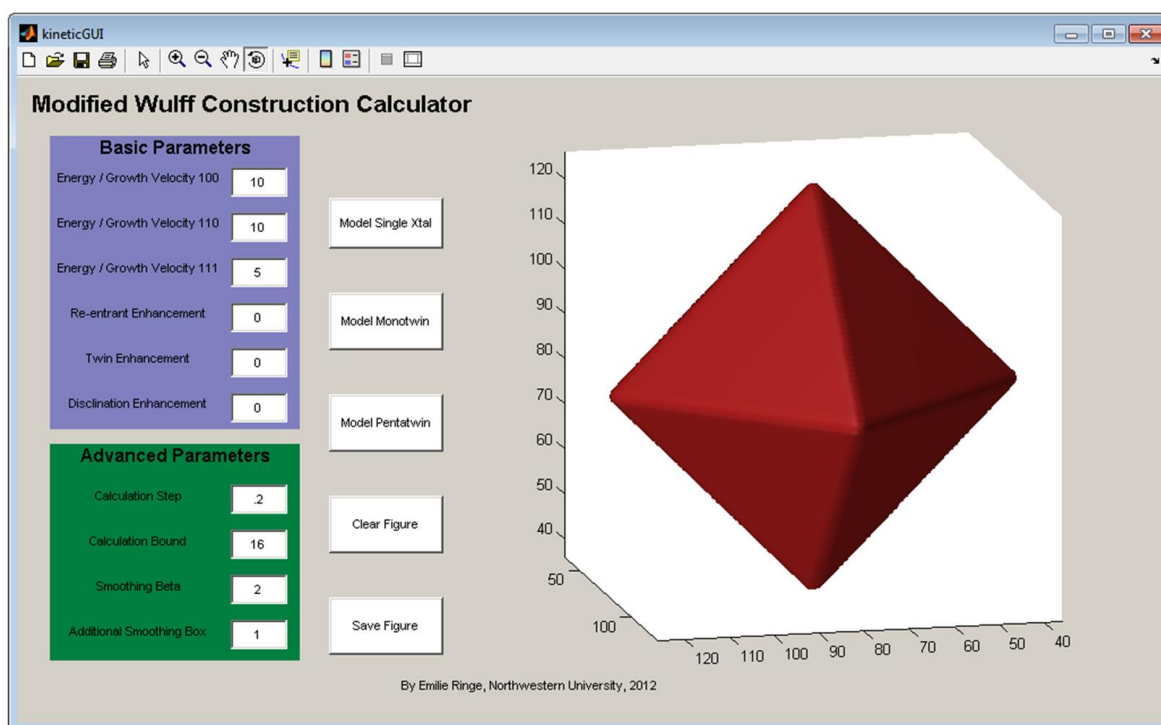


Figure 8.6. MATLAB graphical user interface developed to compute nanoparticle shape based on modified and single crystal Wulff models.

## 8.6 Discussion: Model Limitations and Possible Extensions

While clearly being successful at modeling non-thermodynamic shapes often found in colloidal synthesis, the modified kinetic Wulff developed here contains a few simplifications. Grouping the effects of defects and strain on the growth in a single enhancement factor is a reasonable first approximation, but the enhancement could in principle depend upon solution concentration for liquid-phase synthesis, or depend upon chemical potential gradients in a more exact model. This would be of interest to provide better modeling of nanoparticles on substrates, such as those used for heterogeneous catalysis. The kinetic model developed here is also implicitly for layer-by-layer growth (Figure 8.2) and may not be appropriate in other cases.

A variety of extensions can be applied to this model, some simple, other significantly more complex. In the first category falls adding velocity enhancements to a kinetic Winterbottom<sup>338</sup> or Summertop<sup>160</sup> construction (as was done for the kinetic modeling of two-dimensional island growth<sup>339</sup>). In this case, assuming a zero growth velocity at the particle/substrate interface renders these two models simple extensions of the current construction. More challenging yet feasible problems to tackle are allowing the twin boundary energy to vary, accounting for solution precursor concentration depletion, and including size-dependent growth enhancements (particularly at the disclination where stress relief mechanisms may vary with size).

Overall, this seemingly simple model provides a powerful and user-friendly (GUI available in Appendix A) tool to predict and understand a variety of non-thermodynamic shapes obtained in modern nanoparticle synthesis.

## REFERENCES

- 1 Faraday, M. The Bakerian Lecture: Experimental Relations of Gold (and Other Metals) to Light *Phil. Trans. R. Soc. Lond.* **147**, 145-181 (1857).
- 2 Mie, G. Beiträge zur Optik Trüber Medien, Speziell Kolloidaler Metallösungen. *Ann. Phys.* **25**, 377-445 (1908).
- 3 Winterbottom, W. L. Equilibrium Shape of a Small Particle in Contact with a Foreign Substrate. *Acta Metall.* **15**, 303 (1967).
- 4 Frank, F. C. in *Growth and Perfection of Crystals* (eds R. H. Doremus, B. W. Roberts, & D. Turnbull) (Wiley, 1958).
- 5 Herring, C. Some Theorems on the Free Energies of Crystal Surfaces. *Phys. Rev.* **82**, 87-93 (1951).
- 6 Dinghas, A. Über Einen Geometrischen Satz von Wulff für die Gleichgewichtsform von Kristallen. *Z. Kristallogr.* **105**, 304-314 (1944).
- 7 von Laue, M. Der Wulffsche Satz für die Gleichgewichtsform von Kristallen. *Z. Kristallogr.* **105**, 124-133 (1943).
- 8 Gans, R. Über die Form Ultramikroskopischer Goldteilchen. *Ann. Phys.* **342**, 881-900 (1912).
- 9 Wulff, G. Velocity of Growth and Dissolution of Crystal Faces. *Z. Kristallogr. Minera.* **34**, 449-530 (1901).
- 10 Marks, L. D. & Howie, A. Multiply-Twinned Particles in Silver Catalysts. *Nature* **282**, 196-198 (1979).
- 11 Sinfelt, J. H. Catalysis by Alloys and Bimetallic Clusters. *Acc. Chem. Res.* **10**, 15-20 (1977).
- 12 Yagi, K., Takayanagi, K., Kobayashi, K. & Honjo, G. In situ Observations of Growth Processes of Multiply Twinned Particles. *J. Cryst. Growth* **28**, 117-124 (1975).
- 13 Ino, S. Stability of Multiply-Twinned Particles. *J. Phys. Soc. Jpn* **27**, 941-953 (1969).
- 14 Komoda, T. Study on Structure of Evaporated Gold Particles by Means of a High Resolution Electron Microscope. *Jpn. J. Appl. Phys.* **7**, 27-30 (1968).
- 15 Komoda, T. Study on the Structure of Evaporated Gold Particles by Means of a High Resolution Electron Microscope. *Jpn. J. Appl. Phys.* **7**, 27-30 (1968).
- 16 Allpress, J. G. & Sanders, J. V. Structure And Orientation Of Crystals In Deposits Of Metals On Mica. *Surf. Sci.* **7**, 1-25 (1967).
- 17 Ino, S. & Ogawa, S. Multiply Twinned Particles At Earlier Stages Of Gold Film Formation On Alkali-halide Crystals. *J. Phys. Soc. Jpn* **22**, 1365-1374 (1967).
- 18 Ino, S. Epitaxial Growth of Metals on Rocksalt Faces Cleaved in Vacuum .2. Orientation and Structure of Gold Particles Formed in Ultrahigh Vacuum. *J. Phys. Soc. Jpn* **21**, 346-362 (1966).
- 19 Ajayan, P. M. & Marks, L. D. Phase Instabilities in Small Particles. *Phase Transitions* **24-6**, 229-258 (1990).

- 20 Kirkland, A. I., Edwards, P. P., Jefferson, D. A. & Duff, D. G. The Structure, Characterization, and Evolution of Colloidal Metals. *Prog. Chem. Sect. C: Phys. Chem.* **87**, 247-304 (1990).
- 21 Ajayan, P. M. & Marks, L. D. Experimental Evidence for Quasimelting in Small Particles. *Phys. Rev. Lett.* **63**, 279-282 (1989).
- 22 Ajayan, P. M. & Marks, L. D. Quasimelting and Phases of Small Particles. *Phys. Rev. Lett.* **60**, 585-587 (1988).
- 23 Dundurs, J., Marks, L. D. & Ajayan, P. M. Structural Fluctuations in Small Particles. *Philos. Mag. A* **57**, 605-620 (1988).
- 24 Marks, L. D. & Smith, D. J. High-Resolution Studies of Small Particles of Gold and Silver .1. Multiply-Twinned Particles. *J. Cryst. Growth* **54**, 425-432 (1981).
- 25 Smith, D. J. & Marks, L. D. High-Resolution Studies of Small Particles of Gold and Silver .2. Single-Crystals, Lamellar Twins and Polyparticles. *J. Cryst. Growth* **54**, 433-438 (1981).
- 26 Kneipp, K. *et al.* Single Molecule Detection Using Surface-Enhanced Raman Scattering (SERS). *Phys. Rev. Lett.* **78**, 1667-1670 (1997).
- 27 Nie, S. & Emory, S. R. Probing Single Molecules and Single Nanoparticles by Surface-Enhanced Raman Scattering. *Science* **275**, 1102-1106 (1997).
- 28 Van Duyne, R. P. & Haushalter, J. P. Resonant Raman Spectroelectrochemistry of Semiconductor Electrodes: the Photooxidation of Tetrathiafulvalene at n-Gallium Arsenide (100) in Acetonitrile. *J. Phys. Chem.* **88**, 2446-2451 (1984).
- 29 Jeanmaire, D. L. & Van Duyne, R. P. Surface Raman spectroelectrochemistry: Part I. Heterocyclic, Aromatic, and Aliphatic Amines Adsorbed on the Anodized Silver Electrode. *J. Electroanal. Chem.* **84**, 1-20 (1977).
- 30 T. Okamoto, I. Yamaguchi & Kobayashi, T. Local Plasmon Sensor with Gold Colloid Monolayers Deposited upon Glass Substrates. *Opt. Lett.* **25**, 372-374 (2000).
- 31 Jensen, T. R., Malinsky, M. D., Haynes, C. L. & Van Duyne, R. P. Nanosphere Lithography: Tunable Localized Surface Plasmon Resonance Spectra of Silver Nanoparticles. *J. Phys. Chem. B* **104**, 10549-10556 (2000).
- 32 Kano, H. & Knoll, W. A Scanning Microscope Employing Localized Surface-Plasmon-Polaritons as a Sensing Probe. *Opt. Comm.* **182**, 11-15 (2000).
- 33 Lyon, L. A., Musick, M. D. & Natan, M. J. Colloidal Au-Enhanced Surface Plasmon Resonance Immunosensing. *Anal. Chem.* **70**, 5177-5183 (1998).
- 34 Kahl, M., Voges, E., Kostrewa, S., Viets, C. & Hill, W. Periodically Structured Metallic Substrates for SERS. *Sens. Actuators, B* **51**, 285-291 (1998).
- 35 H. Wei, Z. Wang, X. Tian, M. Käll & Xu, H. Cascaded Logic Gates in Nanophotonic Plasmon Networks. *Nat. Comm.* **2**, 387 (2011).
- 36 M. Sukharev & Seideman, T. Phase and Polarization Control as a Route to Plasmonic Nanodevices. *Nano Lett.* **6**, 715-719 (2006).
- 37 Maksymov, I. S. Optical Switching and Logic Gates with Hybrid Plasmonic-Photonic Crystal Nanobeam Cavities. *Phys. Lett. A* **375**, 918-921 (2011).
- 38 V. E. Ferry, L. A. Sweatlock, D. Pacifici & Atwater, H. A. Plasmonic Nanostructure Design for Efficient Light Coupling into Solar Cells. *Nano Lett.* **8**, 4391-4397 (2008).

- 39 Maier, S. A. *et al.* Local Detection of Electromagnetic Energy Transport Below the Diffraction Limit in Metal Nanoparticle Plasmon Waveguides. *Nat. Mater.* **2**, 229-232 (2003).
- 40 Ferry, V. E. *et al.* Light Trapping in Ultrathin Plasmonic Solar Cells. *Opt. Express* **18**, 237-245 (2010).
- 41 J. A. Schuller *et al.* Plasmonics for Extreme Light Concentration and Manipulation. *Nat. Mater.* **9**, 193-204 (2010).
- 42 Zia, R., Schuller, J. A., Chandran, A. & Brongersma, M. L. Plasmonics - The Wave of Chip-Scale Device Technologies. *Mater. Today* **9**, 20-27 (2006).
- 43 S. A. Maier *et al.* Plasmonics - a Route to Nanoscale Optical Devices. *Adv. Mater.* **13**, 1501-1505 (2001).
- 44 K. R. Catchpole & Polman, A. Plasmonic Solar Cells. *Opt. Express* **16**, 21793-21800 (2008).
- 45 Dionne, J. A., Sweatlock, L. A., Atwater, H. A. & Polman, A. Plasmon Slot Waveguides: Towards Chip-Scale Propagation with Subwavelength-Scale Localization. *Phys. Rev. B* **73**, 035407 (2006).
- 46 W. H. Hung, M. Aykol, D. Valley, W. Hou & Cronin, S. B. Plasmon Resonant Enhancement of Carbon Monoxide Catalysis. *Nano Lett.* **10**, 1314-1318 (2010).
- 47 W. Houa, Z. Liub, P. Pavaskarc, W. H. Hungd & Cronin, S. B. Plasmonic Enhancement of Photocatalytic Decomposition of Methyl Orange Under Visible Light. *J. Catal.* **277**, 149-153 (2011).
- 48 A. L. Pyayt, B. Wiley, Y. Xia, A. Chen & Dalton, L. Integration of Photonic and Silver Nanowire Plasmonic Waveguides. *Nat. Nanotechnol.* **3**, 660-665 (2008).
- 49 Ebbesen, T. W., Genet, C. & Bozhevolnyi, S. I. Surface Plasmon Circuitry. *Physics Today* **61**, 44-50 (2008).
- 50 Johnson, P. B. & Christy, R. W. Optical Constants of Noble Metals. *Phys. Rev. B* **6**, 4370-4379 (1972).
- 51 Sharma, B., Frontiera, R. R., Henry, A.-I., Ringe, E. & Van Duyne, R. P. SERS: Materials, Applications, and the Future. *Mater. Today* **15**, 16-25 (2012).
- 52 Ringe, E. *et al.* Unraveling the Effects of Size, Composition, and Substrate on the Localized Surface Plasmon Resonance Frequencies of Gold and Silver Nanocubes: A Systematic Single-Particle Approach. *J. Phys. Chem. C* **114**, 12511-12516 (2010).
- 53 Bingham, J. M., Anker, J. N., Kreno, L. E. & Duyne, R. P. V. Gas Sensing with High-Resolution Localized Surface Plasmon Resonance Spectroscopy. *J. Am. Chem. Soc.* **132**, 17358-17359 (2012).
- 54 Mayer, K. M. & Hafner, J. H. Localized Surface Plasmon Resonance Sensors. *Chem. Rev.* **111**, 3828-3857 (2011).
- 55 Hall, W. P., Ngatia, S. N. & Duyne, R. P. V. LSPR Biosensor Signal Enhancement Using Nanoparticle-Antibody Conjugates. *J. Phys. Chem. C* **115**, 1410-1414 (2011).
- 56 Huang, H., Liu, X., Liao, B. & Chu, P. K. A Localized Surface Plasmon Resonance Biosensor Based on Integrated Controllable Au<sub>2</sub>S/AuAgS-Coated Gold Nanorods Composite *Plasmonics* **6**, 1-9 (2011).

- 57 Zhang, S., Bao, K., Halas, N. J., Xu, H. & Nordlander, P. Substrate-Induced Fano Resonances of a Plasmonic Nanocube: A Route to Increased-Sensitivity Localized Surface Plasmon Resonance Sensors Revealed. *Nano Lett.* **11**, 1657-1663 (2011).
- 58 Lee, Y. H., Chen, H., Xu, Q.-H. & Wang, J. Refractive Index Sensitivities of Noble Metal Nanocrystals: The Effects of Multipolar Plasmon Resonances and the Metal Type. *J. Phys. Chem. C* **115**, 7997-8004 (2011).
- 59 Svedendahl, M., Chen, S., Dmitriev, A. & Käll, M. Refractometric Sensing Using Propagating versus LSPR: A Direct Comparison. *Nano Lett.* **9**, 4428-4433 (2009).
- 60 Murray, W. A., Auguié, B. & Barnes, W. L. Sensitivity of Localized Surface Plasmon Resonances to Bulk and Local Changes in the Optical Environment. *J. Phys. Chem. C* **113**, 5120-5125 (2009).
- 61 Galush, W. J. *et al.* A Nanocube Plasmonic Sensor for Molecular Binding on Membrane Surfaces. *Nano Lett.* **9**, 2077-2082 (2009).
- 62 Cobley, C. M., Skrabalak, S. E., Campbell, D. J. & Xia, Y. Shape-Controlled Synthesis of Silver Nanoparticles for Plasmonic and Sensing Applications. *Plasmonics* **4**, 171-179 (2009).
- 63 Sepúlveda, B., Angelomé, P. C., Lechuga, L. M. & Liz-Marzán, L. M. LSPR-Based Nanobiosensors. *Nano Today* **4**, 244-251 (2009).
- 64 Anker, J. N. *et al.* Biosensing with Plasmonic Nanosensors. *Nat. Mater.* **7**, 442-453 (2008).
- 65 Chen, H., Kou, X., Yang, Z., Ni, W. & Wang, J. Shape- and Size-Dependent Refractive Index Sensitivity of Gold Nanoparticles. *Langmuir* **24**, 5233-5237 (2008).
- 66 Willets, K. A. & Van Duyne, R. P. Localized Surface Plasmon Resonance Spectroscopy and Sensing. *Annu. Rev. Phys. Chem.* **58**, 267-297 (2007).
- 67 Pastoriza-Santos, I., Sánchez-Iglesias, A., García de Abajo, F. J. & Liz-Marzán, L. M. Environmental Optical Sensitivity of Gold Nanodecahedra. *Adv. Funct. Mater.* **17**, 1443-1450 (2007).
- 68 Lee, K.-S. & El-Sayed, M. A. Gold and Silver Nanoparticles in Sensing and Imaging: Sensitivity of Plasmon Response to Size, Shape, and Metal Composition. *J. Phys. Chem. B* **110**, 19220-19225 (2006).
- 69 Haes, A. J., Chang, L., Klein, W. L. & Van Duyne, R. P. Detection of a Biomarker for Alzheimer's Disease from Synthetic and Clinical Samples Using a Nanoscale Optical Biosensor. *J. Am. Chem. Soc.* **127**, 2264-2271, doi:10.1021/ja044087q (2005).
- 70 A. V. Whitney *et al.* Localized Surface Plasmon Resonance Nanosensor: A High-Resolution Distance-Dependence Study Using Atomic Layer Deposition. *J. Phys. Chem. B* **109**, 20522-20528 (2005).
- 71 A. J. Haes, S. Zou, G. C. Schatz & Van Duyne, R. P. Nanoscale Optical Biosensor: Short Range Distance Dependence of the Localized Surface Plasmon Resonance of Noble Metal Nanoparticles. *J. Phys. Chem. B* **108**, 6961-6968 (2004).
- 72 McFarland, A. D. & Van Duyne, R. P. Single Silver Nanoparticles as Real-Time Optical Sensors with Zeptomole Sensitivity. *Nano Lett.* **3**, 1057-1062 (2003).
- 73 Haes, A. J. & Van Duyne, R. P. A Nanoscale Optical Biosensor: Sensitivity and Selectivity of an Approach Based on the Localized Surface Plasmon Resonance

- Spectroscopy of Triangular Silver Nanoparticles. *J. Am. Chem. Soc.* **124**, 10596-10604 (2002).
- 74 Cortie, M. B. & McDonagh, A. M. Synthesis and Optical Properties of Hybrid and Alloy Plasmonic Nanoparticles. *Chem. Rev.* **111**, 3713-3735 (2011).
- 75 Wilcoxon, J. Optical Absorption Properties of Dispersed Gold and Silver Alloy Nanoparticles. *J. Phys. Chem. B* **113**, 2647-2656 (2009).
- 76 Jellinek, J. Nanoalloys: Tuning Properties and Characteristics Through Size and Composition. *Faraday Discuss.* **138**, 11-35 (2008).
- 77 Sharma, A. K. & Mohr, G. J. On the Performance of Surface Plasmon Resonance Based Fibre Optic Sensor with Different Bimetallic Nanoparticle Alloy Combinations. *J. Phys. D: Appl. Phys.* **41**, 055106 (2008).
- 78 Song, J., Li, H., Li, J. & Zhou, S. Fabrication and Optical Properties of Metastable Cu–Ag Alloys. *Appl. Opt.* **41**, 5413-5416 (2002).
- 79 Link, S., Wang, Z. L. & El-Sayed, M. A. Alloy Formation of Gold-Silver Nanoparticles and the Dependence of the Plasmon Absorption on Their Composition. *J. Phys. Chem. B* **103**, 3529-3533 (1999).
- 80 Bohren, C. F. & Huffman, D. R. *Absorption and Scattering of Light by Small Particles*. (Wiley, 1983).
- 81 Myroshnychenko, V. *et al.* Modelling the Optical Response of Gold Nanoparticles. *Chem. Soc. Rev.* **37**, 1792-1805 (2008).
- 82 Rodríguez-Fernández, J. *et al.* Spectroscopy, Imaging, and Modeling of Individual Gold Decahedra. *J. Phys. Chem. C* **113**, 18623-18631, doi:10.1021/jp907646d (2009).
- 83 Bingham, J. M., Willets, K. A., Shah, N. C., Andrews, D. Q. & Van Duyne, R. P. LSPR Imaging: Simultaneous Single Nanoparticle Spectroscopy and Diffusional Dynamics. *J. Phys. Chem. C* **113**, 16839-16843 (2009).
- 84 Munechika, K., Smith, J. M., Chen, Y. & Ginger, D. S. Plasmon Line Widths of Single Silver Nanoprisms as a Function of Particle Size and Plasmon Peak Position. *J. Phys. Chem. C* **111**, 18906-18911 (2007).
- 85 Wiley, B. J. *et al.* Synthesis and Optical Properties of Silver Nanobars and Nanorice. *Nano Lett.* **7**, 1032-1036 (2007).
- 86 Ringe, E. *et al.* Plasmon Length: A Universal Parameter to Describe Size Effects in Gold Nanoparticles. *J. Phys. Chem. Lett.* **3**, 1479-1483 (2012).
- 87 Henry, A.-I. *et al.* Correlated Structure and Optical Property Studies of Plasmonic Nanoparticles. *J. Phys. Chem. C* **115**, 9291-9305 (2011).
- 88 Morton, S. M., Silverstein, D. W. & Jensen, L. Theoretical Studies of Plasmonics using Electronic Structure Methods. *Chem. Rev.* **111**, 3962-3994 (2011).
- 89 Halas, N. J., Lal, S., Chang, W.-S., Link, S. & Nordlander, P. Plasmons in Strongly Coupled Metallic Nanostructures. *Chem. Rev.* **111**, 3913-3961 (2011).
- 90 Nelayah, J. *et al.* Two-Dimensional Quasistatic Stationary Short Range Surface Plasmons in Flat Nanoprisms. *Nano Lett.* **10**, 902-907 (2010).
- 91 Tcherniak, A., Ha, J. W., Dominguez-Medina, S., Slaughter, L. S. & Link, S. Probing a Century Old Prediction One Plasmonic Particle at a Time. *Nano Lett.* **10**, 1398-1404 (2010).

- 92 Ringe, E. *et al.* Effect of Size, Shape, Composition, and Support Film on Localized Surface Plasmon Resonance Frequency: A Single Particle Approach Applied to Silver Bipyramids and Gold Nanocubes. *Mat. Res. Soc. Symp. Proc.* **1208**, O10-02 (2010).
- 93 Arnold, M. D. & Blaber, M. G. Optical Performance and Metallic Absorption in Nanoplasmonic Systems. *Opt. Express* **17**, 3835-3847 (2009).
- 94 Pietrobon, B., McEachran, M. & Kitaev, V. Synthesis of Size-Controlled Faceted Pentagonal Silver Nanorods with Tunable Plasmonic Properties and Self-Assembly of These Nanorods. *ACS Nano* **3**, 21-26 (2009).
- 95 Lu, X., Rycenga, M., Skrabalak, S. E., Wiley, B. J. & Xia, Y. Chemical Synthesis of Novel Plasmonic Nanoparticles. *Annu. Rev. Phys. Chem.* **60**, 167-192 (2009).
- 96 Zhou, F., Li, Z.-Y., Liu, Y. & Xia, Y. Quantitative Analysis of Dipole and Quadrupole Excitation in the Surface Plasmon Resonance of Metal Nanoparticles. *J. Phys. Chem. C* **112**, 20233-20240, doi:10.1021/jp807075f (2008).
- 97 Pecharroman, C., Pérez-Juste, J., Mata-Osoro, G., Liz-Marzán, L. M. & Mulvaney, P. Redshift of Surface Plasmon Modes of Small Gold Rods Due to Their Atomic Roughness and End-Cap Geometry. *Phys. Rev. B* **77**, 035418 (2008).
- 98 Chan, G. H., Zhao, J., Schatz, G. C. & Van Duyne, R. P. Localized Surface Plasmon Resonance Spectroscopy of Triangular Aluminum Nanoparticles. *J. Phys. Chem. C* **115**, 13958-13963 (2008).
- 99 Bryant, G. W., Garcia de Abajo, F. J. & Aizpurua, J. Mapping the Plasmon Resonances of Metallic Nanoantennas. *Nano Lett.* **8**, 631-636 (2008).
- 100 O. Schubert *et al.* Mapping the Polarization Pattern of Plasmon Modes Reveals Nanoparticle Symmetry. *Nano Lett.* **8**, 2345-2350 (2008).
- 101 Chan, G. H., Zhao, J., Hicks, E. M., Schatz, G. C. & Van Duyne, R. P. Plasmonic Properties of Copper Nanoparticles Fabricated by Nanosphere Lithography. *Nano Lett.* **7**, 1947-1952 (2007).
- 102 B. J. Wiley *et al.* Maneuvering the Surface Plasmon Resonance of Silver Nanostructures through Shape-Controlled Synthesis. *J. Phys. Chem. B* **110**, 15666-15675 (2006).
- 103 Sherry, L. J., Jin, R., Mirkin, C. A., Schatz, G. C. & Van Duyne, R. P. Localized Surface Plasmon Resonance Spectroscopy of Single Silver Triangular Nanoprisms. *Nano Lett.* **6**, 2060-2065 (2006).
- 104 Liz-Marzán, L. M. Tailoring Surface Plasmons through the Morphology and Assembly of Metal Nanoparticles. *Langmuir* **22**, 32-41 (2006).
- 105 H. Wang, D. W. Brandl, F. Le, P. Nordlander & Halas, N. J. Nanorice: A Hybrid Plasmonic Nanostructure. *Nano Lett.* **6**, 827-832 (2006).
- 106 Sherry, L. J. *et al.* Localized Surface Plasmon Resonance Spectroscopy of Single Silver Nanocubes. *Nano Lett.* **5**, 2034-2038, doi:10.1021/nl0515753 (2005).
- 107 Jin, R. *et al.* Controlling Anisotropic Nanoparticle Growth Through Plasmon Excitation. *Nature* **425**, 487-490 (2003).
- 108 Mock, J. J., Smith, D. R. & Schultz, S. Local Refractive Index Dependence of Plasmon Resonance Spectra from Individual Nanoparticles. *Nano Lett.* **3**, 485-491 (2003).
- 109 Mock, J. J., Barbic, M., Smith, D. R., Schultz, D. A. & Schultz, S. Shape Effects in Plasmon Resonance of Individual Colloidal Silver Nanoparticles. *J. Chem. Phys.* **116**, 6755-6759 (2002).

- 110 C. Sönnichsen *et al.* Drastic Reduction of Plasmon Damping in Gold Nanorods. *Phys. Rev. Lett.* **7**, 077402 (2002).
- 111 M. Scharfe *et al.* Do Mie Plasmons Have a Longer Lifetime on Resonance than Off Resonance? *Appl. Phys. B: Lasers Opt.* **73**, 305-310 (2001).
- 112 Link, S. & El-Sayed, M. A. Size and Temperature Dependence of the Plasmon Absorption of Colloidal Gold Nanoparticles. *J. Phys. Chem. B* **103**, 4212-4217 (1999).
- 113 B. Li *et al.* Investigation of Size-Dependent Plasmonic and Catalytic Properties of Metallic Nanocrystals Enabled by Size Control with HCl Oxidative Etching. *Small* **8**, 1710-1716 (2012).
- 114 E. J. Heilweil & Hochstrasser, R. M. Nonlinear Spectroscopy and Picosecond Transient Grating Study of Colloidal Gold *J. Chem. Phys.* **82**, 4762-4770 (1985).
- 115 Gersten, J. & Nitzan, A. Spectroscopic Properties of Molecules Interacting with Small Dielectric Particles *J. Chem. Phys.* **75**, 1139-1152 (1981).
- 116 Hartland, G. V. Optical Studies of Dynamics in Noble Metal Nanostructures. *Chem. Rev.* **111**, 3858-3887 (2011).
- 117 Hu, M., Chen, J., Marquez, M., Xia, Y. & Hartland, G. V. Correlated Rayleigh Scattering Spectroscopy and Scanning Electron Microscopy Studies of Au–Ag Bimetallic Nanoboxes and Nanocages. *J. Phys. Chem. C* **111** (2007).
- 118 C. J. Murphy *et al.* Anisotropic Metal Nanoparticles: Synthesis, Assembly, and Optical Applications *J. Phys. Chem. B* **109**, 13851-13870 (2005).
- 119 Gole, A. & Murphy, C. J. Seed-Mediated Synthesis of Gold Nanorods: Role of the Size and Nature of the Seed. *Chem. Mater.* **16**, 3622-3640 (2004).
- 120 S. O. Obare, N. R. Jana & Murphy, C. J. Preparation of Polystyrene- and Silica-Coated Gold Nanorods and Their Use as Templates for the Synthesis of Hollow Nanotubes. *Nano Lett.* **1**, 601-603 (2001).
- 121 Nehl, C. L. *et al.* Scattering Spectra of Single Gold Nanoshells. *Nano Lett.* **4**, 2355-2359 (2004).
- 122 Xia, Y., Xiong, Y., Lim, B. & Skrabalak, S. E. Shape-Controlled Synthesis of Metal Nanocrystals: Simple Chemistry Meets Complex Physics? *Angew. Chem. Int. Ed.* **48**, 60-103 (2009).
- 123 Rycenga, M., McLellan, J. M. & Xia, Y. Controlling the Assembly of Silver Nanocubes through Selective Functionalization of Their Faces. *Adv. Mater.* **20**, 2416-2420 (2008).
- 124 Xiong, Y., Wiley, B. J. & Xia, Y. Nanocrystals with Unconventional Shapes - a Class of Promising Catalysts. *Angew. Chem. Int. Ed.* **46**, 7157-7159 (2007).
- 125 Skrabalak, S. E., Au, L., Li, X. & Xia, Y. Facile Synthesis of Ag Nanocubes and Au Nanocages. *Nat. Protoc.* **2**, 2182 (2007).
- 126 Wiley, B. J., Xiong, Y., Li, Z.-Y., Yin, Y. & Xia, Y. Right Bipyramids of Silver: A New Shape Derived from Single Twinned Seeds. *Nano Lett.* **6**, 765-768 (2006).
- 127 Sun, Y. & Xia, Y. Shape-Controlled Synthesis of Gold and Silver Nanoparticles. *Science* **298**, 2176-2179, doi:10.1126/science.1077229 (2002).
- 128 Sun, Y., Gates, B., Mayers, B. & Xia, Y. Crystalline Silver Nanowires by Soft Solution Processing. *Nano Lett.* **2**, 165-168 (2002).
- 129 Langille, M. R., Zhang, J. & Mirkin, C. A. Plasmon-Mediated Synthesis of Heterometallic Nanorods and Icosahedra. *Angew. Chem. Int. Ed.* **50**, 3543-3547 (2011).

- 130 Personick, M. L., Langille, M. R., Zhang, J. & Mirkin, C. A. Shape Control of Gold Nanoparticles by Silver Underpotential Deposition. *Nano Lett.* **11**, 3394-3398 (2011).
- 131 Zhang, J., Langille, M. R. & Mirkin, C. A. Photomediated Synthesis of Silver Triangular Bipyramids and Prisms: The Effect of pH and BSPP. *J. Am. Chem. Soc.* **132**, 12502-12510 (2010).
- 132 Zhang, J., Li, S., Wu, J., Schatz, G. C. & Mirkin, C. A. Plasmon-Mediated Synthesis of Silver Triangular Bipyramids. *Angew. Chem. Int. Ed.* **48**, 8878-7791 (2009).
- 133 Jin, R. *et al.* Photoinduced Conversion of silver Nanospheres to Nanoprisms. *Science* **294**, 1901-1903 (2001).
- 134 Barnard, A. S., Young, N. P., Kirkland, A. I., van Huis, M. A. & Xu, H. F. Nanogold: A Quantitative Phase Map. *ACS Nano* **3**, 1431-1436, doi:10.1021/nn900220k (2009).
- 135 Gorshkov, V., Zavalov, A. & Privman, V. Shape Selection in Diffusive Growth of Colloids and Nanoparticles. *Langmuir* **25**, 7940-7953, doi:10.1021/la900613p (2009).
- 136 Wang, C. *et al.* One-Pot Synthesis of Oleyamine Coated AuAg Alloy NPs and their Catalysis for CO Oxidation. *Chem. Mater.* **21**, 433-435 (2009).
- 137 Pietrobon, B. & Kitaev, V. Photochemical Synthesis of Monodisperse Size-Controlled Silver Decahedral Nanoparticles and Their Remarkable Optical Properties. *Chem. Mater.* **20**, 5186-5190 (2008).
- 138 Wang, Y., Chen, P. & Liu, M. Synthesis of Well-Defined Copper Nanocubes by a One-Pot Solution Process. *Nanotechnology* **17**, 6000-6006 (2006).
- 139 A. Sánchez-Iglesias *et al.* Synthesis and Optical Properties of Gold Nanodecahedra with Size Control. *Adv. Mater.* **18**, 2529-2534 (2006).
- 140 Sra, A. K. & Schaak, R. E. Synthesis of Atomically Ordered AuCu and AuCu<sub>3</sub> Nanocrystals from Bimetallic Nanoparticle Precursors. *J. Am. Chem. Soc.* **126**, 6667-6672 (2004).
- 141 Sánchez-Iglesias, A. *et al.* Rapid Epitaxial Growth of Ag on Au Nanoparticles: From Au Nanorods to Core-Shell Au@Ag Octahedrons. *Chem. Eur. J.* **16**, 5558-5563 (2010).
- 142 Carbó-Argibay, E., Rodríguez-González, B., Pastoriza-Santos, I., Pérez-Juste, J. & Liz-Marzán, L. M. Growth of Pentatwinned Gold Nanorods into Truncated Decahedra. *Nanoscale* **2**, 2377-2383 (2010).
- 143 Pastoriza-Santos, I. & Liz-Marzán, L. M. Colloidal Silver Nanoplates. State of the Art and Future Challenges. *J. Mater. Chem.* **18**, 1724-1737 (2008).
- 144 Grzelczak, M., Pérez-Juste, J., García de Abajo, F. J. & Liz-Marzán, L. M. Optical Properties of Platinum-Coated Gold Nanorods. *J. Phys. Chem. C* **2007**, 6183-6188 (2007).
- 145 Liz-Marzán, L. M. Nanometals: Formation and color. *Mater. Today* **7**, 26-31 (2004).
- 146 Tamaru, H., Kuwata, H., Miyazaki, H. T. & Miyano, K. Resonant Light Scattering from Individual Ag Nanoparticles and Particle Pairs. *Appl. Phys. Lett.* **80**, 1826-1828 (2002).
- 147 McMahan, J. M. *et al.* Correlating the Structure, Optical Spectra, and Electrodynamics of Single Silver Nanocubes. *J. Phys. Chem. C* **113**, 2731-2735, doi:10.1021/jp8098736 (2009).
- 148 Itoh, T., Uwada, T., Asahi, T., Ozaki, Y. & Masuhara, H. Analysis of Localized Surface Plasmon Resonance by Elastic Light Scattering Spectroscopy of Individual Au

- Nanoparticles for Surface-Enhanced Raman Scattering. *Can. J. Anal. Sci. Spect.* **52**, 130-141 (2007).
- 149 Blaber, M. G., Henry, A.-I., Bingham, J. M., Schatz, G. C. & Van Duyne, R. P. LSPR Imaging of Silver Triangular Nanoprisms: Correlating Scattering with Structure Using Electrostatics for Plasmon Lifetime Analysis. *J. Phys. Chem. C* **116**, 393-403 (2012).
- 150 Hartland, G. V. Coherent Excitation of Vibrational Modes in Metallic Nanoparticles. *Annu. Rev. Phys. Chem.* **7**, 403-430 (2006).
- 151 Zijlstra, P. & Orrit, M. Single Metal Nanoparticles: Optical Detection, Spectroscopy and Applications. *Rep. Prog. Phys.* **74**, 106401 (2011).
- 152 Barnard, A. S. Modelling of Nanoparticles: Approaches to Morphology and Evolution. *Rep. Prog. Phys.* **73**, 0876502 (2010).
- 153 Sekerka, R. F. Equilibrium and growth shapes of crystals: how do they differ and why should we care? *Crystal Research and Technology* **40**, 291-306, doi:10.1002/crat.200410342 (2005).
- 154 Wettlaufer, J. S., Jackson, M. & Elbaum, M. A Geometric Model for Anisotropic Crystal Growth. *Journal of Physics A: Mathematical and General* **27**, 5957-5967 (1994).
- 155 Ferrando, R., Jellinek, J. & Johnston, R. L. Nanoalloys: From Theory to Applications of Alloy Clusters and Nanoparticles. *Chem. Rev.* **108**, 846-910 (2008).
- 156 F. Calvo, E. Cottancin & Broyer, M. Segregation, Core Alloying, and Shape Transitions in Bimetallic Nanoclusters: Monte Carlo Simulations. *Phys. Rev. B* **77**, 121406 (2008).
- 157 Baletto, F. & Ferrando, R. Structural Properties of Nanoclusters: Energetic, Thermodynamic, and Kinetic Effects. *Rev. Mod. Phys.* **77**, 371-423 (2005).
- 158 Marks, L. D. Experimental Studies of Small-Particle Structures. *Rep. Prog. Phys.* **57**, 603-649 (1994).
- 159 Enterkin, J. A., Poepelmeier, K. R. & Marks, L. D. Oriented Catalytic Platinum Nanoparticles on High Surface Area Strontium Titanate Nanocuboids. *Nano Lett.* **11**, 993-997 (2011).
- 160 Zia, R. K. P., Avron, J. E. & Taylor, J. E. The Summertop Construction: Crystals in a Corner. *J. Stat. Phys.* **50**, 727-736 (1988).
- 161 Ino, S. Epitaxial Growth Of Metals On Rocksalt Faces Cleaved In Vacuum .2. Orientation And Structure Of Gold Particles Formed In Ultrahigh Vacuum. *J. Phys. Soc. Jpn.* **21**, 346-362 (1966).
- 162 Ino, S. & Ogawa, S. Multiply Twinned Particles At Earlier Stages Of Gold Film Formation On Alkali Halide Crystals. *J. Phys. Soc. Jpn.* **22**, 1365-1374 (1967).
- 163 Ino, S. Stability of Multiply-Twinned Particles. *J. Phys. Soc. Jpn.* **27**, 941-953 (1969).
- 164 Hayashi, T., Ohno, T., Yatsuya, S. & Uyeda, R. Formation of Ultrafine Metal Particles by Gas-Evaporation Technique .4. Crystal Habits of Iron and Fcc Metals, Al, Co, Ni, Cu, Pd, Ag, In, Au, and Pb. *Jpn. J. Appl. Phys.* **16** (1997).
- 165 Marks, L. D. Modified Wulff Constructions for Twinned Particles. *J. Cryst. Growth* **61**, 556-566 (1983).
- 166 Marks, L. D. Surface-Structure and Energetics of Multiply Twinned Particles. *Phil. Mag. A* **49**, 81-93 (1984).
- 167 De Wit, R. Partial Disclinations. *J. Phys. C: Solid State* **5**, 529-534 (1972).

- 168 Howie, A. & Marks, L. D. Elastic Strains and the Energy-Balance for Multiply Twinned Particles. *Philos. Mag. A* **49**, 95-109 (1984).
- 169 Young, N. P., van Huis, M. A., Zandbergen, H. W., Xu, H. & Kirkland, A. I. Transformations of Gold Nanoparticles Investigated Using Variable Temperature High-Resolution Transmission Electron Microscopy. *Ultramicroscopy* **110**, 506-516, doi:10.1016/j.ultramic.2009.12.010 (2010).
- 170 Mayoral, A., Barron, H., Estrada-Salas, R., Vazquez-Duran, A. & Jose-Yacaman, M. Nanoparticle Stability from the Nano to the Meso Interval. *Nanoscale* **2**, 335-342 (2010).
- 171 T. Ling *et al.* Icosahedral Face-Centered Cubic Fe Nanoparticles: Facile Synthesis and Characterization with Aberration-Corrected TEM. *Nano Lett.* **9**, 1572-1576 (2009).
- 172 L. C. Gontard *et al.* Aberration-Corrected Imaging of Active Sites on Industrial Catalyst Nanoparticles. *Angew. Chem.* **119**, 3757-3759 (2007).
- 173 M. Varela *et al.* Materials Characterization in the Aberration-Corrected Scanning Transmission Electron Microscope. *Annu. Rev. Mater. Res.* **35**, 539-569 (2005).
- 174 Z. Y. Li *et al.* Three-Dimensional Atomic-Scale Structure of Size-Selected Gold Nanoclusters. *Nature* **451**, 46-48 (2008).
- 175 Dorogin, L. M. *et al.* Crystal Mismatched Layers in Pentagonal Nanorods and Nanoparticles. *Phys. Status Solidi B* **247**, 288-298, doi:10.1002/pssb.200945385 (2010).
- 176 Sohn, K. *et al.* Construction of Evolutionary Tree for Morphological Engineering of Nanoparticles. *ACS Nano* **3**, 2191-2198 (2009).
- 177 Seo, D. *et al.* Shape Adjustment between Multiply Twinned and Single-Crystalline Polyhedral Gold Nanocrystals: Decahedra, Icosahedra, and Truncated Tetrahedra. *J. Phys. Chem. C* **112**, 2469-2475 (2008).
- 178 C. Li, K. L. Shuford, M. Chen, Lee, E. J. & Cho, S. O. A Facile Polyol Route to Uniform Gold Octahedra with Tailorable Size and Their Optical Properties. *ACS Nano* **2** (2008).
- 179 Nikoobakht, B. & El-Sayed, M. A. Preparation and Growth Mechanism of Gold Nanorods (NRs) Using Seed-Mediated Growth Method. *Chem. Mater.* **15**, 6755-6759 (2003).
- 180 P. C. Lee & Miesel, D. Adsorption and Surface-Enhanced Raman of Dyes on Silver and Gold Sols. *J. Phys. Chem.* **86**, 3391-3395 (1982).
- 181 Wang, Y. *et al.* A Method to Correlate Optical Properties and Structures of Metallic Nanoparticles. *Ultramicroscopy* **109**, 1110-1113 (2009).
- 182 Novo, C., Funston, A. M. & Mulvaney, P. Direct Observation of Chemical Reactions on Single Gold Nanocrystals Using Surface Plasmon Spectroscopy. *Nat. Nanotechnol.* **3**, 598-602 (2008).
- 183 Nehl, C. L., Liao, H. & Hafner, J. H. Optical Properties of Star-Shaped Gold Nanoparticles. *Nano Lett.* **6**, 683-688 (2006).
- 184 Kleinman, S. K. *et al.* Single-Molecule Surface-Enhanced Raman Spectroscopy of Crystal Violet Isotopologues: Theory and Experiment. *J. Am. Chem. Soc.* **133**, 4115-4122 (2011).
- 185 Blaber, M. G., Arnold, M. D., Harris, N., Ford, M. J. & Cortie, M. B. Plasmon Absorption in Nanospheres: A Comparison of Sodium, Potassium, Aluminium, Silver and Gold. *Physica B* **394**, 184-187 (2007).

- 186 Malinsky, M. D., Kelly, K. L., Schatz, G. C. & Van Duyne, R. P. Nanosphere  
Lithography: Effect of the Substrate on the LSPR of Silver Nanoparticles. *J. Phys. Chem.  
B* **105**, 2343-2350 (2001).
- 187 Wiley, B. J. *et al.* Maneuvering the Surface Plasmon Resonance of Silver Nanostructures  
through Shape-Controlled Synthesis. *J. Phys. Chem. B* **110**, 15666-15675 (2006).
- 188 Forzani, E. S., Foley, K., Westerhoff, P. & N.Tao. Detection of Arsenic in Groundwater  
Using a Surface Plasmon Resonance Sensor. *Sens. Actuators, B* **123**, 82-88 (2007).
- 189 Blaber, M. G., Arnold, M. D. & Ford, M. J. Search for the Ideal Plasmonic Nanoshell:  
The Effects of Surface Scattering and Alternatives to Gold and Silver. *J. Phys. Chem. C*  
**113**, 3041-3045 (2009).
- 190 Blaber, M. G., Arnold, M. D. & Ford, M. J. Designing Materials for Plasmonic Systems:  
the Alkali–Noble Intermetallics. *J. Phys. Condens. Mat.* **22**, 095501 (2010).
- 191 Elghanian, R., Storhoff, J. J., Mucic, R. C., Letsinger, R. L. & Mirkin, C. A. Selective  
Colorimetric Detection of Polynucleotides Based on the Distance-Dependent Optical  
Properties of Gold Nanoparticles. *Science* **277**, 1078-1081,  
doi:10.1126/science.277.5329.1078 (1997).
- 192 Stiles, P. L., Dieringer, J. A., Shah, N. C. & Van Duyne, R. P. Surface-Enhanced Raman  
Spectroscopy. *Annu. Rev. Anal. Chem.* **1**, 601-626 (2008).
- 193 McFarland, A. D., Young, M. A., Dieringer, J. A. & Van Duyne, R. P. Wavelength-  
Scanned Surface-Enhanced Raman Excitation Spectroscopy. *J. Phys. Chem. B* **109**,  
11279-11285 (2005).
- 194 Zhao, J., Dieringer, J. A., Zhang, X., Schatz, G. C. & Van Duyne, R. P. Wavelength-  
Scanned Surface-Enhanced Resonance Raman Excitation Spectroscopy. *J. Phys. Chem.  
C* **112**, 19302-19310 (2008).
- 195 Haes, A. J., Zou, S., Zhao, J., Schatz, G. C. & Van Duyne, R. P. Localized Surface  
Plasmon Resonance Spectroscopy near Molecular Resonances. *J. Am. Chem. Soc.* **128**,  
10905-10914 (2006).
- 196 Zhao, J. *et al.* Resonance Surface Plasmon Spectroscopy: Low Molecular Weight  
Substrate Binding to Cytochrome P450. *J. Am. Chem. Soc.* **128**, 11004-11005 (2006).
- 197 Rioux, R. M. *et al.* Monodisperse Platinum Nanoparticles of Well-Defined Shape:  
Synthesis, Characterization, Catalytic Properties and Future Prospects. *Top. Catal.* **39**,  
167-174 (2006).
- 198 Grzelczak, M., Pérez-Juste, J., Mulvaney, P. & Liz-Marzán, L. M. Shape Control in Gold  
Nanoparticle Synthesis. *Chem. Soc. Rev.* **37**, 1783-1791 (2008).
- 199 Sánchez-Iglesias, A. *et al.* Synthesis and Optical Properties of Gold Nanodecahedra with  
Size Control. *Adv. Mater.* **18**, 2529-2534 (2006).
- 200 Camargo, P. H. C., Rycenga, M., Au, L. & Xia, Y. Isolating and Probing the Hot Spot  
Formed between Two Silver Nanocubes. *Angew. Chem. Int. Ed.* **48**, 2180-2184 (2009).
- 201 McLellan, J. M., Siekkinen, A., Chen, J. & Xia, Y. Comparison of the Surface-Enhanced  
Raman Scattering on Sharp and Truncated Silver Nanocubes. *Chem. Phys. Lett.* **427**, 122-  
126 (2006).
- 202 M. Rycenga *et al.* Generation of Hot Spots with Silver Nanocubes for Single-Molecule  
Detection by Surface-Enhanced Raman Scattering. *Angew. Chem. Int. Ed.* **50**, 5473-5477  
(2011).

- 203 Mahmoud, M. A., Tabor, C. E. & El-Sayed, M. A. Surface-Enhanced Raman Scattering Enhancement by Aggregated Silver Nanocube Monolayers Assembled by the Langmuir–Blodgett Technique at Different Surface Pressures. *J. Phys. Chem. C* **113**, 5493-5501 (2009).
- 204 McLellan, J. M., Li, Z.-Y., Siekkinen, A. R. & Xia, Y. The SERS Activity of Supported Ag Nanocubes Strongly Depends on its Orientation Relative to Laser Polarization. *Nano Lett.* **7**, 1013-1017 (2007).
- 205 Shukla, R. P., Chowdhury, A. & Gupta, P. D. Interferometric Determination of Thickness of Formvar Films. *Opt. Eng.* **33**, 1881-1884 (1994).
- 206 Sze, S. M. *Physics of Semiconductor Devices*. 852 (Wiley, 1981).
- 207 Haes, A. J., Stuart, D. A., Nie, S. & Van Duyne, R. P. Using Solution-Phase Nanoparticles, Surface-Confined Nanoparticle Arrays and Single Nanoparticles as Biological Sensing Platforms. *J. Fluoresc.* **14**, 355-367 (2004).
- 208 Wang, Y., Qian, W., Tan, Y. & Ding, S. A Label-Free Biosensor Based on Gold Nanoshell Monolayers for Monitoring Biomolecular Interactions in Diluted Whole Blood. *Biosens. Bioelec.* **23**, 1166-1170 (2008).
- 209 Prescott, S. W. & Mulvaney, P. Gold Nanorod Extinction Spectra. *J. Appl. Phys.* **99**, 123504 (2006).
- 210 Taflove, A. & Hagness, S. C. *Computational Electrodynamics: The Finite-Difference Time-Domain Method*. 3<sup>rd</sup> edn, (Artech House, Inc., 2005).
- 211 Hwang, C.-B. *et al.* Synthesis, Characterization, and Highly Efficient Catalytic Reactivity of Suspended Palladium Nanoparticles. *J. Catal.* **195**, 336-341 (2000).
- 212 Novo, C., Funston, A. M., Pastoriza-Santos, I., Liz-Marzán, L. M. & Mulvaney, P. Spectroscopy and High-Resolution Microscopy of Single Nanocrystals by a Focused Ion Beam Registration Method. *Angew. Chem. Int. Ed.* **46**, 3517-3520 (2007).
- 213 Hao, E. & Schatz, G. C. Electromagnetic Fields Around Silver Nanoparticles and Dimers. *J. Chem. Phys.* **120**, 357-366 (2004).
- 214 Kelly, K. L., Coronado, E., Zhao, L. L. & Schatz, G. C. The Optical Properties of Metal Nanoparticles: The Influence of Size, Shape, and Dielectric Environment. *J. Phys. Chem. B* **107**, 668-677 (2003).
- 215 Brioude, A. & Pileni, M. P. Silver Nanodisks: Optical Properties Study Using the Discrete Dipole Approximation Method. *J. Phys. Chem. B* **109**, 23371-23377 (2005).
- 216 Nelayah, J. *et al.* Mapping Surface Plasmons on a Single Metallic Nanoparticle. *Nat. Phys.* **3**, 348-353 (2007).
- 217 Chen, C. K., Heinz, T. F., Ricard, D. & Shen, Y. R. Surface Enhanced Second Harmonic Generation and Raman Scattering. *Phys. Rev. B* **27**, 1965-1978 (1983).
- 218 Lakowicz, J. R. *et al.* Advances in Surface-Enhanced Fluorescence. *J. Fluoresc.* **14**, 425-441 (2004).
- 219 Fort, E. & Grésillon, S. Surface Enhanced Fluorescence. *J. Phys. D: Appl. Phys.* **41**, 013001 (2008).
- 220 Santillán, J. M. J., Scaffardi, L. B. & Schinca, D. C. Quantitative Optical Extinction-Based Parametric Method for Sizing a Single Core-Shell Ag-Ag<sub>2</sub>O Nanoparticle. *J. Phys. D: Appl. Phys.* **44**, 105104 (2011).

- 221 Schinca, D. C. & Scaffardi, L. B. Core and Shell Sizing of Small Silver-Coated Nanospheres by Optical Extinction Spectroscopy. *Nanotechnology* **19**, 495712 (2008).
- 222 Slaughter, L. S. *et al.* Single-Particle Spectroscopy of Gold Nanorods beyond the Quasi-Static Limit: Varying the Width at Constant Aspect Ratio. *J. Phys. Chem. C* **114**, 4934-4938 (2010).
- 223 Murphy, C. J. *et al.* Anisotropic Metal Nanoparticles: Synthesis, Assembly, and Optical Applications. *J. Phys. Chem. B* **109**, 13857-13870 (2005).
- 224 Novo, C., Funston, A. M., Pastoriza-Santos, I., Liz-Marzán, L. M. & Mulvaney, P. Influence of the Medium Refractive Index on the Optical Properties of Single Gold Triangular Prisms on a Substrate. *J. Phys. Chem. C* **112**, 3-7 (2008).
- 225 Dow Chemical Company, I. Refractive Index of Glycerine-Water Solutions at 20°C. (2012).
- 226 M. Rex, F. E. Hernandez & Campiglia, A. D. Pushing the Limits of Mercury Sensors with Gold Nanorods. *Anal. Chem.* **78**, 445-451 (2006).
- 227 M. Leskelä & Ritala, M. Atomic Layer Deposition (ALD): from Precursors to Thin Film Structures. *Thin Solid Films* **409**, 138-146 (2002).
- 228 M. Ritala *et al.* Atomic Layer Deposition of Oxide Thin Films with Metal Alkoxides as Oxygen Sources. *Science* **288**, 319-321 (2000).
- 229 Birch, K. P. & Downs, M. J. An Updated Edlén Equation for the Refractive Index of Air *Metrologia* **30**, 155-162 (1993).
- 230 Edlén, B. The Refractive Index of Air. *Metrologia* **2**, 71-80 (1966).
- 231 A. Bottomley & Ianoul, A. Improved Refractive-Index Sensitivity of Silver-Nanocube Monolayers on Silicon Films. *Chem. Phys. Chem.* **12**, 2912-2914 (2011).
- 232 Tao, A., Sinsermsuksakul, P. & Yang, P. Tunable Plasmonic Lattices of Silver Nanocrystals. *Nat. Nanotechnol.* **2**, 435-440 (2007).
- 233 A. Tao, P. Sinsermsuksakul & Yang, P. Polyhedral Silver Nanocrystals with Distinct Scattering Signatures. *Angew. Chem. Int. Ed.* **45**, 4597-4601 (2006).
- 234 Zhang, X., Whitney, A. V., Zhao, J., Hicks, E. M. & Duyne, R. P. V. Advances in Contemporary Nanosphere Lithographic Techniques. *J. Nanosci. Nanotechnol.* **6**, 1-15 (2006).
- 235 G. K. Joshi, P. J. McClory, Dolai, S. & Sarda, R. Improved Localized Surface Plasmon Resonance Biosensing Sensitivity Based on Chemically-Synthesized Gold Nanoprisms as Plasmonic Transducers. *J. Mater. Chem.* **22**, 923-931 (2011).
- 236 Le Ru, E. C. & Etchegoin, P. G. Single-Molecule Surface-Enhanced Raman Spectroscopy. *Annu. Rev. Phys. Chem.* **63**, 65-87 (2012).
- 237 Dieringer, J. A. *et al.* Surface-Enhanced Raman Excitation Spectroscopy of a Single Rhodamine 6G Molecule. *J. Am. Chem. Soc.* **131**, 849-854 (2009).
- 238 Camden, J. P. *et al.* Probing the Structure of Single-Molecule Surface-Enhanced Raman Scattering Hot Spots. *J. Am. Chem. Soc.* **130**, 12616-12617 (2008).
- 239 Dieringer, J. A., Lettan, R. B., Scheidt, K. A. & Van Duyne, R. P. A Frequency Domain Existence Proof of Single-Molecule Surface-Enhanced Raman Spectroscopy. *J. Am. Chem. Soc.* **129**, 16249-16256 (2007).
- 240 Otto, A. What is Observed in Single Molecule SERS, and Why? *J. Raman. Spec.* **33**, 593-598 (2002).

- 241 Xu, H., Aizpurua, J., Käll, M. & Apell, P. Electromagnetic Contributions to Single-Molecule Sensitivity in Surface-Enhanced Raman Scattering. *Phys. Rev. E* **62**, 4318-4324 (2000).
- 242 Etchegoin, P. G. & Le Ru, E. C. A Perspective on Single Molecule SERS: Current Status and Future Challenges. *Phys. Chem. Chem. Phys.* **10**, 6079-6089 (2008).
- 243 Michaels, A. M., Nirmal, M. & Brus, L. E. Surface Enhanced Raman Spectroscopy of Individual Rhodamine 6G Molecules on Large Ag Nanocrystals. *J. Am. Chem. Soc.* **121**, 9932-9939 (1999).
- 244 Dielbold, E. D., Peng, P. & Mazur, E. Isolating Surface-Enhanced Raman Scattering Hot Spots Using Multiphoton Lithography. *J. Am. Chem. Soc.* **131**, 16356-16357 (2009).
- 245 M. L. Brongersma & Shalaev, V. M. The Case for Plasmonics. *Science* **328**, 440-441 (2010).
- 246 McEachran, M. & Kitaev, V. Direct Structural Transformation of Silver Platelets into Right Bipyramids and Twinned Cube Nanoparticles: Morphology Governed by Defects. *Chem. Comm.*, 5737-5739 (2008).
- 247 Rocha, T. C. R. & Zanchet, D. Structural Defects and Their Role in the Growth of Ag Triangular Nanoplates. *J. Phys. Chem. C* **111**, 6989-6993 (2007).
- 248 G. P. Lee, A. I. Minett, P. C. Innis & Wallace, G. G. A New Twist: Controlled Shape-Shifting of Silver Nanoparticles from Prisms to Discs. *J. Mater. Chem.* **19**, 8294-8298 (2009).
- 249 X. Fan *et al.* Size-Controlled Growth of Colloidal Gold Nanoplates and Their High-Purity Acquisition. *Nanotechnology* **21**, 105602 (2010).
- 250 C. Wang, Z. Ma, T. Wang & Su, Z. Synthesis, Assembly, and Biofunctionalization of Silica-Coated Gold Nanorods for Colorimetric Biosensing. *Adv. Funct. Mater.* **16**, 1673-1678 (2006).
- 251 Nordlander, P., Oubre, C., Prodan, E., Li, K. & Stockman, M. I. Plasmon Hybridization in Nanoparticle Dimers. *Nano Lett.* **4**, 899-903 (2004).
- 252 E. Prodan, C. Radloff, N. J. Halas & Nordlander, P. A Hybridization Model for the Plasmon Response of Complex Nanostructures. *Science* **302**, 419-422 (2003).
- 253 Giannini, V., Fernández-Domínguez, A. I., Heck, S. C. & Maier, S. A. Plasmonic Nanoantennas: Fundamentals and Their Use in Controlling the Radiative Properties of Nanoemitters. *Chem. Rev.* **111**, 3888-3912 (2011).
- 254 Large, N., Abb, M., Aizpurua, J. & Muskens, O. L. Photoconductively Loaded Plasmonic Nanoantennas as Building Blocks for Ultracompact Optical Switches. *Nano Lett.* **10**, 1741-1746 (2010).
- 255 Kupersztych, J., Monchicourt, P. & Raynaud, M. Ponderomotive Acceleration of Photoelectrons in Surface-Plasmon-Assisted Multiphoton Photoelectric Emission. *Phys. Rev. Lett.* **86**, 5180-5183 (2001).
- 256 Polyushkin, D. K., Hendry, E., Stone, E. K. & Barnes, W. L. THz Generation from Plasmonic Nanoparticle Arrays. *Nano Lett.* **11**, 4718-4724 (2011).
- 257 Merschdorf, M., Pfeiffer, W., Thon, A., Voll, S. & Gerber, G. Photoemission from Multiply Excited Surface Plasmons in Ag Nanoparticles. *Appl. Phys. A-Mater. Sci. Process.* **71**, 547-552 (2000).

- 258 Evers, F., Rakete, C., Watanabe, K., Menzel, D. & Freund, H. J. Two-Photon Photoemission from Silver Nanoparticles on Thin Alumina Films: Role of Plasmon Excitation. *Surf. Sci.* **593**, 43-48 (2005).
- 259 Gloskovskii, A., Valdaitsev, D., Nepijko, S. A., Schonhense, G. & Rethfeld, B. Coexisting Electron Emission Mechanisms in Small Metal Particles Observed in fs-Laser Excited PEEM. *Surf. Sci.* **601**, 4706-4713 (2007).
- 260 Rohmer, M. *et al.* Time-Resolved Photoelectron Nano-Spectroscopy of Individual Silver Particles: Perspectives and Limitations. *Phys. Status Solidi B* **247**, 1132-1138 (2010).
- 261 Grubisic, A., Schweikhard, V., Baker, T. A. & Nesbitt, D. J. Plasmon-Mediated Coherent Multiphoton Photoelectron Emission from Individual Supported Au Nanorods: The Critical Role of Electric Near-Field Enhancement *To be published* (2012).
- 262 V. Schweikhard, A. Grubisic, T. A. Baker, I. Thomann & Nesbitt, D. J. Polarization-Dependent Scanning Photoionization Microscopy: Ultrafast Plasmon-Mediated Electron Ejection Dynamics in Single Au Nanorods. *ACS Nano* **5**, 3724-3735 (2011).
- 263 V. Schweikhard, A. Grubisic, T. A. Baker & Nesbitt, D. J. Multiphoton Scanning Photoionization Imaging Microscopy for Single-Particle Studies of Plasmonic Metal Nanostructures. *J. Phys. Chem. C* **115**, 83-91 (2011).
- 264 Richardson, O. W. *Emission of Electricity from Hot Bodies.* (Longmans Green & Co., 1921).
- 265 Dushman, S. Thermionic Emission. *Rev. Mod. Phys.* **2**, 0381-0476 (1930).
- 266 Keldysh, L. V. Ionization In Field Of A Strong Electromagnetic Wave. *Soviet Physics JETP-USSR* **20**, 1307-& (1965).
- 267 Anisimov, S. I., Benderskii, V. A. & Farkas, G. Nonlinear Photoelectric Effect In Metals Produced By A Laser-Radiation. *Uspekhi Fiz. Nauk* **122**, 185-222 (1977).
- 268 Georges, A. T. Theory Of The Multiphoton Photoelectric Effect - A Stepwise Excitation Process. *Phys. Rev. B* **51**, 13735-13738 (1995).
- 269 Yalunin, S. V., Gulde, M. & Ropers, C. Strong-field photoemission from surfaces: Theoretical approaches. *Phys. Rev. B* **84**, 195426 (2011).
- 270 Bechtel, J. H., Smith, W. L. & Bloembergen, N. 2-Photon Photoemission From Metals Induced By Picosecond Laser-Pulses. *Phys. Rev. B* **15**, 4557-4563 (1977).
- 271 O. L. A. Monti, T. A. Baker & Nesbitt, D. J. Imaging Nanostructures with Scanning Photoionization Microscopy. *J. Chem. Phys.* **125**, 154709 (2006).
- 272 Ringe, E. *et al.* Plasmon-Induced Electric Near-Field Enhanced Coherent Multiphoton Photoelectron Emission from Individual, Supported Ag Nanocubes. *Submitted* (2012).
- 273 Bernath, P. F. *Spectra of Atoms and Molecules.* (Oxford University Press, 1995).
- 274 Dweydari, A. W. & Mee, C. H. B. Oxygen Adsorption on (111) Face of Silver. *Phys. Status Solidi A* **17**, 247-250 (1973).
- 275 Tominaga, M., Shimazoe, T., Nagashima, M. & Taniguchi, I. Composition-Activity Relationships of Carbon Electrode-Supported Bimetallic Gold-Silver Nanoparticles in Electrocatalytic Oxidation of Glucose. *J. Electroanal. Chem.* **615**, 51-61 (2008).
- 276 Piccinin, S. *et al.* Alloy Catalyst in a Reactive Environment: The Example of Ag-Cu Particles for Ethylene Epoxidation. *Phys. Rev. Lett.* **104**, 035503 (2010).

- 277 Bracey, C. L., Ellis, P. R. & Hutchings, G. J. Application of Copper-Gold Alloys in Catalysis: Current Status and Future Perspectives. *Chem. Soc. Rev.* **38**, 2231-2243 (2009).
- 278 Gucci, L. Bimetallic Nano-Particles: Featuring Structure and Reactivity. *Catal. Today* **101**, 53-64 (2005).
- 279 Jacobsen, C. J. H. *et al.* Catalyst Design by Interpolation in the Periodic Table: Bimetallic Ammonia Synthesis Catalysts. *J. Am. Chem. Soc.* **123**, 8404-8405 (2001).
- 280 Tominaga, M. *et al.* Electrocatalytic Oxidation of Glucose at Gold-Silver, Silver, and Gold Nanoparticles in Alkaline Solution. *J. Electroanal. Chem.* **590**, 37-46 (2006).
- 281 Wang, A.-Q., Chang, C.-M. & Mou, C.-Y. Evolution of Catalytic Activity of Au-Ag Bimetallic Nanoparticles on Mesoporous Support for CO Oxidation. *J. Phys. Chem.* **109**, 18860-18867 (2005).
- 282 Liotta, L. F. *et al.* Liquid Phase Selective Oxidation of Benzyl Alcohol over Pd-Ag Catalysts Supported on Pumice. *Catal. Today* **66**, 271-276 (2001).
- 283 Wang, A.-Q., Liu, J.-H., Lin, S. D., Lin, T.-S. & Mou, C.-Y. A Novel Efficient Au-Ag Alloy Catalyst System: Preparation, Activity, and Characterization. *J. Catal.* **233**, 186-197 (2005).
- 284 Tsai, S.-H., Liu, Y.-H., Wu, P.-L. & Yeh, C.-S. Preparation of Au-Ag-Pd Trimetallic Nanoparticles and their Application as Catalyst. *J. Mater. Chem.* **13**, 978-980 (2003).
- 285 Gurau, B. *et al.* Structural and Electrochemical Characterization of Binary, Ternary, and Quaternary Platinum Alloy Catalysts for Methanol Electro-oxidation. *J. Phys. Chem. B* **102**, 9997-10003 (1998).
- 286 Molenbroek, A. M., Nørskov, J. K. & Clausen, B. S. Structure and Reactivity of Ni-Au Nanoparticle Catalysts. *J. Phys. Chem. B* **105**, 5450-5458 (2001).
- 287 V. Abdelsayed, A. Aljarash, M. S. El-Shall, Al Othman, Z. A. & Alghamdi, A. H. Microwave Synthesis of Bimetallic Nanoalloys and CO Oxidation on Ceria-Supported Nanoalloys. *Chem. Mater.* **21**, 2825-2834 (2009).
- 288 U. A. Paulus *et al.* Oxygen Reduction on Carbon-Supported Pt-Ni and Pt-Co Alloy Catalysts. *J. Phys. Chem. B* **106**, 4181-4191 (2002).
- 289 H. A. Gasteiger, Markovic, N., P. N. Ross Jr. & Cairns, E. J. Methanol Electrooxidation on Well-Characterized Pt-Ru Alloys. *J. Phys. Chem.* **97**, 12020-12029 (1993).
- 290 T.-Y. Jeon *et al.* Effect of Surface Segregation on the Methanol Oxidation Reaction in Carbon-Supported Pt-Ru Alloy Nanoparticles. *Langmuir* **26**, 9123-9129 (2010).
- 291 C. Della Pina, E. Falletta & Rossi, M. Highly Selective Oxidation of Benzyl Alcohol to Benzaldehyde Catalyzed by Bimetallic Gold-Copper Catalyst. *J. Catal.* **260**, 384-386 (2008).
- 292 Somorjai, G. A. & Park, J. Y. Colloid Science of Metal Nanoparticle Catalysts in 2D and 3D Structures. Challenges of Nucleation, Growth, Composition, Particle Shape, Size Control and Their Influence on Activity and Selectivity *Top. Catal.* **49**, 126-135 (2008).
- 293 Bratlie, K. M., Lee, H., Komvopoulos, K., Yang, P. & Somorjai, G. A. Platinum Nanoparticle Shape Effects on Benzene Hydrogenation Selectivity. *Nano Lett.* **7**, 3097-3101 (2007).
- 294 Narayanan, R. & El-Sayed, M. A. Shape-Dependent Catalytic Activity of Platinum Nanoparticles in Colloidal Solution. *Nano Lett.* **4**, 1343-1348 (2004).

- 295 Tian, N., Zhou, Z.-Y., sun, S.-G., Ding, Y. & Wang, Z. L. Synthesis of Tetrahedral Platinum Nanocrystals with High-Index Facets and High Electro-Oxidation Activity. *Science* **316**, 732-735 (2007).
- 296 Wang, H. Y., Najafabadi, R., Srolovitz, D. J. & Lesar, R. Interfacial Segregation in Silver-Gold, Gold-Palladium, and Copper-Nickel Alloys: I. (100) Surfaces. *Interface Sci.* **1**, 7-30 (1993).
- 297 Wang, G., Van Hove, M. A., Ross, P. N. & Baskes, M. I. Monte Carlo Simulations of Segregation in Pt-Re Catalyst Nanoparticles. *J. Chem. Phys.* **121**, 5410-5422 (2004).
- 298 Wang, G., Van Hove, M. A., Ross, P. N. & Baskes, M. I. Quantitative Prediction of Surface Segregation in Bimetallic Pt-M Alloy Particles (M=Ni, Re, Mo). *Prog. Surf. Sci.* **79**, 28-45 (2005).
- 299 K.-W. Wang, S.-R. Chung & Liu, C.-W. Surface Segregation of Pd<sub>x</sub>Ni<sub>100-x</sub> Alloy Nanoparticles. *J. Phys. Chem. C* **112**, 10242-10246 (2008).
- 300 A. Naitabdi, L. K. Ono, F. Behafarid & Cuenya, B. R. Thermal Stability and Segregation Processes in Self-Assembled Size-Selected Au<sub>x</sub>Fe<sub>1-x</sub> Nanoparticles Deposited on TiO<sub>2</sub>(110): Composition Effects. *J. Phys. Chem. C* **113**, 1433-1446 (2009).
- 301 Khanra, B. C., Bertolini, J. C. & Rousset, J. L. Effect of Surface Segregation on the Catalytic Activity of Alloys: CO Hydrogenation on Pd-Ni(111) Surface. *J. Mol. Catal. A: Chem* **129**, 233-240 (1998).
- 302 K. J. J. Mayrhofer, V. Juhart, K. Hartl, M. Hanzlik & Arenz, M. Adsorbate-Induced Surface Segregation for Core-Shell Nanocatalysts. *Angew. Chem. Int. Ed.* **48**, 3529-3531 (2009).
- 303 Xiao, S. *et al.* Size Effect on Alloying Ability and Phase Stability of Immiscible Bimetallic Nanoparticles. *Eur. Phys. J. B* **54**, 479-484 (2006).
- 304 Wang, L.-L. & Johnson, D. D. Predicted Trends of Core-Shell Preferences for 132 Late Transition Metal Binary Alloy Nanoparticles. *J. Am. Chem. Soc.* **131**, 14023-14029 (2009).
- 305 Dannenberg, A., Gruner, M. K., Hucht, A. & Entel, P. Surface Energies of Stoichiometric FePt and CoPt Alloys and their Implications for Nanoparticle Morphologies. *Phys. Rev. B* **80**, 245438 (2009).
- 306 Shan, B. *et al.* First-Principles-Based Embedded Atom Method for PdAu Nanoparticles. *Phys. Rev. B* **80**, 035404 (2009).
- 307 Vitos, L., Ruban, A. V., Skriver, H. L. & Kollár, J. The surface energy of metals. *Surf. Sci.* **411**, 186-202 (1998).
- 308 Matysina, Z. A., Pogorelova, O. S., Zaginaichenko, S. Y. & Schur, D. V. The Surface Energy of Crystalline CuZn and FeAl Alloys. *J. Phys. Chem. Solids* **56**, 9-14 (1994).
- 309 Methfessel, M., Hennig, D. & Scheffler, M. Trends of the Surface Relaxations, Surface Energies, and Work Functions of the 4d Transition Metals. *Phys. Rev. B* **46**, 4816-4829 (1992).
- 310 Kart, H. H., Tomak, M. & Çağın, T. Thermal and Mechanical Properties of CuAu Intermetallic Alloys. *Modelling Simul. Mater. Sci. Eng.* **13**, 657-669 (2005).
- 311 Orr, R. L. Heats of Formation of Solid Au-Cu Alloys. *Acta Metall.* **8**, 489-493 (1960).
- 312 Rao, C. N. & Rao, K. K. Effect of Temperature on the Lattice Parameters of Some Silver-Palladium Alloys. *Can. J. Phys.* **42**, 1336-1342 (1964).

- 313 Spreadborough, J. & Christian, J. W. High Temperature X-Ray Diffractometer. *J. Sci. Instrum.* **36**, 116-118 (1959).
- 314 Pratt, J. N. The Thermodynamic Properties of Silver-Palladium Alloys. *Trans. Faraday Soc.* **56**, 975-987 (1960).
- 315 Wang, A.-Q., Liu, J.-H., Lin, S. D., Lin, T.-S. & Mou, C.-Y. A novel efficient Au–Ag alloy catalyst system: preparation, activity, and characterization. *J. Catalysis* **233**, 186-197 (2005).
- 316 Herzing, A. A. *et al.* Energy Dispersive X-Ray Spectroscopy of Bimetallic Nanoparticles in an Aberration Corrected Scanning Transmission Electron Microscope. *Faraday Discuss.* **138**, 337-351 (2008).
- 317 Wouda, P. T., Schmid, M., Nieuwenhuys, B. E. & Varga, P. STM study of the (111) and (100) surfaces of PdAg. *Surf. Sci.* **417**, 292-300 (1998).
- 318 Reniers, F. Use of Matrix Corrections in the Calculation of Surface Composition of AgPd Alloys in Auger Electron Spectroscopy. *Surf. Interface Anal.* **23**, 374-380 (1995).
- 319 Meitzner, G., Via, G. H., Lytle, F. W. & Sinfelt, J. H. Structure of Bimetallic Clusters. Extended X-ray Absorption Fine Structure (EXAFS) Studies of Ag-Cu and Au-Cu Clusters. *J. Chem. Phys.* **83**, 4793-4799 (1985).
- 320 Marks, L. D. Surface-Structure and Energetics of Multiply Twinned Particles. *Philos. Mag. A* **49**, 81-93 (1984).
- 321 Ringe, E., Van Duyne, R. P. & Marks, L. D. Wulff Construction for Alloy Nanoparticles. *Nano Lett.* **11**, 3399-3403 (2011).
- 322 McMahan, J. M. *et al.* Gold Nanoparticle Dimer Plasmonics: Finite Element Method Calculations of the Electromagnetic Enhancement to Surface-Enhanced Raman Spectroscopy. *Anal. Bioanal. Chem.* **394**, 1819-1825 (2009).
- 323 S. M. Rupich, E. V. Shevchenko, M. I. Bodnarchuk, B. Lee & Talapin, D. V. Size-Dependent Multiple Twinning in Nanocrystal Superlattices. *J. Am. Chem. Soc.* **132**, 289-296 (2010).
- 324 Marks, L. D. Particle Size Effects on Wulff Constructions. *Surf. Sci.* **150**, 358-366 (1985).
- 325 Lim, B. *et al.* Twin-Induced Growth of Palladium–Platinum Alloy Nanocrystals. *Angew. Chem. Int. Ed.* **48**, 6304-6308 (2009).
- 326 Jun, Y.-W., Choi, J.-S. & Cheon, J. Shape Control of Semiconductor and Metal Oxide Nanocrystals Through Nonhydrolytic Colloidal Routes. *Angew. Chem. Int. Ed.* **45**, 3414-3439 (2006).
- 327 Hofmeister, H. Shape Variations and Anisotropic Growth of Multiply Twinned Nanoparticles. *Z. Kristallogr.* **224**, 528-538 (2009).
- 328 Ni, C., Hassan, P. A. & Kaler, E. W. Structural Characteristics and Growth of Pentagonal Silver Nanorods Prepared by a Surfactant Method. *Langmuir* **21**, 3334-3337 (2005).
- 329 Lyapunov, A. M. *Stability of Motion.* (Academic Press, 1966).
- 330 Boettinger, W. J., Warren, J. A., Beckermann, C. & Karma, A. Phase-Field Simulation of Solidification. *Annu. Rev. Mater. Res.* **32**, 163-194 (2002).
- 331 Kim, F., Connor, S., Song, H., Kuykendall, T. & Yang, P. Platonic Gold Nanocrystals. *Angew. Chem.* **116**, 3759-3763 (2004).

- 332 Lofton, C. & Sigmund, W. Mechanisms Controlling Crystal Habits of gold and Silver Colloids. *Adv. Funct. Mater.* **15**, 1197-1208 (2005).
- 333 Y.K. Du, J.Z. Xu, M. Shen, Yang, P. & Jiang, L. Alkanethiol-Stabilized Decahedron of Gold Nanoparticles. *Colloids Surface A* **257-258**, 535-537 (2005).
- 334 Reyes-Gasga, J. *et al.* On the Structure of Nanorods and Nanowires with Pentagonal Cross-Sections *J. Cryst. Growth* **286**, 162-172 (2006).
- 335 Hofmeister, H., Nepijko, S. A., Ievlev, D. N., Schulze, W. & Ertl, G. Composition and Lattice Structure of Fivefold Twinned Nanorods of Silver. *J. Cryst. Growth* **234**, 773-781 (2002).
- 336 Canizal, G., Ascencio, J. A., Gardea-Torresday, J. & Yacaman, M. J. Multiple Twinned Gold Nanorods Grown by Bio-Reduction Techniques. *J. Nanopart. Res.* **3**, 475-481 (2001).
- 337 Velonia, K. *et al.* Single-Enzyme Kinetics of CALB-Catalyzed Hydrolysis. *Angew. Chem. Int. Ed.* **44**, 560-564 (2005).
- 338 Winterbottom, W. L. Equilibrium Shape of a Small Particle in Contact with a Foreign Substrate. *Acta Metall. Mater.* **15**, 303-310 (1967).
- 339 Berge, B., Faucheux, L., Schwab, K. & Libchaber, A. Faceted Crystal Growth in Two Dimensions. *Nature* **350**, 322-324 (1991).

APPENDIX A  
MATLAB Codes

## A.1 LSPR Analysis Codes

The codes below were used to process the raw data according to the equation (see Chapter 2):

$$\text{Particle Scattering} = \frac{I_{particle} - I_{background}}{I_{lamp} - I_{detector\ dark}}$$

A typical order to run these files would be:

Convert all the spectra .SPE files to .txt files, making sure to convert to one dimension and to have the energy axis as the first column and the intensity in the second column. (this is done in Winspec)

Execute the command

```
background=bcreator(path,base,maxfilenum)
```

where "path" is the location of the files, for example C:\Users\Emilie\Desktop\Data LSPR

and "base" is the filename which is incremented in Winspec, using the auto-increment function, starting at 1 and ending at maxfilenum, for example deca\_jan2012\_batch1\_1s10a\_

Look at B by plotting it, (plot(B(:,1), B(:,2:maxfilenum+1))), remove all the spectra which have higher intensity than most. Record the column number of the suitable background spectra.

Write in a vector called V, which contain the particle number for each of the suitable background, for example V=[2;3;4;6;7];

Average all the suitable background spectra (to reduce noise) by executing

`B=averageforb(background, V);` write out a `B.txt` file using `csvwrite`. Put this file in the same folder as the other ones.

Ensure the lamp and detector dark spectra are in the same folder as the sample spectra, rename them `C` and `D`, respectively

Execute the command

`LSPR=spectramathb(path, base, maxfilenum);`

this provides the LSPR spectra of all the particles. To obtain normalized and smooth spectra, as well as the energy of the peak (obtained from the smooth spectra) use the following command:

`[notsmoothnormalized,smoothnormalized,peaks]=nsnsmpeak(LSPR,b,low,high);`

where `b` is the width of the smoothing Gaussian kernel (5-10 is good), `low` and `high` are the lower and upper boundaries of the peak for normalization and peak finding purposes.

Peak fitting was performed manually in Peakfit. For singly-peaked spectra, the difference between numerical analysis and fitting was negligible. However, when multiple resonances are present, fitting is necessary to obtain accurate peak positions.

### **A.1.1 bcreator**

```
function out = bcreator(path, base, maxfilenum)
```

```
a =load(strcat(path,base,num2str(1),'.txt'));
```

```
out= a(length(a)/2+1:length(a),1);
```

```
for i=1:maxfilenum
```

```
    P=load(strcat(path,base,num2str(i),'.txt'));
```

```
    P=P(length(P)/2+1:length(P),2);
```

```
    out=[out,P];
```

```
end
```

### **A.1.2 averageforb**

```
function out = averageforb(background, v)
```

```
add=0;
```

```
x=background(:,1);
```

```
for i=1:length(v)
```

```
    add=add+background(:,v(i)+1);
```

```
    avg=add./length(v);
```

```
out=[x,avg];
```

```
end
```

### A.1.3 spectramathb

```
function out = spectramathb(path, base, maxfilenum)
```

```
B=load(strcat(path,'B.txt'));
```

```
x=B(:,1);
```

```
B=B(:,2);
```

```
out=x;
```

```
C=load(strcat(path,'C.txt'));
```

```
C=C(1:length(C)/2,2);
```

```
D=load(strcat(path,'D.txt'));
```

```
D=D(1:length(D)/2,2);
```

```
CDdiff = C-D;
```

```
for i=1:maxfilenum
```

```
P=load(strcat(path,base,num2str(i),'.txt'));
```

```
P=P(1:length(P)/2,2);
```

```
Ptran= (P-B)./CDdiff;
```

```
out=[out,Ptran];
```

```
end
```

#### A.1.4 nsnsmpack

```
function [ydsn,ysm,peaks]=nsnsmpack(in,b,low,high)
```

```
c=1/(sqrt(2*pi*.37));
```

```
d=2*.37^2;
```

```
[l,w]=size(in);
```

```
x=in(:,1);
```

```
ysm=x;
```

```
ydsn=x;
```

```
peaks=[];
```

```
for k=2:w;
```

```
    out=[];
```

```
    y=in(:,k);
```

```
    for i=1:l;
```

```

num=0;

den=0;

for j=1:l;

    t = (x(i)-x(j))/b;

    num = num + y(j)*c*exp(-t^2/d);

    den = den + c*exp(-t^2/d);

end

out(i,1)= num/den;

end

[peak,xp]=max(out(low:high));

out =out./peak; %this is the normalization step for the smooth curve

ysm =[ysm, out];

out2=y./peak;

ynsn=[ynsn,out2];

peaks=[peaks,x(low+xp-1)];

end

```

## A.2 Alloy Wulff Construction

Input definitions

lambda0: initial guess on lambda ( $10^8$ - $10^9$  is usually good)

natoms: number of atoms in the particle

step: calculation step

gamma input: 4-dimensional vector representing the linear relationship between the surface energy and the concentration of Au (or other element), 2 columns XXXX

dginput: 4- or 5-dimensional vector of the coefficients of the third order polynomial used to fit the bulk free energy obtained from experimental values, Eq. 7.24-7.25 (the third order codes are shown below; simple modifications were performed to accommodate the fourth order polynomial equation used for AgPd)

unitcellinput:

### A.2.1 Basic Wulff Model

function

```
[lambdaoutfine,h100outfine,h111outfine,auHcheckfine,Energyfine]=wulffmodelbasic(natoms,lambda0,step,gammainput,dginput,unitcellinput)
```

```
%this does not include starvation or segregation effect. fixed bulk=surface
```

```
%conc.
```

```
%set appropriate termination tolerance on x
```

```
options=optimset('TolX', 10^-11);
```

```
%create empty matrices
```

```
calclambdamodel1=[];
```

```
h100raw=[];
```

```
h111raw=[];
```

```
auHcheckraw=[];  
auSoutraw=[];  
Energyraw=[];  
lambdaoutfine=[];  
h100outfine=[];  
lambdaoutfine=[];  
h111outfine=[];  
auHcheckfine=[];  
auSoutfine=[];  
Energyfine=[];  
a100=gammainput(1,1);  
b100=gammainput(2,1);  
a111=gammainput(3,1);  
b111=gammainput(4,1);  
a=dginput(1,1);  
b=dginput(2,1);  
c=dginput(3,1);  
d=dginput(4,1);  
e=unitcellinput(1,1);  
f=unitcellinput(2,1);  
auHlist=[]
```

```

for k=0:step:1; %running index to change auH

    auH=k

    auS=k;

    %tao and unit cells are only a function of auH, no need to put in the

    %inside loop

    unitcell=e*auH+f;

    lambdamodel1=fzero(@(lambda)

wulffbasic(natoms,auH,lambda,gammainput,unitcellinput),lambda0,options); %this first
approximation only depends on the auH, so no need to put it in the inside auS loop

    lambda0=lambdamodel1;

    gammaH100=a100*auS+b100;

    gammaH111=a111*auS+b111;

    h100=gammaH100/lambdamodel1;

    h111=gammaH111/lambdamodel1;

    surfacearea100=6*2*((sqrt(3))*h111-h100)^2;

    surfacearea111=8*((3*(sqrt(3))/2)*h111^2-3*(sqrt(3))*((sqrt(3))*h111-h100)^2);

    %total energy is just the surface energy in this model

    E=(surfacearea100*gammaH100+surfacearea111*gammaH111);

    %outputs

```

```
out=lambdamodel1;
calclambdamodel1=[calclambdamodel1; out];
out2=h100;
h100raw=[h100raw;out2];
out3=h111;
h111raw=[h111raw;out3];
out4=auH;
auHcheckraw=[auHcheckraw;out4];
out5=E;
Energyraw=[Energyraw;out5];
auHlist=[auHlist;auH];

end

lambdaoutfine=[auHlist,calclambdamodel1];
h100outfine=[auHlist,h100raw];
h111outfine=[auHlist,h111raw];
auHcheckfine=[auHlist,auHcheckraw];
Energyfine=[auHlist,Energyraw];

end
```

### A.2.2 Subfunction Wulffbasic

```

function F=wulffbasic(natoms,auH,lambda,gammainput,unitcellinput)
%this is a setup to solve for lambda Wulff (so-called model 1)

a100=gammainput(1,1);
b100=gammainput(2,1);
a111=gammainput(3,1);
b111=gammainput(4,1);

e=unitcellinput(1,1);
f=unitcellinput(2,1);

lambda0=10^8;

options=optimset('TolX', 10^-11);

unitcell=e*auH+f;

gammaH100=a100*auH+b100;
gammaH111=a111*auH+b111;

h100=gammaH100/lambda;
h111=gammaH111/lambda;

surfacearea100=6*2*((sqrt(3))*h111-h100)^2;
surfacearea111=8*((3*(sqrt(3))/2)*h111^2-3*(sqrt(3))*((sqrt(3))*h111-h100)^2);

F=surfacearea100*h100/3+surfacearea111*h111/3-(natoms*unitcell^3)/4;

```

### A.2.3 Number of Surface Atoms in a Basic Wulff Construction Given $h_{111}$ and $h_{100}$

```

function F=nsurfaceatomsbasic(h111,h100,unitcellinput,auHmin,auHmax,step)

auHout=[];

e=unitcellinput(1,1);
f=unitcellinput(2,1);
natout=[];

for i=(auHmin+1):1:((auHmax-auHmin)/step+1);

    auH=i*step-step;

    unitcell=e*auH+f;

    h111value=h111(i,2); %takes the value of h111 (h100 below) corresponding to the minimum
energy value

    h100value=h100(i,2);

    surfacearea100=6*2*((sqrt(3))*h111value-h100value)^2; %note that the model used is the
model in which 111 faces dominate

    surfacearea111=8*((3*(sqrt(3))/2)*h111value^2-3*(sqrt(3))*((sqrt(3))*h111value-
h100value)^2);

    nsurfatoms=surfacearea100*2/(unitcell)^2+surfacearea111*4/((sqrt(3))*unitcell^2);

    natout=[natout;nsurfatoms];

    auHout=[auHout;auH];

end

F=[auHout,natout];

end

```

## A2.4 Alloy Wulff Modeling with Ssegregation but no Starvation

function

```
[lambdaoutfine,h100outfine,h111outfine,auHcheckfine,auSoufine,Energyfine,Energystarv]=wulffmodel2nostarvenergy(natoms,lambda0,step,gammainput,dginput,unitcellinput)
```

%nostarvation in this model

%a flexible code, can change the gammas, dG, unit cell to allow different

%alloys

```
options=optimset('TolX', 10^-11);
```

```
calclambdamodel2=[];
```

```
h100raw=[];%make this intermediate matrices as the final matrices need to be broken up from the output vector
```

```
h111raw=[];
```

```
auHcheckraw=[];
```

```
auSoutraw=[];
```

```
Energyraw=[];
```

```
Energystarva=[];
```

```
Energystarv=[];
```

```
Energystarvraw=[];
```

```
lambdaoutfine=[];
```

```
h100outfine=[];
```

```
lambdaoutfine=[];
```

```
h111outline=[];
auHcheckfine=[];
auSoutfine=[];
Energyfine=[];
a100=gammainput(1,1);
b100=gammainput(2,1);
a111=gammainput(3,1);
b111=gammainput(4,1);
a=dginput(1,1);
b=dginput(2,1);
c=dginput(3,1);
d=dginput(4,1);
e=unitcellinput(1,1);
f=unitcellinput(2,1);
for k=0:step:1; %running index to change auH
    auH=k
    %tao and unit cells are only a function of auH, no need to put in the
    %inside loop
    unitcell=e*auH+f;
    tao100=unitcell/2; %I use 1/2 unit cell (more precisely the distance between 200's), which
    corresponds to about 1 atom deep
```

$\text{tao111}=\text{unitcell}*(\text{sqrt}(3))/3$ ; %for 111, the distance between 2 adjacent planes (222's) is different than for 100s.

$\text{lambdamodel1}=\text{fzero}(@(\text{lambda})$

$\text{wulffbasic}(\text{natoms},\text{auH},\text{lambda},\text{gammainput},\text{unitcellinput}),\text{lambda0},\text{options})$ ; %this first approximation only depends on the auH, so no need to put it in the inside auS loop

$\text{lambda0}=\text{lambdamodel1}$ ;

for  $i=0:\text{step}:1$ ; %running index to change auS

$\text{auS}=i$ ;

$\text{lambdamodel2}=\text{fzero}(@(\text{lambda})$

$\text{model2}(\text{natoms},\text{auS},\text{auH},\text{lambda},\text{gammainput},\text{dginput},\text{unitcellinput}),\text{lambdamodel1},\text{options})$ ;%get lambda from model 2 (no starvation)

%this paragraph calculates cv from lambdamodel2

%this paragraph calculates cv from lambdamodel2

$\text{Gs}=\text{a}*\text{auS}^3+\text{b}*\text{auS}^2+\text{c}*\text{auS}+\text{d}$ ; %bulk free energy. the coefficients are determined by fitting experimental data

$\text{Gh}=\text{a}*\text{auH}^3+\text{b}*\text{auH}^2+\text{c}*\text{auH}+\text{d}$ ; %this is never going to change

$\text{gammaH100}=\text{a100}*\text{auS}+\text{b100}$ ;

$\text{gammaH111}=\text{a111}*\text{auS}+\text{b111}$ ;

$\text{gammacorr100}=\text{gammaH100}+\text{tao100}*(\text{Gs}-\text{Gh})$ ; %this corrects for the fact that the bulk and surface are not the same concentration.

$\text{gammacorr111}=\text{gammaH111}+\text{tao111}*(\text{Gs}-\text{Gh})$ ;

$\text{h100}=\text{gammacorr100}/(\text{lambdamodel2})$ ;

$\text{h111}=\text{gammacorr111}/(\text{lambdamodel2})$ ;

```

surfacearea100=6*2*((sqrt(3))*h111-h100)^2;

surfacearea111=8*((3*(sqrt(3))/2)*h111^2-3*(sqrt(3))*((sqrt(3))*h111-h100)^2);

%total energy

E=(surfacearea100*gammacorr100+surfacearea111*gammacorr111);

%starvation energy (to compare with other models

nsurfatoms=surfacearea100*2/(unitcell)^2+surfacearea111*4/((sqrt(3))*unitcell^2);

auV=(nsurfatoms*(auH-auS)+(natoms-nsurfatoms)*auH)/(natoms-nsurfatoms);

Gv=a*auV^3+b*auV^2+c*auV^1+d;

gammacorr100=gammaH100+tao100*(Gs-Gv); %need to get the appropriate gamma

gammacorr111=gammaH111+tao111*(Gs-Gv);

Vbulk=(natoms-nsurfatoms)*(unitcell^3)/4;

if auV>1;

    Es=0;

elseif auV<0;

    Es=0;

else

    dEstarv=Vbulk*(Gv-Gh) %note here that this depends on volume, so making a particle
bigger makes this contribution also bigger

    Es=(surfacearea100*gammacorr100+surfacearea111*gammacorr111)+dEstarv;

end

%outputs

out=lambdamodel2;

```

```

calclambdamodel2=[calclambdamodel2; out];

out2=h100;

h100raw=[h100raw;out2];

out3=h111;

h111raw=[h111raw;out3];

out4=auH;

auHcheckraw=[auHcheckraw;auH];

out5=auS;

auSoutraw=[auSoutraw;out5];

out6=E;

Energyraw=[Energyraw;out6];

out7=Es;

Energystarva=[Energystarva;out7];

end

end

%this loop breaks up the vector output into square matrices

for l=0:1:(1/step);

    lambdaoutfineraw=calclambdamodel2((1/step)*l+1:(1/step)*l+(1/step)+1+1);

    lambdaoutfine=[lambdaoutfine,lambdaoutfineraw];

    h100outfineraw=h100raw((1/step)*l+1:(1/step)*l+(1/step)+1+1);

    h100outfine=[h100outfine,h100outfineraw];

    h111outfineraw=h111raw((1/step)*l+1:(1/step)*l+(1/step)+1+1);

```

```

h111outfine=[h111outfine,h111outfineraw];

auHcheckfineraw=auHcheckraw((1/step)*l+1+1:(1/step)*l+(1/step)+1+1);

auHcheckfine=[auHcheckfine,auHcheckfineraw];

auSoutfineraw=auSoutraw((1/step)*l+1+1:(1/step)*l+(1/step)+1+1);

auSoutfine=[auSoutfine,auSoutfineraw];

Energyfineraw=Energyraw((1/step)*l+1+1:(1/step)*l+(1/step)+1+1);

Energyfine=[Energyfine,Energyfineraw];

Energystarvraw=Energystarva((1/step)*l+1+1:(1/step)*l+(1/step)+1+1);

Energystarv=[Energystarv,Energystarvraw];

end

```

### A.2.5 Subfunction model2

```

function F = model2(natoms,auS,auH,lambda,gammainput,dginput,unitcellinput) %This is
model 2, for the infinite reservoir modeling, with segregation but no starvation
%natoms is total number of atoms, auS is the surface [Au], auH is the bulk [Au]

a100=gammainput(1,1);

b100=gammainput(2,1);

a111=gammainput(3,1);

b111=gammainput(4,1);

a=dginput(1,1);

b=dginput(2,1);

c=dginput(3,1);

```

```

d=dginput(4,1);
e=unitcellinput(1,1);
f=unitcellinput(2,1);
unitcell=e*auH+f;
Gs=a*auS^3+b*auS^2+c*auS+d;
Gv=a*auH^3+b*auH^2+c*auH+d;
tao100=unitcell/2;
tao111=unitcell*(sqrt(3))/3;
gammaH100=a100*auS+b100;
gammaH111=a111*auS+b111;
gammacorr100=gammaH100+tao100*(Gs-Gv);
gammacorr111=gammaH111+tao111*(Gs-Gv);
h100=gammacorr100/lambda;
h111=gammacorr111/lambda;
surfacearea100=6*2*((sqrt(3))*h111-h100)^2;
surfacearea111=8*((3*(sqrt(3))/2)*h111^2-3*(sqrt(3))*((sqrt(3))*h111-h100)^2);
F=surfacearea100*h100/3+surfacearea111*h111/3-(natoms*unitcell^3)/4;

```

### A.2.6 Main alloy Wulff construction function

[function](#)

```

[lambdautfine,h100outfine,h111outfine,auVcheckfine,auSoutfine,Energyfine]=wulffmodel3flex
(natoms,lambda0,step,gammainput,dginput,unitcellinput)

```

```
% a good lambda0 should be around 5*10^8

%a flexible code, can change the gammas, dG, unit cell to allow different

%alloys; simple changes allow the use of variable boundaries, see next Section

options=optimset( 'TolX', 10^-11);

calclambdamodel3=[];

h100raw=[];

h111raw=[];

auVcheckraw=[];

auSoutraw=[];

Energyraw=[];

lambdaoutfine=[];

h100outfine=[];

lambdaoutfine=[];

h111outfine=[];

auVcheckfine=[];

auSoutfine=[];

Energyfine=[];

a100=gammainput(1,1);

b100=gammainput(2,1);

a111=gammainput(3,1);

b111=gammainput(4,1);

a=dginput(1,1);
```

```

b=dginput(2,1);
c=dginput(3,1);
d=dginput(4,1);
e=unitcellinput(1,1);
f=unitcellinput(2,1);
for k=0:step:1; %running index to change auH
    auH=k
    %tao and unit cells are only a function of auH
    unitcell=e*auH+f;
    tao100=unitcell/2; %I use 1/2 unit cell (more precisely the distance between 200's), which
corresponds to about 1 atom deep
    tao111=unitcell*(sqrt(3))/3; %for 111, the distance between 2 adjacent planes (222's) is
different than for 100s.
    lambdamodel1=fzero(@(lambda)
wulffbasic(natoms,auH,lambda,gammainput,unitcellinput),lambda0,options); %this first
approximation only depends on the auH
    lambda0=lambdamodel1;
    for i=0:step:1; %running index to change auS
        auS=i
        lambdamodel2=fzero(@(lambda)
model2(natoms,auS,auH,lambda,gammainput,dginput,unitcellinput),lambdamodel1,options)%ge
t lambda from model 2 (no starvation)

```

```

if lambdamodel2<10^7 %this is to prevent the code from finding unrealistic values

    lambdamodel2=fzero(@(lambda)

model2(natoms,auS,auH,lambda,gammainput,dginput,unitcellinput),(10^9),options)

else lambdamodel2=lambdamodel2

end

%this paragraph calculates Cv from lambdamodel2

Gs=a*auS^3+b*auS^2+c*auS+d; %bulk free energy. the coefficients are determined by
fitting experimental data

Gh=a*auH^3+b*auH^2+c*auH+d;

gammaH100=a100*auS+b100;

gammaH111=a111*auS+b111;

gammacorr100=gammaH100+tao100*(Gs-Gh); %this corrects for the fact that the bulk and
surface are not the same concentration.

gammacorr111=gammaH111+tao111*(Gs-Gh);

%the following calculate [Au] in the bulk (auV)

h100=gammacorr100/lambdamodel2;

h111=gammacorr111/lambdamodel2;

surfacearea100=6*2*((sqrt(3))*h111-h100)^2; %note that the model used is the model in
which 111 faces dominate

surfacearea111=8*((3*(sqrt(3))/2)*h111^2-3*(sqrt(3))*((sqrt(3))*h111-h100)^2);

```

```

nsurfatoms=surfacearea100*2/(unitcell)^2+surfacearea111*4/((sqrt(3))*unitcell^2); %this
takes into account the fact that the surface density is different for ((100)) and ((111)), ((111))
being more dense

auV=(nsurfatoms*(auH-auS)+(natoms-nsurfatoms)*auH)/(natoms-nsurfatoms); %initial
guess on the starved bulk concentration

if auV>1;

auV=1; %can't get a concentration above 1!

auSm=auH-((auV*(natoms-nsurfatoms)-(natoms-nsurfatoms)*auH)/nsurfatoms);

Gs=a*auSm^3+b*auSm^2+c*auSm+d;

Gv=a*auV^3+b*auV^2+c*auV+d;

dG=Gv-Gh;

%take lambdamodel2 as guess

lambdamodel3=fzero(@(lambda)model3(natoms,auSm,auH,auV,
lambda,gammainput,dginput,unitcellinput),(lambdamodel2+dG),options);

%reiterate because the number of atoms on the surface, hence the
%surface concentration, changes with shape

Gs=a*auSm^3+b*auSm^2+c*auSm+d;

Gv=a*auV^3+b*auV^2+c*auV+d; %this is fixed at auV=1. no need to repeat it

gammaH100=a100*auSm+b100;

gammaH111=a111*auSm+b111;

gammacorr100=gammaH100+tao100*(Gs-Gv); %tao was defined at the beginning of the
loop

```

```

gammacorr111=gammaH111+tao111*(Gs-Gv);

dG=Gv-Gh;%this is fixed too, as auV and auH are fixed

h100=gammacorr100/(lambdamodel3-dG);

h111=gammacorr111/(lambdamodel3-dG);

surfacearea100=6*2*((sqrt(3))*h111-h100)^2;

surfacearea111=8*((3*(sqrt(3))/2)*h111^2-3*(sqrt(3))*((sqrt(3))*h111-h100)^2);

nsurfatoms=surfacearea100*2/(unitcell)^2+surfacearea111*4/((sqrt(3))*unitcell^2);

auSm=auH-((auV*(natoms-nsurfatoms)-(natoms-nsurfatoms)*auH)/nsurfatoms);

lambdamodel3=fzero(@(lambda) model3(natoms,auSm,auH,auV,
lambda,gammainput,dginput,unitcellinput),lambdamodel3,options); %take previous
lambda as guess

%reiterate because the number of atoms on the surface, hence the
%surface concentration, changes with shape

Gs=a*auSm^3+b*auSm^2+c*auSm+d;

gammaH100=a100*auSm+b100;

gammaH111=a111*auSm+b111;

gammacorr100=gammaH100+tao100*(Gs-Gv);

gammacorr111=gammaH111+tao111*(Gs-Gv);

h100=gammacorr100/(lambdamodel3-dG);

h111=gammacorr111/(lambdamodel3-dG);

surfacearea100=6*2*((sqrt(3))*h111-h100)^2;

surfacearea111=8*((3*(sqrt(3))/2)*h111^2-3*(sqrt(3))*((sqrt(3))*h111-h100)^2);

```

```

nsurfatoms=surfacearea100*2/(unitcell)^2+surfacearea111*4/((sqrt(3))*unitcell^2);
auSm=auH-((auV*(natoms-nsurfatoms)-(natoms-nsurfatoms)*auH)/nsurfatoms);
lambdamodel3=fzero(@(lambda) model3(natoms,auSm,auH,auV,
lambda,gammainput,dginput,unitcellinput),lambdamodel3,options);
%recalculate parameters relevant to the calculation of total energy
Gv=a*auV^3+b*auV^2+c*auV+d;
Gs=a*auSm^3+b*auSm^2+c*auSm+d;
gammaH100=a100*auSm+b100;
gammaH111=a111*auSm+b111;
gammacorr100=gammaH100+tao100*(Gs-Gv); %this corrects for the fact that the bulk
and surface are not the same concentration.
gammacorr111=gammaH111+tao111*(Gs-Gv);
surfacearea100=6*2*((sqrt(3))*h111-h100)^2;
surfacearea111=8*((3*(sqrt(3))/2)*h111^2-3*(sqrt(3))*((sqrt(3))*h111-h100)^2);
nsurfatoms=surfacearea100*2/(unitcell)^2+surfacearea111*4/((sqrt(3))*unitcell^2);
%starvation energy
Vbulk=(natoms-nsurfatoms)*(unitcell^3)/4;
dEstarv=Vbulk*(Gv-Gh);
%total energy
E=(surfacearea100*gammacorr100+surfacearea111*gammacorr111)+dEstarv;
%outputs
out=lambdamodel3;

```

```

calclambdamodel3=[calclambdamodel3; out];

out2=h100;

h100raw=[h100raw;out2];

out3=h111;

h111raw=[h111raw;out3];

out4=auV;

auVcheckraw=[auVcheckraw;auV];

out5=auSm;

auSoutraw=[auSoutraw;out5];

out6=E;

Energyraw=[Energyraw;out6];

elseif auV<0;

auV=0; %can't get a concentration below 0!

auSm=auH-((auV*(natoms-nsurfatoms)-(natoms-nsurfatoms)*auH)/nsurfatoms);

Gs=a*auSm^3+b*auSm^2+c*auSm+d;

Gv=a*auV^3+b*auV^2+c*auV+d;

dG=Gv-Gh;

lambdamodel3=fzero(@(lambda) model3(natoms,auSm,auH,auV,

lambda,gammainput,dginput,unitcellinput),(lambdamodel2+dG),options);

%reiterate bcause the number of atoms on the surface, hence the

%surface concentration, changes with shape

Gs=a*auSm^3+b*auSm^2+c*auSm+d;

```

```

Gv=a*auV^3+b*auV^2+c*auV+d; %this is fixed at auV=1. no need to repeat it

gammaH100=a100*auSm+b100;

gammaH111=a111*auSm+b111;

gammacorr100=gammaH100+tao100*(Gs-Gv);

gammacorr111=gammaH111+tao111*(Gs-Gv);

dG=Gv-Gh;%this is fixed too, as auV and auH are fixed

h100=gammacorr100/(lambdamodel3-dG);

h111=gammacorr111/(lambdamodel3-dG);

surfacearea100=6*2*((sqrt(3))*h111-h100)^2;

surfacearea111=8*((3*(sqrt(3))/2)*h111^2-3*(sqrt(3))*((sqrt(3))*h111-h100)^2);

nsurfatoms=surfacearea100*2/(unitcell)^2+surfacearea111*4/((sqrt(3))*unitcell^2);

auSm=auH-((auV*(natoms-nsurfatoms)-(natoms-nsurfatoms)*auH)/nsurfatoms);

lambdamodel3=fzero(@(lambda) model3(natoms,auSm,auH,auV,
lambda,gammainput,dginput,unitcellinput),lambdamodel3,options);

%reiterate bcause the number of atoms on the surface, hence the
%surface concentration, changes with shape

Gs=a*auSm^3+b*auSm^2+c*auSm+d;

gammaH100=a100*auSm+b100;

gammaH111=a111*auSm+b111;

gammacorr100=gammaH100+tao100*(Gs-Gv);

gammacorr111=gammaH111+tao111*(Gs-Gv);

h100=gammacorr100/(lambdamodel3-dG);

```

```

h111=gamma corr111/(lambdamodel3-dG);

surfacearea100=6*2*((sqrt(3))*h111-h100)^2;

surfacearea111=8*((3*(sqrt(3))/2)*h111^2-3*(sqrt(3))*((sqrt(3))*h111-h100)^2);

nsurfatoms=surfacearea100*2/(unitcell)^2+surfacearea111*4/((sqrt(3))*unitcell^2);

auSm=auH-((auV*(natoms-nsurfatoms)-(natoms-nsurfatoms)*auH)/nsurfatoms);

lambdamodel3=fzero(@(lambda) model3(natoms,auSm,auH,auV,
lambda,gammainput,dginput,unitcellinput),lambdamodel3,options);

%recalculate parameters relevant to the calculation of total energy

Gv=a*auV^3+b*auV^2+c*auV+d;

Gs=a*auSm^3+b*auSm^2+c*auSm+d;

gammaH100=a100*auSm+b100;

gammaH111=a111*auSm+b111;

gamma corr100=gammaH100+tao100*(Gs-Gv); %this corrects for the fact that the bulk
and surface are not the same concentration.

gamma corr111=gammaH111+tao111*(Gs-Gv);

h100=gamma corr100/(lambdamodel3-dG);

h111=gamma corr111/(lambdamodel3-dG);

surfacearea100=6*2*((sqrt(3))*h111-h100)^2;

surfacearea111=8*((3*(sqrt(3))/2)*h111^2-3*(sqrt(3))*((sqrt(3))*h111-h100)^2);

nsurfatoms=surfacearea100*2/(unitcell)^2+surfacearea111*4/((sqrt(3))*unitcell^2);

%starvation energy

Vbulk=(natoms-nsurfatoms)*(unitcell^3)/4;

```

```

dEstarv=Vbulk*(Gv-Gh);

%total energy

E=(surfacearea100*gammacorr100+surfacearea111*gammacorr111)+dEstarv;

%outputs

out=lambdamodel3;

calclambdamodel3=[calclambdamodel3; out];

out2=h100;

h100raw=[h100raw;out2];

out3=h111;

h111raw=[h111raw;out3];

out4=auV;

auVcheckraw=[auVcheckraw;auV];

out5=auSm;

auSoutraw=[auSoutraw;out5];

out6=E;

Energyraw=[Energyraw;out6];

else %this needs a few iterations to get the number of surface atoms correct, as the number
of surface %atoms varies in function of the shape

auV=(nsurfatoms*(auH-auS)+(natoms-nsurfatoms)*auH)/(natoms-nsurfatoms);

Gv=a*auV^3+b*auV^2+c*auV+d;

gammaH100=a100*auS+b100;

gammaH111=a111*auS+b111;

```

```

gammacorr100=gammaH100+tao100*(Gs-Gv);
gammacorr111=gammaH111+tao111*(Gs-Gv);
dG=Gv-Gh;
if (lambdamodel2+dG)<0
    lambdaguess=lambdamodel2
else lambdaguess=lambdamodel2+dG
end
lambdamodel3=fzero(@(lambda) model3(natoms,auS,auH,auV,
lambda,gammainput,dginput,unitcellinput),(lambdaguess),options);
%need to recalculate auV from the new lambda
Gv=a*auV^3+b*auV^2+c*auV+d;
gammaH100=a100*auS+b100;
gammaH111=a111*auS+b111;
gammacorr100=gammaH100+tao100*(Gs-Gv);
gammacorr111=gammaH111+tao111*(Gs-Gv);
dG=Gv-Gh;
h100=gammacorr100/(lambdamodel3-dG);
h111=gammacorr111/(lambdamodel3-dG);
surfacearea100=6*2*((sqrt(3))*h111-h100)^2;
surfacearea111=8*((3*(sqrt(3))/2)*h111^2-3*(sqrt(3))*((sqrt(3))*h111-h100)^2);
nsurfatoms=surfacearea100*2/(unitcell)^2+surfacearea111*4/((sqrt(3))*unitcell^2);
auV=(nsurfatoms*(auH-auS)+(natoms-nsurfatoms)*auH)/(natoms-nsurfatoms);

```

```

%from the new auV calculate another lambda

lambdamodel3=fzero(@(lambda) model3(natoms,auS,auH,auV,
lambda,gammainput,dginput,unitcellinput),lambdamodel3,options);

%from the new lambda calculate a new auV

Gv=a*auV^3+b*auV^2+c*auV+d;

dG=Gv-Gh;

gammacorr100=gammaH100+tao100*(Gs-Gv);

gammacorr111=gammaH111+tao111*(Gs-Gv);

h100=gammacorr100/(lambdamodel3-dG);

h111=gammacorr111/(lambdamodel3-dG);

surfacearea100=6*2*((sqrt(3))*h111-h100)^2;

surfacearea111=8*((3*(sqrt(3))/2)*h111^2-3*(sqrt(3))*((sqrt(3))*h111-h100)^2);

nsurfatoms=surfacearea100*2/(unitcell)^2+surfacearea111*4/((sqrt(3))*unitcell^2);

auV=(nsurfatoms*(auH-auS)+(natoms-nsurfatoms)*auH)/(natoms-nsurfatoms);

%recalculate parameters for total energy

Gv=a*auV^3+b*auV^2+c*auV+d;

gammacorr100=gammaH100+tao100*(Gs-Gv);

gammacorr111=gammaH111+tao111*(Gs-Gv);

Vbulk=(natoms-nsurfatoms)*(unitcell^3)/4;

h100=gammacorr100/(lambdamodel3-dG);

h111=gammacorr111/(lambdamodel3-dG);

surfacearea100=6*2*((sqrt(3))*h111-h100)^2;

```

```

surfacearea111=8*((3*(sqrt(3))/2)*h111^2-3*(sqrt(3))*((sqrt(3))*h111-h100)^2);
nsurfatoms=surfacearea100*2/(unitcell)^2+surfacearea111*4/((sqrt(3))*unitcell^2);
dEstarv=Vbulk*(Gv-Gh);

%total energy
E=(surfacearea100*gammacorr100+surfacearea111*gammacorr111)+dEstarv;

%this if loops prevent negative values of auV
if auV>1;
auV=1; %can't get a concentration above 1!
auSm=auH-((auV*(natoms-nsurfatoms)-(natoms-nsurfatoms)*auH)/nsurfatoms);
lambdamodel3=fzero(@(lambda) model3(natoms,auSm,auH,auV,
lambda,gammainput,dginput,unitcellinput),lambdamodel3,options);
%reiterate because the number of atoms on the surface, hence the
%surface concentration, changes with shape
Gs=a*auSm^3+b*auSm^2+c*auSm+d;
Gv=a*auV^3+b*auV^2+c*auV+d; %this is fixed at auV=1. no need to repeat it
gammaH100=a100*auSm+b100;
gammaH111=a111*auSm+b111;
gammacorr100=gammaH100+tao100*(Gs-Gv); %tao was defined at the beginning of the
loop
gammacorr111=gammaH111+tao111*(Gs-Gv);
dG=Gv-Gh;%this is fixed too, as auV and auH are fixed
h100=gammacorr100/(lambdamodel3-dG);

```

```

h111=gamma CORR111/(lambdamodel3-dG);

surfacearea100=6*2*((sqrt(3))*h111-h100)^2;

surfacearea111=8*((3*(sqrt(3))/2)*h111^2-3*(sqrt(3))*((sqrt(3))*h111-h100)^2);

nsurfatoms=surfacearea100*2/(unitcell)^2+surfacearea111*4/((sqrt(3))*unitcell^2);

auSm=auH-((auV*(natoms-nsurfatoms)-(natoms-nsurfatoms)*auH)/nsurfatoms);

lambdamodel3=fzero(@(lambda) model3(natoms,auSm,auH,auV,
lambda,gammainput,dginput,unitcellinput),lambdamodel3,options);

% auV=(nsurfatoms*(auH-auS)+(natoms-nsurfatoms)*auH)/(natoms-nsurfatoms);

%reiterate bcause the number of atoms on the surface, hence the
%surface concentration, changes with shape

Gs=a*auSm^3+b*auSm^2+c*auSm+d;

gammaH100=a100*auSm+b100;

gammaH111=a111*auSm+b111;

gamma CORR100=gammaH100+tao100*(Gs-Gv);

gamma CORR111=gammaH111+tao111*(Gs-Gv);

h100=gamma CORR100/(lambdamodel3-dG);

h111=gamma CORR111/(lambdamodel3-dG);

surfacearea100=6*2*((sqrt(3))*h111-h100)^2;

surfacearea111=8*((3*(sqrt(3))/2)*h111^2-3*(sqrt(3))*((sqrt(3))*h111-h100)^2);

nsurfatoms=surfacearea100*2/(unitcell)^2+surfacearea111*4/((sqrt(3))*unitcell^2);

auSm=auH-((auV*(natoms-nsurfatoms)-(natoms-nsurfatoms)*auH)/nsurfatoms);

```

```

lambdamodel3=fzero(@(lambda) model3(natoms,auSm,auH,auV,
lambda,gammainput,dginput,unitcellinput),lambdamodel3,options);

    %recalculate parameters relevant to the calculation of total energy

Gv=a*auV^3+b*auV^2+c*auV+d;

Gs=a*auSm^3+b*auSm^2+c*auSm+d;

gammaH100=a100*auSm+b100;

gammaH111=a111*auSm+b111;

gammacorr100=gammaH100+tao100*(Gs-Gv); %this corrects for the fact that the bulk
and surface are not the same concentration.

gammacorr111=gammaH111+tao111*(Gs-Gv);

surfacearea100=6*2*((sqrt(3))*h111-h100)^2;

surfacearea111=8*((3*(sqrt(3))/2)*h111^2-3*(sqrt(3))*((sqrt(3))*h111-h100)^2);

nsurfatoms=surfacearea100*2/(unitcell)^2+surfacearea111*4/((sqrt(3))*unitcell^2);

%starvation energy

Vbulk=(natoms-nsurfatoms)*(unitcell^3)/4;

dEstarv=Vbulk*(Gv-Gh);

%total energy

E=(surfacearea100*gammacorr100+surfacearea111*gammacorr111)+dEstarv;

%outputs

out=lambdamodel3;

calclambdamodel3=[calclambdamodel3; out];

out2=h100;

```

```

h100raw=[h100raw;out2];

out3=h111;

h111raw=[h111raw;out3];

out4=auV;

auVcheckraw=[auVcheckraw;auV];

out5=auSm;

auSoutraw=[auSoutraw;out5];

out6=E;

Energyraw=[Energyraw;out6];

elseif auV<0;

    auV=0; %can't get a concentration below 0!

    auSm=auH-((auV*(natoms-nsurfatoms)-(natoms-nsurfatoms)*auH)/nsurfatoms);

    lambdamodel3=fzero(@(lambda) model3(natoms,auSm,auH,auV,

    lambda,gammainput,dginput,unitcellinput),lambdamodel3,options);

    %reiterate bcause the number of atoms on the surface, hence the

    %surface concentration, changes with shape

    Gs=a*auSm^3+b*auSm^2+c*auSm+d;

    Gv=a*auV^3+b*auV^2+c*auV+d; %this is fixed at auV=1. no need to repeat it

    gammaH100=a100*auSm+b100;

    gammaH111=a111*auSm+b111;

    gammacorr100=gammaH100+tao100*(Gs-Gv); %tao was defined at the beginning of the

loop

```

```

gammacorr111=gammaH111+tao111*(Gs-Gv);

dG=Gv-Gh;%this is fixed too, as auV and auH are fixed

h100=gammacorr100/(lambdamodel3-dG);

h111=gammacorr111/(lambdamodel3-dG);

surfacearea100=6*2*((sqrt(3))*h111-h100)^2;

surfacearea111=8*((3*(sqrt(3))/2)*h111^2-3*(sqrt(3))*((sqrt(3))*h111-h100)^2);

nsurfatoms=surfacearea100*2/(unitcell)^2+surfacearea111*4/((sqrt(3))*unitcell^2);

auSm=auH-((auV*(natoms-nsurfatoms)-(natoms-nsurfatoms)*auH)/nsurfatoms);

lambdamodel3=fzero(@(lambda) model3(natoms,auSm,auH,auV,
lambda,gammainput,dginput,unitcellinput),lambdamodel3,options);

%auV=(nsurfatoms*(auH-auS)+(natoms-nsurfatoms)*auH)/(natoms-nsurfatoms);

%reiterate bcause the number of atoms on the surface, hence the
%surface concentration, changes with shape

Gs=a*auSm^3+b*auSm^2+c*auSm+d;

gammaH100=a100*auSm+b100;

gammaH111=a111*auSm+b111;

gammacorr100=gammaH100+tao100*(Gs-Gv);

gammacorr111=gammaH111+tao111*(Gs-Gv);

h100=gammacorr100/(lambdamodel3-dG);

h111=gammacorr111/(lambdamodel3-dG);

surfacearea100=6*2*((sqrt(3))*h111-h100)^2;

surfacearea111=8*((3*(sqrt(3))/2)*h111^2-3*(sqrt(3))*((sqrt(3))*h111-h100)^2);

```

```

nsurfatoms=surfacearea100*2/(unitcell)^2+surfacearea111*4/((sqrt(3))*unitcell^2);
auSm=auH-((auV*(natoms-nsurfatoms)-(natoms-nsurfatoms)*auH)/nsurfatoms);
lambdamodel3=fzero(@(lambda) model3(natoms,auSm,auH,auV,
lambda,gammainput,dginput,unitcellinput),lambdamodel3,options);
%recalculate parameters relevant to the calculation of total energy
Gv=a*auV^3+b*auV^2+c*auV+d;
Gs=a*auSm^3+b*auSm^2+c*auSm+d;
gammaH100=a100*auSm+b100;
gammaH111=a111*auSm+b111;
gammacorr100=gammaH100+tao100*(Gs-Gv); %this corrects for the fact that the bulk
and surface are not the same concentration.
gammacorr111=gammaH111+tao111*(Gs-Gv);
h100=gammacorr100/(lambdamodel3-dG);
h111=gammacorr111/(lambdamodel3-dG);
surfacearea100=6*2*((sqrt(3))*h111-h100)^2;
surfacearea111=8*((3*(sqrt(3))/2)*h111^2-3*(sqrt(3))*((sqrt(3))*h111-h100)^2);
nsurfatoms=surfacearea100*2/(unitcell)^2+surfacearea111*4/((sqrt(3))*unitcell^2);
%starvation energy
Vbulk=(natoms-nsurfatoms)*(unitcell^3)/4;
dEstarv=Vbulk*(Gv-Gh); %note here that this depends on volume, so making a particle
bigger makes this contribution also bigger
%total energy

```

```
E=(surfacearea100*gammacorr100+surfacearea111*gammacorr111)+dEstarv;
```

```
%outputs
```

```
out=lambdamodel3;
```

```
calclambdamodel3=[calclambdamodel3; out];
```

```
out2=h100;
```

```
h100raw=[h100raw;out2];
```

```
out3=h111;
```

```
h111raw=[h111raw;out3];
```

```
out4=auV;
```

```
auVcheckraw=[auVcheckraw;auV];
```

```
out5=auSm;
```

```
auSoutraw=[auSoutraw;out5];
```

```
out6=E;
```

```
Energyraw=[Energyraw;out6];
```

```
else out=lambdamodel3;
```

```
calclambdamodel3=[calclambdamodel3; out];
```

```
out2=h100;
```

```
h100raw=[h100raw;out2];
```

```
out3=h111;
```

```
h111raw=[h111raw;out3];
```

```
out4=auV;
```

```
auVcheckraw=[auVcheckraw;auV];
```

```

    out5=auS;

    auSoutraw=[auSoutraw;out5];

    out6=E;

    Energyraw=[Energyraw;out6];

end

end

end

end

%this loop breaks up the vector output into square matrices
for l=0:1:(1/step);

    lambdaoutfineraw=calclambdamodel3((1/step)*l+l+1:(1/step)*l+(1/step)+l+l);

    lambdaoutfine=[lambdaoutfine,lambdaoutfineraw];

    h100outfineraw=h100raw((1/step)*l+l+1:(1/step)*l+(1/step)+l+l);

    h100outfine=[h100outfine,h100outfineraw];

    h111outfineraw=h111raw((1/step)*l+l+1:(1/step)*l+(1/step)+l+l);

    h111outfine=[h111outfine,h111outfineraw];

    auVcheckfineraw=auVcheckraw((1/step)*l+l+1:(1/step)*l+(1/step)+l+l);

    auVcheckfine=[auVcheckfine,auVcheckfineraw];

    auSoutfineraw=auSoutraw((1/step)*l+l+1:(1/step)*l+(1/step)+l+l);

    auSoutfine=[auSoutfine,auSoutfineraw];

    Energyfineraw=Energyraw((1/step)*l+l+1:(1/step)*l+(1/step)+l+l);

    Energyfine=[Energyfine,Energyfineraw];

```

end

### A.2.7 Main alloy Wulff construction function with flexible start and end initial concentrations

function

```
[lambdaoutfine,h100outfine,h111outfine,auVcheckfine,auSoufine,Energyfine]=wulffmodel3
```

```
(natoms,lambda0,auHmin,auHmax,step,gammainput,dginput,unitcellinput)
```

```
% a good lambda0 should be around  $5 \cdot 10^8$ 
```

```
%now with a variable step
```

```
%a flexible code, can change the gammas, dG, unit cell to allow different
```

```
%alloys
```

```
options=optimset('TolX', 10^-11);
```

```
calclambdamodel3=[];
```

```
h100raw=[];%make this intermediate matrices as the final matrices need to be broken up from  
the output %vector
```

```
h111raw=[];
```

```
auVcheckraw=[];
```

```
auSoutraw=[];
```

```
Energyraw=[];
```

```
lambdaoutfine=[];
```

```
h100outfine=[];
```

```
lambdaoutfine=[];
```

```
h111outline=[];
auVcheckfine=[];
auSoutfine=[];
Energyfine=[];
a100=gammainput(1,1);
b100=gammainput(2,1);
a111=gammainput(3,1);
b111=gammainput(4,1);
a=dginput(1,1);
b=dginput(2,1);
c=dginput(3,1);
d=dginput(4,1);
e=unitcellinput(1,1);
f=unitcellinput(2,1);
for k=auHmin:step:auHmax; %running index to change auH
    auH=k
    %tao and unit cells are only a function of auH, no need to put in the
    %inside loop
    unitcell=e*auH+f;
    tao100=unitcell/2; %I use 1/2 unit cell (more precisely the distance between 200's), which
    corresponds %to about 1 atom deep
```

tao111=unitcell\*(sqrt(3))/3; %for 111, the distance between 2 adjacent planes (222's) is different than %for 100s.

lambdamodel1=fzero(@(lambda)

wulffbasic(natoms,auH,lambda,gammainput,unitcellinput),lambda0,options);

%this first approximation only depends on the auH, so no need to put it in the inside auS loop

lambda0=lambdamodel1;

for i=0:step:1; %running index to change auS

auS=i;

lambdamodel2=fzero(@(lambda)

model2(natoms,auS,auH,lambda,gammainput,dginput,unitcellinput),lambdamodel1,options);

%get lambda from model 2 (no starv.)

%this paragraph calculates cv from lambdamodel2

Gs=a\*auS^3+b\*auS^2+c\*auS+d;

%bulk free energy. the coefficients are determined by fitting experimental data

Gh=a\*auH^3+b\*auH^2+c\*auH+d;

gammaH100=a100\*auS+b100;

gammaH111=a111\*auS+b111;

gammacorr100=gammaH100+tao100\*(Gs-Gh);

%this corrects for the fact that the bulk and surface are not the same concentration.

gammacorr111=gammaH111+tao111\*(Gs-Gh);

%the following calculate [Au] in the bulk (auV)

h100=gammacorr100/lambdamodel2;

```

h111=gamma CORR111/lambdamodel2;

surfacearea100=6*2*((sqrt(3))*h111-h100)^2;

    %note that the model used is the model in which 111 faces dominate

surfacearea111=8*((3*(sqrt(3))/2)*h111^2-3*(sqrt(3))*((sqrt(3))*h111-h100)^2);

nsurfatoms=surfacearea100*2/(unitcell)^2+surfacearea111*4/((sqrt(3))*unitcell^2);

    %this takes into account the fact that the surface density is different for 100 and 111, 111
being %more dense

auV=(nsurfatoms*(auH-auS)+(natoms-nsurfatoms)*auH)/(natoms-nsurfatoms);

    %initial guess on the starved bulk concentration

if auV>1;

    auV=1 %can't get a concentration above 1!

    auSm=auH-((auV*(natoms-nsurfatoms)-(natoms-nsurfatoms)*auH)/nsurfatoms);

    %take lambdamodel2 as guess

Gs=a*auSm^3+b*auSm^2+c*auSm+d;

Gv=a*auV^3+b*auV^2+c*auV+d;

dG=Gv-Gh;

lambdamodel3=fzero(@(lambda) model3(natoms,auSm,auH,auV,
lambda,gammainput,dginput,unitcellinput),(lambdamodel2+dG),options);

    %reiterate because the number of atoms on the surface, hence the
    %surface concentration, changes with shape

Gs=a*auSm^3+b*auSm^2+c*auSm+d;

Gv=a*auV^3+b*auV^2+c*auV+d; %this is fixed at auV=1. no need to repeat it

```

```

gammaH100=a100*auSm+b100;

gammaH111=a111*auSm+b111;

gammacorr100=gammaH100+tao100*(Gs-Gv); %tao was defined at the beginning of the
loop

gammacorr111=gammaH111+tao111*(Gs-Gv);

dG=Gv-Gh;%this is fixed too, as auV and auH are fixed

h100=gammacorr100/(lambdamodel3-dG);

h111=gammacorr111/(lambdamodel3-dG);

surfacearea100=6*2*((sqrt(3))*h111-h100)^2;

surfacearea111=8*((3*(sqrt(3))/2)*h111^2-3*(sqrt(3))*((sqrt(3))*h111-h100)^2);

nsurfatoms=surfacearea100*2/(unitcell)^2+surfacearea111*4/((sqrt(3))*unitcell^2);

auSm=auH-((auV*(natoms-nsurfatoms)-(natoms-nsurfatoms)*auH)/nsurfatoms);

lambdamodel3=fzero(@(lambda) model3(natoms,auSm,auH,auV,
lambda,gammainput,dginput,unitcellinput),lambdamodel3,options); %take previous lambda as
guess

%auV=(nsurfatoms*(auH-auS)+(natoms-nsurfatoms)*auH)/(natoms-nsurfatoms);

%reiterate because the number of atoms on the surface, hence the
%surface concentration, changes with shape

Gs=a*auSm^3+b*auSm^2+c*auSm+d;

gammaH100=a100*auSm+b100;

gammaH111=a111*auSm+b111;

gammacorr100=gammaH100+tao100*(Gs-Gv);

```

```

gammacorr111=gammaH111+tao111*(Gs-Gv);

h100=gammacorr100/(lambdamodel3-dG);
h111=gammacorr111/(lambdamodel3-dG);
surfacearea100=6*2*((sqrt(3))*h111-h100)^2;
surfacearea111=8*((3*(sqrt(3))/2)*h111^2-3*(sqrt(3))*((sqrt(3))*h111-h100)^2);
nsurfatoms=surfacearea100*2/(unitcell)^2+surfacearea111*4/((sqrt(3))*unitcell^2);
auSm=auH-((auV*(natoms-nsurfatoms)-(natoms-nsurfatoms)*auH)/nsurfatoms);
lambdamodel3=fzero(@(lambda) model3(natoms,auSm,auH,auV,
lambda,gammainput,dginput,unitcellinput),lambdamodel3,options);
%recalculate parameters relevant to the calculation of total energy
Gv=a*auV^3+b*auV^2+c*auV+d;
Gs=a*auSm^3+b*auSm^2+c*auSm+d;
gammaH100=a100*auSm+b100;
gammaH111=a111*auSm+b111;
gammacorr100=gammaH100+tao100*(Gs-Gv);
%this corrects for the fact that the bulk and surface are not the same concentration.
gammacorr111=gammaH111+tao111*(Gs-Gv);
surfacearea100=6*2*((sqrt(3))*h111-h100)^2;
surfacearea111=8*((3*(sqrt(3))/2)*h111^2-3*(sqrt(3))*((sqrt(3))*h111-h100)^2);
nsurfatoms=surfacearea100*2/(unitcell)^2+surfacearea111*4/((sqrt(3))*unitcell^2);
%starvation energy

```

```

Vbulk=(natoms-nsurfatoms)*(unitcell^3)/4;

dEstarv=Vbulk*(Gv-Gh);

%total energy

E=(surfacearea100*gammacorr100+surfacearea111*gammacorr111)+dEstarv;

%outputs

out=lambdamodel3;

calclambdamodel3=[calclambdamodel3; out];

out2=h100;

h100raw=[h100raw;out2];

out3=h111;

h111raw=[h111raw;out3];

out4=auV;

auVcheckraw=[auVcheckraw;auV];

out5=auSm;

auSoutraw=[auSoutraw;out5];

out6=E;

Energyraw=[Energyraw;out6];

elseif auV<0;

auV=0; %can't get a concentration below zero

auSm=auH-((auV*(natoms-nsurfatoms)-(natoms-nsurfatoms)*auH)/nsurfatoms);

Gs=a*auSm^3+b*auSm^2+c*auSm+d;

Gv=a*auV^3+b*auV^2+c*auV+d;

```

```

dG=Gv-Gh;

lambdamodel3=fzero(@(lambda) model3(natoms,auSm,auH,auV,
lambda,gammainput,dginput,unitcellinput),(lambdamodel2+dG),options);

%reiterate because the number of atoms on the surface, hence the
%surface concentration, changes with shape

Gs=a*auSm^3+b*auSm^2+c*auSm+d;

Gv=a*auV^3+b*auV^2+c*auV+d; %this is fixed at auV=1. no need to repeat it

gammaH100=a100*auSm+b100;

gammaH111=a111*auSm+b111;

    gammacorr100=gammaH100+tao100*(Gs-Gv); %tao was defined at the beginning of
the loop

    gammacorr111=gammaH111+tao111*(Gs-Gv);

dG=Gv-Gh;%this is fixed too, as auV and auH are fixed

h100=gammacorr100/(lambdamodel3-dG);

h111=gammacorr111/(lambdamodel3-dG);

surfacearea100=6*2*((sqrt(3))*h111-h100)^2;

surfacearea111=8*((3*(sqrt(3))/2)*h111^2-3*(sqrt(3))*((sqrt(3))*h111-h100)^2);

nsurfatoms=surfacearea100*2/(unitcell)^2+surfacearea111*4/((sqrt(3))*unitcell^2);

auSm=auH-((auV*(natoms-nsurfatoms)-(natoms-nsurfatoms)*auH)/nsurfatoms);

lambdamodel3=fzero(@(lambda) model3(natoms,auSm,auH,auV,
lambda,gammainput,dginput,unitcellinput),lambdamodel3,options);

%auV=(nsurfatoms*(auH-auS)+(natoms-nsurfatoms)*auH)/(natoms-nsurfatoms);

```

```

%reiterate because the number of atoms on the surface, hence the
%surface concentration, changes with shape

Gs=a*auSm^3+b*auSm^2+c*auSm+d;

gammaH100=a100*auSm+b100;

gammaH111=a111*auSm+b111;

gammacorr100=gammaH100+tao100*(Gs-Gv);

gammacorr111=gammaH111+tao111*(Gs-Gv);

h100=gammacorr100/(lambdamodel3-dG);

h111=gammacorr111/(lambdamodel3-dG);

surfacearea100=6*2*((sqrt(3))*h111-h100)^2;

surfacearea111=8*((3*(sqrt(3))/2)*h111^2-3*(sqrt(3))*((sqrt(3))*h111-h100)^2);

nsurfatoms=surfacearea100*2/(unitcell)^2+surfacearea111*4/((sqrt(3))*unitcell^2);

auSm=auH-((auV*(natoms-nsurfatoms)-(natoms-nsurfatoms)*auH)/nsurfatoms);

lambdamodel3=fzero(@(lambda) model3(natoms,auSm,auH,auV,
lambda,gammainput,dginput,unitcellinput),lambdamodel3,options);

%recalculate parameters relevant to the calculation of total energy

Gv=a*auV^3+b*auV^2+c*auV+d;

Gs=a*auSm^3+b*auSm^2+c*auSm+d;

gammaH100=a100*auSm+b100;

gammaH111=a111*auSm+b111;

gammacorr100=gammaH100+tao100*(Gs-Gv);

%this corrects for the fact that the bulk and surface are not the same concentration.

```

```

gammacorr111=gammaH111+tao111*(Gs-Gv);
h100=gammacorr100/(lambdamodel3-dG);
h111=gammacorr111/(lambdamodel3-dG);
surfacearea100=6*2*((sqrt(3))*h111-h100)^2;
surfacearea111=8*((3*(sqrt(3))/2)*h111^2-3*(sqrt(3))*((sqrt(3))*h111-h100)^2);
nsurfatoms=surfacearea100*2/(unitcell)^2+surfacearea111*4/((sqrt(3))*unitcell^2);
%starvation energy
Vbulk=(natoms-nsurfatoms)*(unitcell^3)/4;
dEstarv=Vbulk*(Gv-Gh);
%total energy
E=(surfacearea100*gammacorr100+surfacearea111*gammacorr111)+dEstarv;
%outputs
out=lambdamodel3;
calclambdamodel3=[calclambdamodel3; out];
out2=h100;
h100raw=[h100raw;out2];
out3=h111;
h111raw=[h111raw;out3];
out4=auV;
auVcheckraw=[auVcheckraw;auV];
out5=auSm;
auSoutraw=[auSoutraw;out5];

```

```

out6=E;

Energyraw=[Energyraw;out6];

else %this needs a few iterations to get the number of surface atoms correct, as
    %the number of surface atoms varies in function of the shape

    auV=(nsurfatoms*(auH-auS)+(natoms-nsurfatoms)*auH)/(natoms-nsurfatoms);

    Gv=a*auV^3+b*auV^2+c*auV+d;

    gammaH100=a100*auS+b100;

    gammaH111=a111*auS+b111;

    gammacorr100=gammaH100+tao100*(Gs-Gv);

    gammacorr111=gammaH111+tao111*(Gs-Gv);

    dG=Gv-Gh;

    lambdamodel3=fzero(@(lambda) model3(natoms,auS,auH,auV,
    lambda,gammainput,dginput,unitcellinput),(lambdamodel2+dG),options);

    %need to recalculate auV from the new lambda

    Gv=a*auV^3+b*auV^2+c*auV+d;

    gammaH100=a100*auS+b100;

    gammaH111=a111*auS+b111;

    gammacorr100=gammaH100+tao100*(Gs-Gv);

    gammacorr111=gammaH111+tao111*(Gs-Gv);

    dG=Gv-Gh;

    h100=gammacorr100/(lambdamodel3-dG);

    h111=gammacorr111/(lambdamodel3-dG);

```

```

surfacearea100=6*2*((sqrt(3))*h111-h100)^2;

surfacearea111=8*((3*(sqrt(3))/2)*h111^2-3*(sqrt(3))*((sqrt(3))*h111-h100)^2);

nsurfatoms=surfacearea100*2/(unitcell)^2+surfacearea111*4/((sqrt(3))*unitcell^2);

auV=(nsurfatoms*(auH-auS)+(natoms-nsurfatoms)*auH)/(natoms-nsurfatoms);

%from the new auV calculate another lambda

lambdamodel3=fzero(@(lambda) model3(natoms,auS,auH,auV,
lambda,gammainput,dginput,unitcellinput),lambdamodel3,options);

%from the new lambda calculate a new auV

Gv=a*auV^3+b*auV^2+c*auV+d;

dG=Gv-Gh;

gammacorr100=gammaH100+tao100*(Gs-Gv);

gammacorr111=gammaH111+tao111*(Gs-Gv);

h100=gammacorr100/(lambdamodel3-dG);

h111=gammacorr111/(lambdamodel3-dG);

surfacearea100=6*2*((sqrt(3))*h111-h100)^2;

surfacearea111=8*((3*(sqrt(3))/2)*h111^2-3*(sqrt(3))*((sqrt(3))*h111-h100)^2);

nsurfatoms=surfacearea100*2/(unitcell)^2+surfacearea111*4/((sqrt(3))*unitcell^2);

auV=(nsurfatoms*(auH-auS)+(natoms-nsurfatoms)*auH)/(natoms-nsurfatoms);

%recalculate parameters for total energy

Gv=a*auV^3+b*auV^2+c*auV+d;

gammacorr100=gammaH100+tao100*(Gs-Gv);

gammacorr111=gammaH111+tao111*(Gs-Gv);

```

```

Vbulk=(natoms-nsurfatoms)*(unitcell^3)/4;
h100=gammacorr100/(lambdamodel3-dG);
h111=gammacorr111/(lambdamodel3-dG);
surfacearea100=6*2*((sqrt(3))*h111-h100)^2;
surfacearea111=8*((3*(sqrt(3))/2)*h111^2-3*(sqrt(3))*((sqrt(3))*h111-h100)^2);
nsurfatoms=surfacearea100*2/(unitcell)^2+surfacearea111*4/((sqrt(3))*unitcell^2);
dEstarv=Vbulk*(Gv-Gh);
%total energy
E=(surfacearea100*gammacorr100+surfacearea111*gammacorr111)+dEstarv;
%this if loops prevent values of auV above 1
if auV>1;
auV=1
auSm=auH-((auV*(natoms-nsurfatoms)-(natoms-nsurfatoms)*auH)/nsurfatoms);
lambdamodel3=fzero(@(lambda) model3(natoms,auSm,auH,auV,
lambda,gammainput,dginput,unitcellinput),lambdamodel3,options);
%reiterate because the number of atoms on the surface, hence the
%surface concentration, changes with shape
Gs=a*auSm^3+b*auSm^2+c*auSm+d;
Gv=a*auV^3+b*auV^2+c*auV+d; %this is fixed at auV=1. no need to repeat it
gammaH100=a100*auSm+b100;
gammaH111=a111*auSm+b111;

```

```

    gammacorr100=gammaH100+tao100*(Gs-Gv); %tao was defined at the beginning of the
loop
    gammacorr111=gammaH111+tao111*(Gs-Gv);
    dG=Gv-Gh;%this is fixed too, as auV and auH are fixed
    h100=gammacorr100/(lambdamodel3-dG);
    h111=gammacorr111/(lambdamodel3-dG);
    surfacearea100=6*2*((sqrt(3))*h111-h100)^2;
    surfacearea111=8*((3*(sqrt(3))/2)*h111^2-3*(sqrt(3))*((sqrt(3))*h111-h100)^2);
    nsurfatoms=surfacearea100*2/(unitcell)^2+surfacearea111*4/((sqrt(3))*unitcell^2);
    auSm=auH-((auV*(natoms-nsurfatoms)-(natoms-nsurfatoms)*auH)/nsurfatoms);
    lambdamodel3=fzero(@(lambda) model3(natoms,auSm,auH,auV,
    lambda,gammainput,dginput,unitcellinput),lambdamodel3,options);
    % auV=(nsurfatoms*(auH-auS)+(natoms-nsurfatoms)*auH)/(natoms-nsurfatoms);
    %reiterate because the number of atoms on the surface, hence the
    %surface concentration, changes with shape
    Gs=a*auSm^3+b*auSm^2+c*auSm+d;
    gammaH100=a100*auSm+b100;
    gammaH111=a111*auSm+b111;
    gammacorr100=gammaH100+tao100*(Gs-Gv);
    gammacorr111=gammaH111+tao111*(Gs-Gv);
    h100=gammacorr100/(lambdamodel3-dG);
    h111=gammacorr111/(lambdamodel3-dG);

```

```

surfacearea100=6*2*((sqrt(3))*h111-h100)^2;
surfacearea111=8*((3*(sqrt(3))/2)*h111^2-3*(sqrt(3))*((sqrt(3))*h111-h100)^2);
nsurfatoms=surfacearea100*2/(unitcell)^2+surfacearea111*4/((sqrt(3))*unitcell^2);
auSm=auH-((auV*(natoms-nsurfatoms)-(natoms-nsurfatoms)*auH)/nsurfatoms);
lambdamodel3=fzero(@(lambda) model3(natoms,auSm,auH,auV,
lambda,gammainput,dginput,unitcellinput),lambdamodel3,options);
%recalculate parameters relevant to the calculation of total energy
Gv=a*auV^3+b*auV^2+c*auV+d;
Gs=a*auSm^3+b*auSm^2+c*auSm+d;
gammaH100=a100*auSm+b100;
gammaH111=a111*auSm+b111;
gammacorr100=gammaH100+tao100*(Gs-Gv);
%this corrects for the fact that the bulk and surface are not the same concentration.
gammacorr111=gammaH111+tao111*(Gs-Gv);
surfacearea100=6*2*((sqrt(3))*h111-h100)^2;
surfacearea111=8*((3*(sqrt(3))/2)*h111^2-3*(sqrt(3))*((sqrt(3))*h111-h100)^2);
nsurfatoms=surfacearea100*2/(unitcell)^2+surfacearea111*4/((sqrt(3))*unitcell^2);
%starvation energy
Vbulk=(natoms-nsurfatoms)*(unitcell^3)/4;
dEstarv=Vbulk*(Gv-Gh);
%total energy
E=(surfacearea100*gammacorr100+surfacearea111*gammacorr111)+dEstarv;

```

```

%outputs

out=lambdamodel3;

calclambdamodel3=[calclambdamodel3; out];

out2=h100;

h100raw=[h100raw;out2];

out3=h111;

h111raw=[h111raw;out3];

out4=auV;

auVcheckraw=[auVcheckraw;auV];

out5=auSm;

auSoutraw=[auSoutraw;out5];

out6=E;

Energyraw=[Energyraw;out6];

elseif auV<0;

    auV=0; %can't get a concentration above 1!

    auSm=auH-((auV*(natoms-nsurfatoms)-(natoms-nsurfatoms)*auH)/nsurfatoms);

    lambdamodel3=fzero(@(lambda) model3(natoms,auSm,auH,auV,
lambda,gammainput,dginput,unitcellinput),lambdamodel3,options);

    %reiterate because the number of atoms on the surface, hence the
    %surface concentration, changes with shape

    Gs=a*auSm^3+b*auSm^2+c*auSm+d;

    Gv=a*auV^3+b*auV^2+c*auV+d; %this is fixed at auV=1. no need to repeat it

```

```

gammaH100=a100*auSm+b100;

gammaH111=a111*auSm+b111;

gammacorr100=gammaH100+tao100*(Gs-Gv); %tao was defined at the beginning of the
loop

gammacorr111=gammaH111+tao111*(Gs-Gv);

dG=Gv-Gh;%this is fixed too, as auV and auH are fixed

h100=gammacorr100/(lambdamodel3-dG);

h111=gammacorr111/(lambdamodel3-dG);

surfacearea100=6*2*((sqrt(3))*h111-h100)^2;

surfacearea111=8*((3*(sqrt(3))/2)*h111^2-3*(sqrt(3))*((sqrt(3))*h111-h100)^2);

nsurfatoms=surfacearea100*2/(unitcell)^2+surfacearea111*4/((sqrt(3))*unitcell^2);

auSm=auH-((auV*(natoms-nsurfatoms)-(natoms-nsurfatoms)*auH)/nsurfatoms);

lambdamodel3=fzero(@(lambda) model3(natoms,auSm,auH,auV,
lambda,gammainput,dginput,unitcellinput),lambdamodel3,options);

% auV=(nsurfatoms*(auH-auS)+(natoms-nsurfatoms)*auH)/(natoms-nsurfatoms);

%reiterate bcause the number of atoms on the surface, hence the
%surface concentration, changes with shape

Gs=a*auSm^3+b*auSm^2+c*auSm+d;

gammaH100=a100*auSm+b100;

gammaH111=a111*auSm+b111;

gammacorr100=gammaH100+tao100*(Gs-Gv);

gammacorr111=gammaH111+tao111*(Gs-Gv);

```

```

h100=gamma corr100/(lambdamodel3-dG);
h111=gamma corr111/(lambdamodel3-dG);
surfacearea100=6*2*((sqrt(3))*h111-h100)^2;
surfacearea111=8*((3*(sqrt(3))/2)*h111^2-3*(sqrt(3))*((sqrt(3))*h111-h100)^2);
nsurfatoms=surfacearea100*2/(unitcell)^2+surfacearea111*4/((sqrt(3))*unitcell^2);
auSm=auH-((auV*(natoms-nsurfatoms)-(natoms-nsurfatoms)*auH)/nsurfatoms);
lambdamodel3=fzero(@(lambda) model3(natoms,auSm,auH,auV,
lambda,gammainput,dginput,unitcellinput),lambdamodel3,options);
%recalculate parameters relevant to the calculation of total energy
Gv=a*auV^3+b*auV^2+c*auV+d;
Gs=a*auSm^3+b*auSm^2+c*auSm+d;
gammaH100=a100*auSm+b100;
gammaH111=a111*auSm+b111;
gamma corr100=gammaH100+tao100*(Gs-Gv);
%this corrects for the fact that the bulk and surface are not the same concentration.
gamma corr111=gammaH111+tao111*(Gs-Gv);
h100=gamma corr100/(lambdamodel3-dG);
h111=gamma corr111/(lambdamodel3-dG);
surfacearea100=6*2*((sqrt(3))*h111-h100)^2;
surfacearea111=8*((3*(sqrt(3))/2)*h111^2-3*(sqrt(3))*((sqrt(3))*h111-h100)^2);
nsurfatoms=surfacearea100*2/(unitcell)^2+surfacearea111*4/((sqrt(3))*unitcell^2);
%starvation energy

```

```

Vbulk=(natoms-nsurfatoms)*(unitcell^3)/4;

dEstarv=Vbulk*(Gv-Gh);

%note here that this depends on volume, so making a particle bigger makes this
contribution %also bigger

%total energy

E=(surfacearea100*gammacorr100+surfacearea111*gammacorr111)+dEstarv;

%outputs

out=lambdamodel3;

calclambdamodel3=[calclambdamodel3; out];

out2=h100;

h100raw=[h100raw;out2];

out3=h111;

h111raw=[h111raw;out3];

out4=auV;

auVcheckraw=[auVcheckraw;auV];

out5=auSm;

auSoutraw=[auSoutraw;out5];

out6=E;

Energyraw=[Energyraw;out6];

else out=lambdamodel3;

calclambdamodel3=[calclambdamodel3; out];

out2=h100;

```

```

h100raw=[h100raw;out2];

out3=h111;

h111raw=[h111raw;out3];

out4=auV;

auVcheckraw=[auVcheckraw;auV];

out5=auS;

auSoutraw=[auSoutraw;out5];

out6=E;

Energyraw=[Energyraw;out6];

end

end

end

end

%this loop breaks up the vector output into square matrices
for m=0:1:((auHmax-auHmin)/step);

lambdaoutfineraw=calclambdamodel3((1/step)*m+m+1:(1/step)*m+(1/step)+1+m);

lambdaoutfine=[lambdaoutfine,lambdaoutfineraw];

h100outfineraw=h100raw((1/step)*m+m+1:(1/step)*m+(1/step)+1+m);

h100outfine=[h100outfine,h100outfineraw];

h111outfineraw=h111raw((1/step)*m+m+1:(1/step)*m+(1/step)+1+m);

h111outfine=[h111outfine,h111outfineraw];

auVcheckfineraw=auVcheckraw((1/step)*m+m+1:(1/step)*m+(1/step)+1+m);

```

```

auVcheckfine=[auVcheckfine,auVcheckfineraw];

auSoutfineraw=auSoutraw((1/step)*m+m+1:(1/step)*m+(1/step)+1+m);

auSoutfine=[auSoutfine,auSoutfineraw];

Energyfineraw=Energyraw((1/step)*m+m+1:(1/step)*m+(1/step)+1+m);

Energyfine=[Energyfine,Energyfineraw];

```

```
end
```

### A.2.8 Subfunction model3

```
function F = model3(natoms, auS, auH, auV, lambda,gammainput,dginput,unitcellinput)
```

```
%this is model 3, segregation and starvation included
```

```
%natoms is total number of atoms, auS is the surface [Au], auH is the homogeneous bulk, auV is
the %starved bulk [Au]
```

```
a100=gammainput(1,1);
```

```
b100=gammainput(2,1);
```

```
a111=gammainput(3,1);
```

```
b111=gammainput(4,1);
```

```
a=dginput(1,1);
```

```
b=dginput(2,1);
```

```
c=dginput(3,1);
```

```
d=dginput(4,1);
```

```
e=unitcellinput(1,1);
```

```
f=unitcellinput(2,1);
```

```

unitcell=e*auH+f;

Gs=a*auS^3+b*auS^2+c*auS+d;

Gh=a*auH^3+b*auH^2+c*auH+d;

Gv=a*auV^3+b*auV^2+c*auV+d;

tao100=unitcell/2;

tao111=unitcell*(sqrt(3))/3;

gammaH100=a100*auS+b100;

gammaH111=a111*auS+b111;

gammacorr100=gammaH100+tao100*(Gs-Gv);

gammacorr111=gammaH111+tao111*(Gs-Gv);

dG=Gv-Gh;

h100=gammacorr100/(lambda-dG);

h111=gammacorr111/(lambda-dG);

surfacearea100=6*2*((sqrt(3))*h111-h100)^2;

surfacearea111=8*((3*(sqrt(3))/2)*h111^2-3*(sqrt(3))*((sqrt(3))*h111-h100)^2);

F=surfacearea100*h100/3+surfacearea111*h111/3-(natoms*unitcell^3)/4;

```

### A.2.9. Minimum Surface Concentration

```

function minconc=minauSrealflex(Energy,auSin,auHmin,auHmax,step) %works for all size
matrix
auSmin=[];

```

```

auH=[];

for i=1:1:((auHmax-auHmin)/step+1);

    [energyvalue,auSvaluepos]=min(Energy(:,i));

        %gives the energy value and auS value position of the minimum energy
configuration for a %given starting auH

    auSmin=[auSmin,auSin(auSvaluepos,i)];

    auH=[auH;auHmin+(i*step-step)];

end

auSmin=auSmin';

minconc=[auH,auSmin];

end

```

#### A.2.10 Minimum Bulk (Internal) Concentration

```

function minconc=minauVmodflex(Energy,auVin,auHmin,auHmax,step) %works for all size
matrix

auVmin=[];

auH=[];

for i=1:1:((auHmax-auHmin)/step+1);

    [energyvalue,auSvaluepos]=min(Energy(:,i));

        %gives the energy value and auS value position of the minimum energy
configuration for a %given starting auH

    auVmin=[auVmin,auVin(auSvaluepos,i)];

```

```

    auH=[auH;auHmin+(i*step-step)];
end
auVmin=auVmin';
minconc=[auH,auVmin];
end

```

### A.2.11 Minimum Total Energy for Each Starting Composition

```

function minconc=minEnergyrealflex(Energy,auSin,auHmin,auHmax,step) %works for all size
matrix
auSmin=[];
auH=[];
for i=1:1:((auHmax-auHmin)/step+1);
    [energyvalue,auSvaluepos]=min(Energy(:,i));
    %gives the energy value and auS value position of the minimum energy
configuration for a %given starting auH
    auSmin=[auSmin,auSin(auSvaluepos,i)];
    auH=[auH;auHmin+(i*step-step)];
end
auSmin=auSmin';
minconc=[auH,auSmin];
end

```

### A.2.12 Number of Surface Atoms

```

function F=nsurfaceatoms(Energy,h111,h100,unitcellinput,auHmin,auHmax,step)
auHout=[];
e=unitcellinput(1,1);
f=unitcellinput(2,1);
natout=[];
for i=(auHmin+1):1:((auHmax-auHmin)/step+1);
    auH=i*step-step;
    unitcell=e*auH+f;
    [energyvalue,auSvaluepos]=min(Energy(:,i));
    %gives the energy value and auS value position of the minimum energy
    configuration for a %given starting auH
    h111value=h111(auSvaluepos,i);
    %takes the value of h111 (h100 below) corresponding to the minimum energy value
    h100value=h100(auSvaluepos,i);
    surfacearea100=6*2*((sqrt(3))*h111value-h100value)^2;
    %note that the model used is the model in which 111 faces dominate
    surfacearea111=8*((3*(sqrt(3))/2)*h111value^2-3*(sqrt(3))*((sqrt(3))*h111value-
h100value)^2);
    nsurfatoms=surfacearea100*2/(unitcell)^2+surfacearea111*4/((sqrt(3))*unitcell^2);
    natout=[natout;nsurfatoms];

```

```
auHout=[auHout;auH];
```

```
end
```

```
F=[auHout,natout];
```

```
end
```

### A.2.12. h111/h100

```
function h111_h100_rat=h111_h100nmatoms(Energy,h111,h100,step)
```

```
ratioout=[];
```

```
h100out=[];
```

```
h111out=[];
```

```
auH=[];
```

```
for i=1:1:(1/step+1);
```

```
    [energyvalue,auSvaluepos]=min(Energy(:,i));
```

```
        %gives the energy value and auS value position of the minimum energy configuration for  
a given          %starting auH
```

```
    h111value=h111(auSvaluepos,i);
```

```
        %takes the value of h111 (h100 below) corresponding to the minimum energy value
```

```
    h100value=h100(auSvaluepos,i);
```

```
    ratio=h111value/h100value;
```

```
    ratioout=[ratioout;ratio];
```

```
    h100out=[h100out;h100value];
```

```
    h111out=[h111out;h111value];
```

```

    auH=[auH;i*step-step];

end

h111_h100_rat=[auH,h111out,h100out,ratioout];

end

```

### A.3. Kinetic Wulff Construction, GUI

#### A.3.1 Kinetic Wulff Model for a Monotwinned Particle

```

function
[Vtot,Vtotsm,mX,mY,mZ]=modelmono(step,bound,isovalue,box,beta,twin,reentrant,a_100,a_11
0,a_111)

%this models the Wulff construction of a crystal with two twins (one ((111)) twin plane).

%beta should be smaller than the a values

fint=[];

out=[];

g=[];

for x=-bound:step:bound;

    i=round((x+(bound))/step+1); %i is used as the index of the matrix, while x is used as the
coordinate

    for y=-bound:step:bound;

        j=round((y+(bound))/step+1);

```

```

for z=-bound:step:bound;

    m=round((z+(bound))/step+1);

Vtot(i,j,m) = 1;

a = (x+y+z)/3. ;

if a > 0;

    xx = x ; yy = y ; zz = z;

else

    % Mirror about the plane (111)

    % Since (a;a;a) is the vector along (111), subtract twice this

    xx = x -2*a ; yy = y -2*a ; zz = z -2*a;

end

Vscalar=1;

%i.e. if dot with 111 or -1-11 is smaller or equal to zero, the xyz point has a nonzero
value of V

% Loop over all ((100)), ((110)), and ((111)) facets

%this gives the value of the V

for h=-1:1:1;

    for k=-1:1:1;

        for l=-1:1:1;

            if Vscalar>1E-8;

                gg = h*h+k*k+l*l ;

                % If g.(111) is negative, we have re-entrant surfaces

```

```

% kinetic is an input ;

if dot([h;k;l],[1;1;1])<0; %i.e. if the face is re-entrant type
    enhance=1.0+reentrant+twin;

% for the twin boundary growth enhancement, the faces involved
% are the re-entrant (111) above, and the (100) faces
% (only need the positive ones because of symmetry)

elseif h+k+l == 1;
    if k+l == 0;
        enhance=1.0+twin ;
    elseif l+h == 0;
        enhance=1.0+twin ;
    elseif h+k == 0;
        enhance=1.0+twin ;
    else
        enhance=1;
    end
else enhance=1;
end

if abs( gg-1 ) < 1E-8 ;    % This is a trick to avoid numerical inaccuracies
    amp = a_100 ;
elseif abs(gg-2) < 1E-8 ;
    amp = a_110/sqrt(2) ;

```

```

else abs(gg-3) < 1E-8 ;
amp = a_111/sqrt(3) ;
end %end of if elseif elseif statement
g = amp*enhance*[h,k,l] ;
% Multiply, again only the xyz within the boundaries of the twin will have a
non-zero value for V
dotxyz_g=amp*enhance*(xx*h+yy*k+zz*l); %i.e. dot([x;y;z],g)
dotg_g=amp*amp*enhance*enhance*(gg); %gg calculated earlier
if dotxyz_g<dotg_g;
    F1=1;
else
    F1=exp(-beta*(dotxyz_g-dotg_g)*(dotxyz_g-dotg_g));
end
Vscalar = Vscalar*F1;
end % end if the if Vscalar statement
end %end of the for l statement
end %end of the for k statement
end % end of the for h statement
Vtot(i,j,m)=Vscalar;
end % end of the z loop
end % end of the y loop
end % end of the x loop

```

```

Vtotsm=smooth3(Vtot,'box',box);

%create x, y, z grids

[mX,mY,mZ]=meshgrid(1:(((2*bound)/step)+1),1:(((2*bound)/step)+1),1:(((2*bound)/step)+1));

%create patch figure

p=patch(isosurface(mX,mY,mZ,Vtotsm,isovalue));

%set appropriate lighting, color and orientation for initial figure (can
%re-plot at will using the Vtot and Vtotsm outputs)

set(p,'FaceColor',[.6,.1,0.1],'EdgeColor','none');

daspect([1 1 1])

material([0.4,0.3,0.1]);

lighting gouraud

view(135,40);

camlight(0,0);

camlight(0,0);

view(135,-40);

camlight(0,0);

axis tight

end

```

### A.3.2 Kinetic Wulff Model for a Dh Particle

```

function [mX,mY,mZ,Vtot,
Vtotsm]=modelpenta(step,bound,isovalue,box,beta,disclination,reentrant,a_100,a_110,a_111)

%bound/step must be an integer

%create matrix for values

Vtot=zeros(4*bound/step+1,4*bound/step+1,4*bound/step+1);

for x=-bound:step:bound;

    i=((x+(bound))/step+1+bound/step);

    % need to add this because i is used as the index of the matrix, while x is used as the
coordinate

    for y=-bound:step:bound;

        j=((y+(bound))/step+1+bound/step);

        for z=-bound:step:bound;

            m=((z+(bound))/step+1+bound/step);

            %twin segments 0 to 4

            for n=0:1:4;

                angle=72*n;

                angrad=angle*2*pi/360;

                %compute rotation matrix R

                axee=[1,-1,0];

                L = norm(axee);

                axee = axee / L;

                L = 1;

```

```
u = axee(1);
v = axee(2);
w = axee(3);
u2 = u^2;
v2 = v^2;
w2 = w^2;
c = cos(angrad);
s = sin(angrad);
%storage
R = nan(3);
%fill
R(1,1) = u2 + (v2 + w2)*c;
R(1,2) = u*v*(1-c) - w*s;
R(1,3) = u*w*(1-c) + v*s;
R(2,1) = u*v*(1-c) + w*s;
R(2,2) = v2 + (u2+w2)*c;
R(2,3) = v*w*(1-c) - u*s;
R(3,1) = u*w*(1-c) - v*s;
R(3,2) = v*w*(1-c)+u*s;
R(3,3) = w2 + (u2+v2)*c;
dotwith111=dot([x;y;z],R*[1;1;1]);
dotwith_1_11=dot([x;y;z],R*[-1;-1;1]);
```



```

enhance=1.0+reentrant ;
elseif dot([h;k;l],[-1;-1;1])<0;
    %dot(R*[hh;kk;ll],R*[-1;-1;1])<0;
    enhance=1.0+reentrant ;
    %use the same variable name, enhance,
    %for both reentrant and disclination
    %enhancement; they occur on different
    %faces hence never occur at the same time
else
    if disclination==0; %in this case no disclination enhancement was input

```

by the user

```

    enhance=1;

```

```

else

```

```

    %this part of the code only gets

```

```

    %calculated if there is a

```

```

    %disclination enhancement input

```

```

    if h~=0 ;

```

```

        if k~=0;

```

```

            if l~=0;

```

```

                %the disclination enhancement only occurs at the ((111)) facets that are

```

NOT re-entrant

```

                    enhance=1+disclination;

```

```
        else
            enhance=1;
        end
    else
        enhance=1;
    end
else
    enhance=1;
end
end
end

% Which do we have?
% This is a trick to avoid numerical inaccuracies
if abs( gg-1 ) < 1E-8 ;
    amp = a_100 ;
elseif abs(gg-2) < 1E-8 ;
    amp = a_110/sqrt(2) ;
else abs(gg-3) < 1E-8 ;
    amp = a_111/sqrt(3) ;
end

g = amp*enhance*[hh,kk,ll] ;
```



```
clear n
clear ii
clear jj
clear mm
clear R
clear rotated
clear x
clear y
clear z
clear i
clear j
clear m

Vtotm=smooth3(Vtot, 'box', box);

%create x, y, z grids
[mX,mY,mZ]=meshgrid(1:(((4*bound)/step)+1),1:(((4*bound)/step)+1),1:(((4*bound)/step)+1));

%create patch figure
p=patch(isosurface(mX,mY,mZ,Vtotm,isovalue));

%set appropriate lighting, color and orientation for initial figure (can
%re-plot at will using the Vtot and Vtotm outputs)
set(p,'FaceColor',[0.2,.4,0.6],'EdgeColor','none');

daspect([1 1 1])

material([0.4,0.3,0.1]);
```

```
lighting gouraud
axis tight
view(-135,0);
camlight(0,0);
view([45,-60])
camlight(0,0);
view(45,75);
camlight(0,0);
view([90,-90,0]);
end
```

### A.3.3 Kinetic Wulff GUI

```
function varargout = kineticGUI(varargin)
% KINETICGUI M-file for kineticGUI.fig
% This program is based on the modified kinetic Wulff construction by
% Emilie Ringe, Richard P. Van Duyne and Laurence D.
% Marks
%
%
% Additional queries or comments can be directed to Emilie Ringe,
% emilieringe (at) u.northwestern.edu
```

```
%  
  
% Copyright 2012 Emilie Ringe, Northwestern University  
  
%  
  
% Begin initialization code - DO NOT EDIT  
  
gui_Singleton = 1;  
  
gui_State = struct('gui_Name',    mfilename, ...  
                  'gui_Singleton', gui_Singleton, ...  
                  'gui_OpeningFcn', @kineticGUI_OpeningFcn, ...  
                  'gui_OutputFcn', @kineticGUI_OutputFcn, ...  
                  'gui_LayoutFcn', [], ...  
                  'gui_Callback', []);  
  
if nargin && ischar(varargin{1})  
    gui_State.gui_Callback = str2func(varargin{1});  
  
end  
  
if narginout  
    [varargout{1:nargout}] = gui_mainfcn(gui_State, varargin{:});  
  
else  
    gui_mainfcn(gui_State, varargin{:});  
  
end  
  
% End initialization code - DO NOT EDIT  
  
% --- Executes just before kineticGUI is made visible.
```

```
function kineticGUI_OpeningFcn(hObject, eventdata, handles, varargin)
```

```
% This function has no output args, see OutputFcn.
```

```
% hObject handle to figure
```

```
% eventdata reserved - to be defined in a future version of MATLAB
```

```
% handles structure with handles and user data (see GUIDATA)
```

```
% varargin command line arguments to kineticGUI (see VARARGIN)
```

```
% Choose default command line output for kineticGUI
```

```
handles.output = hObject;
```

```
set(hObject, 'toolbar', 'figure');
```

```
% Update handles structure
```

```
guidata(hObject, handles);
```

```
cla
```

```
% UIWAIT makes kineticGUI wait for user response (see UIRESUME)
```

```
% uiwait(handles.figure1);
```

```
% --- Outputs from this function are returned to the command line.
```

```
function varargout = kineticGUI_OutputFcn(hObject, eventdata, handles)
```

```
% varargout cell array for returning output args (see VARARGOUT);
```

```
% hObject handle to figure
```

```
% eventdata reserved - to be defined in a future version of MATLAB
```

```
% handles structure with handles and user data (see GUIDATA)
```

```
% Get default command line output from handles structure
```

```
varargout{1} = handles.output;
```

```
%% THESE ARE THE BASIC INPUTS
```

```
function input100_Callback(hObject, eventdata, handles)
```

```
%store the contents of input100 as a string. if the string
```

```
%is not a number then input will be empty
```

```
input = str2num(get(hObject,'String'));
```

```
%checks to see if input is empty. if so, default input1_editText to 1
```

```
if (isempty(input))
```

```
    set(hObject,'String','1')
```

```
end
```

```
guidata(hObject, handles)
```

```
% --- Executes during object creation, after setting all properties.
```

```
function input100_CreateFcn(hObject, eventdata, handles)
```

```
if ispc && isequal(get(hObject,'BackgroundColor'), get(0,'defaultUicontrolBackgroundColor'))
```

```
    set(hObject,'BackgroundColor','white');
```

```
end
```

```
function input110_Callback(hObject, eventdata, handles)
```

```
input = str2num(get(hObject,'String'));
```

```
%checks to see if input is empty. if so, default input110 to 1
```

```
if (isempty(input))
```

```
    set(hObject,'String','1')
```

```
end
```

```
guidata(hObject, handles);
```

% --- Executes during object creation, after setting all properties.

```
function input110_CreateFcn(hObject, eventdata, handles)
```

```
if ispc && isequal(get(hObject,'BackgroundColor'), get(0,'defaultUicontrolBackgroundColor'))
```

```
    set(hObject,'BackgroundColor','white');
```

```
end
```

```
function input111_Callback(hObject, eventdata, handles)
```

```
input = str2num(get(hObject,'String'));
```

%checks to see if input is empty. if so, default input111 to 1

```
if (isempty(input))
```

```
    set(hObject,'String','1')
```

```
end
```

```
guidata(hObject, handles);
```

% --- Executes during object creation, after setting all properties.

```
function input111_CreateFcn(hObject, eventdata, handles)
```

```
if ispc && isequal(get(hObject,'BackgroundColor'), get(0,'defaultUicontrolBackgroundColor'))
```

```
    set(hObject,'BackgroundColor','white');
```

```
end
```

```
function reentrantenhancement_Callback(hObject, eventdata, handles)
```

```
input = str2num(get(hObject,'String'));
```

%checks to see if input is empty. if so, default input to zero

```
if (isempty(input))
```

```
    set(hObject,'String','0')
```

```

end

guidata(hObject, handles);

% --- Executes during object creation, after setting all properties.

function reentrantenhancement_CreateFcn(hObject, eventdata, handles)

if ispc && isequal(get(hObject,'BackgroundColor'), get(0,'defaultUicontrolBackgroundColor'))

    set(hObject,'BackgroundColor','white');

end

function twinenhancement_Callback(hObject, eventdata, handles)

input = str2num(get(hObject,'String'));

%checks to see if input is empty. if so, default input to zero

if (isempty(input))

    set(hObject,'String','0')

end

guidata(hObject, handles);

% --- Executes during object creation, after setting all properties.

function twinenhancement_CreateFcn(hObject, eventdata, handles)

if ispc && isequal(get(hObject,'BackgroundColor'), get(0,'defaultUicontrolBackgroundColor'))

    set(hObject,'BackgroundColor','white');

end

function disclinationenhancement_Callback(hObject, eventdata, handles)

input = str2num(get(hObject,'String'));

%checks to see if input is empty. if so, default input to zero

```

```

if (isempty(input))
    set(hObject,'String','0')
end

guidata(hObject, handles);

% --- Executes during object creation, after setting all properties.
function disclinationenhancement_CreateFcn(hObject, eventdata, handles)

%checks to see if input is empty. if so, default input to zero
if ispc && isequal(get(hObject,'BackgroundColor'), get(0,'defaultUicontrolBackgroundColor'))
    set(hObject,'BackgroundColor','white');
end

%BELOW ARE THE ADVANCED INPUTS
function calcstep_Callback(hObject, eventdata, handles)

input = str2num(get(hObject,'String'));

%checks to see if input is empty. if so, default calcstep to 0.5
if (isempty(input))
    set(hObject,'String','0.5')
end

guidata(hObject, handles)

% --- Executes during object creation, after setting all properties.
function calcstep_CreateFcn(hObject, eventdata, handles)

if ispc && isequal(get(hObject,'BackgroundColor'), get(0,'defaultUicontrolBackgroundColor'))
    set(hObject,'BackgroundColor','white');
end

```

```
end
```

```
function calcbound_Callback(hObject, eventdata, handles)
```

```
input = str2num(get(hObject,'String'));
```

```
%checks to see if input is empty. if so, default calcbound to 10
```

```
if (isempty(input))
```

```
    set(hObject,'String','10')
```

```
end
```

```
guidata(hObject, handles)
```

```
% --- Executes during object creation, after setting all properties.
```

```
function calcbound_CreateFcn(hObject, eventdata, handles)
```

```
if ispc && isequal(get(hObject,'BackgroundColor'), get(0,'defaultUicontrolBackgroundColor'))
```

```
    set(hObject,'BackgroundColor','white');
```

```
end
```

```
function smbox_Callback(hObject, eventdata, handles)
```

```
input = str2num(get(hObject,'String'));
```

```
%checks to see if input is empty. if so, default smbox to 5
```

```
if (isempty(input))
```

```
    set(hObject,'String','5')
```

```
end
```

```
guidata(hObject, handles)
```

```
% --- Executes during object creation, after setting all properties.
```

```
function smbox_CreateFcn(hObject, eventdata, handles)
```

```

if ispc && isequal(get(hObject,'BackgroundColor'), get(0,'defaultUicontrolBackgroundColor'))
set(hObject,'BackgroundColor','white');
end

function smbeta_Callback(hObject, eventdata, handles)
input = str2num(get(hObject,'String'));
%checks to see if input is empty. if so, default smalpha to 1
if (isempty(input))
    set(hObject,'String','1')
end

guidata(hObject, handles)
% --- Executes during object creation, after setting all properties.

function smbeta_CreateFcn(hObject, eventdata, handles)
if ispc && isequal(get(hObject,'BackgroundColor'), get(0,'defaultUicontrolBackgroundColor'))
    set(hObject,'BackgroundColor','white');
end

%% ACTION BUTTONS
% --- Executes on button press in clearfig. Clears figure
function clearfig_Callback(hObject, eventdata, handles)
%clears all axis
cla
guidata(hObject, handles); %updates the handles
% --- Executes on button press in modelsinglecrystal.

```

```
function modelsinglecrystal_Callback(hObject, eventdata, handles)
```

```
%define inputs
```

```
a_100 = get(handles.input100,'String');
```

```
a_100 = str2num(a_100);
```

```
a_110 = get(handles.input110,'String');
```

```
a_110 = str2num(a_110);
```

```
a_111 = get(handles.input111,'String');
```

```
a_111 = str2num(a_111);
```

```
beta=get(handles.smbeta,'String');
```

```
beta=str2num(beta);
```

```
box=get(handles.smbox,'String');
```

```
box=str2num(box);
```

```
bound=get(handles.calcbound,'String');
```

```
bound=str2num(bound);
```

```
step=get(handles.calcstep,'String');
```

```
step=str2num(step);
```

```
%update handles
```

```
guidata(hObject, handles);
```

```
%this models the wulff construction of a single crystal
```

```
isovalue=0.001;
```

```
for x=-bound:step:bound;
```

```

i=round((x+(bound))/step+1); %need to add this because i is used as the index of the matrix,
while x is used as the coordinate

for y=-bound:step:bound;

    j=round((y+(bound))/step+1);

    for z=-bound:step:bound;

        m=round((z+(bound))/step+1);

        Vtot(i,j,m) = 1;

        a = (x+y+z)/3. ;

        Vscalar=1;

        % Loop over all {100}, {110}, and {111} facets

        %this gives the value of the V

        for h=-1:1:1;

            for k=-1:1:1;

                for l=-1:1:1;

                    if Vscalar>1E-8;

gg = h*h+k*k+l*l ;

if abs( gg-1 ) < 1E-8 ; \

    amp = a_100 ;

elseif abs( gg-2 ) < 1E-8 ;

    amp = a_110/sqrt(2) ;

        else abs( gg-3 ) < 1E-8 ;

            amp = a_111/sqrt(3) ;

```

```

end %end of if elseif elseif statement

g = amp*[h,k,l] ;

% Multiply, again only the xyz within the
boundaries of the twin will have a non-
zero value for V

dotxyz_g=amp*(x*h+y*k+z*l); %i.e.
dot([x;y;z],g)

dotg_g=amp*amp*(gg); %gg calculated earlier
if dotxyz_g<dotg_g;

    F1=1;

else

    F1=exp(-beta*(dotxyz_g-dotg_g)*(dotxyz_g-dotg_g));

end

Vscalar = Vscalar*F1;

end % end if the if Vscalar statement

end %end of the for l statement

end %end of the for k statement

end % end of the for h statement

Vtot(i,j,m)=Vscalar;

end % end of the z loop

end % end of the y loop

end % end of the x loop

```

```
Vtotsm=smooth3(Vtot,'box',box);

%selects axes1 as the current axes, so that

%Matlab knows where to plot the data

axes(handles.axes1)

%create x, y, z grids

[mX,mY,mZ]=meshgrid(1:(((2*bound)/step)+1),1:(((2*bound)/step)+1),1:(((2*bound)/step)+1));

%create patch figure

p=patch(isosurface(mX,mY,mZ,Vtotsm,isovalue));

%set appropriate lighting, color and orientation for figure

set(p,'FaceColor',[.6,.1,0.1],'EdgeColor','none');

daspect([1 1 1])

material([0.4,0.3,0.1]);

lighting gouraud

view(135,40);

camlight(0,0);

camlight(0,0);

view(135,-40);

camlight(0,0);

axis tight

%update handles

guidata(hObject, handles)

% --- Executes on button press in modelmono.
```

```
function [Vtot,mX,mY,mZ]=modelmono_Callback(hObject, eventdata, handles)
```

```
%define inputs
```

```
a_100 = get(handles.input100,'String');
```

```
a_100 = str2num(a_100);
```

```
a_110 = get(handles.input110,'String');
```

```
a_110 = str2num(a_110);
```

```
a_111 = get(handles.input111,'String');
```

```
a_111 = str2num(a_111);
```

```
reentrant = get(handles.reentrantenhancement,'String');
```

```
reentrant=str2num(reentrant);
```

```
twin=get(handles.twinenhancement, 'String');
```

```
twin=str2num(twin);
```

```
beta=get(handles.smbeta,'String');
```

```
beta=str2num(beta);
```

```
box=get(handles.smbox,'String');
```

```
box=str2num(box);
```

```
bound=get(handles.calcbound,'String');
```

```
bound=str2num(bound);
```

```
step=get(handles.calcstep,'String');
```

```
step=str2num(step);
```

```
%update handles
```

```
guidata(hObject, handles);
```

```

%this models the wulff construction of a crystal with two twins (one (111) twin plane).

%alpha should be smaller than the a values!

isovalue=0.001;

fint=[];

out=[];

g=[];

for x=-bound:step:bound;

    i=round((x+(bound))/step+1); %need to add this because i is used as the index of the matrix,
    while x is used as the coordinate

    for y=-bound:step:bound;

        j=round((y+(bound))/step+1);

        for z=-bound:step:bound;

            m=round((z+(bound))/step+1);

            Vtot(i,j,m) = 1;

            a = (x+y+z)/3. ;

            if a > 0; % Note, sign changed here

                xx = x ; yy = y ; zz = z;

            else

%           Mirror about the plane (111)

%           Since (a;a;a) is the vector along (111), subtract twice this

                xx = x -2*a ; yy = y -2*a ; zz = z -2*a;

            end

```

Vscalar=1; %i.e. if dot with 111 or -1-11 is smaller or equal to zero, the xyz point has a nonzero value of V

% Loop over all {100}, {110}, and {111} facets

%this gives the value of the V

for h=-1:1:1;

    for k=-1:1:1;

        for l=-1:1:1;

            if Vscalar>1E-8;

gg = h\*h+k\*k+l\*l ;

% If g.(111) is negative, we have re-entrant surfaces

% kinetic is an input ;

if dot([h;k;l],[1;1;1])<0; %i.e. if the face is re-

entrant type

    enhance=1.0+reentrant+twin;

% for the twin boundary growth enhancement, the faces

involved

% are the re-entrant (111) above, and the (100) faces

% (only need the positive ones because of symmetry)

elseif h+k+l == 1;

    if k+l == 0;

        enhance=1.0+twin ;

```

elseif l+h == 0;
    enhance=1.0+twin ;
elseif h+k == 0;
    enhance=1.0+twin ;
else
    enhance=1;
end
else enhance=1;
end
if abs( gg-1 ) < 1E-8 ;    % This is a trick to avoid
numerical inaccuracies
    amp = a_100 ;
elseif abs(gg-2) < 1E-8 ;
    amp = a_110/sqrt(2) ;
    else abs(gg-3) < 1E-8 ;
    amp = a_111/sqrt(3) ;
end %end of if elseif elseif statement
    g = amp*enhance*[h,k,l] ;
    % Multiply, again only the xyz within the
boundaries of the twin will have a non-
zero value for V

```

```

dotxyz_g=amp*enhance*(xx*h+yy*k+zz*l); %i.e.

    dot([x;y;z],g)

dotg_g=amp*amp*enhance*enhance*(gg); %gg

    calculated earlier

if dotxyz_g<dotg_g;

    F1=1;

else

    F1=exp(-beta*(dotxyz_g-dotg_g)*(dotxyz_g-dotg_g));

end

Vscalar = Vscalar*F1;

end % end if the if Vscalar statement

end %end of the for l statement

end %end of the for k statement

end % end of the for h statement

    Vtot(i,j,m)=Vscalar;

end % end of the z loop

end % end of the y loop

end % end of the x loop

Vtotm=smooth3(Vtot,'box',box);

%selects axes1 as the current axes, so that

%Matlab knows where to plot the data

axes(handles.axes1)

```

```

%create x, y, z grids

[mX,mY,mZ]=meshgrid(1:(((2*bound)/step)+1),1:(((2*bound)/step)+1),1:(((2*bound)/step)+1));

%create patch figure

p=patch(isosurface(mX,mY,mZ,Vtot,m,isovalue));

%set appropriate lighting, color and orientation for figure

set(p,'FaceColor',[.6,.1,0.1],'EdgeColor','none');

daspect([1 1 1])

material([0.4,0.3,0.1]);

lighting gouraud

view(135,40);

camlight(0,0);

camlight(0,0);

view(135,-40);

camlight(0,0);

axis tight

%update handles

guidata(hObject, handles)

% --- Executes on button press in modelpenta.

function [mX,mY,mZ,Vtot]=modelpenta_Callback(hObject, eventdata, handles)

%create matrix for values

```

```
a_100 = get(handles.input100,'String');
a_100 = str2num(a_100);
a_110 = get(handles.input110,'String');
a_110 = str2num(a_110);
a_111 = get(handles.input111,'String');
a_111 = str2num(a_111);
reentrant = get(handles.reentrantenhancement,'String');
reentrant=str2num(reentrant);
disclination = get(handles.disclinationenhancement,'String');
disclination=str2num(disclination);
beta=get(handles.smbeta,'String');
beta=str2num(beta);
box=get(handles.smbox,'String');
box=str2num(box);
bound=get(handles.calcbound,'String');
bound=str2num(bound);
step=get(handles.calcstep,'String');
step=str2num(step);
guidata(hObject, handles);
isovalue=0.001;
%bound/step must be an integer
%create matrix for values
```

```

Vtot=zeros(4*bound/step+1,4*bound/step+1,4*bound/step+1);

for x=-bound:step:bound;

    i=((x+(bound))/step+1+bound/step);

    % need to add this because i is used as the index of the matrix, while x is used as the
coordinate

    for y=-bound:step:bound;

        j=((y+(bound))/step+1+bound/step);

        for z=-bound:step:bound;

            m=((z+(bound))/step+1+bound/step);

            %twin segments 0 to 4

            for n=0:1:4;

                angle=72*n;

                angrad=angle*2*pi/360;

                %compute rotation matrix R

                axee=[1,-1,0];

                L = norm(axee);

                axee = axee / L;

                L = 1;

                u = axee(1);

                v = axee(2);

                w = axee(3);

                u2 = u^2;

```

```

v2 = v^2;

w2 = w^2;

c = cos(angrad);

s = sin(angrad);

%storage

R = nan(3);

%fill

R(1,1) = u2 + (v2 + w2)*c;

R(1,2) = u*v*(1-c) - w*s;

R(1,3) = u*w*(1-c) + v*s;

R(2,1) = u*v*(1-c) + w*s;

R(2,2) = v2 + (u2+w2)*c;

R(2,3) = v*w*(1-c) - u*s;

R(3,1) = u*w*(1-c) - v*s;

R(3,2) = v*w*(1-c)+u*s;

R(3,3) = w2 + (u2+v2)*c;

dotwith111=dot([x;y;z],R*[1;1;1]);

dotwith_1_11=dot([x;y;z],R*[-1;-1;1]);

if dotwith111>0;

% Twin Facet #2

if dotwith_1_11>0;

```

```

Vscalar=1; %i.e. if dot with 111 or -1-11 is smaller or
equal to zero, the xyz point has a nonzero value of V
% Loop over all {100}, {110}, and {111} facets
%this gives the value of the V
for h=-1:1:1;
    for k=-1:1:1;
        for l=-1:1:1;
            if Vscalar>1E-8;
                [hklrot]=R*[h;k;l];
                hh=hklrot(1,1);
                kk=hklrot(2,1);
                ll=hklrot(3,1);
                gg = hh*hh+kk*kk+ll*ll ;
                %a [hkl] will be re-entrant if either its
                %dot product with 111 or with -1-11 is
                %smaller than zero
                if dot([h;k;l],[1;1;1])<0;
                    %dot([hh;kk;ll],R*[1;1;1])<0;
                    enhance=1.0+reentrant ;
                elseif dot([h;k;l],[-1;-1;1])<0;
                    %dot(R*[hh;kk;ll],R*[-1;-1;1])<0;
                    enhance=1.0+reentrant ;
            end
        end
    end
end

```

```

%use the same variable name, renhance,
%for both reentrant and disclination
%enhancement; they occur on different
%faces and NEVER occur at the same time

else

    if disclination==0; %in this case no
disclination enhancement was input by the user
        enhance=1;
    else
        %this part of the code only gets
        %calculated if there is a
        %disclination enhancement input
        if h~=0 ;
            if k~=0;
                if l~=0; %the disclination enhancement only occurs at the {111}
facets which are NOT re-entrant
                    enhance=1+disclination;
                else
                    enhance=1;
                end
            else
                enhance=1;
            end
        end
    end

```

```

        end

    else

        enhance=1;

    end

end

end

if abs( gg-1 ) < 1E-8 ;
    amp = a_100 ;
elseif abs(gg-2) < 1E-8 ;
    amp = a_110/sqrt(2) ;
else abs(gg-3) < 1E-8 ;
    amp = a_111/sqrt(3) ;
end

g = amp*enhance*[hh,kk,ll] ;

% Multiply, again only the xyz within the
boundaries of the twin will have a non-
zero value for V

dotxyz_g=amp*enhance*(x*hh+y*kk+z*ll);
                                %i.e. dot([x;y;z],g)

dotg_g=amp*amp*enhance*enhance*(gg);
                                %gg calculated earlier

if dotxyz_g<dotg_g;

```

```
        F1=1;

    else

        F1=exp(-beta*(dotxyz_g-dotg_g)*(dotxyz_g-dotg_g));

    end

    Vscalar = Vscalar*F1;

end

end

end

end

Vtot(i,j,m)=Vscalar;

end

end

end

end

end

end

clear n

clear ii

clear jj

clear mm

clear R

clear rotated
```

```
clear x

clear y

clear z

clear i

clear j

clear m

%selects axes1 as the current axes, so that

%Matlab knows where to plot the data

axes(handles.axes1)

Vtotm=smooth3(Vtot, 'box', box);

%create x, y, z grids

[mX,mY,mZ]=meshgrid(1:(((4*bound)/step)+1),1:(((4*bound)/step)+1),1:(((4*bound)/step)+1));

%create patch figure

p=patch(isosurface(mX,mY,mZ,Vtotm,isovalue));

%set appropriate lighting, color and orientation for figure

set(p,'FaceColor',[0.2,.4,0.6],'EdgeColor','none');

daspect([1 1 1])

material([0.4,0.3,0.1]);

lighting gouraud

axis tight

view(-135,0);

camlight(0,0);
```

```

view([45,-60])

camlight(0,0);

view(45,75);

camlight(0,0);

view([90,-90,0]);

handles.particledata=Vtot;

guidata(hObject, handles)

% --- Executes on button press in savefigure.

function savefigure_Callback(hObject, eventdata, handles)

axesObject = handles.axes1;

%stores savepath for the phase plot

[filename, pathname] = uiputfile({ '*.emf','Enhanced Meta File (*.emf)';...
    '*.bmp','Bitmap (*.bmp)'; '*.fig','Figure (*.fig)'}, ...
    'Save picture as','default');

%cancel save command

if isequal(filename,0) || isequal(pathname,0)

    return

end

%new fig

newFig = figure;

%get the units and position of the axes object

axes_units = get(axesObject,'Units');

```

```
axes_pos = get(axesObject,'Position');  
  
%copies axesObject onto new figure  
axesObject2 = copyobj(axesObject,newFig);  
  
%realign the axes object on the new figure  
set(axesObject2,'Units',axes_units);  
  
set(axesObject2,'Position',[15 5 axes_pos(3) axes_pos(4)]);  
  
%adjusts the new figure  
set(newFig,'Units',axes_units);  
  
set(newFig,'Position',[15 5 axes_pos(3)+30 axes_pos(4)+10]);  
  
%saves the plot  
saveas(newFig,fullfile(pathname, filename))  
  
%closes the figure  
close(newFig)
```

## VITA

# EMILIE RINGE

Department of Chemistry, Northwestern University,  
2145 Sheridan Road, Evanston, IL 60208-3113 USA  
E-mail: emilieringe@u.northwestern.edu

## EDUCATION

---

- Ph.D.**            **Northwestern University, Evanston, IL, USA**            2012  
Materials Chemistry  
Research advisors: Prof. Richard P. Van Duyne and Laurence D. Marks  
Thesis Title: *Building the Nanoplasmonics Toolbox Through Shape Modeling and Single Particle Optical Studies*
- Northwestern University, Evanston, IL, USA**            2011  
Kellogg Certificate in Management for Scientists and Engineers
- B.A./M.S.**       **Northwestern University, Evanston, IL, USA**            2008  
Inorganic Chemistry (transfer from McGill), Summa Cum Laude  
Research advisor: Prof. James A. Ibers  
Thesis Title: *Structure Determination and Characterization of UCuOP, UCu<sub>0.6</sub>Sb<sub>2</sub> and UFeSe<sub>3</sub>, Three Uranium Compounds Containing a First Row Transition Metal*
- McGill University, Montreal, Qc, Canada**            2003  
Two out of three years towards Bachelor of Science in Chemistry

## RESEARCH EXPERIENCE

---

- Research Fellow**, Trinity Hall, Cambridge University, UK            Starting October 2012  
**Graduate Student**, Northwestern University, Evanston, IL, USA            2008-2012  
**Visiting Researcher**, The University of Melbourne, Melbourne, VIC, Australia (3 months)            2011  
**Undergraduate Researcher**, Northwestern University, Evanston, IL, USA            2006-2008  
**Intern Formulation Researcher**, Merck Frosst Canada, Kirkland, Qc, Canada (16 months)            2005-2006

## TEACHING & MENTORING

---

- Guest Lecturer**, TEM sample preparation of nanoparticles, undergraduate and graduate TEM classes, Northwestern University            2012  
**Graduate Researcher Mentor**, Northwestern University            2011-present  
**Undergraduate Researcher Mentor**, Northwestern University            2009-2010  
**Summer Intern Mentor**, Northwestern University            2009-2011  
**General Chemistry Teaching Assistant**, Northwestern University            2008-2010  
**General Chemistry Tutor**, Northwestern University            2007- 2009  
**General Chemistry Teaching Assistant**, CEGEP Andre-Laurendeau, Qc            2002- 2003

## LEADERSHIP &amp; OUTREACH

---

<b>Gordon Research Seminar Chair</b> , Noble Metal Particles Conference	2012
<b>Science Books Reader and Recorder, Guide Runner</b> , Blind Services Association	2009-present
<b>Materials Research Center Student Leader</b> , Northwestern University	2011-2012
<b>Outreach Chair</b> , Presidential Fellows Society, Northwestern University	2011-2012
<b>Volunteer Speaker</b> , Science Speaker Corps, Northwestern University	2009-2012
<b>Assistant and Props Master</b> , ETOPIA, science-themed plays, Northwestern University	2009-2011
<b>Outreach Volunteer</b> , Middle and Elementary school science clubs	2009-2011
<b>Chemistry Laboratory Tour Guide</b> , NanoScout day, Bring your daughter to work day	2009-2010
<b>Outreach Leader</b> , Chute Middle School	2009

## FELLOWSHIPS, SCHOLARSHIPS, AND GRANTS

---

<b>Science Research Fellowship</b> , Trinity Hall, Cambridge University	2012
<b>Presidential Fellowship</b> , Northwestern University	2011
<b>International Research Fellowship</b> , The University of Melbourne	2011
<b>MRSEC Special Merit Fellowship</b> , Northwestern University	2010
<b>Lewis H. Sarrett Scholarship</b> , Northwestern University	2007
<b>Undergraduate Research Grant</b> , Northwestern University	2007
<b>Herbert Brennen Scholarship</b> , McGill University	2005

## DISTINCTIONS AND AWARDS

---

<b>Anna Louise Hoffman Excellence Award</b> , Iota Sigma Pi Society for Women in Chemistry	2012
<b>Featured in the Office for Research Excellence in Research Report</b> , Northwestern University	2012
<b>Best Poster Award</b> , 5 <sup>th</sup> International Conference on Surface Plasmon Photonics	2011
<b>Best Poster Award</b> , Noble Metal Particles Gordon Research Conference	2010
<b>B.A. Summa Cum Laude, with Departmental Honors</b> , Northwestern University	2008
<b>Dean's Honor List</b> , Northwestern University	2008
<b>Marple-Schweitzer Memorial Award</b> , Northwestern University	2008
<b>Award for Outstanding Suggestion on Procedure Improvement</b> , Merck Frosst	2005

## PUBLICATIONS

---

(17) **E. Ringe**, A.-I. Henry, B. Sharma, L. D. Marks, and R. P. Van Duyne “Single Particle Studies of Plasmonic Systems: Fundamentals and Applications”, Invited Review, *Phys. Chem. Chem. Phys.*, *In Preparation*

(16) **E. Ringe\***, A. Grubisic\*, C. Cobley, Y. Xia, L. D. Marks, R. P. Van Duyne, and D. J. Nesbitt “Plasmon-induced Electric Near-field Enhanced Coherent Multiphoton Photoelectron Emission from Individual, Supported Ag Nanocubes”, *Submitted*

- (15) L. Koscielski, **E. Ringe**, R. P. Van Duyne, D. E. Ellis, and J. A. Ibers “Single-Crystal Structures, Optical Absorption, and Electronic Distributions of Thorium Oxychalcogenides ThOQ (Q = S, Se, Te)”, *Submitted*
- (14) **E. Ringe**, R. P. Van Duyne, and L. D. Marks “Kinetic and Thermodynamic Modified Wulff Constructions for Twinned Nanoparticles”, *Submitted*
- (13) **E. Ringe**, J. Zhang, M. R. Langille, C. A. Mirkin, L. D. Marks, and R. P. Van Duyne “Correlating the Structure and Localized Surface Plasmon Resonance of Single Silver Right Bipyramids”, (2012) *Nanotechnology*, *In Press*
- (12) **E. Ringe**, M. R. Langille, K. N. Sohn, J. Huang, C. A. Mirkin, R. P. Van Duyne, and L. D. Marks “Plasmon Length: A Universal Parameter to Describe Size Effects in Gold Nanoparticles”, *J. Phys. Chem. Lett.* (2012), 3, 1479-1483
- (11) B. Sharma, A.-I. Henry, R. R. Frontiera, **E. Ringe**, and R. P. Van Duyne “Plasmonic Materials Enable New Directions in Surface Enhanced Raman Spectroscopy”, *Mater. Today* (2012), 15, 16-25
- (10) G. Oh, **E. Ringe**, R. P. Van Duyne, and J. A. Ibers “Synthesis, Structure, and Optical Properties of CsU<sub>2</sub>(PO<sub>4</sub>)<sub>3</sub>”, *J. Solid State Chem.* (2012), 185, 124-129
- (9) **E. Ringe**, R. P. Van Duyne, and L. D. Marks, “Wulff Construction for Alloy Nanoparticles”, *Nano Lett.* (2011), 11, 3399-3403. **Science Editor's Choice, Aug. 5 2011**
- (8) A.-I. Henry, J. M. Bingham, **E. Ringe**, L. D. Marks, G. C. Schatz, and R. P. Van Duyne, “Correlated Structure and Optical Property Studies of Plasmonic Nanoparticles”, *J. Phys. Chem. C* (2011), 115, 9291-9305
- (7) S. L. Kleinman, **E. Ringe**, N. Valley, K. L. Wustholz, E. Phillips, K. A. Scheidt, G. C. Schatz, and R. P. Van Duyne, “Single-Molecule Surface-Enhanced Raman Spectroscopy of Crystal Violet Isotopologues: Theory and Experiment”, *J. Am. Chem. Soc.* (2011), 133, 4115-4122
- (6) D. M. Wells, **E. Ringe**, D. Kaczorowski, G. Andre, D. E. Ellis, and J. A. Ibers, “Structure, Properties, and Theoretical Electronic Structure of UCuOP and NpCuOP”, *Inorg. Chem.*, (2011), 50, 576-589
- (5) **E. Ringe**, J. M. McMahon, K. N. Sohn, C. Cobley, Y. Xia, J. Huang, G. C. Schatz, L. D. Marks, and R. P. Van Duyne, “Unraveling the Effects of Size, Composition, and Substrate on the Localized Surface Plasmon Resonance Frequency of Gold and Silver Nanocubes: A Systematic Single Particle Approach”, *J. Phys. Chem. C* (2010), 114, 12511-12516
- (4) G. B. Jin, **E. Ringe**, G. J. Long, F. Grandjean, M. T. Sougrati, E. S. Choi, D. M. Wells, M. Balasubramanian, and J. A. Ibers, “Structural, Electronic, and Magnetic Properties of UFeS<sub>3</sub> and UFeSe<sub>3</sub>”, *Inorg. Chem.* (2010), 49, 10455-10467
- (3) **E. Ringe**, J. Zhang, M. R. Langille, K. N. Sohn, C. Cobley, L. Au, Y. Xia, C. A. Mirkin, J. Huang, L. D. Marks, and R. P. Van Duyne, “Effect of Size, Shape, Composition, and Support Film on Localized Surface Plasmon Resonance Frequency: A Single Particle Approach Applied to Silver Bipyramids and Gold Nanocubes”, *Mat. Res. Soc. Symp. Proc.* (2010), 1208-O10-02

(2) P. Li, C. L. Stender, **E. Ringe**, L. D. Marks, and T. W. Odom, “Synthesis of TaS<sub>2</sub> Nanotubes From Ta<sub>2</sub>O<sub>5</sub> Nanotube Templates”, *Small* (2010), 6, 1096-1099

(1) **E. Ringe** and J. A. Ibers, “Partial Cu Occupancy in Uranium Copper Diantimonide, UCu<sub>0.60(4)</sub>Sb<sub>2</sub>”, *Acta Crystallogr. Sect. C Cryst. Struct. Comm.* (2008), 64, i76-i78

## CONFERENCES AND PRESENTATIONS

---

**E. Ringe**, R. P. Van Duyne, and L. D. Marks, “Nanoplasmonics: Harnessing Light at the 100 nm Level”, Advanced Photon Source, Argonne National Laboratory, IL, USA, invited presentation (2012)

**E. Ringe**, R. P. Van Duyne, and L. D. Marks, “Size, Shape, and Composition Effects on Plasmonic Properties of Nanoparticles”, 3<sup>rd</sup> International Conference on Metamaterials, Photonic Crystals and Plasmonics, Paris, France, invited presentation (2012)

**E. Ringe**, R. P. Van Duyne, and L. D. Marks, “Fundamental and Applications of Plasmonic Particles”, Chemistry Seminar, Olive Harvey College, Chicago, IL, USA, presentation (2012)

**E. Ringe**, R. P. Van Duyne, and L. D. Marks, “Nanotechnology Research at Northwestern University”, Seminar to Chemistry Undergraduates; “Nanoparticle Shape: Effects and Modeling”, Department of Chemistry Seminar, New York University, New York, NY, USA, presentation (2011)

**E. Ringe**, M. A. Langille, J. Zhang, C. A. Mirkin, L. D. Marks, and R. P. Van Duyne, “Single Particle Correlated LSPR/HRTEM Studies: Making Leaps Towards Fundamental Understanding of Structure-Function Relationships in Plasmonic Nanoparticles”, Nanoplasmonics Sensors and Spectroscopy Conference, Gothenburg, Sweden, presentation (2011)

**E. Ringe**, R. P. Van Duyne, and L. D. Marks, “Nanoparticle Shape: Effects and Modeling”, Department of Physics, Imperial College London, London, UK, presentation (2011); Department of Materials Science and Metallurgy, Cambridge University, Cambridge, UK, presentation (2011)

**E. Ringe**, M. A. Langille, J. Zhang, C. Cobley, Y. Xia, C. A. Mirkin, R. P. Van Duyne, and L. D. Marks, “Nanoplasmonics, One Particle at a Time”, 5<sup>th</sup> International Conference on Surface Plasmon Photonics, Busan, South Korea, poster (2011)

**E. Ringe**, L. D. Marks, and R. P. Van Duyne, “Nanoplasmonics: One Particle at a Time”, Department of Physics, The University of Melbourne, Melbourne, VIC, Australia, presentation (2011)

**E. Ringe**, L. D. Marks, and R. P. Van Duyne, “Nanoparticles: Applications and Current Research”, Oakton Community College STEM Mentoring Program, Des Plaines, IL, USA, presentation (2010); Evanston Township High School AP Physics Class, Evanston, IL, USA, presentation (2010)

**E. Ringe**, J. M. McMahon, K. N. Sohn, C. Cobley, Y. Xia, J. Huang, G. C. Schatz, L. D. Marks, and R. P. Van Duyne, “Unraveling the Effects of Size, Composition, and Substrate on the Localized Surface Plasmon Resonance Frequency of Gold and Silver Nanocubes: A Systematic Single Particle Approach”, Gordon Research Conference on Noble Metal Particles, South Hadley, MA, USA, poster (2010)

**E. Ringe**, J. Zhang, M. R. Langille, K. N. Sohn, C. Cobley, L. Au, Y. Xia, C. A. Mirkin, J. Huang, L. D. Marks, and R. P. Van Duyne, “Effect of Size, Shape, Composition, and Support Film on Localized Surface Plasmon Resonance Frequency: A Single Particle Approach Applied to Silver Bipyramids and Gold Nanocubes”, Materials Research Society Fall Meeting, Boston, MA, USA, presentation (2009)

**E. Ringe**, D. M. Wells, and J. A. Ibers, “Structure Determination and Characterization of UCuOP, UCu<sub>0.6</sub>Sb<sub>2</sub>, and UFeSe<sub>3</sub>”, Undergraduate research symposium, Northwestern University, Evanston, IL, USA, poster (2008)